

Grenoble Geomechanics Group

Activity Report #3

Equipe GéoMécanique
Laboratoire 3SR
October 2020

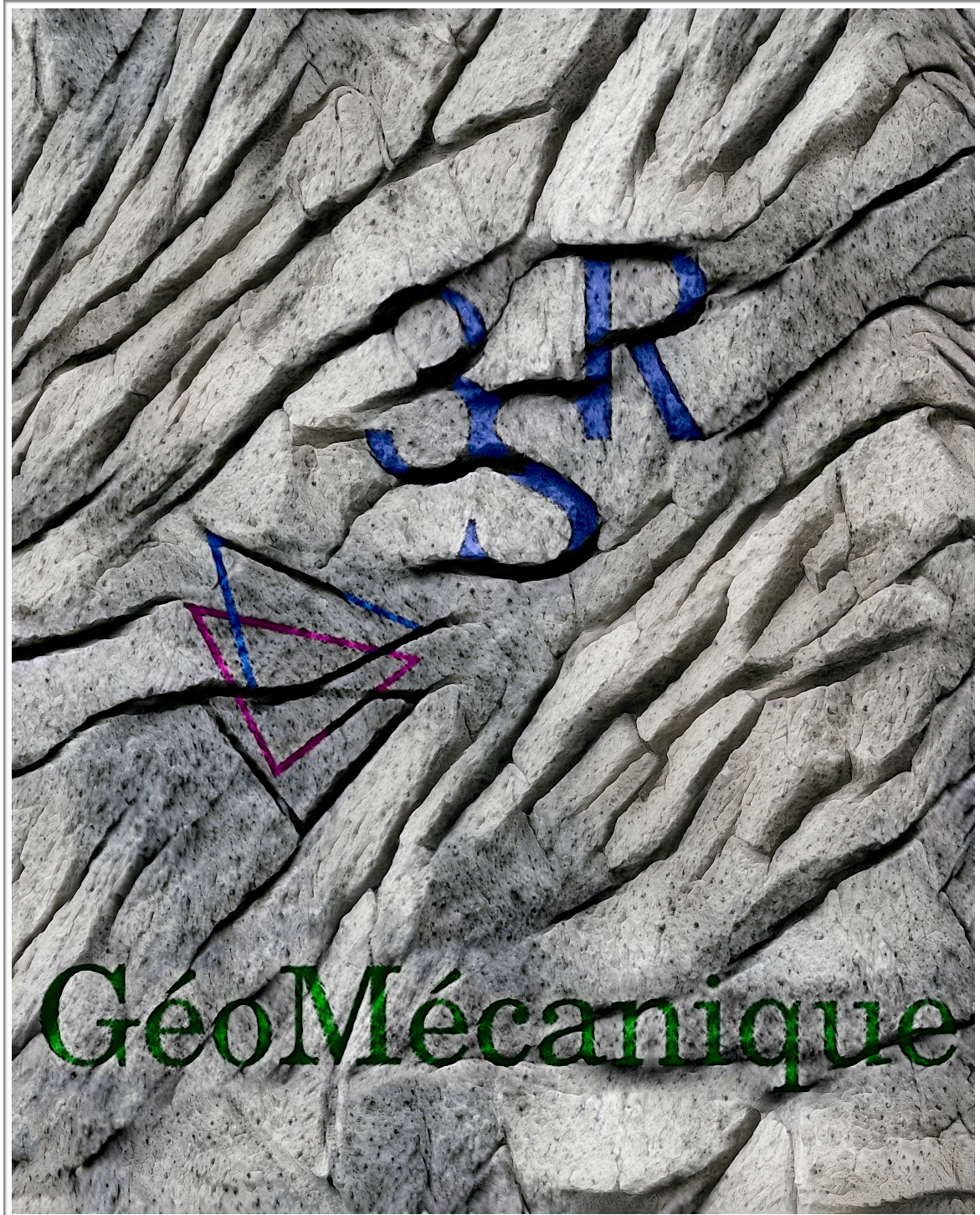


Image produced by Robert Caulk

Grenoble Geomechanics Group

Laboratoire 3SR

Université Grenoble Alpes

Domaine Universitaire

BP 53

38041 Grenoble cedex 9 France

Website: <https://3sr.univ-grenoble-alpes.fr>

Grenoble Geomechanics Group

Activity Report #3 (October 2020)

Issued by Vincent Richefeu & Antoine Mertz

Foreword

This book is the 3rd edition of the Activity Report of Grenoble Geomechanics Group, following the two reports published in 2014 and 2017. For the first time, it coincides with the presentation to the HCERES (High Council for Evaluation of Research and Higher Education in France) of the full record of activity of Laboratoire 3SR over the last 5 years. It was also an opportunity for the team to look to the future and to define the objectives and main themes that we would like to study over the next five years.

This report is by no means an exhaustive collection of the team's publications over the last 3 years, but it has been thought as an illustration of current and ongoing research topics, mainly in the context of PhD and post-docs. It also shows the variety of approaches developed by the team.

It corresponds to only a small part of the more than 200 papers published in the last 5 years by the staff members and PhD or MSc students (in the last 5 year period, 43 PhD theses and over 100 MSc projects have been defended).

Today, Grenoble Geomechanics Group is composed of 14 researchers (Université Grenoble Alpes, Grenoble Institute of Technology, and CNRS) and more than 25 PhD students on average, as well as 2 post-docs. The contributions included in the present Activity Report are organised in 4 themes:

- I. Multi-scale analysis of geomaterials
- II. Interfaces, soil–structure interactions and civil engineering structures
- III. Bio-chemo-mechanical interactions
- IV. Thermo-hydro-mechanical coupling

These themes define the research plan for the next 5 years that we have presented to the HCERES. The first two themes correspond to historical research domains of the team, while the last two are new topics to be developed in the next 5 years.

Enjoy reading these papers!

Contents

I Multi-scale analysis of geomaterials	5
Measuring the fabric evolution of particulate media during load reversals in triaxial tests	6
<i>Max WIEBICKE, Edward ANDÒ, Ivo HERLE, Gioacchino VIGGIANI</i>	
DEM modelling of brittle, crushable, hollow grains	13
<i>Marta STASIAK, Gaël COMBE, Vincent RICHEFEU, Pascal VILLARD</i>	
Effect of inherent anisotropy on fabric evolution of granular materials	20
<i>Gustavo PINZÓN, Edward ANDÒ, Alessandro TENGATTINI, Gioacchino VIGGIANI, Jacques DESRUES</i>	
NeXT-Grenoble, the Neutron and X-ray Tomograph in Grenoble	30
<i>Alessandro TENGATTINI, Nicolas LENOIR, Edward ANDÒ, Benjamin GIROUD, Duncan ATKINS, Jerome BEAUCOUR, Gioacchino VIGGIANI</i>	
A one parameter damageable contact law for the DEM study of cohesive granular materials	45
<i>Cyrille COUTURE, Jacques DESRUES, Vincent RICHEFEU, Pierre BÉSUELLE</i>	
II Interfaces, soil–structure interactions and civil engineering structures	53
Comparison of discrete element and material point methods for unsteady flow modelling	54
<i>Fabio GARCIA, Vincent RICHEFEU, Pascal VILLARD</i>	
Probabilistic modeling of tunnel seismic deformations: global sensitivity analysis	61
<i>Qiangqiang SUN, Daniel DIAS</i>	
Long-term monitoring of a geogrid installed beneath a ballast layer in operating conditions	73
<i>Olatoude YABA, Fabrice EMERIAULT, Oriane JENCK, J.-F. FERELLEC, A. DHEMAIED</i>	
Contribution to the analysis of the mechanical behaviour of the Laurichard rock glacier (French Alps) in the last decades and evaluation of its correlation with recent climatic changes	80
<i>Samia MELKI, Dominique DAUDON, Xavier BODIN, Emmanuel THIBERT</i>	
A simplified analytical method to estimate long term concrete lining stress in deep underground galleries	91
<i>Valentin MARTYNIK, Fabrice EMERIAULT, Roland PLASSART, Francois LAIGLE</i>	
Discrete numerical modelling of a cohesive soil layer reinforced by geosynthetic sheet using an advanced constitutive law	99
<i>Maria DELLI CARPINI, Pascal VILLARD, Fabrice EMERIAULT</i>	
Considerations for discrete modeling of geogrid-reinforced layers	106
<i>Marcus GUARDAGNIN MORAVIA, Pascal VILLARD, Delma DE MATTOS VIDAL</i>	

III Bio-chemo-mechanical interactions	115
Interaction between sand and a growing root studied by x-ray tomography	116
<i>Floriana ANSELMUCCI, Edward ANDÒ, Nicolas LENOIR, Robert PEYROUX, Gioacchino VIGGIANI, Glyn BENGOUGH, Chloé ARSON, Luc SIBILLE</i>	
IV Thermo-hydro-mechanical coupling	124
Micromechanical interpretation of thermo-plastic behaviour of clays	125
<i>Angela CASARELLA, Alessandro TARANTINO, Alice DI DONNA</i>	
Imaging hydromechanics of water-sensitive granular media	136
<i>Ilija VEGO, Alessandro TARANTINO, Edward ANDÒ, Gioacchino VIGGIANI, Nicolas LENOIR</i>	
Modelling the evolution of porosity distributions in compacted clay pellets during imbibition	142
<i>Robert CAULK, Nadia MOKNI, Bruno CHAREYRE</i>	

Part I

Multi-scale analysis of geomaterials

Measuring the fabric evolution of particulate media during load reversals in triaxial tests

Max WIEBICKE^{1,2,*}, Edward ANDÒ^{1,†}, Ivo HERLE^{2,‡}, Gioacchino VIGGIANI^{1,§}

¹ Univ. Grenoble Alpes, CNRS, Grenoble INP, 3SR, F-38000 Grenoble, France

² Institute for Geotechnical Engineering, Technische Universität Dresden, D-01062 Dresden, Germany

Abstract: The behaviour of granular materials upon load reversal is not yet fully understood. In order to experimentally reveal the microstructure of a specimen subjected to load-unload cycles, a triaxial compression test on lentils is carried out in the x-ray scanner. Before analysing the acquired tomographies, a benchmark analysis is conducted to validate the image analysis tools that are used to extract the fabric from these images. The contact fabric evolves strongly with the shearing in the experiment on lentils. However, only very slight changes of the anisotropy within the cycles are observed.

1 Introduction

Numerous studies have shown that the fabric of granular materials plays a fundamental role in its macroscopic behaviour. Due to technical limitations this fabric remained inaccessible in real experiments until recently. Thus, the research concentrated on either two-dimensional experiments [6] or post-mortem analyses of real specimen [8]. Discrete element simulations [2], on the other hand, served as a numerical tool to access the grain scale.

With the increasing use and capability of x-ray tomography in the mechanics of granular materials, the grain scale of real three-dimensional specimen finally became accessible. Special apparatus allow to acquire tomographies during a loading process. Determining the fabric from X-ray tomographies remains relatively challenging due to various inherent imaging properties, but recent developments improved the quantitative determination of fabric.

In this contribution we investigate the evolution of fabric due to load reversals. Load reversals lead to abrupt changes of the stiffness of granular materials, e.g., the stiffness increases whenever the loading is reversed. In [9] the fabric evolution in a triaxial test with load reversals has been investigated using discrete element simulations. It remains to be shown whether a similar behaviour can be measured from experiments on real granular materials. Another open question is whether the changes in fabric are sufficiently strong to be measured quantitatively considering the accuracy of these measurements [14].

At first, a benchmark study on the measurement of fabric changes in experiments with load reversals is carried out. Following the benchmark presented in [15] a series of synthetic, but realistic images is created from simulations with the discrete element method (DEM). DEM serves as the ground truth and enables a quantification of the accuracy of the image analysis tools that are to be used on real tomographies.

To investigate the evolution of contact fabric in a real experiment, a triaxial compression test with several unloading and reloading cycles was conducted in the x-ray scanner in Laboratoire

*Email: max.wiebicke@tu-dresden.de

†Email: edward.ando@3sr-grenoble.fr

‡Email: ivo.herle@tu-dresden.de

§Email: cino.viggiani@3sr-grenoble.fr

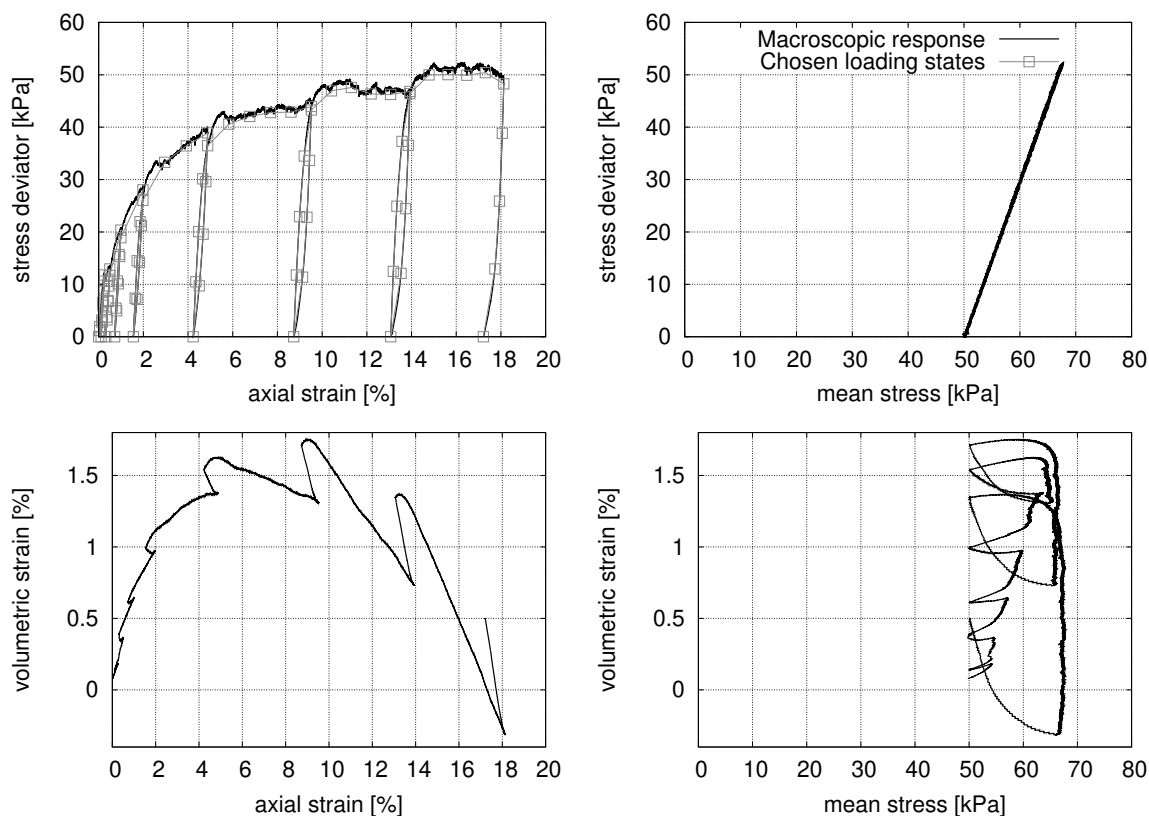


Figure 1: Macroscopic behaviour of the axisymmetric compression test of the DEM simulation. The chosen states for the image analysis are indicated by the grey squares

3SR in Grenoble. Here, we present preliminary results of the image analysis of the tomographies acquired during the experiment.

2 A numerical benchmark

In [15] we presented a benchmarking strategy to evaluate image analysis tools regarding their accuracy for measuring contact fabric. The example chosen was a monotonic axisymmetric compression test. As the aim of this study is the measurement of contact fabric and its changes during load reversals, another benchmark is carried out.

For this purpose, a discrete element simulation is carried out with the software woodem [11]. The boundaries in this simulation are periodic and a simple linear (Cundall) contact model with the following parameters is used: Young's modulus $E = 50 \cdot 10^6$ kPa, a ratio between normal and tangent stiffness of $k_t/k_n = 0.4$ and a friction angle of $\tan \varphi = 0.4$. A linear particle size distribution between $(3.2 \text{ and } 4.8) \cdot 10^{-4}$ m is chosen.

The sample of 5522 spheres is isotropically compressed to a pressure of 50 kPa. It is then compressed in the axial direction at constant radial stress. The loading is reversed until the isotropic stress state is reached and reloaded at several stages of the shearing. At chosen states, mainly when the loading direction is changed, the fabric of the specimen (positions of the spheres and contact orientations) is recorded. The macroscopic behaviour of the specimen is shown in Figure 1.

As in [15], images are created from these states using Kalisphaera [10], a tool to create images of spheres mathematically correct regarding the partial volume effect [12]. Inherent image deficiencies such as noise and blur are applied to the images to obtain realistic representations

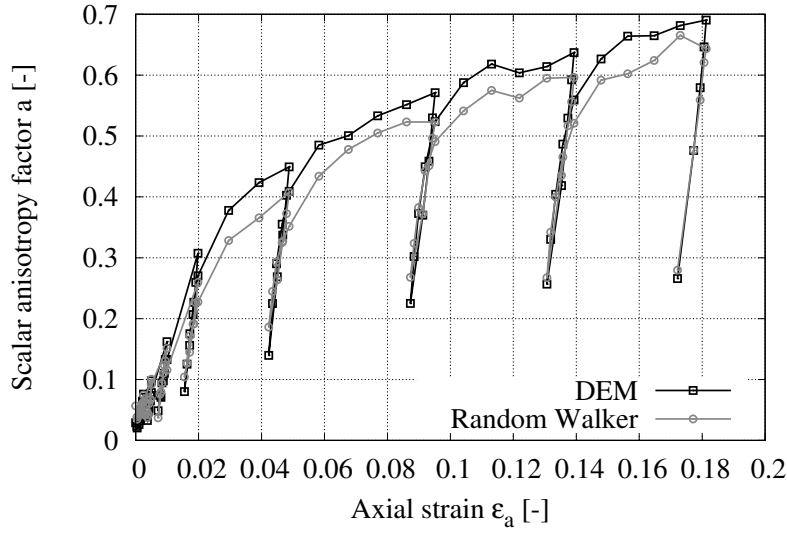


Figure 2: Evolution of the scalar anisotropy factor. Comparison between the ground truth of the simulation and the results of the image analysis.

of real tomographies, see [14] for further details. The image analysis is carried out with the open source software spam [1]. All analysis tools developed in [14] are implemented in spam. The grey-scale images are binarised first and then initially segmented with a VTK watershed. Contacts are detected in the labelled image and the systematic over-detection of contacts happening for grains of non-angular shape is addressed with a local refinement. The orientations are then calculated using the random walker segmentation [4] on each pair of contacting grains. See [14] for more details.

In this small study, we focus on the evolution of the anisotropy of the fabric tensor. The common second order fabric tensor \mathbf{N} [7] is chosen to statistically capture the contact orientations \mathbf{o} :

$$\mathbf{N} = \frac{1}{C} \sum_{\alpha=1}^C \mathbf{o}^{\alpha} \otimes \mathbf{o}^{\alpha} \quad (1)$$

with C being the number of orientations. The deviator of this tensor is calculated by:

$$\mathbf{D} = \frac{15}{2} (\mathbf{N} - \frac{1}{3} \mathbf{I}) \quad (2)$$

with \mathbf{I} being the identity tensor. A scalar anisotropy value a can be calculated from [5]:

$$a = \sqrt{\frac{3}{2} \mathbf{D} : \mathbf{D}} \quad (3)$$

The evolution of the scalar anisotropy factor in both, the reference DEM simulation and the image analysis, is plotted in Figure 2. With ongoing shearing the anisotropy is increasing as expected and shown in [15]. Upon reversing the loading direction, the anisotropy experiences a serious drop – at low strains the initial anisotropy is almost fully recovered, whereas at larger strains the anisotropy is not decreasing until its initial value. The results of the image analysis agree qualitatively to the reference and are only slightly lower in value. With these results, we expect to qualitatively and quantitatively capture the anisotropy in real experiments with load reversals.

All data necessary to carry out and repeat this benchmark or test other image analysis tools on the synthetic images is available in an open access repository [13].

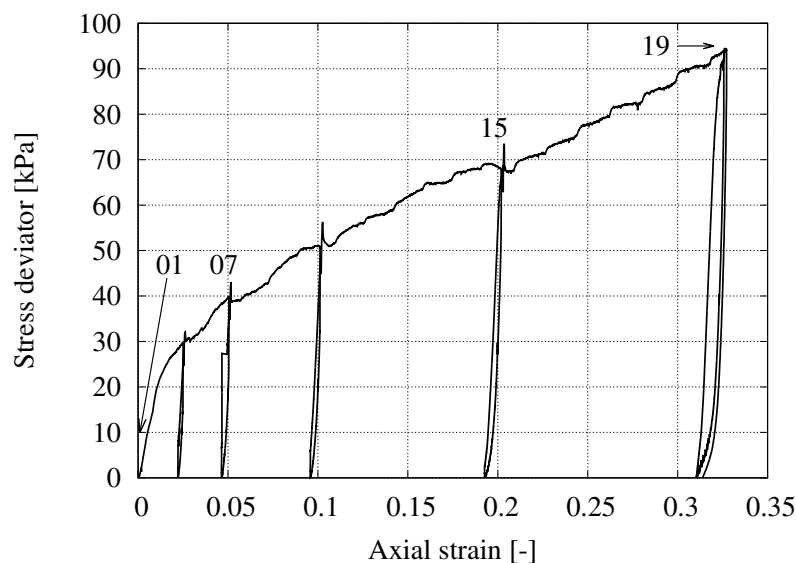


Figure 3: Stress-strain behaviour of the triaxial compression test on lentils. The identifiers mark the states that are analysed further.

3 Triaxial compression test on Lentils

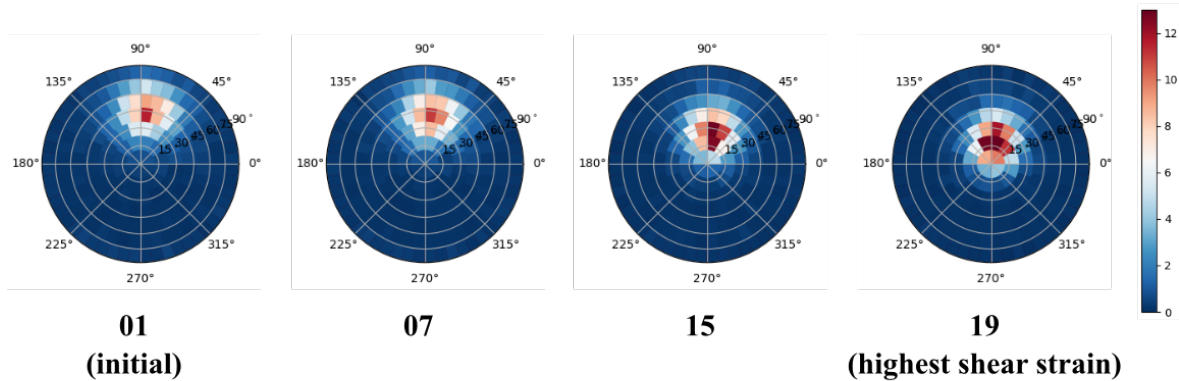
The experiment presented in this study is a triaxial compression test on Lentils. Lentils are chosen as part of a bigger study on the effect of initial anisotropy on the macroscopic as well as microscopic behaviour. The study, however, will not be discussed in this contribution.

The lentils are spooned into a mould in a way to have a 45° angle with respect to the axial direction in the final specimen. The dry specimen is then isotropically compressed to a pressure of 50 kPa. Similarly to the DEM simulation, the specimen is then sheared to chosen states. At these states, the loading direction is reversed until the initial isotropic stress state is almost reached and the specimen is reloaded again. Figure 3 shows the stress-strain behaviour of the specimen during the experiment.

The image analysis is carried out as described above for the synthetic images from DEM using the image analysis software spam. The evolution of contact as well as particle orientations is depicted in Figure 4 as Lambert azimuthal projection plots for the states marked in Figure 3. The particle orientations are calculated from the moment of inertia and its eigenvectors. The eigenvector corresponding to the largest eigenvalue represents the smallest representative length of the particle. Due to the shape of lentils, this eigenvector is considered to be the significant particle orientation and plotted in Figure 4. The particle fabric agrees well with the fabric that was targeted in the preparation of this specimen, an inherent 45° angle towards the vertical direction. The contact fabric is more spread, but also aligned to this targeted initial anisotropy. The wider spread is to be expected as the contacts have to provide stability in other directions than only the particle orientation. With ongoing shear the particle and contact orientations realign towards the major principal stress direction, *i.e.* the centre of the projection plots, but do not reach it at the highest applied shear strain.

The anisotropy as defined in equation (3) expresses the spread of the orientations of either contacts or particles. If the fabric is isotropically distributed, the anisotropy is zero, but in the extreme case it can obtain values of up to 7.5 if all orientations are pointing in the same direction. The evolution of the contact and particle fabric anisotropy is shown in Figure 2. As observed in Figure 4 the specimen inherently has a high initial anisotropy. In the first loading stage the contact anisotropy drops slightly, but with ongoing shear, this anisotropy is

Particle orientations



Contact orientations

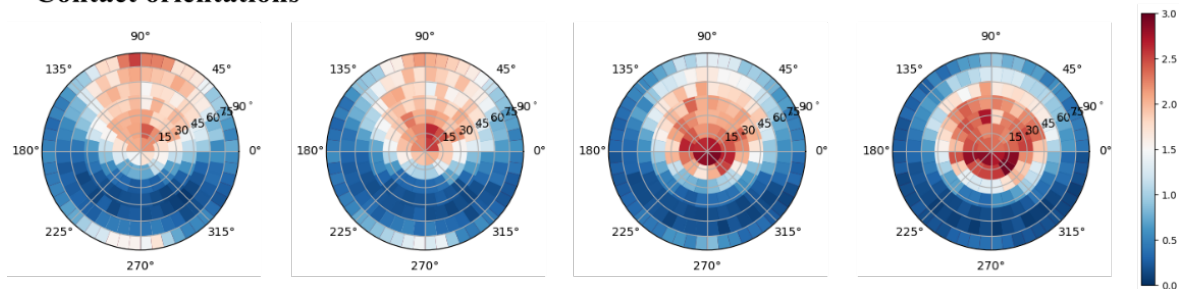


Figure 4: Lambert azimuthal equal area plots of particle and contact orientations at several states of the loading. The center of the image is the axial direction whereas the outer ring represents the axial plane. The orientations in each bin are normalised by the average orientations per bin.

increasing, which means that the orientations are concentrating even further in one direction. In the first load-unload cycles, the anisotropy stays almost constant but for the short spike at 0.05 axial strain. The latter cycles show a slight change of contact anisotropy that is increasing at increasing axial strain. This change, however is much smaller than the change in the DEM simulations from the benchmark simulation or [9]. The striking difference is the particle shape as well as the strong inherent anisotropy. It appears that the fabric is locked, which might be explained by the strong and inherent alignment of the lentils that prevents particles to realign. This locked state in terms of particle orientations is observed from the evolution of particle anisotropy in Figure 5. The anisotropy of the particle orientations stays almost constant upon unloading for the low strain as well as for the higher strain cycles.

Contact and particle anisotropy evolve with a highly similar slope. The main difference is the magnitude of the actual values, but the range of change and thus, the rate of change is identical. This is in strong accordance with the findings from 2D DEM simulations on ellipses in [3]¹.

4 Conclusion and perspectives

In this contribution, we present a preliminary analysis of a triaxial compression test on lentils regarding the fabric evolution due to unloading-reloading cycles. To benchmark the image analysis tools that should be used to extract the contact fabric from the real tomographies, a

¹It should be noted that our principal particle orientation is the short axis in contrast to [3], in which the longest axis was used as the reference particle orientation.

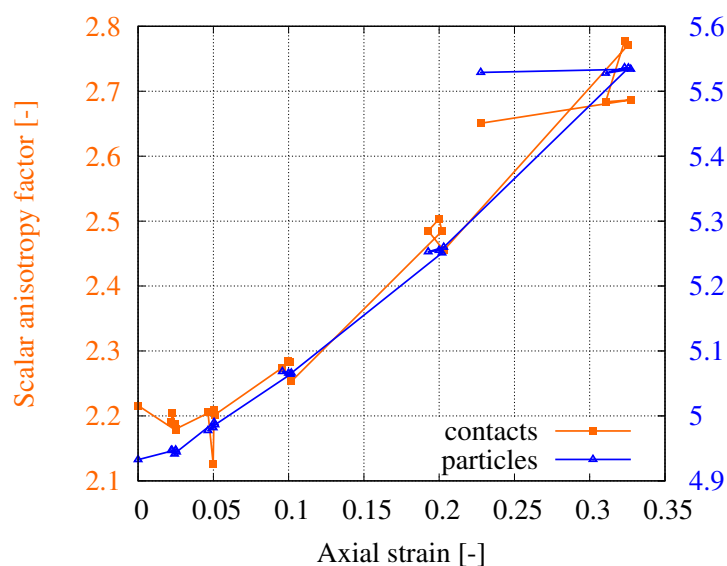


Figure 5: Evolution of anisotropy of contact and particle fabric in the triaxial compression test on lentils.

series of realistic, synthetic images was created on the basis of a DEM simulation. The image analysis of the synthetic images agrees qualitatively and quantitatively to the reference DEM simulation.

The experiment is prepared to have a strong inherent anisotropy with particles oriented 45° to the vertical direction. This initial anisotropy is increased further with shearing as the principal fabric direction aligns with the major principal stress. A serious change of fabric within the unload-reload cycles cannot be observed. A possible reason can be a locking of the fabric due to the strong inherent anisotropy and the similar particle shape of all particles. Another reason for the observations could be the fabric tensor we chose. Employing a different normalisation of the fabric tensor and/or a higher degree of approximation might show a different behaviour. Especially, at higher macroscopic shear strains, deformation localised in the specimen. An analysis extracting subsets might reveal a different and/or more pronounced fabric evolution. Subsets inside and outside the zones of localised deformation are to be extracted and the fabric will be calculated in these.

References

- [1] E. Andò, R. Cailletaud, E. Roubin, O. Stamati, and the spam contributors. spam: The software for the practical analysis of materials. <https://ttk.gricad-pages.univ-grenoble-alpes.fr/spam/>, 2017–.
- [2] P. A. Cundall and O. D. L. Strack. A discrete numerical model for granular assemblies. *Géotechnique*, 29(1):47–65, 1979.
- [3] Pengcheng Fu and YF Dafalias. Fabric evolution within shear bands of granular materials and its relation to critical state theory. *International Journal for Numerical and Analytical Methods in Geomechanics*, 35(18):1918—1948, 2011.
- [4] Leo Grady. Random walks for image segmentation. In *IEEE Transactions on Pattern Analysis and Machine Intelligence*, volume 28, 2006.

- [5] X. Gu, J. Hu, and M. Huang. Anisotropy of elasticity and fabric of granular soils. *Granular Matter*, 19(2):1–15, 2017.
- [6] K. Wiendieck. Zur Struktur körniger Medien. *Die Bautechnik*, 6:196–199, 1967.
- [7] K.-I. Kanatani. Distribution of directional data and fabric tensors. *International Journal of Engineering Science*, 22(2):149 – 164, 1984.
- [8] M. Oda. Initial fabrics and their relations to mechanical properties of granular material. *Soils and Foundations*, 12(1), 1972.
- [9] C. O’Sullivan and L. Cui. Micromechanics of granular material response during load reversals: Combined DEM and experimental study. *Powder Technology*, 193(3):289–302, aug 2009.
- [10] A. Tengattini and E. Andò. Kalisphera: an analytical tool to reproduce the partial volume effect of spheres imaged in 3D. *Measurement Science and Technology*, 26(9), 2015.
- [11] V. Šmilauer. *Woo Documentation*. 2016. <https://woodem.org>.
- [12] S. Weis and M. Schröter. Analyzing X-Ray tomographies of granular packings. *Review of Scientific Instruments*, (88), 2017.
- [13] M. Wiebicke. Benchmark analysis of synthetical images – source code and example dem data. <http://dx.doi.org/10.25532/OPARA-14>.
- [14] M. Wiebicke, E. Andò, I. Herle, and G. Viggiani. On the metrology of interparticle contacts in sand from x-ray tomography images. *Measurement Science and Technology*, 28(12):124007, 2017.
- [15] M. Wiebicke, V. Šmilauer, I. Herle, E. Andò, and G. Viggiani. Validation of Synthetic Images for Contact Fabric Generated by DEM. In *Proceedings of China-Europe Conference on Geotechnical Engineering*, 2018.

DEM modelling of brittle, crushable, hollow grains

Marta STASIAK^{1,*}, Gaël COMBE^{1,†}, Vincent RICHEFEU^{1,‡}, Pascal VILLARD^{1,§}

¹ Univ. Grenoble Alpes, CNRS, Grenoble INP, 3SR, 38000 Grenoble, France

Abstract: This paper is a brief overview of a work conducted over the course of PhD thesis. The work was made of discrete modelling of brittle, hollow particles which assembly shows highly compressible capacity. Grain breakage was the major aspect of investigations both at micro and macro scale. The numerical approach contributed to the field of modelling advanced shapes and the bonding particle technique, whereas the experimental campaign addressed some aspects of material characterisation.

1 Industrial motivation

Presented hereinafter research has been conducted for the benefit of the french agency of radioactive waste management, shortly referred to as Andra (*Agence nationale pour la gestion des déchets radioactifs*). This unit acts across various disciplines of science and engineering to pursue a construction of safe and long lasting underground repositories [1]. Aiming the efficiency of the deep-situ tunnel structure, a new type of the lining made of mono-block compressible arch-segment (*Voussoir Monobloc Compressible* VMC in French), has been proposed back in 2014 [2, 3, 4]. The VMC technology combines a standard reinforced concrete segment with an innovative compressible layer placed on the extrados. The layer is a peculiar, porous composite with weak cementation and a highly porous aggregate. A priori to this thesis, the standard geo-engineering tests (odometer and standard triaxial compression) have indicated that the granular core plays a key role in the layer compressibility, whereas the weak cementation is an improvement in terms of the bearing capacity. Eventually, our research work was dedicated to this highly porous, crushable granular material. The understanding of the mechanical behaviour, generating a numerical model and an analytical prediction were three main objective of the thesis. The analysis was conducted mainly within the numerical domain of Discrete Element modelling, yet an experimental part has been found most fruitful and beneficial in terms of the material characterisation.

2 Grain breakage at the micro scale

The compressible granulate is composed of the brittle, tubular particles; Figure 1. The hollow geometry of grain was designed especially to provide a large grain porosity. The tube and the cylindrical internal void are equal in volume, and therefore, the assembly becomes extremely porous. Within a sample, the particles were uniform in size and this study included two different grain sizes separately (diameter 2.0 cm or 1.8 cm; relative diameter 0.7; diameter to height ratio 1). The tubular geometry with a thin wall can be addressed as a cylindrical shell, thus, onwards word *shell* ought to be comprehended as an intact particle/grain.

*Email: marta.stasiak@3sr-grenoble.fr

†Email: gael.combe@3sr-grenoble.fr

‡Email: vincent.richefeu@3sr-grenoble.fr

§Email: pascal.villard@univ-grenoble-alpes.fr



Figure 1: Cylindrical *shell* – a brittle constituent of highly porous granular material.

At first, we engaged in the grain scale investigations. The work started with an experimental characterisation of shell breakage in the campaign of the uniaxial radial compression. Each shell compressed by a diametrical force experienced a brittle failure. The majority of shells broke radially into 4 parts and all the cracks have initiated in the point of the maximum tensile stress and propagated respecting mode *I* fracture (*i.e.*, the crack opening) [5]. As anticipated, the variability of the loading force was characterised as Weibullian, with wide distribution of the survival probability due to the geometrical imperfection and material heterogeneities. This step has essentially contributed to the generation of a reliable model of a breakable shell in terms of grain strength and breakage pattern.

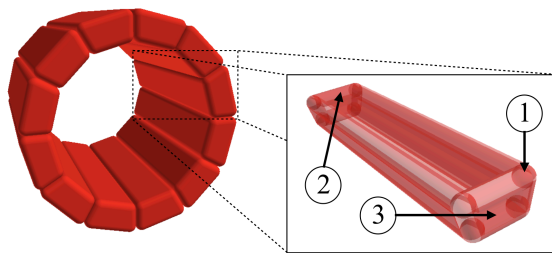


Figure 2: A tube-shaped shell modelled as a cluster of 12 rigid *sphero-polyhedral* elements called *sectors*. The sector is itself composed of sub-elements (spheres ①, tubes ② and thick planes ③) with no relative movement.

Numerically, the work relayed on Discrete Element Method that received a considerable attention in the domain of granular material and already offers a choice of the approach simulating breakage. The model was build upon the Bonded Particle Method in which smaller sub-particles are clustered together by means of the links, that is the cohesive contacts [6, 7, 8]. In-house code ROCKABLE (developed by V. Richefeu) offers an interesting alternative to generate highly complex shapes with *sphero-polyhedra*. A sphero-polyhedron is a rigid assemblage of simpler 3D shapes: spheres, tubes and thick planes; Figure 2. Those elements replace, respectively, the corners, edges and faces of classic, sharp-edged polyhedron. Clustering shapes other than sphere is rather a recent trend, and the technic of clustering sphero-polyhedra has been newly introduced in the field of geomechanics.

Respecting the radial slicing observed in the campaign of uniaxial radial compression URC, the elongated sphero-polyhedra have been joined together to form the cylindrical shell. Those elongated elements are called *sectors*; Figure 2. Within the cluster, there appears only the cohesive contact type, *link*, in which the elastic forces act. Then, the forces are constrained by a breakage criterion ruled by two user-specified parameters representing the material cohesion resistant to a pure tension f_I^* and a pure shear f_{II}^* for a predefined shape of the breakage criterion. Note that the model includes also the classic, linearly elastic and frictional contacts (between shells and/or in the torn links). Then, the characteristics of DEM require a whole more set of the discrete, numerical parameters (contact stiffnesses, friction coefficient and so forth). At

this point, the investigations of micro-scale aspects were dedicated to an identification of discrete parameters. Hence, a shell scale parametric study were conducted. Few adjustments, concerning the tensile failure, relayed on data form the experimental uniaxial radial shell compression (URC). Two significant relationships between the contact and shell variables were determined. The normal contact stiffness controlled the slope of the linear elastic mechanical response¹ of shell. The diametric force (for URC) was adjusted throughout the tensile yield contact force f_I^* (referring to the tensile strength of the material). Remaining parameters for the shear breakage were estimated using a numerical scheme. This part also pre-investigated the effect of the number of sectors per cluster. If division modifies the number of links breaking either in pure tension or pure shear, the force thresholds of links were affected, respectively. Similarly, when varying the radial slicing, the contact stiffnesses must have been adjusted. It was therefore significant to choose the amount and size of sectors prior to the large scale modelling. For the sake of calculation efficiency, the preferable discretisation included only the circumferential division into 12 sectors; Figure 2. However, this choice resulted in large sector size, actually, leading to a validity limit.

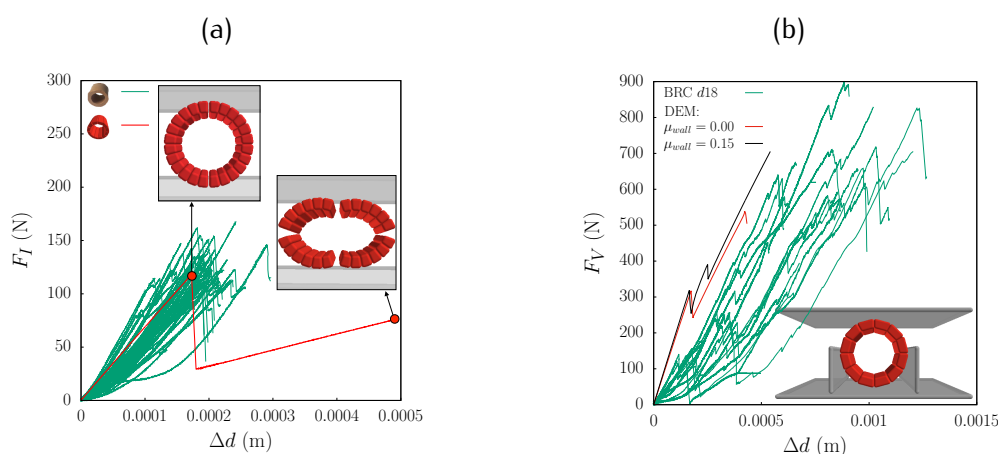


Figure 3: Comparison between model and experiment of the shell's mechanical response to: (a) uniaxial radial compression URC and (b) biaxial radial compression BRC. Set of green lines represent the experimental force. Red and black lines stands for discrete modelling. Symbols: F_I – uniaxial diametrical force, Δd – displacement of top plate, F_V – vertical force applied on the top plate in BRC and μ_{wall} – friction coefficient between shell and wall.

Finally, the experimental response to URC was successfully reproduced numerically as shown in Figure 3 (a). Noticeable discrepancy of Δd was caused by model simplifications. Figure 3 (b) shows an additional verification of the cluster model in the simulation of shell under biaxial compression. The second, minor compressive force was a consequence of the horizontal strain constraints added to loading conditions of URC. Thanks to the experimental results, it was confirmed that the model is capable to simulate the micro-mechanics of shell.

3 Towards assembly

At the assembly scale, the work begun with a characterisation of the sample fabric, naturally, limited to those aspects that were experimentally feasible for this case. It included simpler experimental measurement of the density and the estimation of the coordination number. More challenging aspect concerned the shell spatial orientation. Firstly, the scans of the true samples

¹ The force-displacement relationship.

(cut out from the tunnel segment) have been acquired using x-ray imaging techniques (with RX-Solutions scanner administrated by Laboratoire 3SR). The analysis tool, called 3DSHELLFINDER, was developed for this study as an alternative algorithm to overcome the issues arose during the classical watershed segmentation (cause by the internal hole within shell). 3DSHELLFINDER takes advantage of the tubular geometry to efficiently detect the shells on the reconstructed image of three-dimensional sample volume. The detection was indeed successful and provided necessary data for a statistical analysis. To this end, a definition of shell orientation specify the characteristic axis in terms of the strong, axial direction. Benefiting from the symmetry of the cylindrical shell and classic axis-symmetric loading, the analysis of the 3D spatial orientation was simplified to the inclination with respect to the vertical. Strong anisotropy towards horizontal orientation was reported for the true samples. Then, those results were related to the numerical samples. Using DEM, we have simulated a deposit by rain to obtain the assembly. The experimental characterisation served the numerical reproduction of the true packings in terms of the density and the distribution of shell orientations. Further, the discrete element assembly must be probed under mechanical load.

4 Numerical campaign of oedometer tests

Soil compressibility refers to a capability to decrease its volume while being subjected to a compressive loading. In the laboratory conditions, the soil compressibility can be observed in one-dimensional compression with the horizontal strain constrains, commonly known as an oedometer test. The experimental oedometer tests with the unload-reload cycles have been conducted by *Euro-Géomat-Consulting EGC* on commission of Andra; Figure 4; and the reproduction of this physical behaviour is the first aim of macro scale modelling.

The preliminary modelling respected the dimensions of experimental samples (diameter 35.0 cm, height 13 cm). The packing of 1 926 breakable clusters made of 12 sectors (23 112 sectors in total) was subjected to one-dimensional strain-controlled compression under the quasi-static conditions till the axial stress of 18.2 MPa was reached. Consequential study of the macroscopic mechanical behaviour covered:

- Sample size independence
- Parametric study (link elasticity, particle strength, *etc.*)
- The influence of the initial state (density of packing, orientations anisotropy)
- Model validity due to sector characteristics (number of shell, thickness of ring)

This extensive investigations characterised the influence of variables (or its lack), brought a better understanding of the model and build up the confidence in the technic. Among all probed aspects, those of greatest importance to the mechanical behaviour were detected: tensile strength and initial density. Those inputs were finally adjusted such that they mismatched the experimental estimations to some extend but the model most adequately reproduced the experimental stress-strain response, shown in Figure 4. The mechanical curve also pronounced the validity limit due to coarse sector size (*i.e.*, lower numerical strain).

The mechanical behaviour was extensively commented in the context of breakage evolution. Firstly, breakage has been quantified as a simple proportion of broken shells with respect to initial undamaged state. It was demonstrated that the landmarks on the stress-stain relationship correspond to a certain amount of breakage; Figure 5 (a). Those characteristic thresholds of breakage level corresponds to the onset of comminution, the inflexion point and the inhibition of breakage. Secondly, the evolution breakage was analysed in detail using the grain size distributions (GDS). Laboratory *Navier* hosted for us few tests aiming determination of the

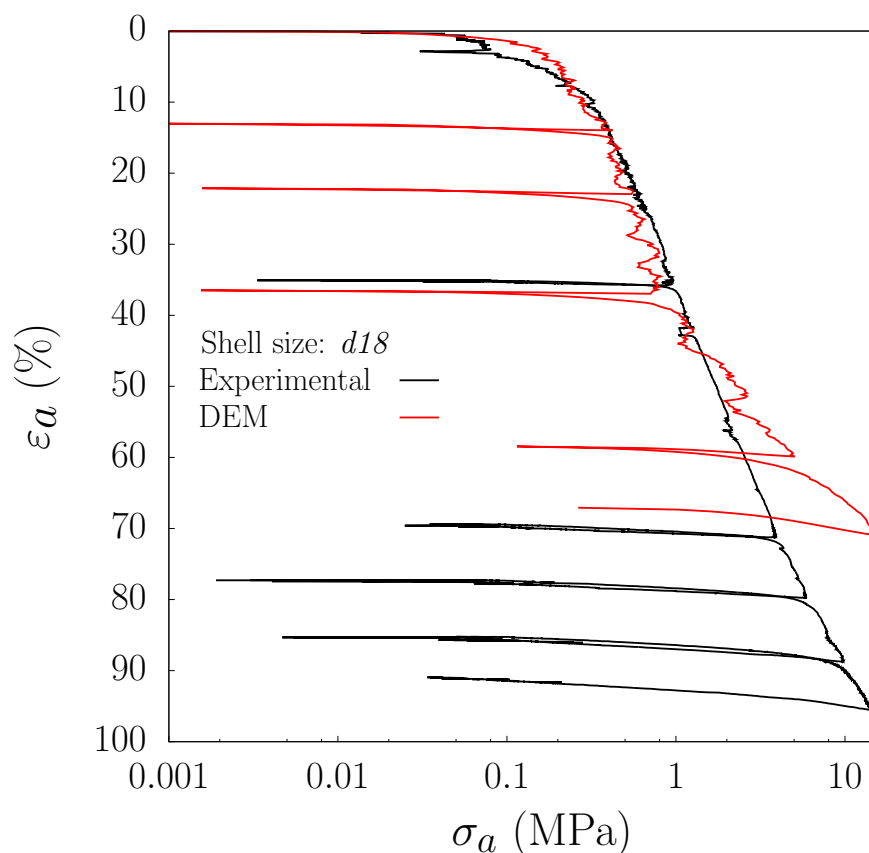


Figure 4: Experiment *versus* DEM. Comparison of mechanical responses to oedometric compressions. Experimental data courtesy of *Euro-Géomat-Consulting EGC*. σ_a – axial stress and ε_a – axial (vertical) strain.

breakage manner at different stress levels, especially for the onset of breakage. The numerical GDS framework has been adapted for comparison with the experimental results. The importance of micro-mechanics for the macroscopic evolution of breakage has been pronounced on GSDs.

Finally, the thesis proved the origins of high compressibility. Classically, the compressibility of soil derives from grain rearrangements filling the free space. Due to shell breakage followed by the collapse of shell's pore, the internal porosity makes essentially contribution to this phenomenon. The consolidation curves formed standard, always decreasing trend, often observed for other granular geo-materials. The definition of void ratio has been herein redefined in the framework of accessible and inaccessible space, instead of solid and void. For intact cylindrical shell, the centre pore cannot be filled by matter because of geometric exclusions. The inside void is then treated as inaccessible. Once broken, the void can be occupied by fragments, thus, it contributes to the accessible space. This approach resulted in a modification of consolidation curve trend such that increase of void was observed during the extensive breakage and it decreased only for final densification of sample; Figure 5 (b). As long as the increase is observed high compressibility of the layer can be exploit. Thus, an analytically determined constitutive model to predict stress-void ratio relationship has been proposed. The first step was to build its equivalent with respect to strain. This model was based purely on the transformations of the basic, mathematical definitions for void ratio and natural strain. Still, it already included the breakage, classic void ratio, the initial state variable and the geometrical extrusions. This

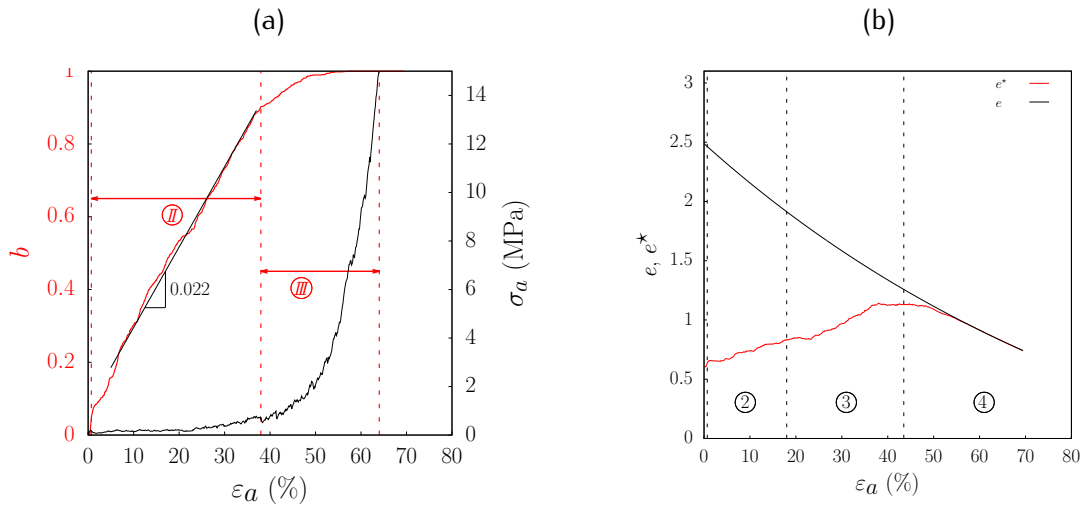


Figure 5: (a) Evolution of breakage ratio b (red curve) on the example of dense sample. The mechanical behaviour $\sigma_a : \epsilon_a$ shown in black. (b) Evolution of modified void ratio e^* (red). Note that classic void ratio evolution (black curve) has been imposed due to strain controlled test.

geometric-model provided a rough yet proper estimation of compressive behaviour. It was remarkable to find the prediction reliable while relying on such a basic concept. Furthermore, it became a starting point to the development of the final model referencing the macroscopic stress. The model was inspired by the isotopic compression law ruled by the soil hardness and shape parameter. It employed analytical relationship using the characteristic thresholds of breakage². The main goal achieved by the model was a successful prediction of macroscopic behaviour while reducing the number of input parameters, that are also straightforward and easy to determine experimentally or to estimate. Essentially, the model requires 2 macroscopic parameters for the state variable (the initial and final classic void ratio) and 2 microscopic parameters: the tensile shell strength and micro-porosity of shell (the geometrical extrusions). The model resulted in robust and true to its assumption prediction, allowing to estimate the highly-compressible regime.

5 Conclusions

Herein, the authors have presented a brief summary of PhD thesis. This overview discusses the generation and calibration of breakable, cluster model most suitable for hollow, cylindrical shells. Various experimental approaches were proposed such that each of them supports the reliability of the model at different scale and/or in different aspect. Thanks to the extensive modelling campaign of oedometric compressions, we were allowed to understand the complex behaviour and investigate the high compressibility in terms of breakage level. The observations led to redefinition of void ratio and proposition of 1D analytical constitutive model to predict the behaviour and evaluate the compressible capacities of double-porous material.

For more detailed information about aspect of this work we recommend the following sources: [9, 10, 11].

²Thresholds of b that mark the zones ① - ④ in Figure 5 (b).

Acknowledgements

On behalf of Andra (R&D Division, MHM URL , 55290 Bure, France) the work was monitored by Gilles ARMAND and Jad ZGHONDI.

References

- [1] Andra (2005) *Synthesis: Evaluation of the feasibility of a geological repository in an argillaceous formation*, Meuse/Haute-Marne site, Report
- [2] Andra (2016) *Rapport d'activité R&D*, Report
- [3] J. Zghondi, G. Armand, J.M. Bosgiraud, J. Simon (2018) *Qualification, construction and analysis of a precasted compressible Arch Segments drift test in the Andra Meuse/Haute-Marne Underground Research Laboratory (URL)*, World Tunnel Congress, Dubai
- [4] Andra & CMC, Patent, Publication No. FR3021346
- [5] M. Stasiak, G. Combe, J. Desrues, V. Richefeu, P. Villard, G. Armand, J. Zghondi (2017) *Experimental investigation of mode I fracture for brittle tube-shaped particles*, Powders & Grains, Montpellier, France
- [6] C. Thornton, K. K. Yin, M. J. Adams (1996) *Numerical simulation of the impact fracture and fragmentation of agglomerates*, Journal of Physics D Applied Physics **29**, pp. 424-435
- [7] M. D. Bolton, Y. Nakata, Y. P. Cheng (2008) *Micro- and macro-mechanical behaviour of DEM crushable materials*, Géotechnique **58**(6), pp.471-480
- [8] J. F. Wang, H. B. Yan (2011) *3D DEM simulation of crushable granular soils under plane strain compression condition*, Procedia Engineering **14**, pp. 1713-1720
- [9] M. Stasiak (2019) *Uniaxial compression of a highly crushable granular material – a 3D DEM study*, PhD thesis, Université Grenoble Alpes
- [10] M. Stasiak, G. Combe, V. Richefeu, P. Villard, J. Desrues, G. Armand, J. Zghondi (2018) *Discrete element modelling of crushable tube-shaped grains*, Micro to MACRO Mathematical Modelling in Soil Mechanics, Reggio di Calabria, Italy, pp. 347-360
- [11] M. Stasiak, G. Combe, V. Richefeu, P. Villard, G. Armand, J. Zghondi. *High-pressure compression of granular assemblies of brittle hollow particles*, Computational Particle Mechanics, to be submitted

Effect of inherent anisotropy on fabric evolution of granular materials

Gustavo PINZÓN^{1,*}, Edward ANDÒ^{1,†}, Alessandro TENGATTINI^{1,‡}, Gioacchino VIGGIANI^{1,§},
Jacques DESRUES^{1,¶}

¹ Univ. Grenoble Alpes, CNRS, Grenoble INP, 3SR, 38000 Grenoble, France

Abstract:

Inherent anisotropy can be easily observed in sand samples due to bedding planes created during deposition processes. The fabric response and evolution to the inherent anisotropy of the sample, has been mainly studied by means of Discrete Element Method simulations, given the possibility of retrieving the contact network and the kinematics of the particles. In this work, x-ray tomography is used to image triaxial compression tests on lentils samples, in order to observe the effect of inherent anisotropy over the fabric evolution. Each sample is prepared in a way such that all the particles present a unique mean orientation, reproducing the effect of bedding planes. Two samples are used, with an initial orientation of $\alpha = 45^\circ$ and $\alpha = 90^\circ$, with respect to the loading direction. The particle orientation fabric, the contact normal fabric, and the branch vector fabric are measured and followed through the test. The results show that the spatial distribution of the particle orientation fabric and contact normal fabric, display an evolution towards the direction of the principal stress. However, the response is not the same for the two samples, pointing to the effect of the bedding angle on the fabric evolution.

1 Introduction

Natural sand deposits often display layered patterns known as bedding planes, created by deposition under gravity. This deposition process can cause particles to be aligned, resulting in an anisotropic granular arrangement. This inherent anisotropic granular array creates a unique configuration of the internal structure (or fabric) that characterise the initial state of the sample. It is known that this initial anisotropy has a direct effect on the mechanical response of the material. Additionally, the understanding of the link between the macro-behaviour and the fabric anisotropy is at the very core of the granular media research, since multiple efforts have been made in order to describe this link.

In order to examine the mechanical behaviour of granular materials with an anisotropic fabric, undisturbed samples and remolded samples from natural deposits have been studied in the literature by means of different experimental tests such as, the hollow cylinder torsion [1, 2], plane strain [3, 4, 5], triaxial compression [3, 5], and triaxial extension [5]. All these studies proved that the initial fabric direction of the sample affects the stress-strain behaviour. However, even though the relevance of anisotropy has been stated and proved before, it has been often ignored in theoretical studies. Li and Dafalias [6] presented an Anisotropic Critical State Theory (ACST) that takes into account fabric anisotropy and its evolution in order to define the critical state.

*Email: gustavo.pinzon@3sr-grenoble.fr

†Email: edward.ando@3sr-grenoble.fr

‡Email: alessandro.tengattini@3sr-grenoble.fr

§Email: cino.viggiani@3sr-grenoble.fr

¶Email: jacques.desrues@3sr-grenoble.fr

In this study, they established, within the Critical State Theory (CST) framework, [7, 8], that the ACST defines a fabric tensor and describes its evolution towards a critical value, direction-wise and norm-wise. On the other hand, computational efforts using the discrete element method (DEM) allow the evaluation of quantities at the particle scale level, enabling the quantification of the evolution of fabric. Previous studies on 2D DEM simulations [9, 10, 11] have shown that the fabric of the material is directly affected by its inherent anisotropy. The results are in agreement with the statements of ACST, as the samples become anisotropic upon shearing and the fabric tends to align with the direction of the main stress. Within physical experiments, it is almost impossible to retrieve the fabric evolution during a test without direct imaging. For that reason, *in-situ* x-ray tomography imaging can be considered as an ideal tool to measure and follow the evolution of the material fabric for the first time, since it allows the generation of a complete 3D reconstruction of the specimen being studied. Therefore, the present paper focuses on the effect of the *bedding* angle over the evolution of the fabric, making use of x-ray tomography. For this, two samples are created with particles oriented with a specific bedding angle with respect to the loading axis; and the effect of inherent anisotropy is observed on the evolution of the particle orientation fabric, the contact orientation fabric, and the branch vector fabric, during the test.

2 Experiments

Two triaxial compression tests (Test 02, and Test 05) on lentils (2.3 mm in diameter and 1.3 mm in height) are performed inside the x-ray scanner, each of them characterised by a given initial orientation of the particles. During each test, the sample is scanned at different axial strain levels, and a complete 3D attenuation field of the sample is obtained. The attenuation field is thresholded, and a watershed-based technique is used to identify each individual particle, assigning it a unique label. The samples have a diameter of 60 mm and a height of 145 mm, and 138 mm for test 02 and 05, respectively. Lentils can be approximated mathematically as oblate ellipsoids, and are characterised by a symmetry plane. The normal vector of this plane can be decomposed into an orthogonal coordinate system and described by its azimuth (α) and zenith (θ) angles, as shown in Fig. 1. In order to inspect the effect of the inherent anisotropy, each sample is prepared in a way such that the particles present a preferential initial orientation. Test 02 is characterised by a mean particle orientation of $\alpha = 45^\circ$, while Test 05 has a mean orientation aligned with the z axis ($\alpha = 90^\circ$).

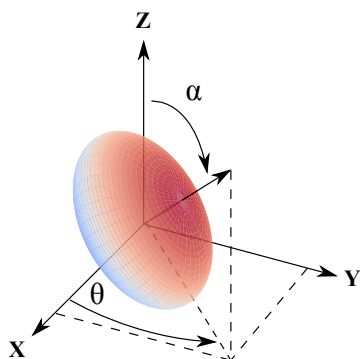


Figure 1: Characterisation of the orientation vector of a particle

In order to build the sample, the lentils are lined-up in a holder and then carefully placed inside the sample container. This method allows complete control over the initial orientation of the particles while generating a loose sample with a void ratio of 0.75. A flexible latex membrane

is placed around the sample to apply a confining stress during the test. The top and bottom plates of the setup enable only vertical displacement, restricting any other degrees of freedom. The confining pressure is applied by compressed air, while an external loading frame allows the application of the axial stress (σ_a). A confining pressure (σ_r) of 50 kPa is applied in both tests. A summary of the test conditions of the experimental campaign is presented on Tab. 1

Table 1: Test summary

Test ID	Type of Test	σ_r [kPa]	Initial α [°]
02	Compression	50	45
05	Compression	50	90

3 Measuring fabric from images

Using the 3D attenuation field obtained at each scan, one can identify each lentil and assign it a unique label. This allows the quantification of several particle properties (*e.g.*, centre of mass, volume, moment of inertia) and provides the opportunity to examine its interaction with its neighbours (*e.g.*, contact detection, contact orientation, branch vector). All of these image-based measurements are performed using the software *spam* (The Software for the Practical Analysis of Materials) [12].

The first step towards the fabric analysis is the correct identification of the lentils, specifically, assigning each voxel to one of the two phases present in the sample (void or solid) in a procedure known as binarisation. However, this process is not straightforward since some voxels present an intermediate grey value between the two phases. This is due to the partial volume effect encountered on 3D x-ray tomography images [13]. In order to reduce this effect and facilitate the binarisation, a combination of morphological operations is performed over the images. First, a grey-based morphological reconstruction [14] is performed in order to homogenise the greylevel distribution inside each phase. Subsequently, the Laplacian operator is applied, and the edges of the particles are identified. This algorithm shows a substantial effect on minimising the partial-volume effect of tomography images and allows a sharp outline of the contour of the particle to be defined. The binarisation process creates a binary image that is fed to a watershed algorithm, identifying each grain and assigning a unique label to each one. The orientation of each particle can be easily obtained by computing the eigenvectors of the moment of inertia tensor; in the case of the lentils, the eigenvector that corresponds to the maximum eigenvalue is aligned with the vector normal to the lentil plane, and thus used as the orientation vector of the particles (see Fig. 1).

The challenges of establishing whether two particles are in contact from x-ray tomography images arise from the physical interpretation of a contact, since two particles can be infinitesimally close but not touching each other [15]. A contact-detection algorithm is applied, as presented in Wiebicke *et al.* [16], making use of a global threshold to identify possible contacts and a local threshold to refine the detection process. Additionally, a random walker algorithm is used to determine the plane of the contact zone, and the contact orientation is taken as the normal vector to the contacting plane [17].

Through the image processing presented above, several orientation quantities that describe the internal micro-structure of the material can be obtained. Therefore this study focuses on the evolution of three vectorial data: the branch vector (the vector connecting the centre of two contacting particles), the particle orientation vector, and the contact orientation vector. In order to describe statistically the distribution of these quantities, the Kanatani [18] definition of fabric tensor is adopted. For a given orientation n^β , the fabric tensor \mathbf{N} is defined as the average of

the tensor product of all orientation:

$$\mathbf{N} = \frac{1}{N} \sum_{\beta=1}^N n^{\beta} \otimes n^{\beta} \quad (1)$$

where N is the total number of orientations. This tensor is referred to as the fabric tensor of the first kind, and contains all the relevant information of the distribution of the vectorial data. Furthermore, the anisotropy of the distribution is expressed by the deviatoric part (\mathbf{D}) of \mathbf{N} :

$$\mathbf{D} = \frac{15}{2} \left(\mathbf{N} - \frac{1}{3} \mathbf{I} \right) \quad (2)$$

where \mathbf{I} corresponds to the identity tensor. Additionally, a scalar anisotropy factor (\mathbf{a}) is proposed in [19] as a lower-order descriptor of the anisotropy of \mathbf{D} , and is computed as:

$$\mathbf{a} = \sqrt{\frac{3}{2} \mathbf{D} : \mathbf{D}} \quad (3)$$

Finally, a 3D surface of the spatial distribution of \mathbf{D} is useful to visualise the evolution of the anisotropy and the possible existence of preferential directions or planes. The distribution density function for the deviatoric fabric tensor \mathbf{D} is computed for any direction o_i in 3D as

$$f(n) = \frac{1}{4\pi} (1 + \mathbf{D}_{ij} o_i o_j) \quad (4)$$

4 Fabric evolution

The macro-mechanical response of both samples can be seen in Fig. 2. The relaxation segments correspond to the stages at which the test was halted for the acquisition of the x-ray tomography images. Both samples studied in this research show a typical response of loose granular materials, where the shear strength gradually increases and no stress peak is observed. Despite having a different initial particle orientation, both samples show a similar behaviour. This result is rather surprising, since previous studies [10, 20, 11] have shown that the bedding angle of the sample has a direct effect on the mechanical response of granular materials to deviatoric loading. However, those results were obtained for dense samples (the reported void ratio is between 0.11–0.25), while the samples used in these experiments were rather loose (the sample preparation method yielded a void ratio of 0.75). Additionally, the greater differences in the response to deviatoric loading observed by these authors were for samples with $\alpha = 0^\circ$, while the samples between $\alpha = 30^\circ$ and $\alpha = 90^\circ$ exhibit a slightly different response. The scalar anisotropy factor \mathbf{a} can be used as a first descriptor of the anisotropy of the selected fabric quantities, since higher values of \mathbf{a} reveal a preferential orientation, while lower values point to a more isotropic distribution. Figure 3 presents the evolution of the scalar anisotropy factor \mathbf{a} of the branch vector, the particle orientation vector and the contact orientation vector throughout the two tests. From these fabric quantities, the particle orientation shows a higher initial value, while the branch vector presents a smaller amount. The first thing that is remarkable is that the two samples studied essentially start from the same level of anisotropy for each quantity, being in agreement with previous studies [10, 11, 9]. However, once the deviator stress starts to increase, the behaviour of the scalar anisotropy factor is radically different for the two tests. For the particle orientation there is a gradual increase of \mathbf{a} on Test 02, while for Test 05 there is a constant decrease. This behaviour implies that particles in Test 02 start to align towards a common orientation, while the distribution of particle orientations in Test 05 becomes more isotropic. The contact orientation anisotropy presents a similar behaviour as the

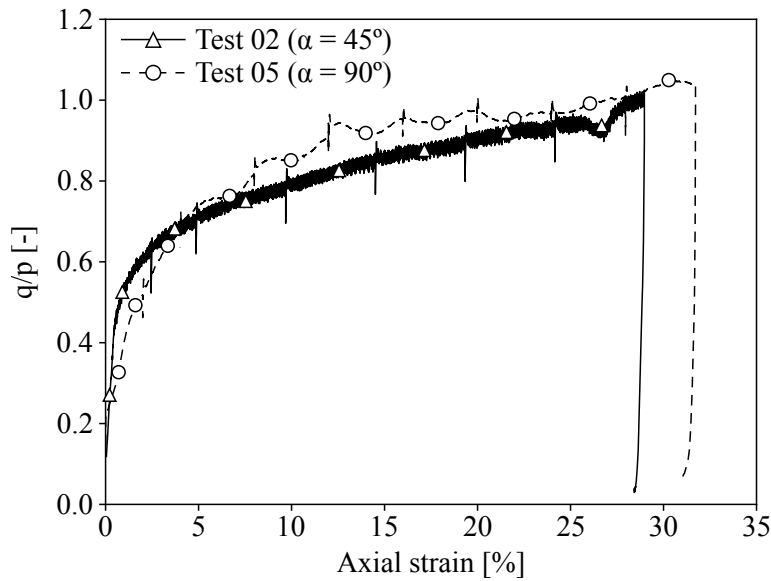


Figure 2: Macro stress-strain evolution

particle orientation for both samples: a steady increase is observed in Test 02, while Test 05 shows a continuous decrease, in agreement with previous studies [10, 9, 11]. Interestingly, the branch vector evolution doesn't show any major changes as the previous quantities. For Test 02 it remains almost constant, while for Test 05 it increases slightly and then decreases to reach a similar value as at the initial configuration. This implies that the anisotropy of the branch vector does not change as the axial strain increases.

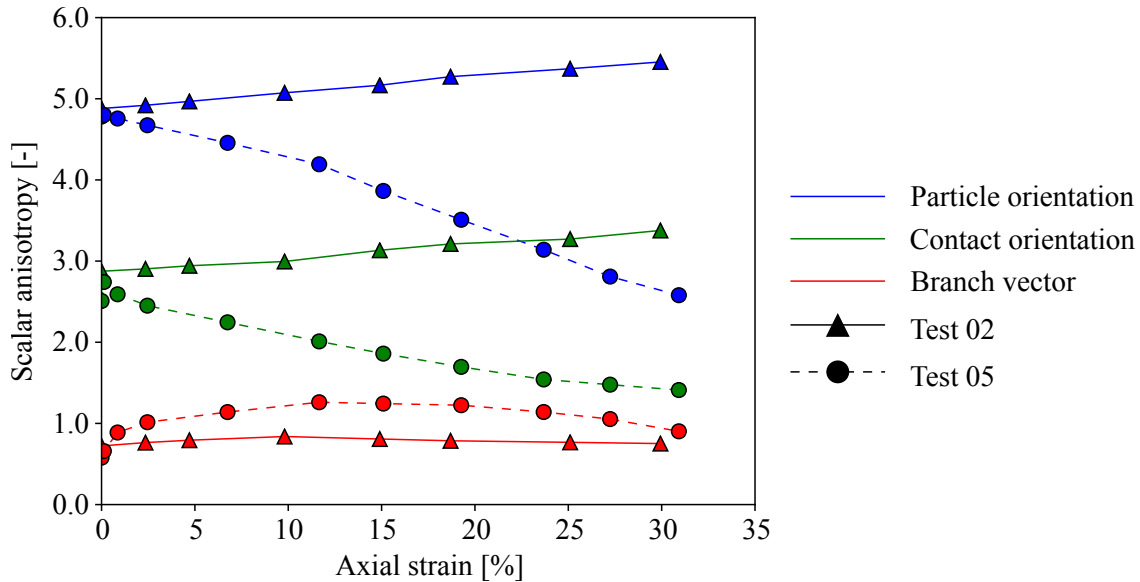


Figure 3: Scalar anisotropy factor a evolution for branch vector (red), particle orientation (blue), and contact normal orientation (green).

The distribution of \mathbf{D} , as per equation 4, for Test 02 is presented in Fig. 4 for selected steps of axial strain. As expected, the distribution density of the particle orientation shows a preferential direction along $\alpha = 45^\circ$ for the initial step. As the axial strain increases, the distribution rotates towards $\alpha = 0^\circ$ maintaining its overall shape. These results are in agreement with the findings of [21], since the particle orientation fabric distribution tends to shift towards the direction of

the principal stress. The contact normal orientation shows a similar distribution as the particle orientation, displaying a preferential orientation aligned with the particles initial orientation. [10] found that the initial state of the contact normal fabric distribution is oriented according to the initial bedding angle. This is also observed for the results of Test 02. When analysing the width of the lobe in comparison to the particle orientation, a greater contact orientation distribution can be found, implying a broader distribution along the preferential orientation. As the test goes by, the distribution density shifts towards $\alpha = 0^\circ$ maintaining its general shape. Once again, this result agrees with previous findings [9, 17, 20, 11], considering that the contact normal shifts towards the directions of the principal stress. In contrast, the branch vector presents a drastically different distribution. Due to the lentils shape and the sample preparation method, the lentils organise radially to each other. This arrangement results in a distribution shaped as a biconcave disk oriented perpendicular to the particles initial orientation. As the axial strain increases, the distribution shows a slight growth over a preferential direction. However, at the end of the test, the overall shape returns to a similar state as in the initial configuration.

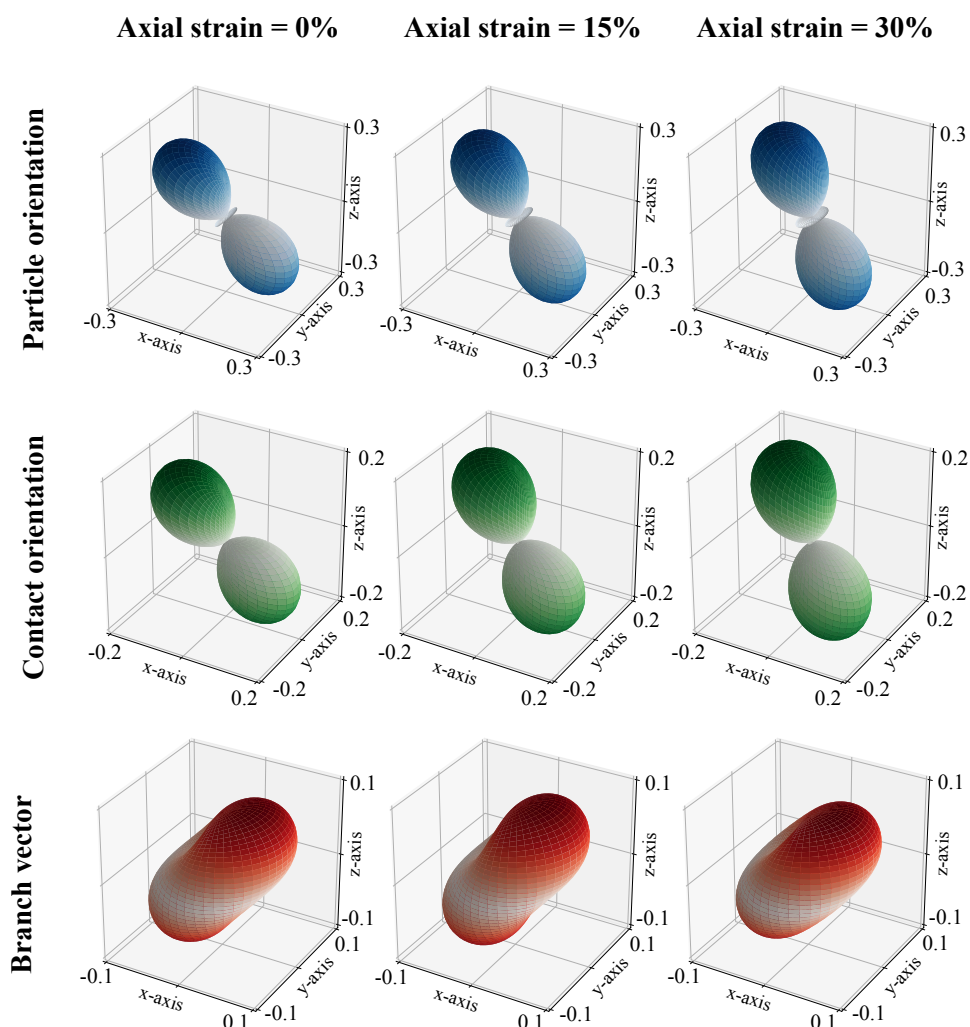


Figure 4: Surface plot of the distribution density of the deviatoric fabric tensor \mathbf{D} for Test 02 for several loading states. Upper row: branch vector. Middle row: particle orientation. Lower row: contact normal orientation.

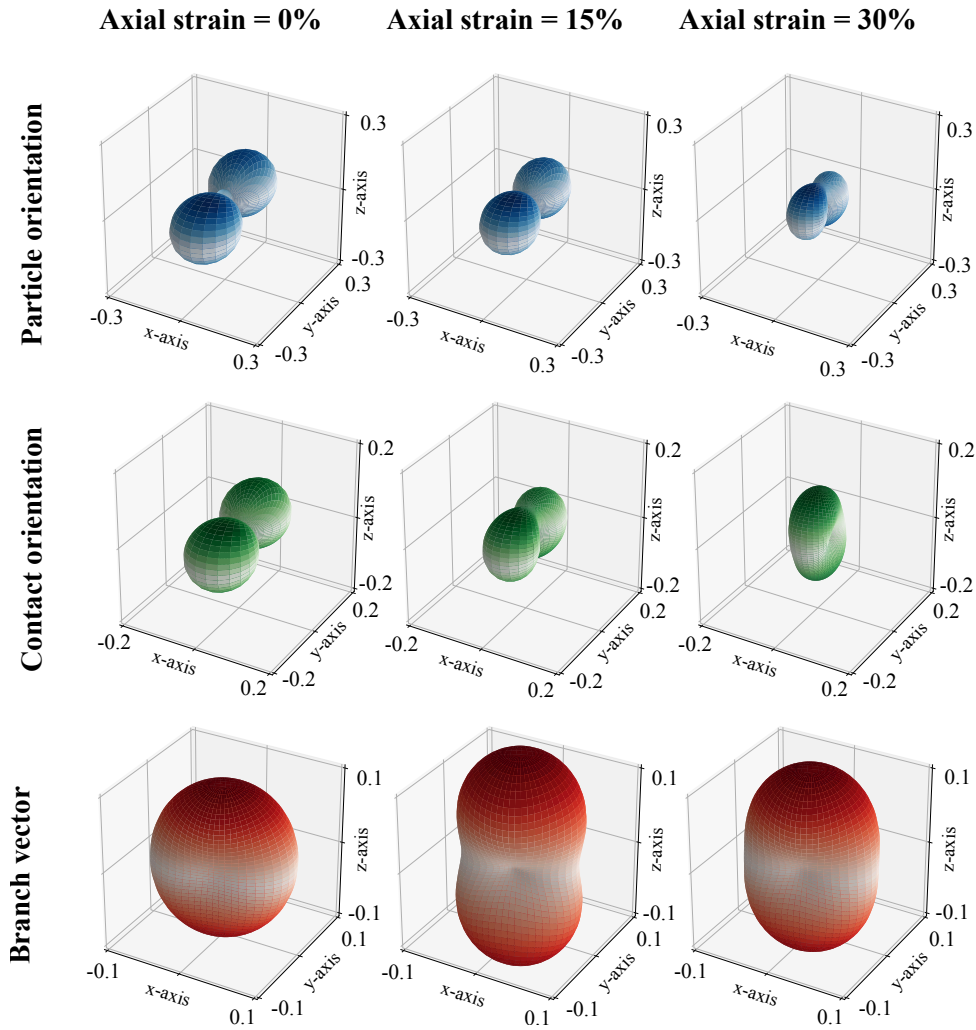


Figure 5: Surface plot of the distribution density of the deviatoric fabric tensor \mathbf{D} for Test 05 for several loading states. Upper row: branch vector. Middle row: particle orientation. Lower row: contact normal orientation.

Figure 5 presents the distribution of \mathbf{D} in Test 05 for selected steps of axial strain. The initial particle orientation fabric distribution reveals once again the initial orientation of the sample, showing a preferential orientation at $\alpha = 90^\circ$. However, as the axial strain increases, the overall shape of the distribution shifts. The lobes start to reduce in size and the frequency along the z-axis increases. These shape variations explain the decrease of the scalar anisotropy factor observed before. The distribution starts to lose its preferential orientation and becomes less anisotropic. Interestingly, the growth of the distribution along the z-axis may suggest an alignment of the fabric distribution with the orientation of the principal stress, as observed for the particle orientation fabric in Test 02. One may think that if the axial strain increases indefinitely, the distribution will eventually show a highly anisotropic distribution with two lobes centred around $\alpha = 0^\circ$. The contact orientation fabric distribution shows an alignment with the bedding planes of the sample, validating the results of [10]. Similar to the particle orientation fabric, as the axial strain increases, the contact orientation distribution starts to decrease the size of the horizontal lobes. At the end of the test, the distribution shows a preferential direction along the z-axis. These results are in agreement with the observations of [11], and are a result of the creation of new contacts along the loading direction, while the existing contacts are lost. The resemblance between the particle orientation fabric and the contact orientation fabric is

remarkable, although it seems that the latter evolves faster than the former. In Test 05 it is easier to observe the biconcave disk shape of the branch vector distribution, with an orientation perpendicular to the particle orientation fabric distribution. As the axial strain increases, the distribution starts to show a preferential orientation, aligned with the principal stress direction, while the frequency along the perpendicular plane decreases. However, at the end of the test, the anisotropy of the distribution decreases and returns to a shape similar to the one observed at the initial state.

5 Conclusion

The study of the effect of fabric on the microstructure of granular materials is of utmost importance, in order to fully understand the relation between the micro-behavior and macro-response. For natural soils, the deposition of particles under the action of gravity can induce an anisotropy characterised by bedding planes inside the material. In the present paper, two triaxial tests were performed over samples of lentils with a preferential initial orientation. X-ray tomography imaging allows the labeling of each individual particle inside the sample, enabling the quantification of the fabric evolution of the material. The particle orientation vector, contact normal orientation vector, and branch vector are chosen as representative indicators of the internal fabric, and their evolution is followed throughout the test. A tensorial representation allows the measurement of the anisotropy of the fabric quantities. The initial scalar anisotropy factor (α) of each fabric descriptor is indifferent to the initial orientation of the particles, but a difference is observed once the axial strain increases. For the particle orientation vector and contact orientation vector, the bedding plane generates a gradual increase of α for Test 02, while a constant decrease is observed in Test 05. Remarkably, the branch vector scalar anisotropy factor evolution seems indifferent to the initial orientation of the particles. For Test 02 the scalar anisotropy factor remains nearly constant, while for Test 05 a small increase is observed, followed by a decrease towards the initial state value.

The spatial distribution of the fabric tensor is obtained from the distribution density function, allowing the observation of the development of preferential orientations. The results reveal that the particle orientation fabric and contact orientation fabric always shift towards the direction of the principal stress, regardless of the initial bedding angle. The initial orientation does affect the rate of the evolution, but ultimately the fabric tensor will align with the direction of the principal stress, validating the observations of [6] on Anisotropic Critical State theory. The results show an agreement with previous studies, even though the samples differ radically in terms of the initial void ratio, pointing to a possible indifference of the fabric response due to sample density. The fabric computation performed in this paper, is representative of the whole sample. However, one must bear in mind the strain localisation phenomena that characterises granular media. Further work should be focused on the quantification of fabric evolution inside and outside the developing shear band, in order to establish the incidence of bedding planes over the evolution of strain localisation and fabric.

References

- [1] M. Yoshimine, K. Ishihara, and W. Vargas, "Effects of principal stress direction and intermediate principal stress on undrained shear behavior of sand," *Soils and Foundations*, vol. 38, no. 3, pp. 179–188, 1998.
- [2] Y. Nakata, M. Hyodo, H. Murata, and N. Yasufuku, "Flow deformation of sands subjected to principal stress rotation," *Soils and Foundations*, vol. 38, no. 2, pp. 115–128, 1998.

- [3] M. Oda, I. Koishikawa, and T. Higuchi, "Experimental study of anisotropic shear strength of sand by plane strain test," *Soils and foundations*, vol. 18, no. 1, pp. 25–38, 1978.
- [4] F. Tatsuoka, S. Nakamura, C. HUANG, and K. Tani, "Strength anisotropy and shear band direction in plane strain tests of sand," *Soils and foundations*, vol. 30, no. 1, pp. 35–54, 1990.
- [5] W.-K. Lam and F. Tatsuoka, "Effects of initial anisotropic fabric and σ_2 on strength and deformation characteristics of sand," *Soils and Foundations*, vol. 28, no. 1, pp. 89–106, 1988.
- [6] X. S. Li and Y. F. Dafalias, "Anisotropic Critical State Theory: Role of Fabric," *Journal of Engineering Mechanics*, vol. 138, no. 3, pp. 263–275, 2012.
- [7] K. H. Roscoe, A. Schofield, and a. P. Wroth, "On the yielding of soils," *Geotechnique*, vol. 8, no. 1, pp. 22–53, 1958.
- [8] A. Schofield and P. Wroth, *Critical state soil mechanics*. McGraw-hill, 1968.
- [9] M. M. Sazzad and K. Suzuki, "Micromechanical behavior of granular materials with inherent anisotropy under cyclic loading using 2d dem," *Granular Matter*, vol. 12, no. 6, pp. 597–605, 2010.
- [10] E. S. Hosseininia, "Investigating the micromechanical evolutions within inherently anisotropic granular materials using discrete element method," *Granular Matter*, vol. 14, no. 4, pp. 483–503, 2012.
- [11] Z. Mahmood and K. Iwashita, "Influence of inherent anisotropy on mechanical behavior of granular materials based on dem simulations," *International journal for numerical and analytical methods in geomechanics*, vol. 34, no. 8, pp. 795–819, 2010.
- [12] E. Andò, R. Cailletaud, E. Roubin, and O. Stamati, "the spam contributors, spam: The software for the practical analysis of materials," 2017.
- [13] A. Tengattini and E. Andò, "Kalisphera: an analytical tool to reproduce the partial volume effect of spheres imaged in 3d," *Measurement Science and Technology*, vol. 26, no. 9, p. 095606, 2015.
- [14] R. C. Gonzalez, R. E. Woods, and S. L. Eddins, *Digital image processing using MATLAB*. Pearson Education India, 2004.
- [15] T. Aste, M. Saadatfar, and T. Senden, "Geometrical structure of disordered sphere packings," *Physical Review E*, vol. 71, no. 6, p. 061302, 2005.
- [16] M. Wiebicke, E. Andò, I. Herle, and G. Viggiani, "On the metrology of interparticle contacts in sand from x-ray tomography images," *Measurement Science and Technology*, vol. 28, no. 12, p. 124007, 2017.
- [17] M. Wiebicke, E. Andò, G. Viggiani, and I. Herle, "Measuring the evolution of contact fabric in shear bands with X-ray tomography," *Acta Geotechnica*, vol. 15, pp. 79–93, jan 2020.
- [18] K. Ken-Ichi, "Distribution of directional data and fabric tensors," *International journal of engineering science*, vol. 22, no. 2, pp. 149–164, 1984.
- [19] X. Gu, J. Hu, and M. Huang, "Anisotropy of elasticity and fabric of granular soils," *Granular Matter*, vol. 19, no. 2, p. 33, 2017.

- [20] M. Oda, S. Nemat-Nasser, and J. Konishi, "Stress-induced anisotropy in granular masses," *Soils and foundations*, vol. 25, no. 3, pp. 85–97, 1985.
- [21] X. Li and X.-S. Li, "Micro-macro quantification of the internal structure of granular materials," *Journal of engineering mechanics*, vol. 135, no. 7, pp. 641–656, 2009.

NeXT-Grenoble, the Neutron and X-ray Tomograph in Grenoble

Alessandro TENGATTINI^{1,2,*}, Nicolas LENOIR^{1,†}, Edward ANDÒ^{1,‡}, Benjamin GIROUD^{2,§}
Duncan ATKINS^{2,¶}, Jerome BEAUCOUR^{2,} Gioacchino VIGGIANI^{1,**}

¹ Univ. Grenoble Alpes, CNRS, Grenoble INP, 3SR, 38000 Grenoble, France

² Institut Laue-Langevin (ILL), 71 Avenue des Martyrs, 38000 Grenoble, France

Abstract: NeXT-Grenoble is a Neutron and X-ray Tomograph launched from the collaboration between the Université Grenoble Alpes (UGA) and the Institut Laue Langevin (ILL). The design started in February 2016 shortly followed by its construction at ILL. A first version of the instrument has been opened to users since October 2016. One of the peculiarities of the instrument is that, as suggested by the name, the instrument allows the acquisition of *truly* simultaneous neutron and x-ray tomographies, taking advantage of the high complementarity of these two beams. Also by virtue of the uniquely high flux at the ILL, the instrument can provide unprecedented spatial resolution (around 4 μm true resolution, in few tens of seconds) and acquisition speed (1.5 second tomographies). This contribution details the adopted technical solutions and performances achieved, reviews some of the key published results and outlines the future direction of the instrument.

1 Introduction

NeXT-Grenoble is a Neutron and X-ray Tomograph launched in 2016 from the joint effort of Université Grenoble Alpes, UGA (and specifically Laboratoire 3SR) and the Institut Laue-Langevin, ILL, and takes advantage of its world-leading neutron flux. Design started in February 2016 and the instrument was available to users in October 2016. It is currently fully open for proposals through its dedicated website <https://next-grenoble.fr>.

The high neutron flux available automatically makes this a unique instrument, since tomography performance (in terms of spatial resolution, temporal resolution and measurement noise) is wholly dependent by noise in data collection and therefore flux. Another key feature of the instrument is the possibility to perform x-ray absorption imaging, in order to take advantage of the high complementarity of these two techniques, sketched in Fig. 1. The design of the instrument is conceived with both fundamental and engineering studies in mind and therefore with the possibility of housing complex *in-situ* testing apparatus for a variety of thermo-chemo-hydro-mechanical experiments. The instrument uses a particularly “cold” beam (with flux peaking at 2.8 Å) which increases the contrast due to the energy dependence of the absorption cross-section, at the cost of a reduced penetration capacity. Neutron imaging has a broad range of applications ranging from renewable energies to biology, and from paleontology to porous media, as outlined in multiple review papers (*e.g.*, [1, 2])

*Email: alessandro.tengattini@3sr-grenoble.fr

†Email: nicolas.lenoir@3sr-grenoble.fr

‡Email: edward.ando@3sr-grenoble.fr

§Email: giroud@ill.fr

¶Email: atkins@ill.fr

Email: beaucour@ill.fr

**Email: cino.viggiani@3sr-grenoble.fr

In this paper we describe the layout of NeXT-Grenoble, the neutron and x-ray imaging equipment and their performances as well as a few selected examples of the published results achieved thus far. This paper is meant to be the principal reference for the current status of the instrument, superseding the previous one [3]. A significant upgrade of the instrument, including for example monochromation and polarisation options, is foreseen in 2021/2022, as detailed in Section 6. This might be followed by a dedicated publication on its novelties. No significant interruption of public availability is currently foreseen to perform this upgrade. For one of the more complex aspects of the facility, simultaneous x-ray and neutron imaging, a dedicated publication is under development. Therein theoretical considerations, technical details and practical applications will be more adequately explored. It goes without saying that the presented instrument benefits from the experience matured by the neutron imaging community, as well as the developments in synchrotron and lab scanners over the last decades, as detailed below.

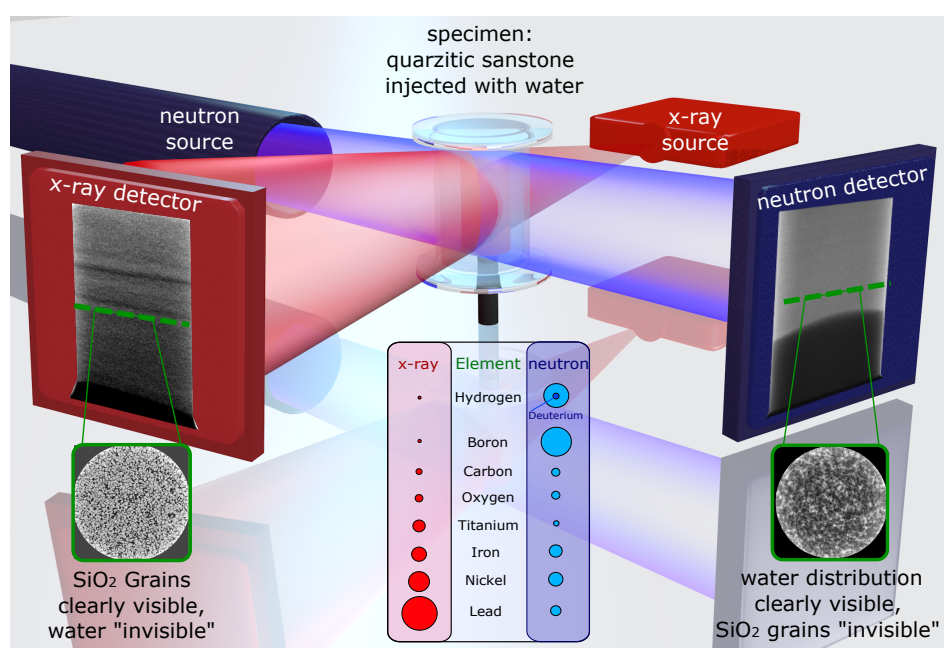


Figure 1: Sketch of the underlying concept of NeXT: the high complementarity of the two techniques generally makes the combination of the two superior to the sum of the parts. In the example of *in-situ* testing of fluid flow in porous media, x-ray is ideal for detecting the solid skeleton and measuring its deformation whereas neutrons are best suited to study the hydraulic response.

2 Source and guides

Built in 1967 and refurbished between 1991 and 1995, the ILL is a heavy-water cooled and moderated swimming pool-type reactor, operating with a thermal power of 58.3 MW, which provides the most intense continuous neutron flux in the world (1.5×10^{15} n/cm²/s in the moderator region).

NeXT is situated at the end of the H521 guide which is fed by the Horizontal Cold source SFH ("Source Froide Horizontale", in French). The H5 beam tube is followed by a 13 m long guide with a radius of 4000 m, then by a 30 m segment with 1500 m curvature and finally by 30 m of straight guide. All these segments ex-pile are supermirror-coated for $m=2$. This relatively uncommon curvature significantly reduces the amount of thermal neutrons and gamma radiation

produced in the reactor reaching the instrument.

The location of the instrument within the ILL is shown in Fig. 2. The H521 guide starts with a 117x120 mm rectangular section, which becomes a 150x60 mm section after about 20 m, which is then maintained in the last 28 m. Two pneumatic safety shutters made of boron carbide and lead are positioned immediately at the end of H521 and 5 m behind it.

From this rectangular guide only a 30 mm circle in the topmost section is currently used for imaging, although more will be used in future upgrades (which will be detailed in section 6).

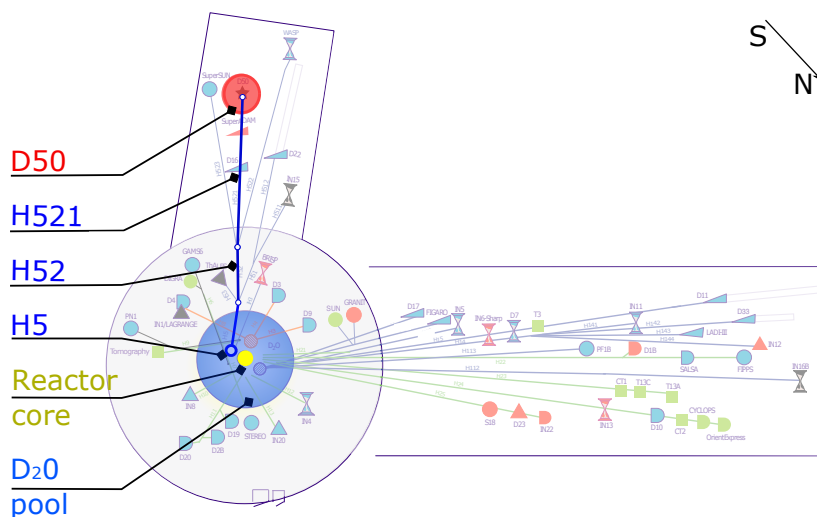


Figure 2: Schematic plan of all instruments at ILL, highlighting the position of NeXT-Grenoble. Modified from <https://www.ill.eu/users/instruments/>.

3 Instrument layout

At the end of the H521 cold guide lies the “D50” experimental station. It currently houses two separate instruments/configurations: the Neutron and X-ray Tomograph (NeXT-Grenoble), which is the object of this paper, as well as the Rainbows reflectometer described in [4]. In brief, the peculiarity of this reflectometer is that instead of using the more traditional time of flight approach to discern the wavelength of neutrons, it takes advantage of the wavelength-dependency of their deflection by a prism. The wavelengths are then measured with a high spatial resolution detector. The construction of the reflectometer was initiated in 2014, and financed by the French government initiative “Programme d’Investissement d’Avenir” funded by the IRT Nanoelec and more specifically by its program led by the ILL, dedicated to bridge the gap between industry and large scale research facilities. As aforementioned, the imaging station was added in 2016, financed by the Université Grenoble Alpes. The two instruments, sketched in Fig. 3, currently work in alternation, as detailed below. At the end of the guide lie both a set of sintered B4C pinholes for the tomograph (30, 23, 15, 12.5, 10, 7 and 5 and 2.5 mm in diameter), as well as a number of vertical slits for the reflectometer. Additionally, a pneumatic fast shutter made of boron carbide as well as two graphite filters (5 mm and 10 mm thick) can be positioned in the beam. Further downstream, there are two 5 m long parallel vacuum flight tubes, optimised for imaging and reflectometry respectively. The tubes are placed on a rail which allows their alignment with the neutron beam depending on the operation mode. Rainbows reflectometry employs the wavelength-dependent deflection of a prism to study the reflective properties of matter employing the full white beam, which is detected at 4 m from the sample with a scintillator-based detector as sketched in Fig. 4. When the instrument is

operated in Imaging mode, all the reflectometry components are either removed or displaced sideways to allow for an additional 5 m long vacuum flight tube to be added along the beam path. In summary, for the purpose of this work, the end of the neutron guide is followed by a series of beam shapers and then by a 10 m long flight tube, which leads to the imaging station itself. The radioprotective bunker of the tomograph is made of modular concrete blocks (unlike the rest of the instruments upstream whose shielding is made from lead and B4C) to simplify the compliance with the magnetic constraints of a neighbouring instrument (the spin-echo spectrometer "WASP"). The roof is made of long concrete beams which can be rapidly removed by crane for the installation of large pieces of equipment in the bunker.

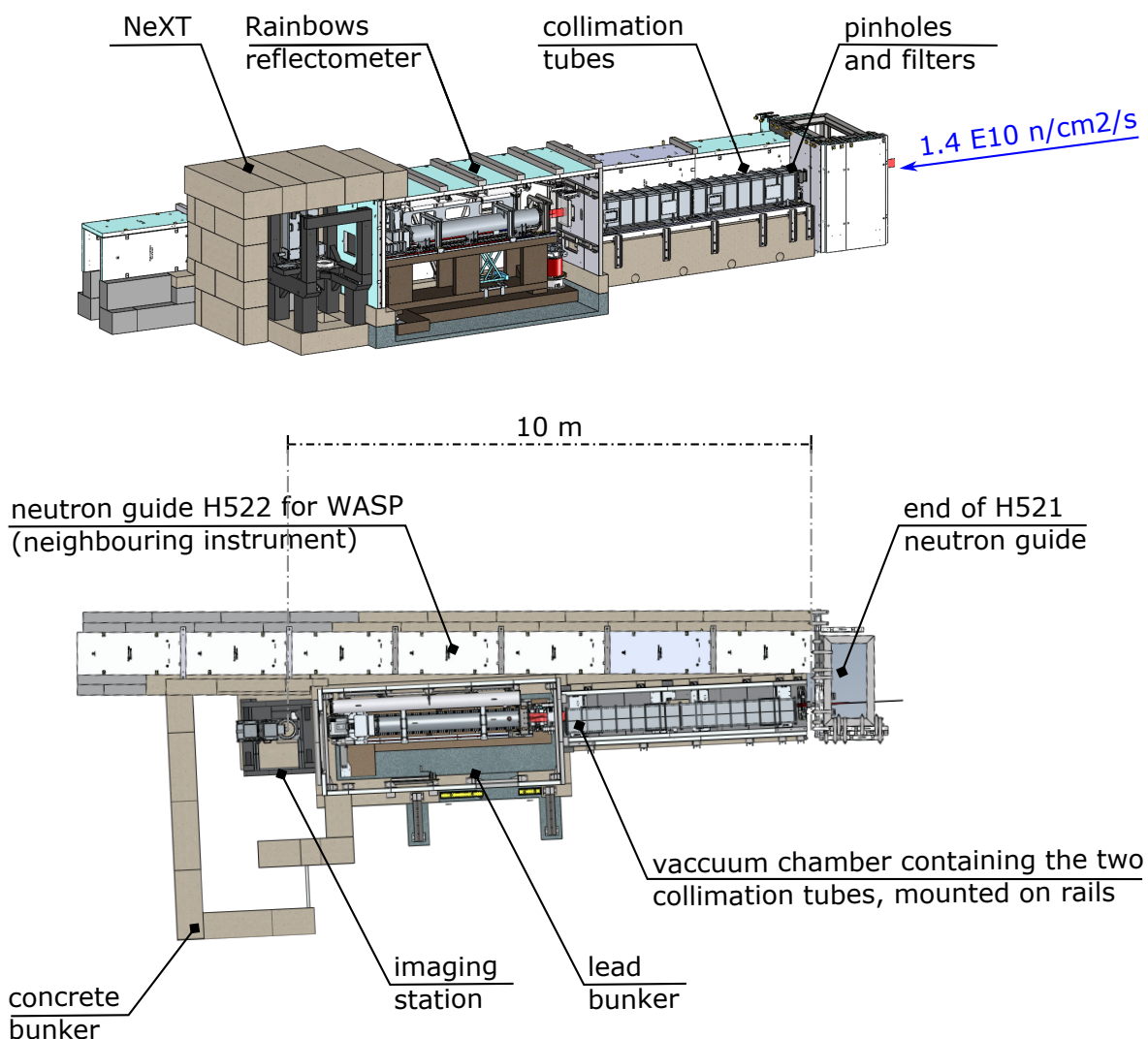


Figure 3: Side and top view of the D50 instrument in its entirety, including the tomograph and the reflectometer

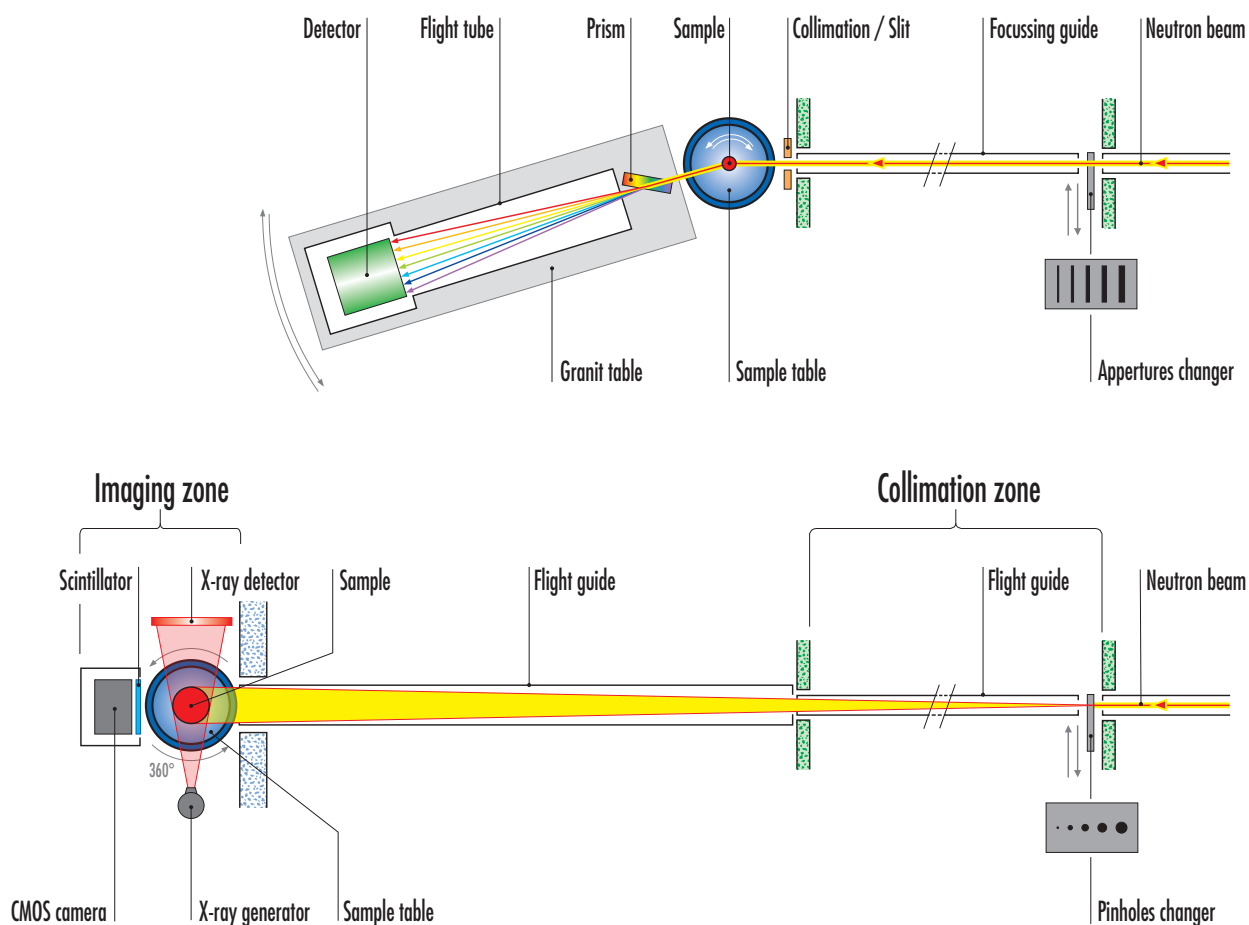


Figure 4: Conceptual description of the two components of D50: the rainbows reflectometer (top) and the tomograph (bottom).

From <https://www.i11.eu/users/instruments/instruments-list/d50/description/instrument-layout/>.

It should be noted that after the neutron guide and shutters no element is in common between the two instruments. A 10-meter beam collimation tube is placed in lieu of all the elements in the top part of the figure as detailed in the text.

3.1 Beam characteristics

The flux, as measured by gold foil, at the end of the H521 guide is of 1.4×10^{10} n/cm²/s, which, to the best of the authors' knowledge, makes NeXT-Grenoble the imaging station with the highest neutron flux in the world. With the largest pinhole currently available, the maximum flux at the sample position is of 3×10^8 n/cm²/s for an L/D of 333 at the sample position, and future upgrades (Section 6) intend to explore the higher flux at lower L/D ratios. To compare it to other notable facilities for an arbitrary collimation ratio L/D of 400, at FRM2 (ANTARES beamline) there is a reported flux of 1×10^8 n/cm²/s (without any of the elements available to reduce fast neutron and gamma background), while NIST (BT-2 beamline) the flux is of about

$6 \times 10^7 \text{ n/cm}^2/\text{s}$ (without the Beryllium filter) and at PSI (ICON beamline) it would be of about $1 \times 10^7 \text{ n/cm}^2/\text{s}$ (as *estimated* from a reported $1.3 \times 10^7 \text{ n/cm}^2/\text{s}$ for an L/D of 343). At ILL for the collimation ratio L/D of 400 the flux would be of about $2 \times 10^8 \text{ n/cm}^2/\text{s}$.

The spectrum peaks around 11 meV, corresponding to a wavelength of 2.8 \AA as highlighted in Fig. 5. This spectrum was measured by the reflectometer, 5 m from the end of the guide. The two visible dips in the spectrum at 4.518 \AA and 5.241 \AA are caused by two fixed monochromators upstream as part respectively of the D16 diffractometer and the SuperADAM reflectometer. The beam is not perfectly homogeneous, as highlighted in Fig. 6 (a). Figs. 6 (b) and (c) show the vertical and horizontal profiles of the beam intensity of the central part of the beam for a selection of the available pinholes. These profiles highlight how the beam is relatively homogeneous (above 70 % of the maximum value) within the central 100 mm and that the larger pinholes generate a slightly more homogeneous beam than the smaller ones. Some of the finer details of this inhomogeneity are induced by the limited reflection at the joints of the beam guides upstream, and can be partly compensated by employing the graphite filters detailed in section 3.

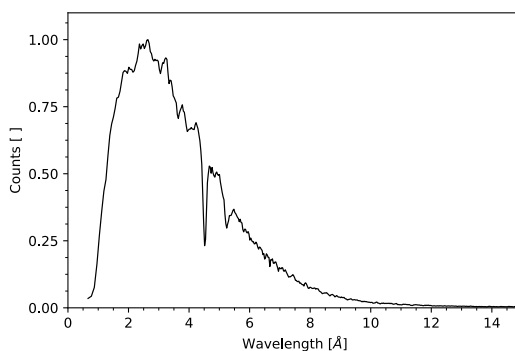


Figure 5: The neutron spectrum at NeXT, as determined by the Rainbows reflectometer introduced in section 3. The used method might justify some of the higher frequency fluctuations in the plot.

4 Imaging station

4.1 Neutron detectors

Three neutron detectors are currently available at NeXT: a medium resolution detector, with a continuously variable field of view, detailed in section 4.1.1 and two high resolution detectors, each optically optimised for a discrete number of fields of view, detailed in section 4.1.2. The detectors are mounted onto a rotating plate which allows for the swapping of two positions, one with the medium resolution detector and one which allows for mounting either of the high resolution detectors with high repeatability thanks to high accuracy dowel pins.

4.1.1 Medium resolution detector

The Medium Resolution detector at NeXT, shown in Fig. 7, follows a common approach in neutron imaging: scintillator, mirror and camera plus optics. One of the peculiarities of this detector is the fact that the scintillators can be mounted onto protruding “noses”. This is meant to allow minimal distance between sample and detector (to reduce the so called penumbra blurring thus maximising the true spatial resolution) in the case of complex sample environments (*e.g.*, flanged

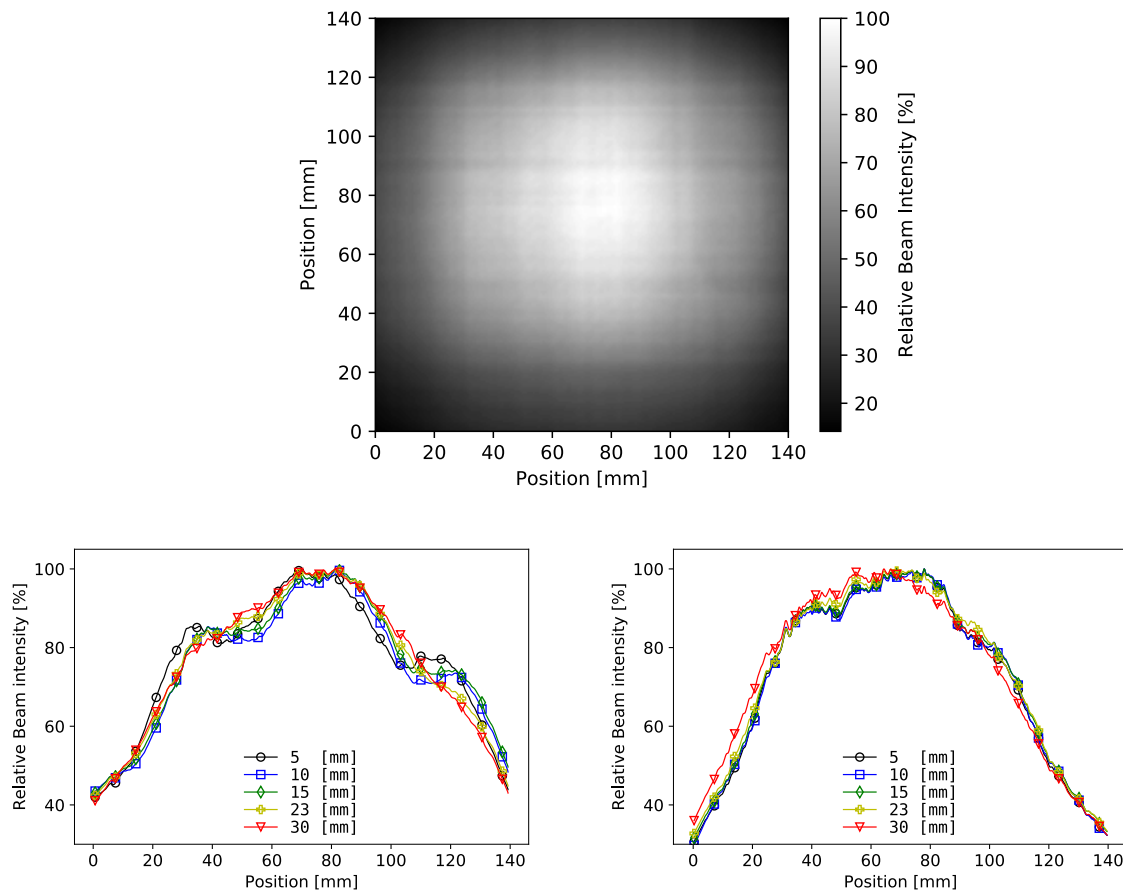


Figure 6: Map of the beam distribution (a) Horizontal (b) and Vertical (c) profiles of the central 140 mm of beam intensity for different pinholes.

mechanical testing rigs, where the cell diameter in the middle region can be significantly smaller than at its extremities), in line with the user-oriented philosophy of the instrument. Multiple available noses of different sizes can be mounted on the detector to allow for different scintillator/mirror distance as well as different scintillator sizes. The scintillators are held in place by a counterframe screwed on the nose itself, which also ensures light-tightness. This elongated nose also removes the risk of multiple reflections between mirror and scintillator. This detector has its longest axis oriented vertically to minimise the encumbrance in the working plane. At the moment of this writing, the set of available scintillators includes $ZnS/{}^6LiF$ scintillators of different thicknesses (200, 100 and 50 μm), as well Gadolinium Oxysulfides (20, 10, 5 μm $Gd^2O^2S : Tb/{}^6LiF$ and a 3 μm one, this latter one enriched with the isotope 157 of Gadolinium: ${}^{157}Gd^2O^2S : Tb$). These gadolinium scintillators can also be (and are predominantly) used in the high resolution detectors detailed in the next section. Given the high neutron flux, their efficiency decreases with time and they are therefore periodically replaced, and new scintillators of different sizes, thicknesses and compositions will be added to the above set, depending on the necessities. A mirror is placed behind the scintillator at an angle of 45° , held by a mechanically adjustable frame, which ensures a 90° image reflection. This common solution is adopted to keep the camera electronics out of the primary beam in order to minimise radiation damage. While the choice of the mirror was initially optimised for optical efficiency, this has resulted in a relatively high gamma count near the camera which can reduce its life expectancy, increase noise and induce occasional camera errors. Currently a 0.5 mm thick SiO_2 wafer coated by

pure aluminium layer is used as a mirror, with a noticeable reduction of measured gammas, and an acceptable loss of light. Images are acquired by a Hamamatsu ORCA-Flash4.0 V2 sCMOS camera, which is actively water cooled. This camera has an array of 2048x2048 pixels 6.5 μm in size. In this case a sCMOS camera was chosen over a CCD for the higher (100 Hz) maximum reading speed, essential given the high flux of the instrument, albeit the addition of a new CCD camera for the higher resolution is planned in the future. This camera can mount a set of lenses including a 24 mm f./0.9, 50 mm f./1.2, 60 mm macro f./2.8, 85 mm f./1.2, 100 mm f./2.0 macro, 105 mm f./1.4, 180 mm macro f./3.5 as well as 1.4x and 2.0x teleconverters, for a continuous range of fields of view from 165 mm \times 165 mm down to potentially below 20 mm \times 20 mm (although below 30 mm the high resolution setups are optically more efficient) as highlighted in Fig. 8.

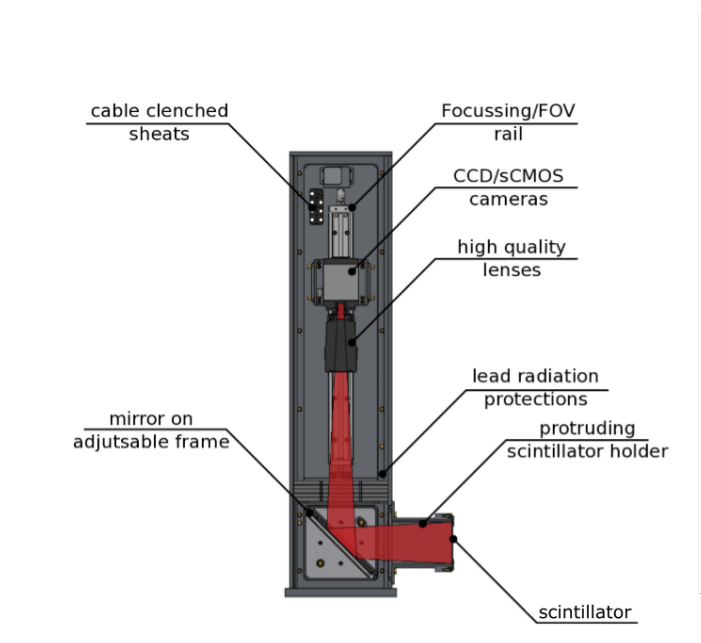


Figure 7: Commented design of the medium resolution detector at NeXT.

The camera is mounted on a high accuracy rail (nominally $\pm 3 \mu\text{m}$ position repeatability) coupled with a high precision optical encoder (down to 50 nm), which permits the adjustment of the field of view as well as to finely tune the focus. The entire mechanics (choice of granite as construction material, as well as the high accuracy of the linear actuators and encoders down to few microns in accuracy and repeatability as will also be the case for the x-ray setup in section 4.2) was conceived for thermal and mechanical stability of the setup to enable the desired high spatial resolutions across a tomography in a non-temperature controlled bunker, as well as for experimental repeatability. Once the manual pre-focusing is performed with an optical target, a number of images of a known target at regularly spaced camera positions are acquired. Their frequency content is then analysed to determine the sharpest image and therefore the optimal focusing position. The high reproducibility of the setup permits to then go back to this ideal position. The highest spatial resolution achieved with this setup is of 30 μm . The setup is encased within a box which ensures light tightness including light-tight sheaths to pass the control cables. Multiple 2 cm thick lead sheets coupled with 0.5 mm boron carbide sheets are then used to further reduce the radiation damage to the optical components. To have a *general indication* of the overall efficiency of this setup, it takes 0.5 s to almost saturate the camera in binning 1 using a 100 μm $ZnS/{}^6LiF$ scintillator, for a field of view of about 100 mm (using the 50 mm lens). This implies that in binning 4 it takes indicatively 30 ms to almost

saturate the camera, (*i.e.* the signal to noise ratio goes below 10 only around 1 ms exposure). This in turn implies that fast tomographies composed for example of 200 or 300 projections can be acquired with sub-second exposures. For example the tomographies in Fig. ?? are a recent result from [5], and were acquired in 1.5 s, highlighting a water imbibition front in a loose soil containing Lupine roots, underlining the potential of the technique for imaging of high speed processes.

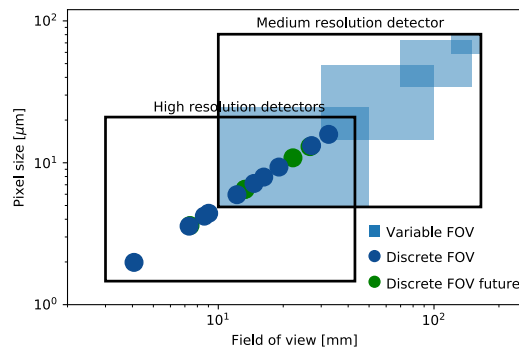


Figure 8: Range of available (and forthcoming) fields of view and corresponding pixel sizes achievable with the medium resolution and the suite of high resolution detectors

4.1.2 High resolution setups

To achieve better spatial resolutions, a higher degree of collimation (L/D , where L is the pinhole/sample distance and D is the pinhole size) of the beam is necessary, which reduces the effective neutron density at the sample position. Additionally, given the higher magnification required, the density of neutrons *per pixel per second* is also reduced. Smaller effective pixel size also requires higher magnification lenses which have a lower numerical aperture (their photon acceptance). Finally, the higher light output scintillators (*e.g.*, the $ZnS/{}^6LiF$ ones) cannot be employed : in these scintillators, in fact, the capture process begins with the activation of 6Li , which emits triton and alpha particles, exciting the ZnS , which in turn emits photons. The mean free path for these triton particles in $Li6/ZnS$ is $130\ \mu m$, which is incompatible with higher resolutions. Conversely, Gadox scintillation works through electrons whose mean free path is $12\ \mu m$. The drawback is that while $10\ \mu m$ of Gd can stop 90% of the beam, the photon emission per neutron is orders of magnitude lower than $Li:F$ scintillators. Consequently, while the detector detailed in the previous section could in principle be adopted for higher resolutions, the exposure times rapidly becomes unsustainable. The approach followed here for the higher resolutions is therefore to adopt optically optimised solutions covering a number of discrete fields of view (rather than allowing its continuous variation as for the medium resolution detector) to partially compensate for the lower photon flux. It makes use of the infinity corrected optics approach described in [6] and adopted in other leading centres such as the Helmholtz Zentrum Berlin (from which this design was inspired). It employs an “imaging lens” (usually a telephoto or tube lens) to form a parallel light image which is then captured by one of the high aperture “objective lenses” detailed above. NeXT-Grenoble currently employs two setups relying on one of two right-angle lenses manufactured by Rodenstock: an XR-Heliflex $f = 122\ mm$ $f/2.6$ (Numerical Aperture $NA = 0.2$) and a TV-Heliflex $f = 55\ mm$, $f/1.0$, ($NA = 0.41$), with a third, intermediate detector mounting an XR-Heliflex $f = 100\ mm$, $f/1.50$, ($NA = 0.32$) currently under construction. Depending on the combination of imaging and objective lenses used, the *effective* pixel size changes. This is usually expressed through the magnification factor M , which in this case is simply the ratio between the focal lengths of the Objective and the Imaging lenses. One

of the several possible configurations allowed by this setup, combines the 55 mm TV-Heliflex, coupled with the 180 mm Canon objective lens, which yields a magnification factor of 3.27, which, when the Hamamatsu ORCA sCMOS camera detailed above is used, gives a virtual pixel size of $6.5/3.27=1.99\ \mu\text{m}$. While zoom lenses could be adopted for this setup, allowing intermediate fields of view, these lenses have generally a lower numerical aperture, which increases the exposure time and lower sharpness. Fig. 9a shows a rendering of the detector mounting a 55 mm TV-Heliflex in a configuration coupling it with a the 50 mm f/1.2 Canon (*i.e.* in this case the virtual and real pixel sizes coincide). Unique to this design is the possibility to change the objective lenses while maintaining the distance to the imaging lens constant, essential to minimise photon losses. Different scintillators can be mounted on either detectors. The design allows the minimisation of the sample/detector distance by virtue of the shape of the scintillator holder as well any potential interactions with the x-ray setup thanks to the compact design and to the possibility to orient the detector in three different positions (with camera to the right, the left or above the beam). At the moment of this writing this setup achieves a resolution of about $4\ \mu\text{m}$, as highlighted in Figure 9b. This compares favourably with the existing results from the literature. For example, the PSI Neutron Microscope Project follows a classic scintillator/mirror/lens design but adopts a bespoke, high numerical aperture lens with a fixed focal length. To the best of the authors' knowledge its current highest resolution of $4.5\ \mu\text{m}$ was achieved based on 40 individual radiographs over about 20 minutes when it was recently tested at the Institut Laue Langevin. Approaches based on single event reconstruction provide spatial resolutions as low as $2\ \mu\text{m}$, albeit coming at the cost of the acquisition of about 10^5 frames, which, with the current technology, translates to more than one hour per radiograph, not accounting for the time needed for the data treatment as centroid recuperation. This was achieved by combining the 55 mm TV-Heliflex lens, the 180 mm objective and the $3\ \mu\text{m}\ ^{157}\text{Gd}^2\text{O}^2\text{S} : \text{Tb}$ scintillator detailed in and produced and sold by the Paul Scherrer Institute. To provide a *general indication* of the overall efficiency of this setup, it takes less than one minute to saturate the 16 bit camera with a standard $5\ \mu\text{m}\ \text{Gd}^2\text{O}^2\text{S} : \text{Tb}$ scintillator and an effective pixel size of $3.2\ \mu\text{m}$ pixel size, yielding a $7\ \mu\text{m}$ resolution (55 mm TV-Heliflex, 100 mm f/2.0 Zeiss lens). This would be about twice as long with the setup yielding a $4\ \mu\text{m}$ resolution.

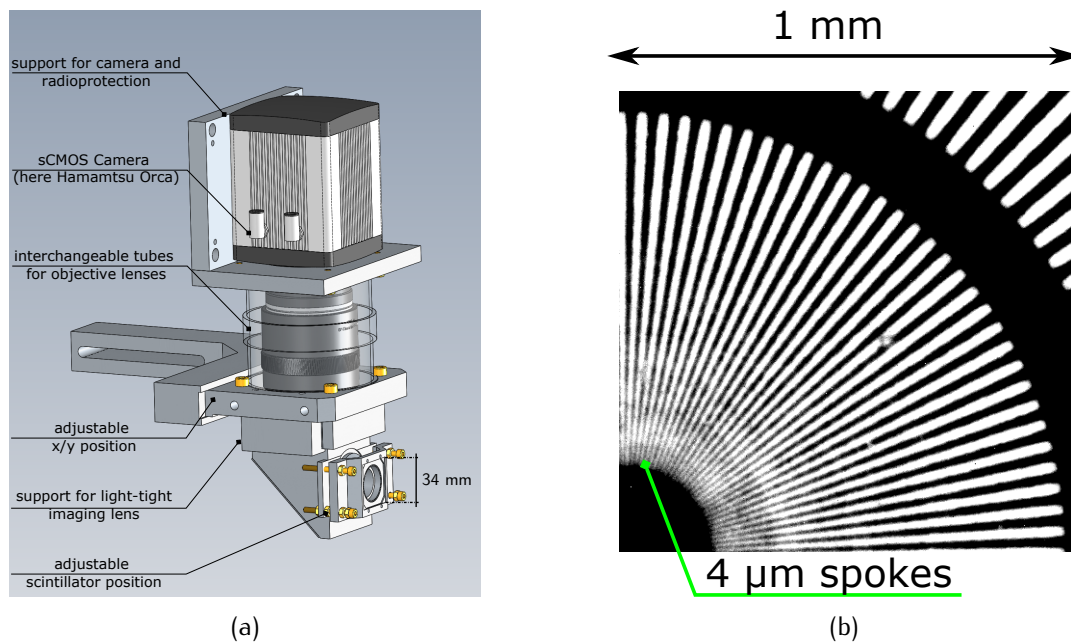


Figure 9: Commented design of the high resolution detector at NeXT (a). The highest spatial resolution achieved, around $4\ \mu\text{m}$, is highlighted by the visible $4\ \mu\text{m}$ spokes at the centre of the Siemens Star target produced and sold by PSI in (b).

4.2 X-ray setup

The x-ray setup is constituted by a microfocus x-ray generator, a detector as well as by the corresponding mechanics, as highlighted in Fig. 10a. The x-ray source is a Hamamatsu L12161-07, a sealed microfocus source with a Tungsten target and a Beryllium window. It can accelerate electrons towards the target with up to 150 kV and up to $500\ \mu\text{A}$, with a minimal focal spot size of $5\ \mu\text{m}$. To maximise the lifetime of the source by reducing the damage caused by any scattered neutron, the source is encased by an aluminium box containing 6 mm of lead and 10 mm of boron carbide except in the exact point of exit of the beam, where a removable boron carbide plaque is placed. The detector is a Varex PaxScan[®] 2530HE, where the HE stands for “High Energy”. In this particular model in fact the electronics is moved to the sides of the active area of the detector (rather than behind it). This allows the masking of the electronics with additional shielding, for nominal use above 225 kV. In our case, a supplementary aluminium frame was installed to allow the addition of an extra sheet of 6 mm of lead as well as 10 mm sheets of boron carbide to cover the deported electronics. The active area of the detector also has a protective layer of 5 mm of Boron Carbide which only reduces the x-ray flux by a few percent while attenuating 99.9% of the scattered neutrons. The use of lithiated polyethylene was also tested with comparable effects. These additional protections are particularly important at ILL, given the flux. The detector has 1792×2176 pixels $139\ \mu\text{m} \times 139\ \mu\text{m}$ in size and is oriented in portrait mode, and has a maximum speed of 9 Hz (or 33 Hz in binning 2). The scintillator chosen was Caesium Iodide (rather than the Gadolinium Oxide one) following the logic that the Gadolinium oxide one is also very sensitive to neutrons, meaning that it would more promptly detect unwanted neutrons scattered towards the flat panel. Furthermore, Caesium Iodide scintillators are more efficient than Gadolinium Oxide ones at higher x-ray energies, which is coherent with the types of samples more likely to be tested at NeXT. It should be noted that the choice of the source and detector adopted, as well as of multiple other details regarding the x-ray setup, follows the successful example of the laboratory scanner of Laboratoire 3SR, partner in the development of this instrument. The source and detector are mounted onto a granite arch (as shown in Fig. 10 a) and their

distance is step-wise fixed (the source holder allows for four different position 20 mm apart). The shortest distance is of 500 mm, chosen to be slightly larger to the maximum illuminated area given the 43° of opening of the beam, and by geometrical considerations. The zoom is made possible by an axis moving this ensemble with respect to the sample. This ensemble can also pivot by $\pm 20^\circ$ to reduce the cross-talk between the x-ray and the neutron setup as well as be moved into a “parking position” beside the neutron flight tube. This setup can achieve spatial resolutions as small as 5 μm and fields of view in principle almost as large as the 30 cm \times 25 cm detector depending on the geometry of the object. Further details about the setup including the reasoning behind these technological choices, the cross-talk between techniques, the overall calibration of the setup and the data integration go beyond the purpose of this paper and will be detailed in a future publication. NeXT-Grenoble, whose x-ray capabilities were added less than one year after its entrance into operation (*i.e.*, in 2017 [3]), is not the only instrument allowing for simultaneous x-ray and neutron imaging. The aforementioned BT2 instrument at NIST also allows for simultaneous x-ray imaging, and first instrument description was published around the same period, albeit some abstracts reporting the use of the technique date to 2016). PSI started instead introducing the possibility for combined x-ray and neutron imaging in 2015, with early results in 2016, as detailed in. It should be noted that in all these setups the x-ray capabilities are comparable to those of commercial $\mu\text{-CT}$ scanners, with resolutions around a few micro-meters. At the moment of this writing, several commercial x-ray scanners allow for significantly higher resolutions, even in the hundreds of nanometer range, allowing studies at spatial and temporal scales inaccessible to neutrons. While this is of great interest for numerous scientific problems, it comes at the cost of higher thermal and mechanical constraints, and can limit the possibility of a direct comparison between the x-ray and neutron images, which justifies the choice of the setup detailed above.

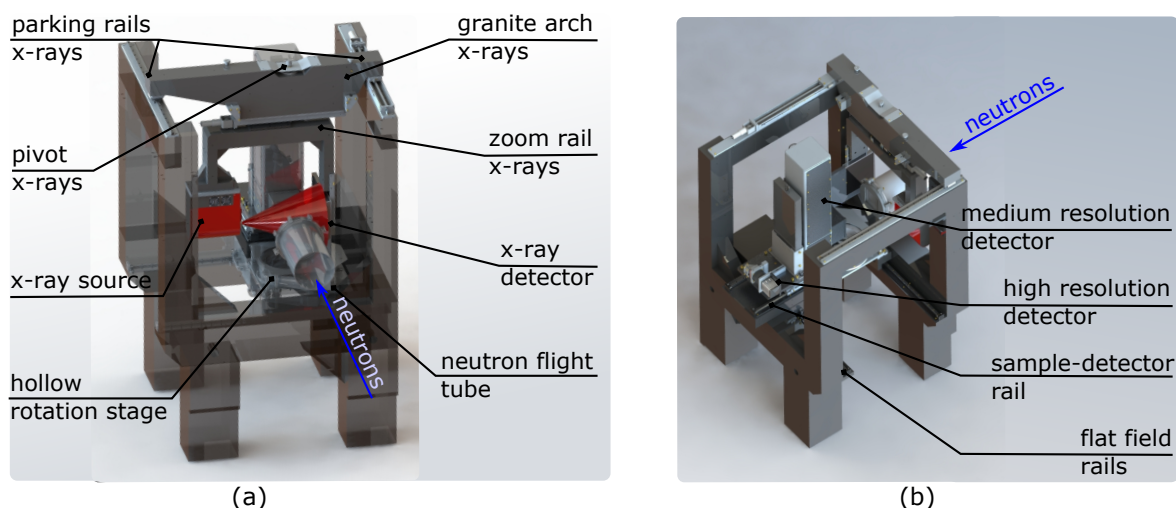


Figure 10: Design of the sample station highlighting the x-ray setup (a) and the neutron detectors (b).

4.3 Sample environment

The aforementioned x-ray and neutron setups are mounted on the granite structure in Fig. 10 and at <https://youtu.be/4gPLJsk-9Ig>. Granite was chosen for its thermal and mechanical stability, essential given the high spatial resolutions sought and the current lack of thermal buffers to the environmental temperature variations of the hall. One of the unique aspects of the setup is the adoption of a large, hollow rotation table (350 mm inner diameter). This allows for a variety of complex thermo-chemo-hydro-mechanical testing rigs to be installed with

ease. Some sample environments can require heavy and cumbersome equipment, which is best placed below the rotation table where its weight stabilises the setup. This also allows the thickness of most apparatus (*e.g.*, triaxial, tension, flow rigs) to be minimised since the cell only needs to withstand the imposed loads. To maximise the space available to the testing rigs the rotation stage is therefore placed 1050 mm from the ground (*i.e.*, 260 mm below the centre of the beam, which is at 1310 mm from the ground) and an additional rectangular hole 450 mm deep is carved in the floor underneath it. The table can nominally withstand loads up to 500 kg with ± 5.0 millidegree accuracy. An especially designed vertical axis allows for up to 90 mm vertical displacement without encumbering the region underneath the hole of the table. A number of hollow or solid interface plates as well as an x, y, z and tilt axes can be added on top of the rotation stage depending on the application. To acquire “open beam” or “flat field” images with ease, the rotation stage and the granite slab to which it is attached are mounted on rails moving both transversely to the neutron beam. The detectors are on a rail system, which allows the regulation of their distance to the sample position. Near the sample environment a number of experiment infrastructure are available including AC (220 V and 380 V) and tunable DC electrical supplies (0–30 V, 0–3 A), exhaust gases recuperation system, compressed air (700 kPa), industrial input and output water systems, USB and Ethernet cables, monitoring cameras *etc.* Additional external gas bottle supply pipes and corresponding monitors (*e.g.*, hydrogen) are also currently under development.

4.4 Control software

The motion components, cameras, x-ray source and detector are all controlled by a user-friendly adaptive graphical user interface (GUI) specially developed with imaging in mind by the company RX-Solutions (France) over the past 15 years (<https://www.rxsolutions.fr/>). This software, initially developed for x-ray imaging, was adapted and optimised for combined x-ray and neutron acquisitions in collaboration with this company. This Qt, C++ based software allows a live flat and dark-field image correction, has a live 3D CAD model of the current position of all axes, can be controlled by both user interface and command line and is fully scriptable. Most importantly, the setup is fully calibrated so that the reconstruction parameters and pixel size are known for any given axis combination for both the x-ray and the neutron tomographies.

5 Selected examples of early results

A selection of examples coming from this instrument can be found in [7] (upon which this contribution is based) as well as in [8] (which provides a broader summary of the contribution of neutron imaging to geomechanics).

6 Summary and future outlook

NeXT-Grenoble combines the world-leading flux of the ILL with high performance detectors, a high stability sample environment conceived for *in-situ* testing as well as a highly complementary x-ray setup allowing for fully simultaneous bi-modal acquisition. The version of the instrument detailed above focuses on white beam cold neutrons and x-ray imaging. Additionally, it currently shares the available ILL beam-time with a rainbows reflectometer. Thanks to the technical accomplishments and the high demand, the team involved has recently secured funding for a major upgrade of the instrument, within the Endurance Phase II program of ILL, which is expected to be delivered in 2021/2022. The instrument will become a standard ILL public instrument, thus accessing the entirety of available beamtime, available through the ILL proposal system. This

new upgraded instrument will maintain the collaboration with the Université Grenoble Alpes with the addition of a partnership with the Helmholtz-Zentrum Berlin, including the integration of components and developments from the CONRAD-II imaging instrument [9, 10]. The future plan of the instrument, sketched in Fig. 11, foresees the addition of energy selective options (double crystal monochromator, velocity selector), polarised neutron imaging as well as grating interferometry, and generally the improvement of user facilities and instrument performance. These upgrades open a plethora of new options to tackle a variety of open scientific questions, as detailed by recent reviews focussing on advanced neutron imaging techniques (*e.g.*, [2, 9, 1]). For example, energy selective options [11] allow an enhancement in element sensitivity, provide insight into phase distributions in structural metals and geomaterials and give access to structural phase transitions and even strain fields [12]. Grating interferometry decouples angular and spatial resolutions and allows for detecting phase contrast (*i.e.*, shift of phase due to refraction) as well as dark-field contrast (due to small-angle scattering), thus allowing the study of structures whose sizes are below the resolution of the detector [13]. For example, dark-field enables the study of the wall between two magnetic domains for high-permeability steel laminates. Through phase contrast it is possible, for example, to distinguish Copper and Titanium where the neutron attenuation contrast is modest by virtue of their different refractive index. Finally, by studying the change in orientation of polarised neutrons it is possible to study the fundamental magnetic properties and basic phenomena in condensed matter, such as the characterisation of magnetic flux in superconductors below the critical temperature and the skin effect in conductors or magnetic domain distributions in bulk ferromagnets [14].

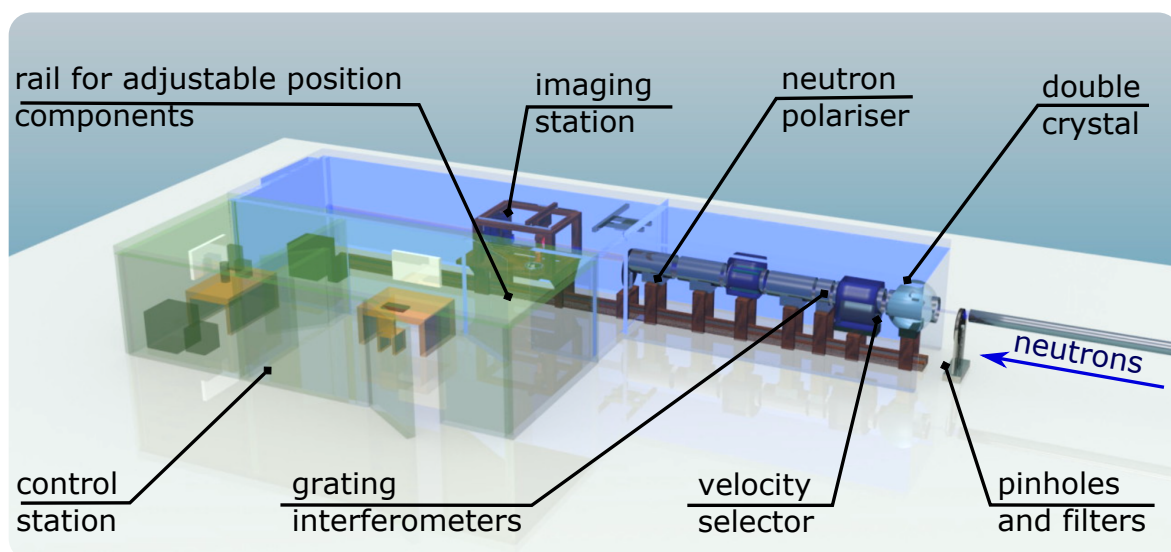


Figure 11: Conceptual drawing of the future upgrade of the instrument.

Acknowledgements

This work is supported by the French National Research Agency in the framework of the "Investissements d'avenir" program (ANR-15-IDEX-02) as well as by the company TOTAL. The authors also wish to thank the members of the Committees of the instrument (in alphabetical order I. Betremieux, J. Desrues, G. Fragneto, G. Galliero, S. Hall, M. Johnson, M. Letiche, P. Moonen, C. Simon, N.C. Tranh) for their help and support. We also wish to thank the help of Nikolay Kardjilov and Jaime Segura, as well as the essential technical support of K. Buckley. Finally, the authors wish to thank the anonymous reviewers for their helpful comments and recommendations, which helped improve the quality of this paper.

References

- [1] M. Strobl, I. Manke, N. Kardjilov, A. Hilger, M. Dawson, J. Banhart, Advances in neutron radiography and tomography, *Journal of Physics D: Applied Physics* 42 (24) (2009) 243001.
- [2] N. Kardjilov, I. Manke, R. Woracek, A. Hilger, J. Banhart, Advances in neutron imaging, *Materials Today* 21 (6) (2018) 652–672.
- [3] A. Tengattini, D. Atkins, B. Giroud, E. Ando, B. J. G. Viggiani, Next-grenoble, a novel facility for neutron and x-ray tomography in grenoble, *Proceedings of ICTMS2017-163* 88 (03).
- [4] R. Cubitt, J. Segura Ruiz, W. Jark, Rainbows: refractive analysis of the incoming neutron beam over the white spectrum. a new fast neutron reflectometry technique exploiting a focusing prism, *Journal of Applied Crystallography* 51 (2) (2018) 257–263.
- [5] C. Tötze, N. Kardjilov, N. Lenoir, I. Manke, S. E. Oswald, A. Tengattini, What comes next?—high-speed neutron tomography at ill, *Optics Express* 27 (20) (2019) 28640–28648.
- [6] S. Williams, A. Hilger, N. Kardjilov, I. Manke, M. Strobl, P. Douissard, T. Martin, H. Riese-meier, J. Banhart, Detection system for microimaging with neutrons, *Journal of Instrumentation* 7 (02) (2012) P02014.
- [7] A. Tengattini, N. Lenoir, E. Andò, B. Giroud, D. Atkins, J. Beaucour, G. Viggiani, Next-grenoble, the neutron and x-ray tomograph in grenoble, *Nuclear Instruments and Methods in Physics Research Section A: Accelerators, Spectrometers, Detectors and Associated Equipment* (2020) 163939.
- [8] A. Tengattini, N. Lenoir, E. Andò, G. Viggiani, Neutron imaging for geomechanics, a review, submitted.
- [9] N. Kardjilov, I. Manke, A. Hilger, M. Strobl, J. Banhart, Neutron imaging in materials science, *Materials Today* 14 (6) (2011) 248–256.
- [10] N. Kardjilov, A. Hilger, I. Manke, R. Woracek, J. Banhart, Conrad-2: the new neutron imaging instrument at the helmholtz-zentrum berlin, *Journal of Applied Crystallography* 49 (1) (2016) 195–202.
- [11] E. Lehmann, G. Frei, P. Vontobel, L. Josic, N. Kardjilov, A. Hilger, W. Kockelmann, A. Steuwer, The energy-selective option in neutron imaging, *Nuclear Instruments and Methods in Physics Research Section A: Accelerators, Spectrometers, Detectors and Associated Equipment* 603 (3) (2009) 429–438.
- [12] R. Woracek, J. Santisteban, A. Fedrigo, M. Strobl, Diffraction in neutron imaging—a review, *Nuclear Instruments and Methods in Physics Research Section A: Accelerators, Spectrometers, Detectors and Associated Equipment* 878 (2018) 141–158.
- [13] M. Strobl, R. P. Harti, C. Grünzweig, R. Woracek, J. Plomp, Small angle scattering in neutron imaging—a review, *Journal of Imaging* 3 (4) (2017) 64.
- [14] M. Strobl, H. Heimonen, S. Schmidt, M. Sales, N. Kardjilov, A. Hilger, I. Manke, T. Shinohara, J. Valsecchi, Polarization measurements in neutron imaging, *Journal of physics d-applied physics* 52 (12) (2019) 123001.

A one parameter damageable contact law for the DEM study of cohesive granular materials

Cyrille COUTURE^{1,*}, Jacques DESRUES^{1,†}, Vincent RICHEFEU^{1,‡}, Pierre BÉSUELLE^{1,§}

¹ Univ. Grenoble Alpes, CNRS, Grenoble INP, 3SR, 38000 Grenoble, France

Abstract: A novel type of damageable cohesive law is presented for paired particle interactions in a DEM granular arrangement. It is designed in the spirit of a mixed breakage criterion for solid cohesion interaction, which can be implemented in parallel to a granular-frictional contact law. The evolution of damage at the contact level can be easily modulated to enable a progressive transition from an initially linear elastic response to a loss of cohesion, by using a single parameter χ^* . In a straightforward numerical implementation, the effect of this contact model is presented for a 3D periodic boundary condition DEM code. The results from a series of simulations show that, for a constant peak resistance of the cohesion, a more progressive damage result in an increase of the peak stress in a particle assembly, as well as a continuous transition in the stiffness of the stress-strain response around the peak stress.

1 Introduction

The discrete element methods (DEM) are well suited to the study of granular materials, where the kinematic of individual particles in a granular assembly can be simultaneously resolved by the equations of motion. The sum of forces acting on the particles is dependant on their morphological properties, the contact laws governing their interactions, as well as the spacial organisation of the particles in a complex connectivity network. In the simplest implementations of a particle geometry and contact laws, such as dry frictional contact for spherical particles, the spacial organisation and evolution of the granular system has proven to successfully reproduce the rich phenomenological behavior of various types of granular materials. The DEM has therefore found numerous applications in geological processes, agronomic transformation and powder technology.

For applications involving different types of granular media, different enriched DEM contact models have been developed to take into account complex physico-chemical inter-particle interactions and coupling effects with the interstitial solid and fluid phases in the porous media [7]. The contact models are usually formulated to capture the physical behavior of a particular granular media while retaining a low computational cost. This last requirement is of great importance for the DEM framework to remain effective in its application to large modeling domains. In this case long simulation times are expected due to the large number of particle interactions be computed and updated at every time step.

In this context, we present a damageable cohesive contact model which accounts for the progressive loss of cohesion between particles using a single additional damage parameter. It is here generally introduced within the limiting cohesion criterion for mixed interactions presented in [3]. We then present the results for a simple implementation of this modified contact law for DEM simulations performed over a representative elementary volume (REV), subjected to biaxial loading conditions.

*Email: cyrille.couture@3sr-grenoble.fr

†Email: jacques.desrues@3sr-grenoble.fr

‡Email: vincent.richefeu@3sr-grenoble.fr

§Email: pierre.besuelle@3sr-grenoble.fr

2 Damageable contact law

Within a general three-dimensional DEM framework, based on the approach introduced by [2] and sometimes referred to as “molecular dynamics”, the particles are modeled as soft spheres which are, in the event of a detected contact, allowed to overlap and generate repulsive forces. These forces are usually decomposed between the normal direction to the contact orientation and the frictional forces acting in the tangential plane perpendicular to the contact orientation (Figure 1a). Additionally, a state of solid cohesion may exist between two particles, for which the forces are also decomposed in the same normal direction and tangential plane. The components of the resulting force vector for each interaction is therefore decomposed both in the spacial directions and in a parallel action of the granular-frictional and cohesive part of the contact law (Figure 1b). According to this decomposition, the resulting force between two particles, q and r , can be written as

$$\vec{F}^{q/r} = \left(F_n^{gran} + (1 - D)F_n^{coh} \right) \vec{n} + \vec{F}_t^{gran} + (1 - D)\vec{F}_t^{coh} \quad (1)$$

where the denomination “gran” indicates the part of the interaction generating a granular-frictional force, i.e. the normal repulsive and tangential frictional forces; while the denomination “coh” indicates the part of the interaction contributed by the (damageable) cohesive forces. The damage variable D evolves depending on the state of the contact between 0 to 1, according to the cohesion criteria detailed in Section 2.

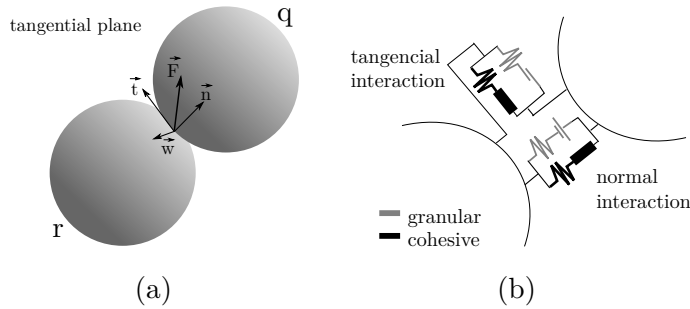


Figure 1: Schematic representation of a paired interaction in 3D (a), and associated parallel implementation of the contact model (b).

The contact law governing the mechanical response between each paired interaction relates the forces to the relative motion of the particles in a paired interaction. In the present model, a simplified approach to the Hertzian contact model is considered, using an independent linear elastic relation for each of the force component. The calculation of the 3D displacements δ_n and incremental displacement δ_t are based on an objective formulation [4]. Figure 2 illustrates the behavior of the contact laws. As illustrated in this schematic representation, the granular-frictional contact state is determined by the relative position of the particles, and the detection of an overlap. The tangential part equally vanishes if no contact is detected. However, in order to determine the state of solid cohesive, a cohesion criterion is used to obtain a value of the damage variable (D).

2.1 Brittle cohesion criterion

The state of solid cohesion, which may exist between any two particles in the REV, is tested against a cohesion breakage criterion at every time-step. This criterion can be formulated as a surface in a hyperspace accounting for the combined contribution of the different deformation mechanisms acting at the contact point of the paired interaction [3]. In a formulation accounting

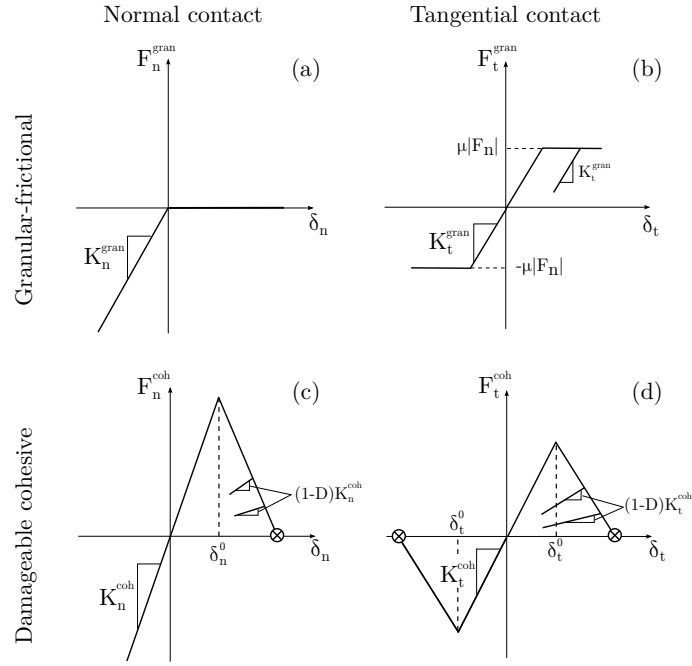


Figure 2: Normal and tangential action of the granular-frictional and cohesive contact laws.

for the normal and tangential effects, it is expressed as

$$G_D(\delta_n, \delta_t) = \frac{\delta_n}{\delta_n^0} + \left(\frac{\delta_t}{\delta_t^0} \right)^\alpha - 1 = 0 \quad (2)$$

where δ_{n0} and δ_{t0} are respectively the normal and tangential displacements. The subscript "0" in equation (1) denotes the three surface intercepts with the principal axis and are prescribed parameters influencing the level of resistance of the cohesive forces to the different deformation mechanisms. In a 2D parametric space, equation 2 is represented by an open ended quadratic surface around the δ_n axis (see figure). For this breakage surface, the criterion cannot be satisfied from the single action of normal compression at the contact point. The integer parameter α determine the shape of this surface and thus the resistance of the bond to the combined effect of the different types of motions.

In the instance of an instantaneous loss of cohesion, i.e. no progressive damage, the cohesive part of the contact vanishes as the breakage surface is attained within any given time step. Therefore, the damage variable holds a binary value,

$$D = \begin{cases} 0, & \text{if } G < 0 \\ 1, & \text{elsewise} \end{cases} \quad (3)$$

where the cohesive contact is either linear elastic ($D = 0$) or broken ($D = 1$). However, in this implementation, the abrupt change in the cohesive state between a pair of particles induces a discontinuity in the local contact force. In fact this type of event instantaneously releases stored strain energy from individual contacts into the particulate arrangement, and thus may result in kinematic instabilities as well as large fluctuations in the neighboring contact forces with the propagation of elastic waves. Such event may result from small relative displacement in the contact or numerical noise as the breakage surface is approached.

2.2 Damage cohesion criterion

To mitigate the non-physical effect of an abrupt discontinuity in the contact force, a damageable cohesive law is introduced at the contact level. This extended formulation of the initial cohesive induces a progressive transition between the peak resistance of the cohesive contact, as the breakage criterion is first satisfied, and a complete loss of cohesion. The modified damage criterion from equation 1 takes the form,

$$G_D(\delta_n, \delta_t, \chi) = \frac{\delta_n}{\chi \delta_n^0} + \left(\frac{\delta_t}{\chi \delta_t^0} \right)^\alpha - 1 = 0 \quad (4)$$

where $\chi \in [1, \chi^*]$ introduces a homothetic transformation of the initial criterion. The damage threshold parameter χ^* , at which the cohesive part of the contact is lost (i.e. $D = 0$), is a user-defined constant for the model. The evolution of a damage variable D , associated with each cohesive contact, is therefore relative to the current surface (χ) and the maximum surface (χ^*). For each time step, where i denotes the value of the variables from the previous time step and f the value of the variables calculated in the current time step, if $G_D(\delta_n^f, \delta_t^f, \chi^i) > 0$, then the value of χ^f is updated to restore the equality in equation 4. Otherwise, it remains unchanged, i.e. $\chi^f = \chi^i$. Additionally, as the cohesive contact is incrementally damaged, the cohesive state is not restored during unloading and retains the maximum damaged state experienced by the contact, i.e. $\chi^f \geq \chi^i$. The damage variable D in the cohesive part of the contact law is thus calculated as

$$D^f = \begin{cases} 0, & \text{if } G_D \leq 0 \text{ and } \chi^f = 1 & (1) \\ \frac{\chi^f - 1}{\chi^* - 1}, & \text{if } G_D > 0 \text{ and } \chi^f \in]1, \chi^*[& (2) \\ D^i, & \text{if } G_D \leq 0 \text{ and } \chi^f \in]1, \chi^*[& (3) \\ 1, & \text{if } G_D > 0 \text{ and } \chi^f > \chi^* & (4) \end{cases} \quad (5)$$

with the different cases (1-4) illustrated in Figure 3, for an idealized loading path in the $\delta_t - \delta_n$ plane. The damage variable evolves from: (1) an intact cohesive bond in segment OA , (2) a continuously increasing damage in segment \overline{AB} and \overline{DE} , (3) an elastic unloading and reloading at stable value of D in segment \overline{BC} and \overline{CD} , and (4) a permanent breakage of the bond past point E .

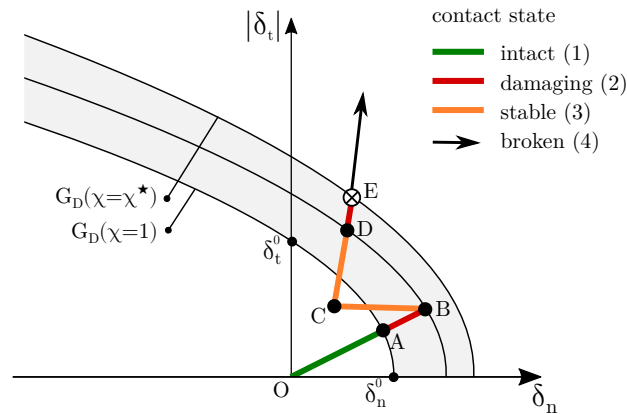


Figure 3: Evolution of the damage variable (D) in a paired interaction for an idealized loading path, illustrating the four different cases of equation 5.

The damage variable D of a contact is therefore completely determined by the maximum value of χ experienced in the contact, relative to the evolution of the normal and tangential displacements, as well as the single additional model parameter χ^* . With a value of $\chi^* = 1$,

the damageable model is seen to reduce to the binary brittle model. As higher values of χ^* are selected, the reduction of the cohesive force becomes more progressive before breakage.

The presented damageable contact law can be easily extended to account for additional deformation mechanisms, such as relative rotation of the particles. Additional terms can simply be added to equation 4. Other types of hypersurfaces may also be used to form breakage and damage criteria, which could account for the effect of compressive forces.

3 DEM implementation

The contact model presented in Section 2 is implemented in a DEM code named PBC3D. This code was specifically developed as a compact and efficient DEM algorithm to be used as a standalone program or as part of a multiscale implementation, e.g. in a FEM×DEM architecture. The domain geometry consists of a three-dimensional elementary volume (REV) of spherical particles, bounded by periodic condition in all directions.

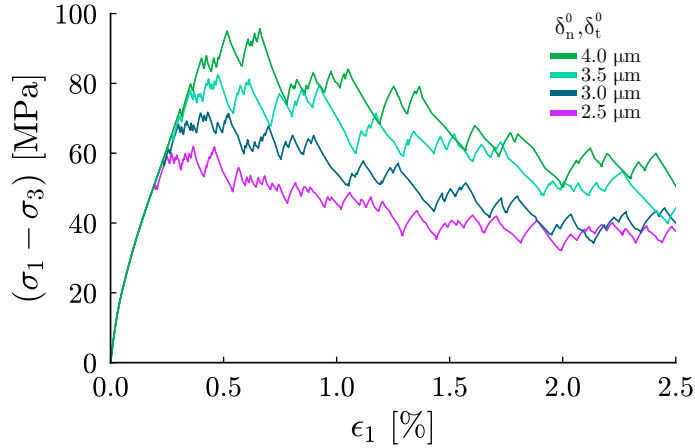
To evaluate the effect of the damageable cohesive law coupled with the granular-frictional law, a series of simulations is performed in biaxial loading conditions, where $\dot{\epsilon}_2 = 0$ and $\dot{\sigma}_3 = 0$, while the vertical axial strain ϵ_1 is monotonically increased. The subscripts 1, 2, 3 denote the principal directions of stress and strain, aligned with the geometry of the REV. The constant parameters of the model are summarized in table 1. To simplify the assumptions of the model, the ratio of tangential to normal elastic parameters (K_t/K_n) and cohesion parameters (δ_t^0/δ_n^0) are set to 1.

Table 1: Particles and contact law parameters

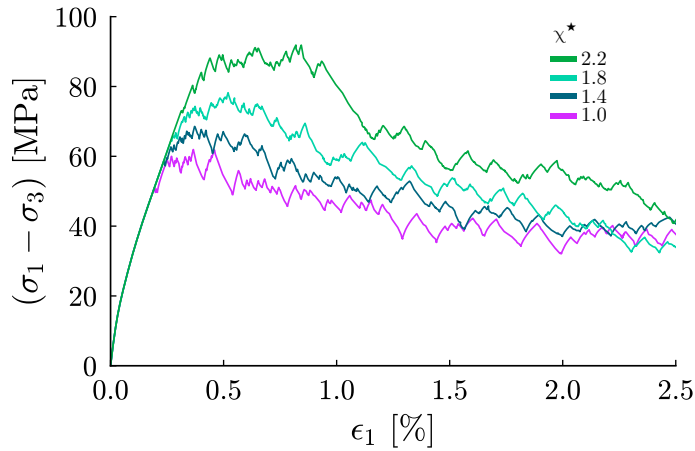
Particles	
number of particles	1000
radius ($a_{min} - a_{max}$)	250-350 μm
density (ρ)	2700 kg/m^3
Granular frictional law	
K_n^{gran}	10 kN/m
K_t^{gran}/K_n^{gran}	1
μ	0.5
Cohesive damageable law	
K_n^{coh}	10 kN/m
K_t^{coh}/K_n^{coh}	1
δ_t^0/δ_n^0	1
α	4

The simulations represented in figure 4 are performed at $\sigma_3 = 20$ MPa for different values of δ_n^0 and δ_t^0 (figure 4a), and χ^* (figure 4b), where the stress and strain are homogenized quantities over the REV domain. The lower curve in both graphs are identical. For both parameters, the contribution from the cohesive part of the interaction increases as the surface of the failure criterion expands. In the first series of simulation, with $\chi^* = 1$, the loss of cohesion occurs instantaneously at higher values of the relative displacement of each of the particles. At the REV level, this results in large fluctuations in the stress-strain response as the level of cohesion increases. This behavior is noticeable around the peak stress and during the post-peak regime. In contrast, in the second series of simulations, where χ^* increases, the maximum cohesive force remains unchanged, but the cohesive forces are decreasing progressively. The higher peak stress

in this case is attributable to the stabilization of damaging contact forces in the the assembly, which is seen to be important at the scale of the REV. As χ^* increases, it can also be noted that the fluctuations in the stress-strain response tend to decrease. This result in a smoother transition around the peak stress, where a stable hardening phase can be identify during the late pre-peak section of the curves. The parameter χ^* also influences the softening slope of the REV response after stress peak.



(a) Influence of δ_n, δ_t at $\chi^*=1.0$



(b) Influence of χ^* at $\delta_n = \delta_t = 2.5 \mu\text{m}$

Figure 4: Comparison of the mechanical response of an REV for different failure surface parameters (a) and damage parameter (b).

The influence of the damage parameter on the stress level and shape of the stress-strain curve should be considered when calibrating the cohesion parameters of the contact law. The network effect of individual interactions in a particle assembly is here seen to be important in the redistribution of forces during the progression of damage and loss of cohesion. Therefore, the addition of a damage parameter in the cohesive contact law is seen as a more physical representation of a state and evolution of solid cohesion between the particles.

The increased stability of the REV in the presence of a damage parameter also has advantageous implications for hierarchical numerical modeling using DEM to model the behavior of cohesive material [8, 1]. In the context of a FEM-DEM implementation, the stress-strain relation of individual REVs at every FEM time step serves as a constitutive model at the integration

points of the FEM mesh [6, 5]. As such, the solution of the implicit scheme solved at the macroscopic FEM level relies on the stability of the REV to obtain a continuous spacial distribution of the nodal forces. Therefore, the avoidance of large fluctuations as the cohesion starts to occur, enables a better global convergence in the transition towards the post-peak regime.

4 Conclusion

In this communication, we presented a one parameter damageable cohesive law, which extends the class mixed interaction breakage criteria for cohesive bonding of discrete particles. This damage parameter can be modulated to, on one hand, reduce to a brittle loss of cohesion, or on the other hand, provide an increasingly progressive loss of cohesion at the contact level. The usefulness of this enriched criterion is demonstrated in its application to an open-ended superquadratic breakage surface for a normal and tangential relative motion of the particles, but can be extended without difficulty to other types of surfaces and additional deformation mechanisms.

In the presented application example to a 3D periodic boundary condition elementary volume, the damage criterion is shown to result in an increase the contribution of cohesion in the macroscopic response. It results in an increase of the peak stress, and a smoother transition through a hardening phase into the post-peak regime. A stable evolution of the response, encouraged by the effect of a continuous damage of the cohesive interaction, is desirable for applications which require a stable convergence of the resulting stresses, such as in the case of FEM-DEM coupling.

Acknowledgements

This paper was prepared and submitted to the conference Powders and Grains 2021 at Buenos Aires, Argentina. It is reprinted here almost identically.

References

- [1] Cyrille Couture. *Mechanical Characterization of Porous Sandstones in True Triaxial Conditions: Diffuse and Localized Deformation, Effect of Anisotropy*. PhD thesis, Grenoble Alpes, Grenoble, France, October 2020.
- [2] Peter A Cundall and Otto DL Strack. A discrete numerical model for granular assemblies. *geotechnique*, 29(1):47–65, 1979.
- [3] Jean-Yves Delenne, Moulay Saïd El Youssoufi, Fabien Cherblanc, and Jean-Claude Béné. Mechanical behaviour and failure of cohesive granular materials: Behavior of cohesive granular materials. *International Journal for Numerical and Analytical Methods in Geomechanics*, 28(15):1577–1594, December 2004.
- [4] Jacques Desrues, Albert Argilaga, Denis Caillerie, Gaël Combe, Trung Kiên Nguyen, Vincent Richefeu, and Stefano Dal Pont. From discrete to continuum modelling of boundary value problems in geomechanics: An integrated FEM-DEM approach. *International Journal for Numerical and Analytical Methods in Geomechanics*, 43(5):919–955, April 2019.
- [5] Ning Guo and Jidong Zhao. A coupled FEM/DEM approach for hierarchical multiscale modelling of granular media: Hierarchical multiscale modelling of granular media. *International Journal for Numerical Methods in Engineering*, 99(11):789–818, September 2014.

- [6] Michał Nitka, Gaël Combe, Cristian Dascalu, and Jacques Desrues. Two-scale modeling of granular materials: A DEM-FEM approach. *Granular Matter*, 13(3):277–281, June 2011.
- [7] Farhang Radjai and Frédéric Dubois. *Discrete-Element Modeling of Granular Materials*. Wiley-Iste, 2011.
- [8] Huanran Wu, Jidong Zhao, and Weijian Liang. Pattern transitions of localized deformation in high-porosity sandstones: Insights from multiscale analysis. *Computers and Geotechnics*, 126:103733, October 2020.

Part II

Interfaces, soil–structure interactions and civil engineering structures

Comparison of discrete element and material point methods for unsteady flow modelling

Fabio GRACIA^{1,2,}, Vincent RICHEFEU^{1,†}, Pascal VILLARD^{1,‡}*

¹ Univ. Grenoble Alpes, CNRS, Grenoble INP, 3SR, 38000 Grenoble, France
² IMSRN, Montbonnot, F-38330, France

Abstract: In order to provide a comprehensive comparison between two current numerical methods employed in the modelling of rock avalanches, the Discrete Element Method (DEM) [3] and the Material Point Method (MPM) [1] were used to simulate the mass propagation along a 45° plane transitioning to an horizontal plane. When using the DEM, a 3D code using tetrahedral elements was used and the flow was channelised by means of frictionless walls. For the MPM simulations, a 2D code was developed and plane strain simulations were run. Comparisons were made in terms of run-out distance and energy dissipated. Influence of parameters such as initial sample geometry, basal friction coefficient and shape of blocks composing the sample was studied.

1 Introduction

Numerical studies involving DEM and MPM were carried out in order to test the ability and the relevance of two kinds of numerical methods (discrete and continuous methods) to reproduce the kinematics of granular avalanches (propagation distances and amounts of dissipated energies). In the field of rock mechanics, the continuum approaches are generally considered when large volumes (*i.e.* large number of blocks) are involved. For this study, the MPM was chosen over the continuum-based methods because of its hybrid Lagrangian and Eulerian descriptions, which gives it the ability to manage naturally large deformations. This makes it an ideal method for the modelling of granular avalanches involving large masses. However, the continuity assumption may also limit the domain of validity of continuum approaches, specifically when dealing with rock flows. Additionally, the computational times required by the MPM simulations are significantly low, but the dissipations means and more generally the rheologies have to be given explicitly by macroscopic constitutive laws with, unavoidably, the continuity of the medium in mind.

On the other hand, the DEM requires an accurate definition of the initial condition for the terrain, block shapes and families of discontinuities, together with prohibitive computation times. As a consequence DEM turns out to be more appropriate for medium sized volume (*i.e.*, few hundred blocks). Moreover, the complex rheologies inherent in granular materials, are naturally well captured by the DEM – provided that a minimum set of features are taken into account. In our case, these features are the block shapes and adequate dissipative contact models. The price to pay is however long computational times.

The aim of this paper is to compare the two types of methods on the base of numerical simulations that consist, first, in the release of randomly packed bricks within a parallelepiped box for the DEM, and second, in a continuum mass governed by an elastoplastic law for the MPM. The setup is depicted in Figure 1.

*Email: fabio.garcia@3sr-grenoble.fr

†Email: vincent.richefeu@univ-grenoble-alpes.fr

‡Email: pascal.villard@univ-grenoble-alpes.fr

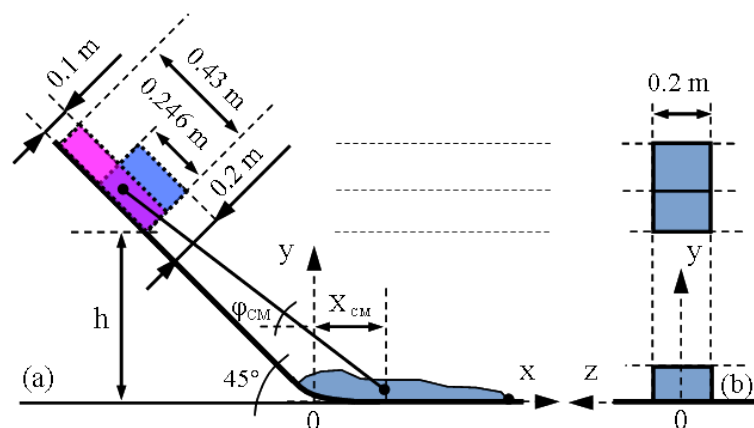


Figure 1: Geometry of the simulation setup

A total of 27 configurations were setup using both numerical methods in order to study the influence of parameters such as initial sample geometry, basal friction coefficient and shape of blocks composing the sample (the latter affecting DEM only).

2 Numerical setup

For all the configurations, randomly packed blocks (cubes of $0.01 \times 0.01 \times 0.01 \text{ m}^3$ or cuboid elements of $0.02 \times 0.01 \times 0.005 \text{ m}^3$) were used for the DEM simulations while a continuum mass governed by an elastoplastic law was considered for the MPM simulations. The container was positioned on an inclined plane at a given height, which is one of the parameters to be studied. Between the slope and the horizontal area, a smooth transition was set by means of a curvature with 0.3 m as radius. DEM simulations were performed in a three-dimensional configuration; the flow was thus channelised to make the comparison possible with the two-dimensional MPM simulations. The canal width was set to 0.2 m to make the flowing truly three-dimensional while limiting the number of elements. This width was chosen so that the ratio between the width and the size of a DEM particle was at least 10. Two different types of containers with varying aspect ratios were used as can be seen in Figure 1. The plane inclination angle was fixed at 45° , while the height at which the block was placed (which refers to the height of the corner closer to the horizontal plane) had three different values: 0.4, 0.8 and 1.6 m.

3 MPM and DEM constitutive laws

As mentioned above, simulations based on the DEM were run using a 3D code while simulations based on the MPM were run using a 2D code. In order to compare the results coming from both methods in an appropriate manner, considerations such as using plane strain when running the MPM simulations and adjusting the MPM material bulk density had to be taken into account to deal with the same mass of material. A classical Mohr-Coulomb elastoplastic law was used to describe the granular material mechanical behaviour. A constant dilatancy angle, close to zero, was used in order to prevent volume increase of the sample. For MPM elastoplastic parameters, the Young Modulus was 0.8 MPa, the Poisson ratio was 0.42, the friction angle was 28.6° , no cohesion was set and the dilatancy angle was close to zero. Within the mass the

energy dissipation \mathcal{W}^* is given by:

$$\mathcal{W}^*(t) = \sum_p \int_0^t V_p(\sigma : \dot{\varepsilon}) dt \quad (1)$$

where V_p , σ and $\dot{\varepsilon}$ are respectively the volume, the stress and the strain increment held by each material point p . Note that, the index p is not used here for the total stress and total strain to avoid any confusion with plastic terms. Note also that, here and in the following, a parameter super-scripted with a star (\star) relates to the bulk material. Otherwise the parameter concerns the interface between the flowing material and the slope.

For the DEM, the interactions between the blocks are governed by a specific contact law established at each contact point, allowing dissipation in the normal and tangential direction of the contact [2][4]. In the perpendicular direction of the contact a linear elastic law with two different normal stiffnesses (k_n), depending on whether it is loading or unloading, is used. The two stiffnesses relate by using a restitution parameter e_n^2 with a value between 0 and 1 which allows for normal energy dissipation. In the tangential direction, a Coulomb frictional model was used, while using k_t as tangential stiffness and μ as friction parameter defined as $\mu = \tan \phi$ with ϕ being the friction angle. The contact parameters governing the mechanical behaviour of the DEM elements were: $k_n^* = 10^4$ N/m, $k_t^*/k_n^* = 0.4$, $\mu^* = 0.7$, and $(e_n^*)^2 = 0.2$.

The elastic contact law and Coulomb frictional model that were used for the normal and tangential contact between particles in the DEM was used to model the boundary conditions (slope, transition and horizontal plane) in both MPM and DEM. The DEM parameters were: $k_n = 10^4$ N/m, $k_t/k_n = 0.4$ and $e_n^2 = 0.2$. This external force will be added directly to the particles in DEM, while in MPM it will be included in the body forces term involved in the conservation of linear momentum equation.

Concerning the energy dissipation between the blocks (DEM) and the boundary conditions (DEM and MPM), the overall cumulated dissipation was split into 3 contributions: (1) the cumulated work \mathcal{W}_n of the normal forces (contacts and collisions) at the base of the flow, (2) the cumulated work \mathcal{W}_t of the tangential forces (friction) at the base of the flow, and (3) the work \mathcal{W}^* of all internal action in the flowing mass. For the DEM, the dissipation within the mass is simply obtained as the sum of cumulated works of contact forces between the blocks in the normal and tangential directions:

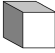

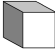

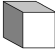


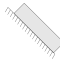

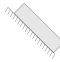

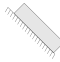
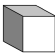

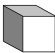

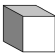

$$\mathcal{W}^*(t) = \mathcal{W}_n^*(t) + \mathcal{W}_t^*(t) \quad (2)$$

4 Selected results

The numerical configurations were defined by varying the height of release h , the shape of the blocks and the shape of the container (A, B, C), and the basal friction coefficient μ . These configurations are summarised in Table 1.

We compared first (Figure 2) the kinematics of the flow for DEM and MPM in a particular case (simulation #C1, $\mu = 0.3$). We then compared (Tables 2 and 3) the position of the center of mass X_{CM} (called *propagation distance* here) once the mass had stopped, as well as the distribution of the mass around it. Results were grouped using the basal friction, which is one of the driving parameters in our study. The distribution of the mass was quantified using the standard deviation σ_X of the positions of all blocks or material points depending on the method. In Figure 2 (the figure at the top corresponds to the DEM simulations, while the one at the bottom refers to the MPM ones) we see that the flow evolution from the beginning through the very end correlates properly. Some minor discrepancies can be seen in the shape of the final deposit, as the MPM final deposit spreads a little further. The few blocks that escaped from

Table 1: Configurations defined by changing the release height, the shape of the blocks, and the shape of the container

	Height (m)	Block Shape	Container shape
#A1	0.8		
#A2	1.6		
#A3	0.4		
#B1	0.8		
#B2	1.6		
#B3	0.4		
#C1	0.8		
#C2	1.6		
#C3	0.4		

the mass (spotted at the front of the DEM deposit) are completely absent in the MPM deposit because of its continuous nature.

However, even if in some cases there are outstanding similarities, when taking a closer look to the position of the center of mass and the standard deviation around it, the shape of the final deposits are not exactly the same. In particular, the curvature near the slope transition differs between MPM and DEM simulations, and the scattering of the blocks in front of the deposit is completely missed by the MPM. Apart from that, the main mismatch seems to appear at the very end, when the final heap is forming.

All configurations were first tested with a relatively low friction coefficient at the base: the friction angle was set to 16.7° , which is considerably lower than the internal friction angle of the granular material of 28.6° . The results obtained in terms of propagation and spreading of the mass, and total dissipation modes are summarised in Table 2 for both MPM and DEM simulations. Close correlations between the two methods can be seen.

In regard to the center of mass, X_{CM} , (see Table 2), the value reached by both methods is very similar in most of the simulations. This first observation is rather surprising when one realises that the constitutive model used in the MPM is rather simple.

In terms of energy dissipation, Table 2 clearly shows that the driving means of dissipation is the friction at the base for both DEM and MPM simulations. This is an expected result since the internal friction angle (*i.e.*, an input parameter of the constitutive model for the MPM, and a parameter mainly related to the friction between blocks in the DEM) is higher than the basal friction coefficient. Internal dissipation achieves nearly the same values in both MPM and DEM. It is however slightly greater for higher container (cases #A). The cases correlating the least (although not largely different) happen to be the ones with higher release heights (cases #B2 and #C2) for which the constitutive model has a larger influence in the stretching of flowing mass.

As for #C1, (shown in Figure 2), results correlated properly for the other simulations (from #A1 to #C3). Nonetheless, when using bricks instead of blocks in the DEM simulations, the spreading (σ_X) of the final deposit was reduced; This reduced spreading is an expected result since the rotation of single elements is greatly dependent on its shape, in this case being hindered by the use of bricks. The continuum approach however is not naturally able to simulate it in the way the DEM does.

The container shape becomes important, as well as the block shape, when analysing the amount of energy dissipated within the granular mass. When using the square container, the energy dissipated in the bulk is larger. These differences might be attributed to the constitutive model itself or to the parameters used since calibration at a very early stage was performed. In order to give a stronger role to the constitutive model, a second series of simulations were

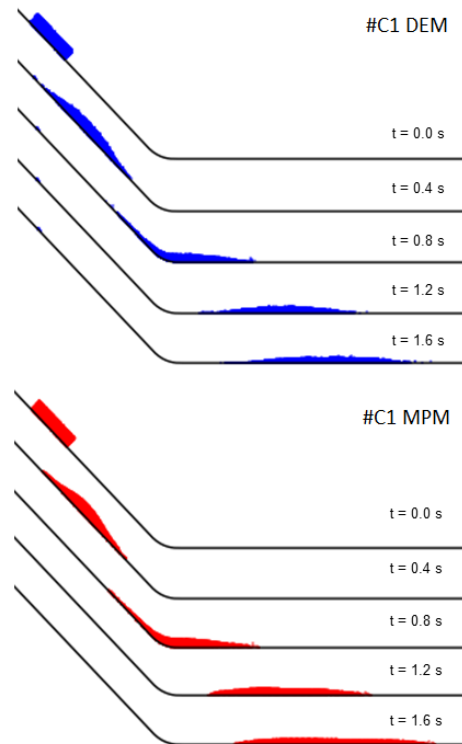


Figure 2: Simulation #C1. DEM (top) and MPM (bottom). The friction coefficient at the base is $\mu = 0.3$

Table 2: MPM and DEM run-out and energy dissipation results with a basal friction coefficient of 0.3

> MPM, $\mu = 0.3$

	X_{CM} (m)	σ_X (m)	\mathcal{W}_n (J)	\mathcal{W}_t (J)	\mathcal{W}^* (J)
#A1	1.32	0.44	0.15	151.89	15.49
#A2	2.48	0.55	0.38	293.45	18.12
#A3	0.74	0.37	0.10	80.17	14.65
#B1	1.42	0.44	0.09	111.23	6.70
#B2	2.57	0.57	0.19	205.70	8.80
#B3	0.84	0.35	0.05	63.99	5.37
#C1	1.40	0.42	0.09	112.55	6.65
#C2	2.56	0.55	0.20	209.38	8.76
#C3	0.82	0.33	0.05	64.08	5.39

> DEM, $\mu = 0.3$

	X_{CM} (m)	σ_X (m)	\mathcal{W}_n (J)	\mathcal{W}_t (J)	\mathcal{W}^* (J)
#A1	1.30	0.39	0.98	135.40	14.34
#A2	2.46	0.55	1.51	261.29	17.72
#A3	0.71	0.31	0.79	71.18	13.29
#B1	1.40	0.33	0.16	121.82	6.97
#B2	2.55	0.41	0.26	217.34	9.86
#B3	0.83	0.28	0.11	70.57	5.14
#C1	1.39	0.39	0.60	122.04	7.51
#C2	2.54	0.51	0.99	205.51	10.21
#C3	0.81	0.30	0.39	69.51	5.89

Table 3: MPM and DEM run-out and energy dissipation results with a basal friction coefficient of 0.5

> MPM, $\mu = 0.5$					
	X_{CM} (m)	σ_X (m)	\mathcal{W}_n (J)	\mathcal{W}_t (J)	\mathcal{W}^* (J)
#A1	0.45	0.32	0.27	90.71	67.86
#A2	0.76	0.40	0.37	229.41	73.64
#A3	0.29	0.27	0.25	33.42	53.29
#B1	0.47	0.29	0.9	78.40	35.14
#B2	0.82	0.38	0.18	185.74	27.02
#B3	0.30	0.24	0.09	37.16	27.61
#C1	0.46	0.29	0.10	80.29	34.56
#C2	0.81	0.36	0.15	174.32	39.42
#C3	0.30	0.23	0.09	36.96	27.96

> DEM, $\mu = 0.5$					
	X_{CM} (m)	σ_X (m)	\mathcal{W}_n (J)	\mathcal{W}_t (J)	\mathcal{W}^* (J)
#A1	0.42	0.28	4.10	99.82	44.18
#A2	0.77	0.41	7.20	208.90	62.37
#A3	0.25	0.22	2.68	46.31	32.49
#B1	0.45	0.24	0.28	114.32	13.46
#B2	0.81	0.32	0.41	214.78	18.82
#B3	0.26	0.20	0.19	64.12	9.61
#C1	0.45	0.25	3.21	94.23	30.93
#C2	0.80	0.37	5.79	186.45	44.13
#C3	0.27	0.19	1.81	50.65	20.97

carried out with a higher friction at the base.

The friction coefficient at the base was then set to $\mu = 0.5$ corresponding to an angle of 26.6° , which is still below but close to the internal angle of friction of 28.6° . The Table 3 summarises the results obtained. At first glance it can be seen that similar results are found when comparing DEM and MPM in terms of propagation distance and spreading of the deposit, regardless of the aspect ratio of the starting box, release height or shape of blocks.

When compared with the results obtained with the low basal friction, $\mu = 0.3$, the propagation distances and spreading of the deposit were found to be smaller for all configurations. The observations made with low basal friction are still valid with a basal friction angle close to the internal friction angle.

In regard to the internal dissipation due to plastic straining, an increase can be seen. It is interesting to notice that the better matches are obtained when using a shallow container and cubic blocks for which the assumption of continuity is somehow more appropriate. In other configurations (in particular with bricks), the difference of internal dissipation is more pronounced because of the simplicity of the constitutive model. Despite this, the total amount of dissipated energy is rebalanced thanks to an increase of the friction dissipation at the base.

5 Conclusions

The use of the material point method has been evaluated in the case of a flow in the transient regime that involves finite strains. In the comparisons presented, the DEM results were taken as the ground truth. Although an extensive simplification has been considered in the continuous model, the MPM has proven to be of interest in the modelling of large size rock avalanches or landslides. In terms of energy dissipated, with the assumptions made for the constitutive law of the continuum model (Mohr-Coulomb and values of parameters) some discrepancies started to become evident as the basal friction coefficient was increased (which involves shearing within

the granular mass), but the results were still related.

In the field of soil (hydro-)mechanics or computational fluid dynamics, many constitutive models exist. The MPM provides a framework that is not more restrictive than all approaches based of the continuum assumption. Accordingly, some events such as debris flows, mud flows or snow avalanches – deemed more complex to model – can be dealt with by implementing the best suited constitutive models. A more ambitious project is to make use of two-scale modelling by replacing the constitutive law by DEM simulations (representative to the material) for each material point.

Acknowledgements

The Laboratoire 3SR is part of the LabEx Tec 21 (Investissements d'Avenir, Grant Agreement No. ANR-11-LABX-0030).

References

- [1] D. Sulsky, Z. Chen, H. L. Schreyer, *Computer Methods in Applied Mechanics and Engineering* **118**, pp. 179-196 (1994)
- [2] G. Mollon, V. Richefeu, P. Villard, D. Daudon, *Journal of Geophysical Research – Earth Surface* **117** (2012)
- [3] P. A. Cundall, O. D. L. Strack, *Géotechnique* **29**, pp. 47-65 (1979)
- [4] V. Richefeu, G. Mollon, D. Daudon, P. Villard, *Engineering Geology* **149**, pp. 78-92 (2012)
- [5] V. Richefeu and P. Villard , *Modeling Gravity Hazards from Rockfalls to Landslides* (ISTE Press Ltd, Elsevier Ltd, UK, 2016) 161 pp

Probabilistic modeling of tunnel seismic deformations: Global sensitivity analysis

Qiangqiang SUN^{1,}, Daniel DIAS^{2,†}*

¹ Univ. Grenoble Alpes, CNRS, Grenoble INP, 3SR, F-38000, Grenoble, France

² Antea Group, F-92160, Antony, France

Abstract: The application of the global sensitivity analysis (GSA) using surrogate models for the uncertainty quantification is increasing since it permits to quantify efficiently the relative importance of each input parameter with relatively small computational costs. This study aims at investigating the feasibility of applying this method to tunnel seismic deformations, considering the uncertainty of the soil-tunnel system. An advanced technique named sparse polynomial chaos expansions (SPCE) is introduced to build a surrogate model that allows performing the GSA combined with the Sobol' indices. The accuracy and efficiency of the adopted SPCE-GSA method are illustrated by comparison with the true numerical predictions and the Monte Carlo simulation. The influences of the sampling size and polynomial degree of the SPCE model on the variability of the sensitivity indices are discussed as well. The results show that the soil shear wave velocity and modulus reduction factor are the two variables that have the most significant influence on the tunnel seismic deformations.

1 Introduction

Severe tunnel damages in historical earthquakes have denoted the importance of a safe seismic design. Many efforts have been devoted to gaining a better understanding of the tunnel seismic performance against ground shaking and earthquake-induced ground failure through a series of analytical, numerical, and experimental studies [2, 3, 4, 7, 23]. The above mentioned works consider the deterministic geotechnical parameters, but they neglect any parameter uncertainty which can only be examined with a probabilistic analysis.

Due to the inherent uncertainty in nature and the presence of measurement error, soil parameters inevitably present variation and uncertainty [1, 8, 12, 20, 21]. This leads to the prediction of the seismic tunnel response is also highly uncertain. To rationally consider the uncertainty of a soil-tunnel system, the probabilistic analysis appears to necessary as it provides an easy quantification of the response variability. For any uncertainty quantification problems, the identification of the important variables is a basic but vital issue. In this regard, sensitivity analysis (SA) proves to be able to effectively quantify the relative importance of each variable on the variance of the predicted model response [16, 24]. In addition, by discarding unimportant variables, the probabilistic analysis and design works will be simplified.

Numerous techniques are nowadays used to perform SA, which can be grouped into two categories [24]: local SA (i.e., LSA) and global SA (i.e., GSA). LSA focuses on the local impact of input parameters on the model by computing the response gradient with respect to its parameters around a nominal value. Methods such as the Tornado diagram, FORM, and Monte Carlo simulation [17, 18] are commonly adopted. However, the limitations of LSA are obvious. It ignores the combination influence (interaction effect) between variables and probably output inaccurate sensitivity index in the presence of strongly nonlinear dependence between variables.

*Email: qiangqiang.sun@3sr-grenoble.fr

†Email: d.dias69@gmail.com

In addition, the computational cost increases significantly with increasing number of variables. Oppositely, GSA is an attractive and powerful tool since it can effectively tackle the above limitations [14, 15, 19, 29]. This technique offers extensive possibilities for ranking the individual and combination effects of variables simultaneously. Recently, significant attention has been given to the GSA method based on the surrogate models [25] since they permit to provide accurate information with relatively small computational costs (i.e., the original computationally expensive models are substituted by surrogate models).

The probabilistic analysis of a tunnel in seismic conditions is rarely reported [13, 18]. This could be attributed to the following reasons. Firstly, the probabilistic analysis or reliability design concept is not widely accepted both in academia and in engineering practice, design of tunnels employed in modern seismic codes is currently based on deterministic soil properties. Secondly, the ground motion variability rather than the soil parameter uncertainty is supposed to have a more pronounced influence. The record-to-record variability in terms of magnitude and frequency characteristic for a specific site is hard to assess precisely since the prediction of a future earthquake is always difficult. The third reason comes from the sophisticated and computationally expensive dynamic time-history numerical analysis. The dynamic response is generally associated with strong nonlinearity and high dimensional problems. More realizations of the computationally expensive numerical simulations are then required to build a satisfactory surrogate model. Besides, many probabilistic methods fail to represent properly the model dynamic responses although high performances are observed in static analyses.

The sparse chaos expansion based global sensitivity analysis (SPCE-GSA) method has recently been applied to the sensitivity analysis of tunnel static behaviors [19], but its capability for tunnel seismic response has never been examined especially in the strong nonlinearity and high dimensional. Furthermore, the important variables that significantly influence the variability of the tunnel seismic deformation remain unclear. This short report aims to briefly investigate these two issues in the probabilistic tunnel analysis.

2 Method

2.1 Polynomial chaos expansion

The link between the input parameters and output responses can be defined by:

$$\mathbb{Y} = M(X) \quad (1)$$

where $X = \{x^1, x^2, \dots, x^M\}$ is a random vector that parameterizes the variability of the input parameters with a dimension of M . Y is the vector of model responses $\mathbb{Y} = \{y^1, y^2, \dots, y^M\}$. In PCE, a surrogate model is built by expanding the system response on a suitable basis:

$$M(X) = \sum_{\alpha \in \mathbb{N}^M} k_\alpha \Psi_\alpha(X) \quad (2)$$

where the $\Psi_\alpha(X)$ are multivariate polynomials, $k_\alpha \in \mathbb{R}$ are the unknown coefficients, $\alpha \in \mathbb{N}^M$ is a multidimensional index. The multivariate polynomials $\Psi_\alpha(X)$ is the tensor product of univariate orthonormal polynomials $\Psi_{\alpha_i}(x_i)$. Hermite polynomials are selected for representing the univariate polynomials [15, 19]. Considering a finite sum in Eq. 2, the truncated polynomial chaos expansion is introduced [5]:

$$M(X) \approx M^{PC}(X) = \sum_{\alpha \in \mathcal{A}} k_\alpha \Psi_\alpha(X) \quad (3)$$

where $\mathcal{A} \subset \mathbb{N}^M$ is the set of selected multi-indices of multivariate polynomials. A hyperbolic (or q -norm) truncation scheme [22], is adopted for selecting the multivariate polynomials $\Psi_\alpha(X)$:

$$\mathcal{A}^{M,p,q} = \{\alpha \in \mathcal{A}^M : \|\alpha\|_q = \left(\sum_{i=1}^M \alpha_i^q\right)^{\frac{1}{q}} \leq p\} \quad (4)$$

where the term p refers to the maximum degree of a PCE model. The maximum number of unknown coefficients equals to $(M+p)!/(M!p!)$. In this study, $q=0.75$ ($0 \leq q \leq 1$) is adopted to reduce high order interaction terms [22]. The unknown coefficients $\{k_\alpha\}_{\alpha \in \mathcal{A}^{M,p,q}}$ can then be computed using the least-square minimization method [5]:

$$\hat{y} = \operatorname{argmin} \mathbb{E}[k^T \Psi(X) - M(X^2)] \quad (5)$$

An adaptive PCE calculation strategy based on the Least Angle Regression (LAR) algorithm [5] is applied to select the most important candidate polynomial basis while all the other coefficients are set to zero (i.e., sparse PCE). Furthermore, the SPCE used here allows adaptively choosing the best polynomial degree (p) from a degree range and almost without sacrificing accuracy [6, 26].

2.2 Sobol' indices

The sensitivity index measures the relative contribution of the partial variances D_{i_1, \dots, i_s} of each group of variables $\{x_{i_1}, \dots, x_{i_s}\}$ on the total variance D of all variables, is given by:

$$S_{i_1, \dots, i_s} = \frac{D_{i_1, \dots, i_s}}{D} \quad (6)$$

The first order Sobol' indices S_i represent the effect of a single input variable alone, while the second order sensitivity indices S_{ij} ($i \neq j$), study the interaction effects of the variable i and j on the output variance [24, 29]. The total Sobol' index S_i^T is the sum of all the Sobol' indices involving variable i , which represents its individual effect and the combination effect with other variables on the output variance.

$$S_i^T = \sum_{i_1, \dots, i_s} S_{i_1, \dots, i_s} \quad (7)$$

Theoretically $0 \leq S_i \leq S_i^T \leq 1$, and $S_i = S_i^T = 0$ means that the model output does not depend on variable i while $S_i = S_i^T = 1$ means that the model output depends only on variable i .

2.3 Error estimation

The leave-one-out error ε_{LOO} , compares the SPCE ($M^{PC \setminus i}$) predictions on the excluded point x^i with the real value y^i . It can be written as [5]:

$$\varepsilon_{LOO} = \frac{\sum_{i=1}^{N_{ED}} (M(x^i) - M^{PC \setminus i}(x^i))^2}{\sum_{i=1}^{N_{ED}} (M(x^i) - \mu_Y)^2} \quad (8)$$

where μ_Y is the sample mean of the experimental design response.

Another error estimator ε_{VAL} , is adopted by comparing the SPCE predictions with the true responses of additional deterministic models (i.e., N_{VAL} validation cases).

$$\varepsilon_{LOO} = \frac{\sum_{i=1}^{N_{VAL}} (M(x^i) - M^{PC}(x^i))^2}{N_{VAL} \operatorname{Var}[\sum_{i=1}^{N_{VAL}} (M(x^i))]} \quad (9)$$

where $\operatorname{Var}[\sum_{i=1}^{N_{VAL}} (M(x^i))]$ is the variance of the true response of validation cases.

2.4 Numerical procedure

The main scheme to perform the global sensitivity analysis using sparse polynomial chaos expansions focuses on the following steps (Fig. 1):

- Step 1: Generation of a set of input parameters using the Latin Hypercube Sampling method [24].
- Step 2: Definition of a soil-tunnel numerical model.
- Step 3: Calculation of the tunnel seismic deformations.
- Step 4: Construction of the SPCE model until the target accuracy is satisfied.
- Step 5: Calculation of the Sobol' indices based on the SPCE coefficients.

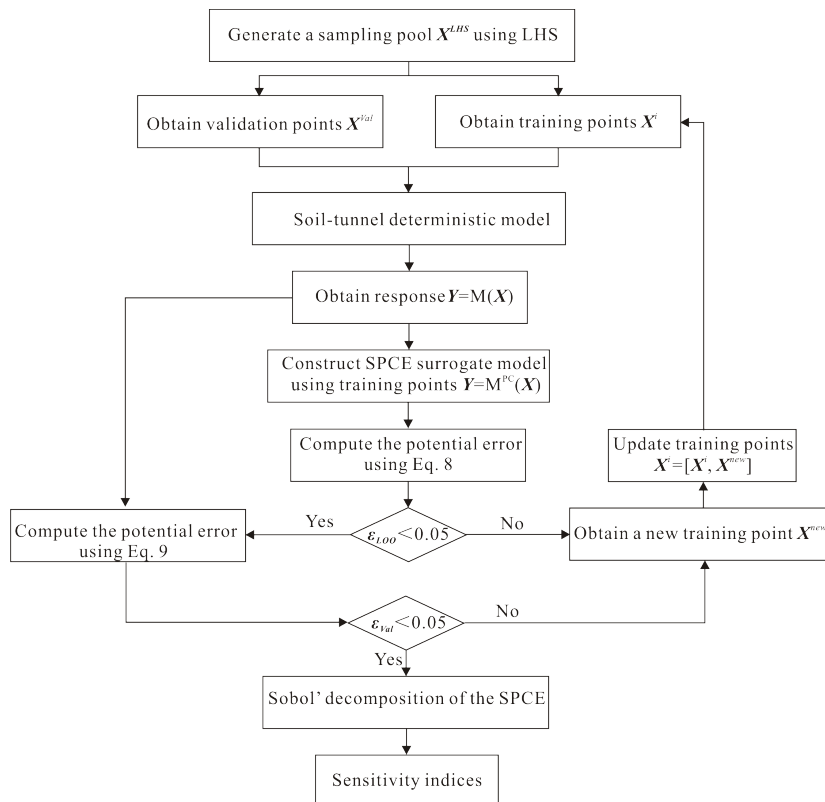


Figure 1: Flowchart of the adopted SPCE-GSA method

3 Soil-tunnel numerical model

3.1 Model details

The Bologna-Florence high-speed railway tunnel in Italy is selected as a reference case [28]. Two-dimensional numerical model is built with the finite difference program FLAC [10]. The parametric analysis indicates that a model width of 100 m (height of 40 m) with a mesh size of 0.8×0.8 m is sufficient to avoid the boundary effects and maintain model stability (Fig. 2c). It corresponds to a computational time of 310 s of each deterministic model evolution (Intel Xeon CPU E5-2620 v4 2.1 GHz, two processors).

The tunnel lining is modeled as linear-elastic and the soil nonlinearity is simulated with an elastic-perfectly plastic constitutive model following the Mohr-Coulomb shear failure criterion.

The deterministic (mean) properties of the soil and tunnel lining are taken from [28]. To consider the shear stiffness degradation in the small strain range, the variation of the shear modulus reduction (G/G_{max}) with the cyclic strain (γ , in percent) for clay proposed by Sun et al. [27] is incorporated in the model, using the function suggested by Hardin and Drnevich [9], as follows:

$$G/G_{max} = \frac{1}{1 + \gamma/\gamma_{ref}} \quad (10)$$

The value of γ_{ref} is determined from the strain at which the modulus reduction factor is equal to 0.5, which corresponds to a value of 0.234 in the deterministic analysis. Also, a Rayleigh damping with a minimum damping ratio of 0.5 % is adopted to remove the possible high frequency noise [11]. The Friuli ground motion is adopted as the seismic input, after high frequency cutoff and baseline correction (Figs. 2a and 2b). The artificial boundary conditions in the numerical model are the same as the ones used in [10] and [28].

This study assumes a perfect bonding between the tunnel and the soil under the seismic shaking [3]. The tunnel deformation ΔD , is defined as the relative maximum horizontal displacement between the tunnel top and bottom (red points in Fig. 2c). Fig. 2d respectively presents the deformation time-histories in deterministic analyses.

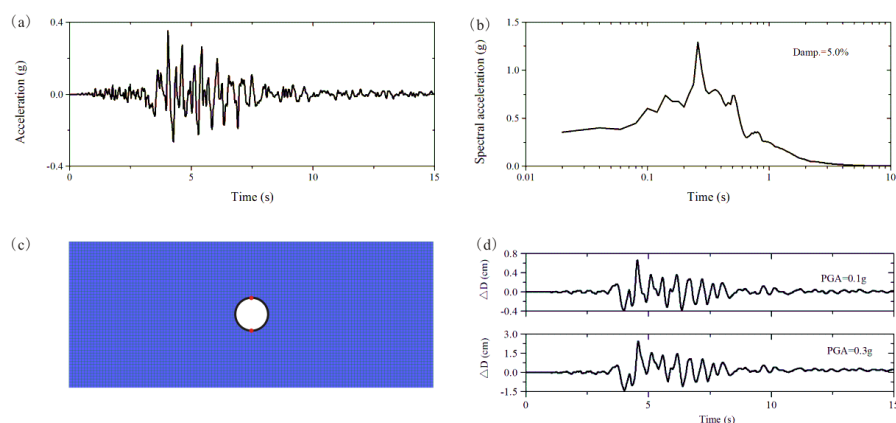


Figure 2: Seismic input, numerical model and deterministic seismic analysis

3.2 Probabilistic input models of variables

Uncertainties associated with six soil parameters and the center frequency of the Rayleigh damping are considered herein (see Table 1). The probabilistic input models of each variable in terms of coefficient of variation (COV) and distribution type are taken from the literature and correspond to real variability measured in the laboratory or in-situ tests [1, 8, 12, 14, 15, 16, 17, 18, 19, 20, 21]. The variables are considered as inter-independent since the adopted Sobol' decomposition method is invalid for correlated variables. To avoid the unrealistic values generation, the distribution tails need to be truncated to describe the variables in a meaningful way. In this study, the lower bound (LB) and the upper bound (UB) are respectively determined based on the mean ± 2 times of the standard deviation. This step is helpful to reduce the computational burden as well since the small value of V_s could result in refined meshes.

Table 1: Probabilistic input models of variables in the benchmark case.

	Symbol	Unit	Mean	COV	Distribution	LB	UB
Density	ρ	kN/m ³	17	0.05	Normal	15.3	17.8
Shear wave velocity	V_s	m/s	200	0.2	Normal	120	280
Poisson's ratio	ν_s	-	0.3	0.15	Normal	0.21	0.39
Internal friction angle	φ	degree	37	0.2	Normal	22.2	51.8
Cohesion	c	kPa	5.0	0.3	Normal	2.0	8.0
Modulus reduction factor	M_s	-	0.5	0.19	Normal	0.31	0.69
Center frequency	f_{min}	Hz	2.75	0.18	Normal	1.65	3.85

4 Method validation

4.1 SPCE model

To demonstrate the efficiency of the adopted SPCE-GSA method in seismic conditions, the probabilistic input models listed in Table 1 are adopted to perform the global sensitivity analysis. The comparison is respectively performed for low and high levels of soil nonlinearity: one considering a ground motion intensity $PGA=0.1$ g, and another considering a higher intensity with a $PGA=0.3$ g.

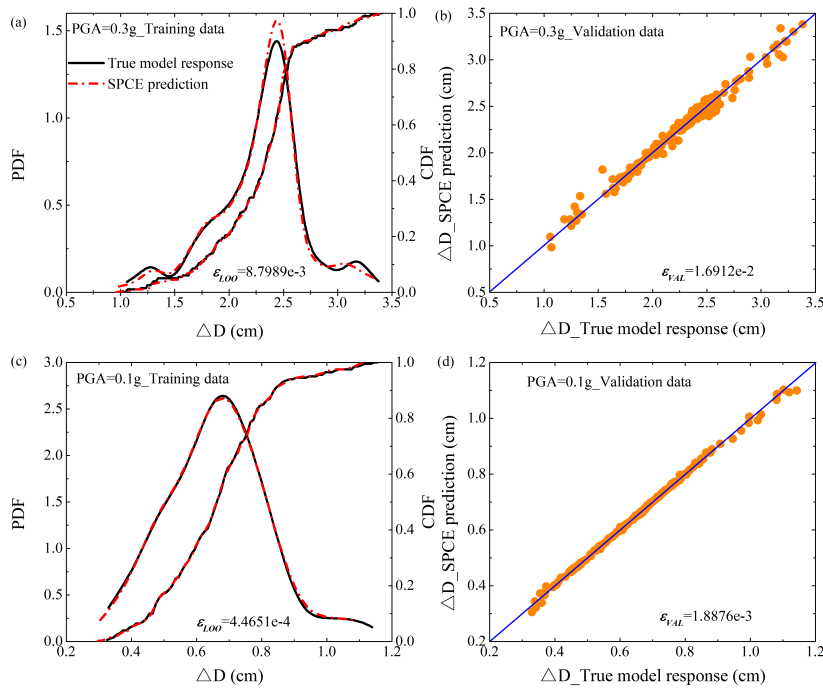


Figure 3: Comparison between PDF, CDF of training points and SPCE predictions in the case of (a) $PGA=0.3$ g; and (c) $PGA=0.1$ g; deformations of true numerical and predicted by SPCE model in the case of (b) $PGA=0.3$ g; and (d) $PGA=0.1$ g.

The comparisons between the probability density function (PDF), cumulative distribution function (CDF) of the 400 training points and SPCE predictions are respectively shown in Figs. 3a and 3c for $PGA=0.3$ g and 0.1 g. Two figures show that the SPCE model is a good substitute to the original time-history numerical models. According to the PDF and CDF under the two studied intensities, it is possible to make some remarks. The tunnel deformations distribution is almost normal in the case of low intensity (Fig. 3c). The SPCE model reproduces well the

response of training points (the corresponding error ε_{LOO} is very small). On the contrary, the deformation distribution is more complex for $PGA=0.3$ g, having three peaks and a long tail towards left. The SPCE model is not able to reproduce these local features very well and the corresponding error ε_{LOO} is relatively large compared to the 0.1 g case one. These local peaks probably result from the soil nonlinearity and the increased interaction terms between variables.

The trained SPCE model is then employed to predict the tunnel deformation using 200 validation points. Figs. 3b and 3d respectively show the deformation predicted by the SPCE model and the true model responses for two intensity cases. The SPCE predictions agree well with the true deterministic model responses, particularly in the case of $PGA=0.1$ g.

4.2 Sensitivity indices

A Monte Carlo simulation based stochastic analysis is performed to have a direct look at the tunnel deformation variability and determine the relative importance of each variable in the framework of LSA. The idea behinds the Monte Carlo simulation based SA method is simple and straightforward: the change in the model output is evaluated for all sampling points, and the input variable which causes the largest change in the model output is given the highest rank in the sensitivity analysis. Its sensitivity analysis strategy is to vary one input variable at a time while remaining the other variables constant (i.e., mean values), the sensitivity index of each variable can then be respectively calculated.

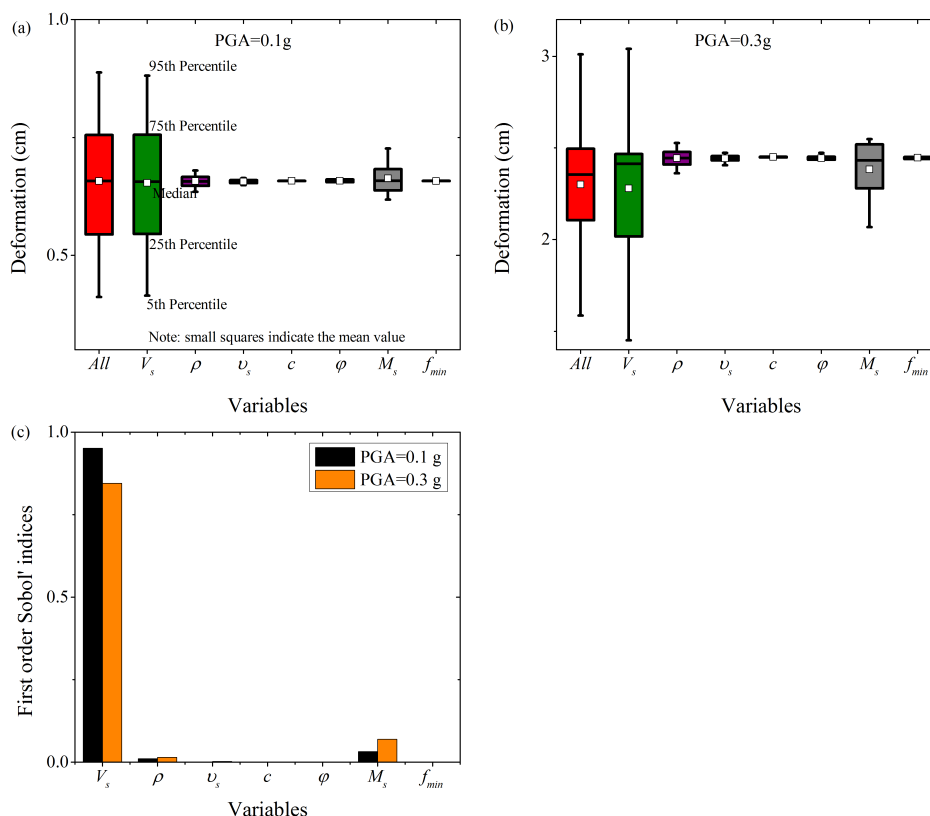


Figure 4: Tunnel deformations corresponding to all variables or a single variable in the case of (a): $PGA=0.1$ g; (b) $PGA=0.3$ g; and (c) first order Sobol' indices calculated by SPCE-GSA method.

The sampling size of $N = 200$ that efficiently covers the parameter space is randomly selected for each scenario in the Monte Carlo simulation based LSA. The analyzed scenarios correspond

to the probabilistic input models listed in Table 1 in the case of $PGA=0.1$ g and 0.3 g, meaning that 3200 ($200 \times 8 \times 2$) deterministic time-history numerical analyses are performed. Besides, for computing the Sobol' sensitivity indices via the SPCE-GSA method, 800 samples (400×2) are additionally generated, bringing the total simulation runs to 4000 (around 14.5 days).

The variability of the tunnel deformation for different cases computed with the Monte-Carlo simulation is shown in Figs. 4a and 4b. Fig. 4c depicts the first order Sobol' indices estimated by the SPCE-GSA method. The deformation variability is large and could be attributed to the uncertainty of shear wave velocity and the modulus reduction factor (Fig. 4a), while the contributions of the modulus reduction factor and density increase as the input motion intensity increases (Fig. 4b). The center frequency, Poisson's ratio, cohesion, and internal friction angle have ignorable importance. The SPCE-GSA method quantitatively provides the same relative importance of each variable, but using less numerical evolution (Fig. 4c).

5 Discussion

It appears from the above study that the Sobol' indices are significantly influenced by the accuracy of the constructed surrogate model. It is related to the given target accuracy, sampling size, and polynomial degree. In this study, the SPCE surrogate model uses an algorithm to choose adaptively the optimal polynomial degree in the range from 1 to 12, combined with a target accuracy of 0.05. To better understand the role of the polynomial degree and sampling size, and to evaluate the reliability of the calculated sensitivity indices for the given target accuracy, 10000 additional deterministic dynamic time-history analyses are performed (solution time is around 36 days). These analyses correspond to the benchmark case (Table 1), subjected to a ground motion with a magnitude of 0.3 g. A range of sampling size N , from 50 to 800, is randomly selected from this 10000 sampling pool, and for each sampling size, 1000 replications are applied. The SPCE of different degrees p , from 1 to 10, is then accordingly trained. It means that for each p order SPCE, 1000 surrogate models are constructed which correspond to 1000 sensitivity indices of each variable.

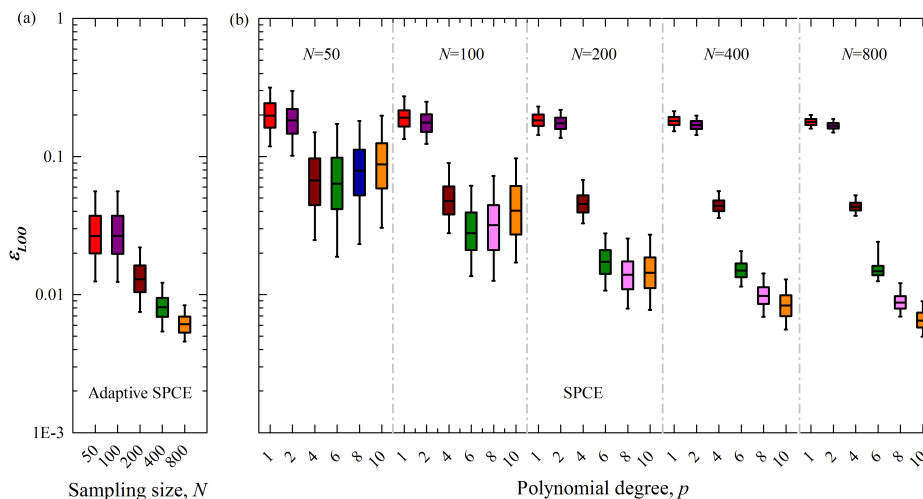


Figure 5: Evolution of ϵ_{LOO} with sampling size and polynomial degree (a) adaptive SPCE; (b) SPCE.

Fig. 5a shows the evolution of ϵ_{LOO} with the sampling size using the adaptive SPCE while the results of various orders SPCE are presented in Fig. 5b. The percentile ranges

in the box plots are the same as those in Fig. 4. For the adaptive SPCE, the model error decreases with the increase of the sampling size N and it permits to construct the surrogate model more explicitly even with less N (i.e., 200). As shown in Fig. 5b, the first and second order SPCE models always produce larger errors, indicating that they cannot represent the complex numerical response even with large number of training points (i.e., 800). Increasing the polynomial degree p , the SPCE tends to perform well if N is large enough to train the surrogate model because as the p increases, the number of unknown coefficients in the SPCE greatly increases (Eq. 4). This also explains why high order SPCE models still result in large errors in the case of $N = 50$ and 100 (i.e., insufficient training data).

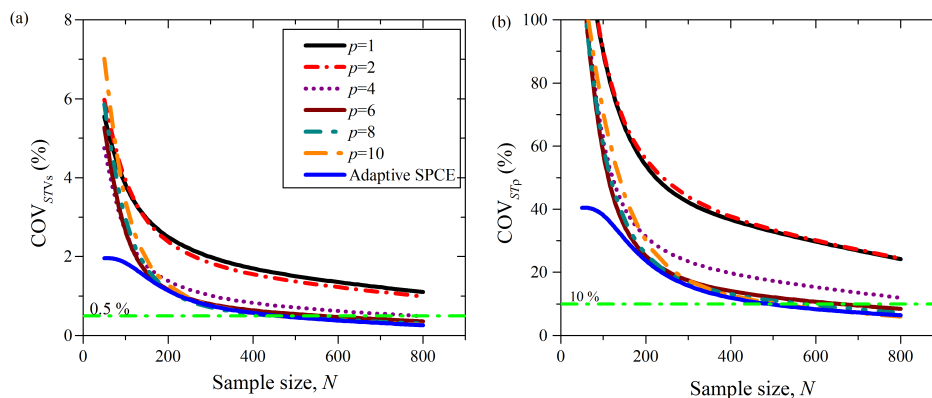


Figure 6: Variation of the total Sobol' indices of (a) shear wave velocity; and (b) density, for different sampling sizes and polynomial degree.

The variations of the total Sobol' index of the shear wave velocity V_s and density ρ with the sampling size for different polynomial degrees are presented respectively in Figs. 6a and 6b. It appears that the sensitivity index variability generally decreases with the increase of the sampling size and polynomial degree. When the sampling size is small ($N = 50$ and 100), the sensitivity indices predicted by different order SPCE models show a large variation. This comes from the large model error and associated variation of the model error (Fig. 5). Further, an over-fitting frequently occurs when fewer training data is used. This leads to calculation errors and a wrong ranking of the sensitivity index of each variable even if a small model error is observed. An illustrative example of over-fitting is presented in Fig. 7. Further increase the sampling size, higher order SPCE models greatly reduce the variability of the calculated sensitivity indices, since the over-fitting is effectively reduced and the surrogate model permits to accurately predict the true numerical responses.

6 Conclusions

This study presents a global sensitivity analysis based on the sparse polynomial chaos expansions method to investigate the relative importance of seven variables on the variance of tunnel deformations under an earthquake loading in a probabilistic framework. Based on the study performed here, the following conclusions could be drawn.

The high accuracy and efficiency of the SPCE-GSA method are verified especially in the case of strong nonlinearity and high dimensional through the comparison with the Monte-Carlo simulation based LSA. The soil shear wave velocity and modulus reduction factor are the two variables that have the most significant influence on the tunnel seismic deformations. The true values of these two parameters are necessary to be accurately measured to increase the reliability of the tunnel analysis and design.

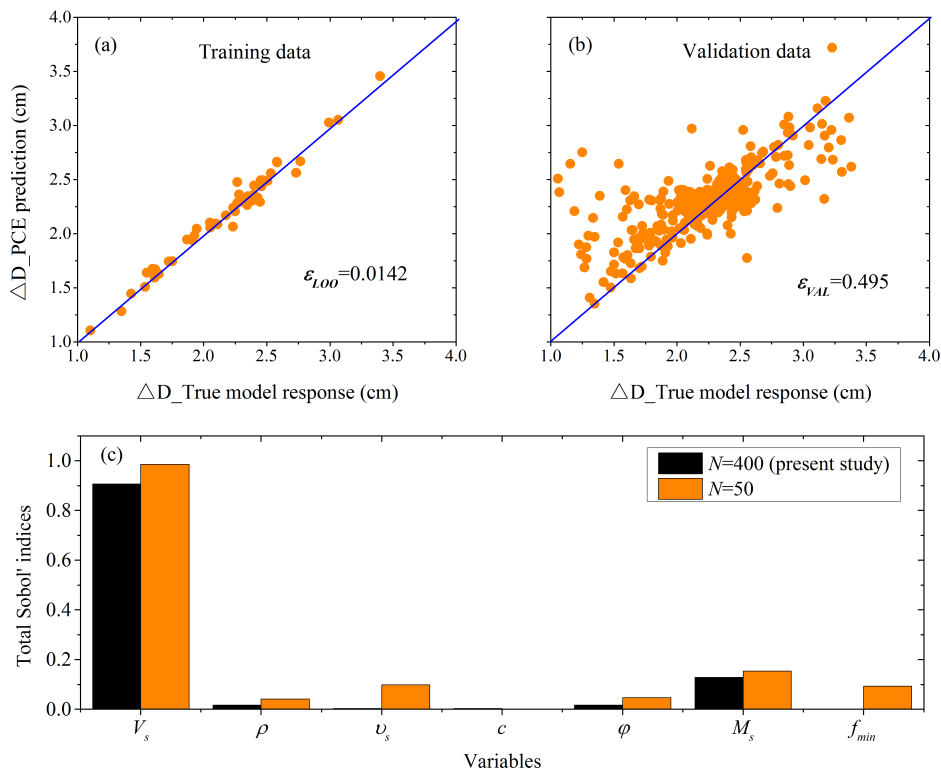


Figure 7: An illustrative example of over-fitting due to insufficient training data and the corresponding total Sobol' indices (PGA=0.3 g).

The Sobol' indices predicted by the SPCE-GSA method are related to the accuracy of the constructed surrogate model. The best optimal manner to reduce the variability of the calculated sensitivity index is to get more training points and select an appropriate polynomial degree. For the former, this in general is practically difficult due to the limits of computational cost. Also, this seems not a cost-effective way since the greatly increased sampling size corresponds to a slow decrease in the sensitivity index variability when the threshold is exceeded (Fig. 6). For the latter, it is difficult to, *a priori*, know which SPCE order can exactly represent the true model response while high order surrogate models induce more training points. Thus, an algorithm to choose adaptively the optimal polynomial degree used in this study is important.

7 Acknowledgments

The authors gratefully acknowledge the financial support provided by the China Scholarship Council (201708130080).

References

- [1] T. Al-Bittar, A.H. Soubra, J. Thajeel (2018) *Kriging-based reliability analysis of strip footings resting on spatially varying soils*, J Geotech Geoenviron Eng 144, pp. 1-11
- [2] A. Amorosi, D. Boldini (2009) *Numerical modeling of the transverse dynamic behaviour of circular tunnels in clayey soils*, Soil Dyn Earthq Eng 29, pp. 1059-1072
- [3] A. Bobet (2010) *Drained and undrained response of deep tunnels subjected to far-field shear loading*, Tunn Undergr Sp Technol 25, pp. 21-31

- [4] E. Bilotta, G. Lanzano, SPG. Madabhushi, F. Silvestri (2014) *A numerical Round Robin on tunnels under seismic actions*, Acta Geotech **9**, pp. 563-579
- [5] G. Blatman, B. Sudret (2011) *Adaptive sparse polynomial chaos expansion based on least angle regression*, J Comput Phys **230**, pp. 2345-2367
- [6] G. Blatman, B. Sudret (2010) *Efficient computation of global sensitivity indices using sparse polynomial chaos expansions*, Reliab Eng Syst Saf **95**, pp. 1216-1229
- [7] U. Cilingir, SPG.Madabhushi (2011) *A model study on the effects of input motion on the seismic behaviour of tunnels*, Soil Dyn Earthq Eng **31**, pp. 452-462
- [8] A. Fenton (1999) *Estimation for stochastic soil models*, J Geotech Geoenvironmental Eng **125**, pp. 470-485
- [9] BO. Hardin, VP. Drnevich (1972) *Shear modulus and damping in soils: design equations and curves*, J Soil Mech Found D **7**, pp. 667-691
- [10] Itasca (2011) *FLAC – Fast Lagrangian Analysis of Continua – Version 7.0 User’s Guide*, Itasca Consulting Group, Minneapolis
- [11] AOL. Kwok, JP. Stewart, YMA. Hashah, N. Matasovic, R. Pyke, ZL. Wang, ZH. Yang (2007) *Use of exact solutions of wave propagation problems to guide implementation of nonlinear seismic ground response analysis procedures*, J Geotech Geoenviron Eng **133**, pp. 1385-1398
- [12] HM. Kroetz, NA. Do, D. Dias, AT. Beck (2018) *Reliability of tunnel lining design using the Hyperstatic Reaction Method*, Tunn Undergr Sp Technol **77**, pp. 59-67
- [13] GD. Manolis, G. Stefanou, AA. Markou (2020) *Dynamic response of buried pipelines in randomly structured soil*, Soil Dyn Earthq Eng **128**, 105873
- [14] G. Mollon, D. Dias, AH. Soubra (2013) *Probabilistic analyses of tunneling-induced ground movements*, Acta Geotech **8**, pp. 181-199
- [15] G. Mollon, D. Dias, AH. Soubra (2009) *Probabilistic analysis of circular tunnels in homogeneous soil using response surface methodology*, J Geotech Geoenvironmental Eng **135**, pp. 1314-1325
- [16] UJ. Na, SR. Chaudhuri, M. Shinozuka (2008) *Probabilistic assessment for seismic performance of port structures*, Soil Dyn Earthq Eng **28**, pp. 147-158
- [17] UJ. Na, SR. Chaudhuri, M. Shinozuka (2009) *Effects of spatial variation of soil properties on seismic performance of port structures*, Soil Dyn Earthq Eng **29**, pp. 537-545
- [18] D. Nedjar, M. Hamane, M. Bensafi, SM. Elachachi, D. Breyse D (2007) *Seismic response analysis of pipes by a probabilistic approach*, Soil Dyn Earthq Eng **27**, pp. 111-115
- [19] QJ. Pan, D. Dias (2018) *Probabilistic analysis of a rock tunnel face using polynomial chaos expansion method*, Int J Geomech **18**, pp. 1-11
- [20] KK. Phoon, FH. Kulhawy (1999) *Characterization of geotechnical variability*, Can Geotech J **36**, pp. 612-624
- [21] KK. Phoon, FH. Kulhawy (1999) *Evaluation of geotechnical property variability*, Can Geotech J **36**, pp. 625-639

- [22] R. Schöbi, B. Sudret (2019) *Global sensitivity analysis in the context of imprecise probabilities (p-boxes) using sparse polynomial chaos expansions*, Reliab Eng Syst Saf **187**, pp. 129-141
- [23] I. Shahrour, F. Khoshnoudian, M. Sadek, H. Mroueh (2010) *Elastoplastic analysis of the seismic response of tunnels in soft soils*, Tunn Undergr Sp Technol **25**, pp. 478-482
- [24] IM. Sobol, YL. Levitan (1999) *On the use of variance reducing multipliers in Monte Carlo computations of a global sensitivity index*, Comput Phys Commun **117**, pp. 52-61
- [25] B. Sudret, CV. Mai (2015) *Computing derivative-based global sensitivity measures using polynomial chaos expansions*, Reliab Eng Syst Saf **134**, pp. 241-250
- [26] B. Sudret (2008) *Global sensitivity analysis using polynomial chaos expansions*, Reliab Eng Syst Saf **93**, pp. 964-979
- [27] JI. Sun, R. Goleorkhi, HB, Seed (1988) *Dynamic moduli and damping ratios for cohesive soils*, Earthquake Engineering Research Center, University of California, Berkeley, Report No. UCB/EERC-88/15
- [28] QQ. Sun, D. Dias (2019) *Seismic behavior of circular tunnels: Influence of the initial stress state*, Soil Dyn Earthq Eng **126**, 105808
- [29] M. Zoutat, SM. Elachachi, M. Mekki, M. Hamane (2018) *Global sensitivity analysis of soil structure interaction system using N2-SSI method*, Eur J Environ Civ Eng **22**, pp. 192-211

Long-term monitoring of a geogrid installed beneath a subballast layer in operating conditions

Olatounde YABA^{1,2,}, Fabrice EMERIAULT^{2,†}, Orianne JENCK^{2,‡},
Jean-Francois FERELLEC^{1,§}, Amine DHEMAIED^{1,¶}*

² Univ. Grenoble Alpes, CNRS, Grenoble INP, 3SR, 38000 Grenoble, France

Abstract: The use geogrids to improve railway track beds is one of the solutions proposed by the French National Rail Company (SNCF) to conduct renovations. This paper presents a monitoring scheme which was installed on one of these improved track beds. It provides practical feedback concerning the installation process and an analysis of the preliminary results.

1 Introduction

The increase in rail traffic and traffic speeds impose large cyclic loads on the French Rail Network's (FRN) track beds, thus contributing to the appearance of defects in track geometry. These defects can impact train safety and passenger comfort. SNCF (French National Rail Company) has launched major renovations to address these problems on its conventional (non-high speed) rail network. Meanwhile, railway infrastructure managers are faced with increasingly stringent environmental and budgetary challenges. All these constraints sparked a search for innovative solutions which could enable renovations to be carried out at a lower cost while guaranteeing the network's structural resilience and ensuring that modern environmental standards are respected. One potential solution is the use of geogrids to improve railway track beds. Geogrids are geosynthetics that are used in the construction industry in the form of a reinforcing or stabilizing material [1]. They have planar structures formed by a regular network of tensile elements with apertures of sufficient size to allow interlocking with surrounding soil, rock, earth, or any other geotechnical material to perform their functions [2].

Presently, knowledge on the mechanical behaviour of geogrids and their contributions to the improvement of railway operating conditions is limited. Most studies in the field have focused on the interaction of geogrids with the ballast layer [3, 4, 5, 6, 7]. These studies have shown the effectiveness of geogrids in reducing ballast wear and lateral spreading. However, they do not allow one to draw satisfactory conclusions regarding the improvement of the subballast layers. In addition, for several reasons, the installation of a geogrid in (or immediately below) the ballast layer is not compatible with the FRN's operating conditions (maintenance techniques, traffic, etc.). Hence, it is interesting to set up an in-situ experiment on the FRN which measures the strains on a subballast geogrid, as well as the stresses and settlements in the track bed. The aim is to quantify the improvements provided by a geogrid which is installed beneath the subballast layer (in operating conditions), and to study the mechanisms by which this improvement is achieved.

*Email: olatounde.yaba@3sr-grenoble.fr

†Email: fabrice.emeriault@3sr-grenoble.fr

‡Email: orianne.jenck@3sr-grenoble.fr

§Email: jean-francois.ferellec@reseau.sncf.fr

¶Email: amine.dhemaied@reseau.sncf.fr

2 Methods

The monitoring equipment was installed on a 30 m stretch of track with daily traffic of 80,000 to 130,000 equivalent tonnes. The stretch is near a turnout (switch) with a 90 km/h speed limit. The monitoring equipment was installed during the renovation of approximately one kilometre of track, which was proposed in conjunction with the routine replacement of the turnout.

The preliminary investigations revealed the presence of a weak subgrade composed of silty-clay, beneath the track components (rail, sleepers and ballast). The renewal of track components could have worsened the situation; thus, a geogrid was included beneath the proposed subballast layer, to reduce the volume of required earthworks and improve bearing capacity. A multiaxial geogrid with a secant modulus of 480 kN/m at low strain (0.5%) and 100% junction efficiency [8] (according to the manufacturer) was chosen. Lightweight Falling Deflectometer tests were performed during the earthworks (using a minidyn™ [9]). They confirmed that the subgrade was indeed weak (E_{v2} stiffness ≤ 30 MPa).

The monitored stretch is divided into 4 cross-sections (labelled S0 to S3, see figures below) which can be identified based on their distance from a nearby sign post. S0 is a control section (no geogrid) while the other 3 are improved using the geogrid. The monitoring scheme consists of the following sensors.

- 12 strain gauges (bonded to the geogrid): to measure its strains and track their development over the long-term (Figure 1).
- 2 temperature probes: to measure the geogrid/subballast temperature and apply thermal corrections to strain measurements (Figure 1).
- 3 pressure transducers: to indirectly measure settlements by measuring water pressure above the transducers (Figure 2).
- 5 total pressure cells: to measure soil stresses (Figure 3).
- 2 smart fishplates (developed by SNCF Réseau, DGII - VA - T3): to detect the passage of trains and measure their axle loads (removed after 9 days).

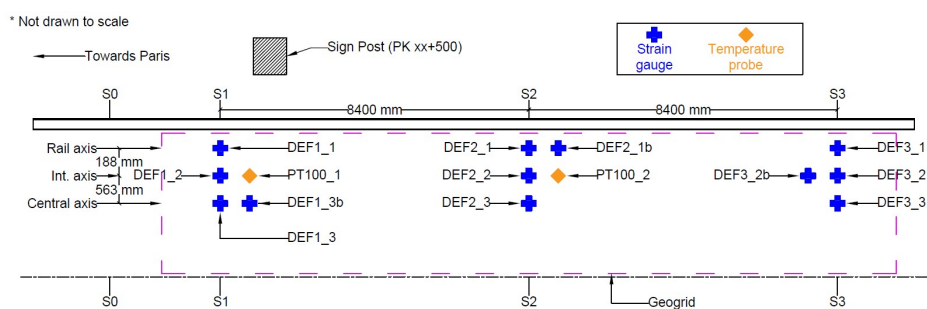


Figure 1: Strain gauge and temperature probe locations (plan view).

The characteristics of each type of sensor are summarized in Table 1. Note that they were reused on this site following the cancellation of a previous site and therefore, may be inadequate (with regards to the orders of magnitude of our measurements).

The sensors were connected to a Campbell Scientific CR-1000 datalogger, which takes measurements every 10 minutes and records the average of the 6 measurements taken every hour. This preliminary approach has been deemed inadequate. More powerful dataloggers will be used on future sites in conjunction with a trigger system. Thus, enabling dynamic measurements during the passage of trains.

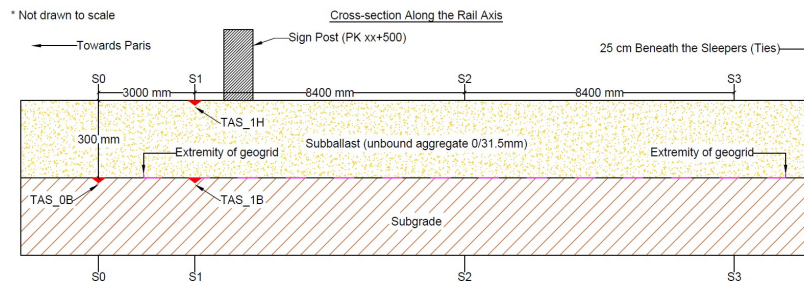


Figure 2: Settlement sensor locations (cross-section).

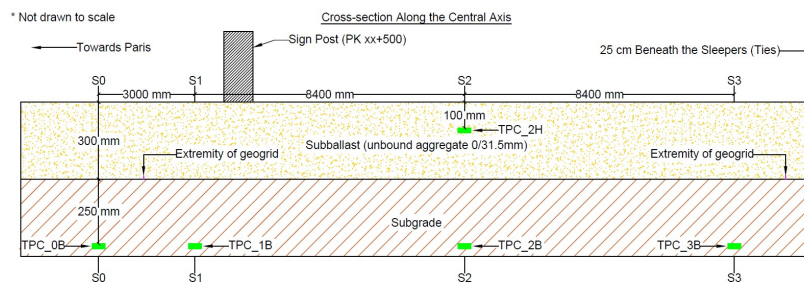


Figure 3: Pressure cell locations (cross-section).

3 Results

The current results are those available as of December 2019. Considering that the experiment was designed to monitor long-term behaviour, it is too early to perform an in-depth analysis of these preliminary results. However, they provide insight and allow one to draw some qualitative conclusions.

For context, the sensors were activated in September 2019 and the renovation of track components continued above the monitored trackbed until October 2019. During this period, traffic consisted mainly of engineering trains (during the day) and passenger trains (in the evening). Normal traffic was restored in mid-October; it consists mostly of passenger trains (approximately 4 trains/hour) and occasional freight trains (at night).

The first observation is that the geogrid experiences very low strains with a maximum of $2.26 \mu\text{m/m}$ and a median of $0.87 \mu\text{m/m}$. In addition, the recorded strains seem to result mainly from temperature fluctuations. This influence is apparent in Figures 4 to 6. The thermal sensitivity of the geogrid will be analysed in the lab. This analysis, coupled with the strain measurements over the coming seasons, will facilitate the extraction of the strains that result

Table 1: Sensor specifications.

Sensors	Manufacturer	Reference	Measurement Range	Precision	Resolution	Operating Temperature
Strain Gauge	Micro-Measurements	EP-08-015DJ-120	$\pm 10\%$	$0.02 \mu\text{m/m}$	$0.001 \mu\text{m/m}$	-75 to $+205^\circ\text{C}$
Temperature Probe	RS-Pro	PT100	-20 to $+200^\circ\text{C}$	$\pm 0.15^\circ\text{C}$	0.01°C	-20 to $+200^\circ\text{C}$
Total Pressure Cell	Telemac	TPC 229 mm	0 to 2000 kPa	$\pm 10 \text{ kPa}$	0.5 kPa	-50 to $+150^\circ\text{C}$
Pressure Transducer	Keller-Druck	PR-35X	0 to 300 mbar	$\pm 0.12 \text{ mbar}$	0.006 mbar	-10 to $+80^\circ\text{C}$

from mechanical stresses. Thus, providing a better understanding of the stress–strain behaviour.

Secondly, although the decreasing temperature has generally caused contraction (recorded with a positive sign), a closer look at the strains shows that:

- in the rail axis, there are occasionally some small but measurable extensions, recorded with a negative sign (Figure 7);
- in the intermediate axis, there are more limited extensions (Figure 8);
- in the central axis, however, there are increased contractions at the same time as the extensions of the other axes (Figure 9).

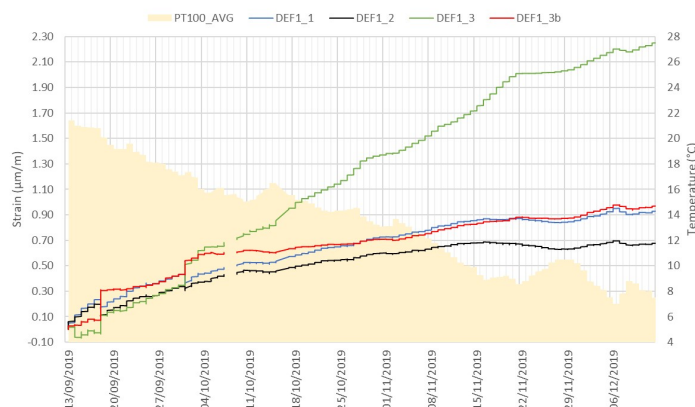


Figure 4: Effect of temperature change on strain at cross-section S1.

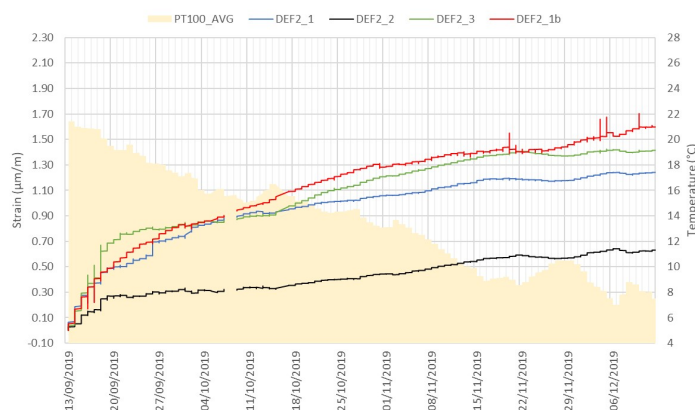


Figure 5: Effect of temperature change on strain at cross-section S2.

Crossing the strain data with the traffic data (axle loads during the first 9 days after installation), reveals that these extensions and contractions coincide with periods of high traffic. Presumably, traffic loads push the unbound aggregates of the subballast from beneath the rails; this is in line with expectations, because much higher stresses are expected under the rails than in the central axis.

Soil stresses are also in line with expectations and present occasional peaks during periods of heavy traffic (Figure 10). The stress measurements have been corrected to take temperature fluctuations into account (correction factors supplied by the manufacturer). Note that there was a slight easing of stresses after normal traffic was restored.

No measurements can be presented for settlements, because there are none yet.

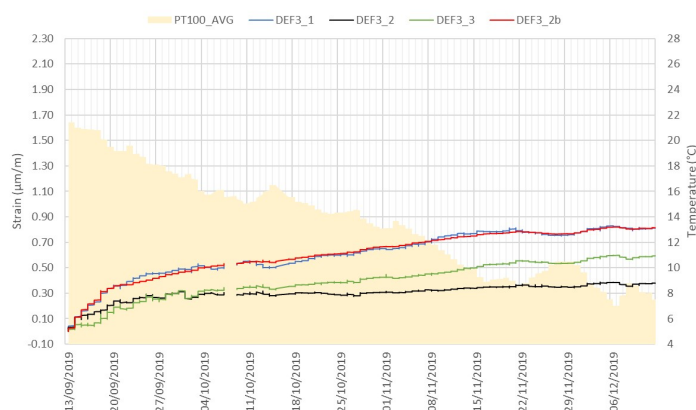


Figure 6: Effect of temperature change on strain at cross-section S3.

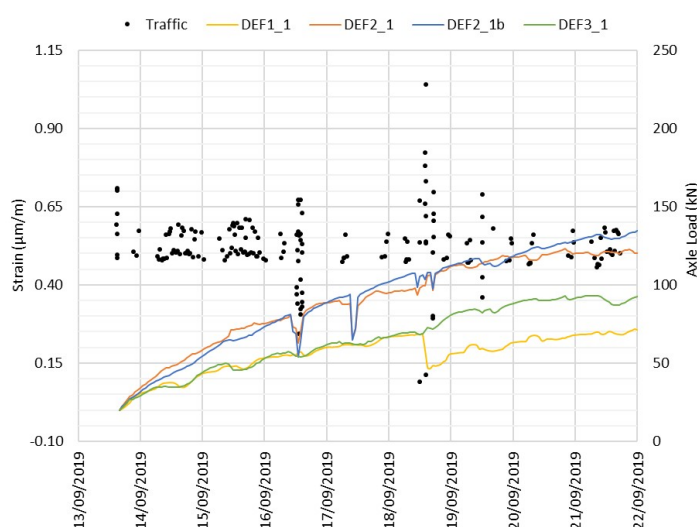


Figure 7: Strains along the rail axis.

4 Conclusions and contributions

This paper presented the implementation of a monitoring scheme for a railway track bed which was improved using a geogrid. The experiment has shown that it is not only possible to implement this type of scheme under standard operating conditions on the French Rail Network, but also that it is possible to do so without damaging any sensors during installation. Analysis of the preliminary results has shown that all the installed sensors are still functional, and that the system can be expected to have several years of service life. Furthermore, this analysis has revealed some of this monitoring scheme's drawbacks, the most notable of which is the lack of an integrated trigger system for detecting oncoming trains. These drawbacks have been taken into consideration and the feedback has led to the improvement of the datalogging protocols for this site and the design of an improved monitoring scheme for future sites. In addition to these improvements, the current measurements (which are all provided by embedded sensors) will be supplemented with periodic measurements of track alignment, measurements of sleeper displacement under traffic, and Lightweight Falling Deflectometer test (for this and all future sites). Over the long-term, the data from this site and others like it will be used to:

- analyse the mechanisms by which geogrids can improve a subballast layer (confinement, stabilization, reinforcement...);

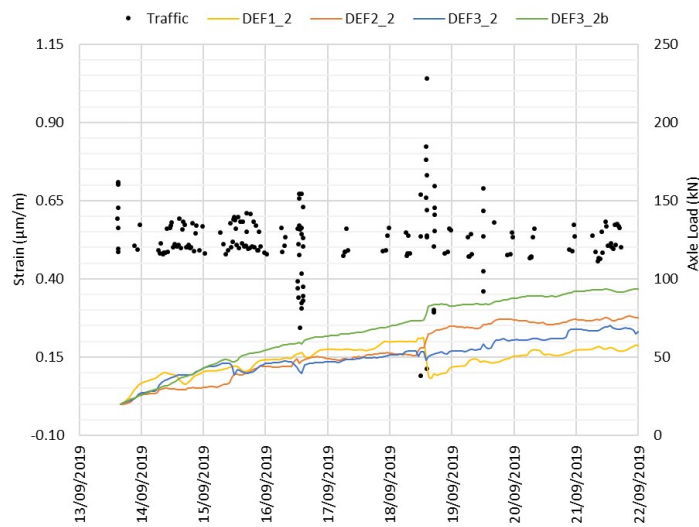


Figure 8: Strains along the intermediate axis.

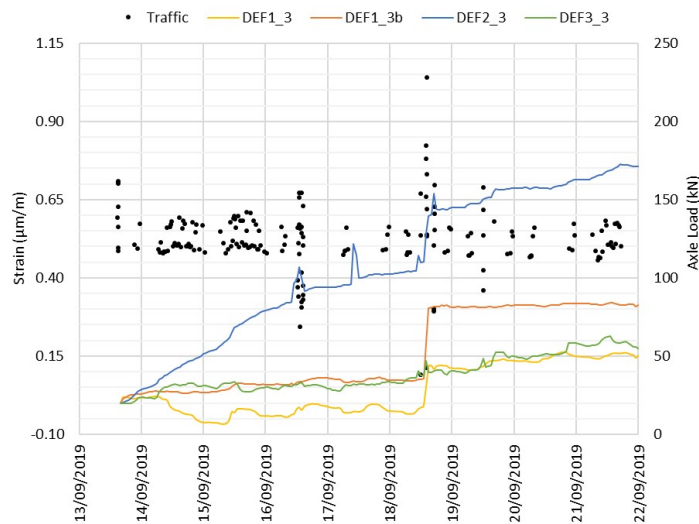


Figure 9: Strains along the central axis.

- quantify the improvements that are achieved by these mechanisms;
- develop numerical models for further research on the service life of subballast layers that have been improved using geogrid;
- and finally provide detailed design and maintenance recommendations for the adequate implementation of geogrids on the French Rail Network.

Acknowledgements

The authors would like to thank the various SNCF Réseau teams that made this experiment possible, especially the field measurement section (SNCF Réseau, DGII – VA – T3).

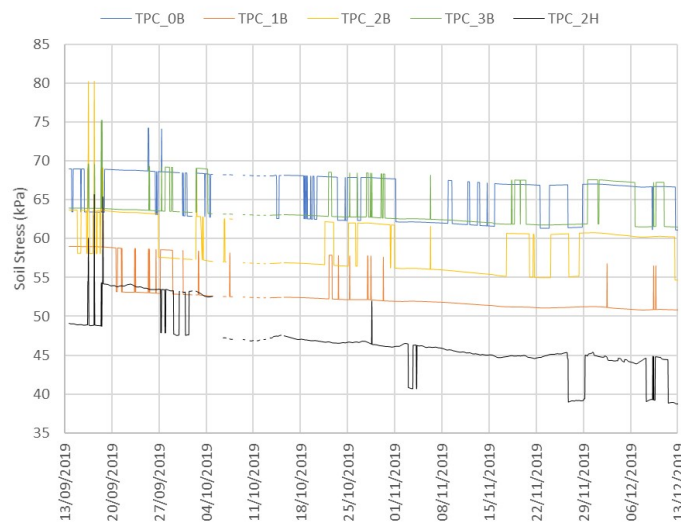


Figure 10: Soil stress in the track bed.

References

- [1] International Geosynthetics Society (2018) *Guide to the Specification of Geosynthetics*, IGS Secretariat, Jupiter, Florida.
- [2] R. J. Carroll (1988) *Specifying Geogrids*, Geotechnical Fabrics Report 6(12).
- [3] L. Horníček, P. Břešťovský et P. Jasans (2017) *Application of geocomposite placed beneath ballast bed to improve ballast quality and track stability*, IOP Conference Series: Materials Science and Engineering 236(11), p. 012039.
- [4] S. Nimbalkar et B. Indraratna (2016) *Improved performance of ballasted rail track using geosynthetics and rubber shockmat*, Journal of Geotechnical and Geoenvironmental Engineering, 142(18), pp. 04016031-1 - 04016031-13.
- [5] S. Lenart et J. Klompaker (2014) *Geogrid reinforced railway embankment on soft soil – Experiences from 5 years of field monitoring*, chez 10th International Conference on Geosynthetics, Berlin.
- [6] G. Fernandes, E. M. Palmeira et R. C. Gomes (2008) *Performance of geosynthetic-reinforced alternative sub-ballast material in a railway track*, Geosynthetics International, 15(15), pp. 311-321.
- [7] P. Sharpe, M. Brough et J. Dixon (2006) *Geogrid trials at coppull moor on the west coast main line*. Railway Foundations, chez International Conference on Railway Foundations.
- [8] European Organisation for Technical Approvals (2017) *Non-reinforcing hexagonal geogrid for the stabilization of unbound granular layers by way of interlock with the aggregate*, Brussels.
- [9] Rincent ND Technologies (2017) *Plaque dynamique légère Manuel d'utilisation*, Courcouronnes.

Contribution to the analysis of the mechanical behaviour of the Laurichard rock glacier (French Alps) in the last decades and evaluation of its correlation with recent climatic changes

Samia MELKI^{1,}, Dominique DAUDON^{1,†}, Xavier BODIN^{2,‡}, Emmanuel THIBERT^{2,§}*

¹ Univ. Grenoble Alpes, CNRS, Grenoble INP, 3SR, F-38000, Grenoble, France

² USMB-CNRS-EDYTEM-Chambery 3: UGA, INRAE, UR ETGR, Grenoble, France

Abstract: Climate change is of evident influence in cryosphere evolutions especially in highest altitude morphological and geological forms. Rock glaciers motion may be a marker of those changes. In French Alps, some of this forms are surveyed for decades. The evolution of their surface velocity flow can be characterized by various influencing parameters such as temperature, ice proportion and mechanical properties (fluidity/viscosity). To improve the understanding of the processes influencing thermal control and the seasonal and inter-annual variations in the kinematics of Laurichard rock glaciers in France, this study is proposed based on long-term observations over the last 30 years. First, using a statistical approach [16], correlations between surface velocity variations and air temperature anomalies on the study site are analysed. Then, an effective viscosity parameter is evaluated using surface velocities with geometrical consideration and steady shear flow hypothesis [14]. Variations on its mean values are analysed in correlation with the temperature evolution in last decades.

1 Introduction

As global warming is an increasing scenario, attention is intensifying to identify the impact of climate change on the cryosphere and its consequences. One of its markers in the mountain's areas is the destabilization of rock glaciers which are mixtures of rocks debris and ice in permafrost conditions (remaining at temperatures below or at 0°C for two or more consecutive years) that moves slowly down on mountain slopes under the influence of gravity. A study of [13] aimed to give insights into the extent of destabilizing rock glaciers in the French Alps. Involving 46 active landforms in the region, around 11% turn out to be potentially destabilized. The phenomena of destabilization of permafrost structures can generate risks for territories. The example of the Lou rock glacier's collapsing events (active layer detachment which triggered a debris flow that flooded and damaged infrastructures on the village Lanslevillard, France, 2015) was one of various destabilization incidents occurring much often in the past few decades. In fact, the relative slow motion of rock glaciers seems to be accelerating in accordance to main temperatures increase.

Although cases of potential destabilization have been identified, rock glaciers that have a low index of destabilization and are located in areas with a high sensitivity to defrosting were identified as having a high potential to show future destabilization. The results of [13] study indicated that these rock glaciers had a large area of high susceptibility to destabilization and

*Email: samia.melki@3sr-grenoble.fr

†Email: Dominique.Daudon@3sr-grenoble.fr

‡Email: xavier.bodin@univ-savoie.fr

§Email: emmanuel.thibert@inrae.fr

should be monitored for risk assessment (Figure 1a). In particular, the Laurichard rock glacier is a site currently under surveillance which presents a medium to high sensitivity to destabilization [13, 5].

1.1 Study site

Located in the southern French Alps (45.018N, 6.378E), the Combe of Laurichard catchment is a well surveyed mountain permafrost area [8, 9, 6]. Characterized by high rock faces extending from 2700 m to 3000 m above sea level, it is composed of densely fractured granite. At the bottom (Between 2400 and 2700 m above sea level), the slopes exposed to the north are affected by permafrost. The rock glacier extends from the rooting zone (2650 m above sea level) in contact with the rock face to 2450 m above sea level at its front. It measures 490 m long, between 80 and 200 m wide and has an apparent thickness (based on the vertical height of the sides and front) of 20 to 30 m. It has typical morphological characteristics of an active relief form [4].

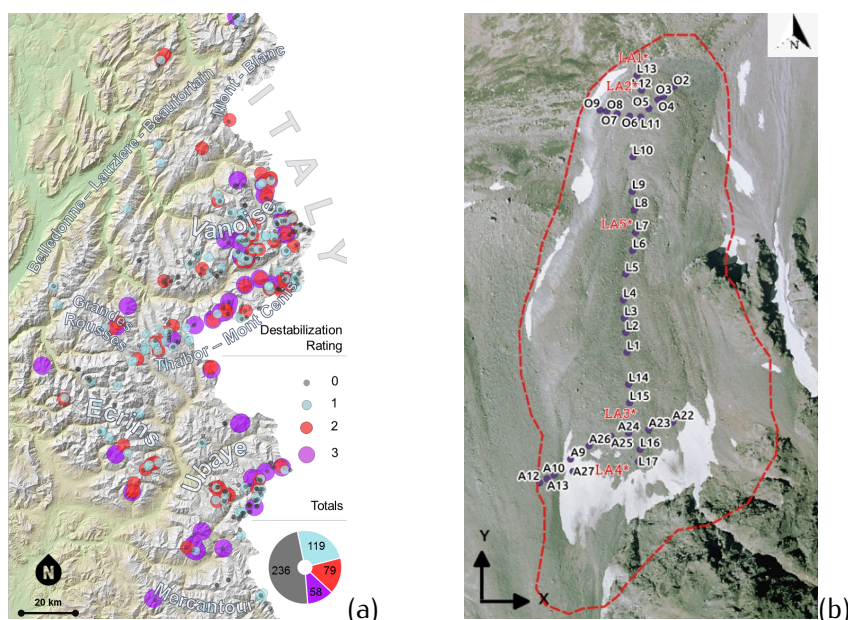


Figure 1: (a) Map and pie chart of destabilization rating of rock glaciers in France (Marcer et al. 2019). (b) aerial map of Laurichard rock glacier and locations of its GPS (Li, Ai, Oi) and GST (LAi) surveyed blocs.

To survey its motion, 13 rocks were marked in the mean longitudinal line on September 1983 (L1 to L13; from the top to the bottom of the rock glacier). Then, four other rocks in the upper part (L14 to L17) were added to the series on 2002. The two transversal profiles; A at the top and O at the bottom, were added respectively on 2002 and 2008 to complete the network. Temperature are measured on 6 points named LA1 to LA6. All locations are shown in Figure 1b.

In regard to the slope angle and the ice fraction in the composition of each part of the rock glacier, a zoning is opted. The classification is indicated in the annexed table.

1.2 Observed velocities

Velocities of rock glaciers in the French Alps ranges from 10 cm/yr to 2 m/yr. At Laurichard rock glacier, the evaluation of the very high resolution DEMs and surface displacement maps derived from those datasets [3] shows an accelerating surface motion with a mean value above 1.5 m/year between 2012 and 2015 (Figure 2). That is not catastrophic comparing with the rupture in the

Bérard rock glacier (Southern Alps-2006) that presented before it's collapse velocities reaching the mean value of 3.3 m/yr and up to 8 m/yr at some points [6]. It allows to study a relatively quite rock glacier not to much affected by the climate changes.

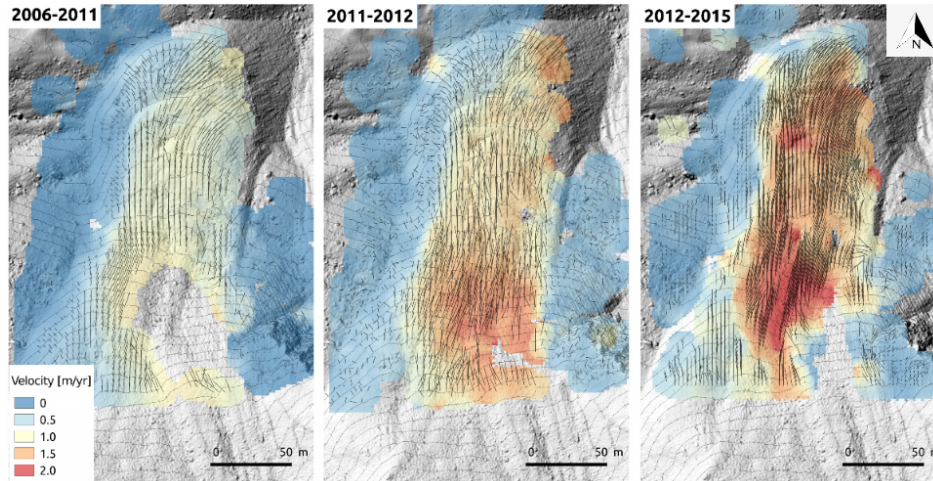


Figure 2: Maps of the surface velocity of the Laurichard rock glacier at three different time periods, as derived from image correlation using HR DEMs [3].

Studies suppose that the thermal inertia of permafrost and the slow motion of rock glaciers lead them to react to long-term climatic trends. Thibert et al. [17] uses the long record of surface velocity of Laurichard rock glacier (a spatial-temporal dataset of annual rocks displacements starting from 1984) to identify the time response of the overall glacier dynamics. The time signal from this dataset is expected to be homogeneous to year-to-year changes in climate conditions.

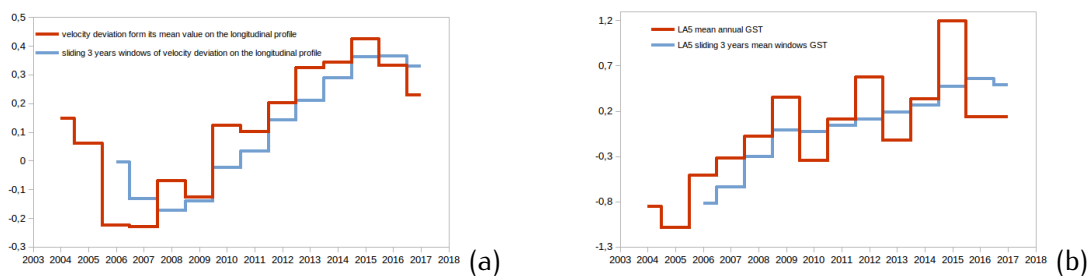


Figure 3: (a) Velocity deviations representing immediate time response and that shifted by 3 years sliding window mean at all measurement points of Laurichard rock glacier from 2004 to 2017. (b) Annual mean ground surface temperature on the central zone of Laurichard rock glacier (LA5) and its sliding 3 years window mean from 2004 to 2017.

This time signal provides the best possible estimate of Laurichard rock glacier's response in surface velocity to climate profile control [17]. In fact, considering variations in annual temperature averages at the same time interval, a correlation between variations in surface velocity and climatic conditions seems to be relevant as the representation of the annual mean ground surface temperature at the middle zone of Laurichard (LA5) shows.

To verify this assumption in our study case, a statistical analysis approach of [16] based on COUP model [11, 12] and experimented on different rock glaciers in Switzerland (Permafrost monitoring sites) is opted. Method and results are presented in the second part of this report.

2 Laurichard rock glacier kinetics and temperature variations

The superficial thermal conditions and the relative importance of temperature variations at depth in addition to the infiltration of meltwater are of special importance in the kinetics of rock glaciers [16]. A statistical methodology is developed in [16] to characterize rock glacier motion in regard to thermal variations “anomaly” relative to reference temperatures. For various Swiss rock glaciers, this approach allowed to connect the kinetic anomalies (*i.e.*, acceleration or deceleration) to a thermal anomaly (*i.e.*, increase or decrease of temperature from a mean reference). This characterization is done by a time lag, and a time duration: *i.e.*, over a period of 5 to 10 years of observation, the methodology searches the best correlation between velocities anomalies, for a given month, and corresponding temperature anomalies’s month that may be delayed of some months (called time-lag period) representing the “time” for the temperature wave anomaly to penetrate in the glacier and to control the kinetic behaviour in the shear zone. this time lag is searched on a period of influence from 1 to a maximum of 36 months (called window). The time lag period obtained was verified with borehole’s controlled temperatures.

Applying this methodology to the rock glacier of Laurichard (with the temperature measurements taken at the surface points LA1, LA3 and LA5 and for the longitudinal profile of L1 to L17 velocities points) allows to find the kinematic response to short-term meteorological conditions in rock glaciers and evaluate their importance.

2.1 Method

The statistical approach of [16] proposes to reconstruct variations in the ground temperature of rock glaciers without relying on data from boreholes. A method to calculate a synthetic ground temperature anomaly (GT_{synt}) for arbitrary time intervals of 10 years ($n = 120$ months between 2004 and 2014) has been calculated based on ground surface temperature monthly averages (GST_{month} , *i.e.*, the series: January 2004, February 2004...December 2014), reference values for each month ($GST_{\text{month}}^{\text{ref}}$, *i.e.* for example mean January temperature of the series (January 2004, January 2005...January 2014) and an offset of the time interval (t_{lag}) as described in the following equation:

$$GT_{\text{synt}}[K] \simeq \frac{1}{n} \sum_{-t_{\text{lag}}}^{n-t_{\text{lag}}} \left(GST_{\text{month}} - GST_{\text{month}}^{\text{ref}} \right) \quad (1)$$

From the available data, three daily GST loggers are selected (LA2, LA3 and LA5). The GST time series GST_{month} used for this study were averaged by month. This approach benefits from the fact that seasonal variations in temperature are more important factors than their day-to-day and inter-annual variability. Therefore, the results are used to define a correlation factor between GT_{synt} anomalies (K) and changes in the horizontal surface velocity (%) using a Rscript developed by Staub [16] and giving the t_{lag} period and a window period who generate the influence period of anomaly.

2.2 Results

As example, the analysis of the L9 velocity points with the LA5 temperature logger, provides a 22 months window period of anomalies that correlates with 4 months of t_{lag} shift (*i.e.*, acceleration from 22 months of high temperature arrives after 4 months). For each cases the correlation with the best exponential relation velocity anomalies versus temperature anomalies is provided.

Figure 4a shows a large central zone (velocity measurement point from L14 to L12 in the topographical order) that is very well correlated with the LA5 logger for temperature time series. In fact, the more the slope, the more the creep mechanism and, as the creep depends on the temperature, the higher the correlation with the temperature. For each L_i rock measurement

point over the 10 years of considered observations, the power law of velocity deviation versus the temperature deviation is calculated. An example for the L5 and L9 velocity versus LA5 temperature is plotted in Figure 4b.

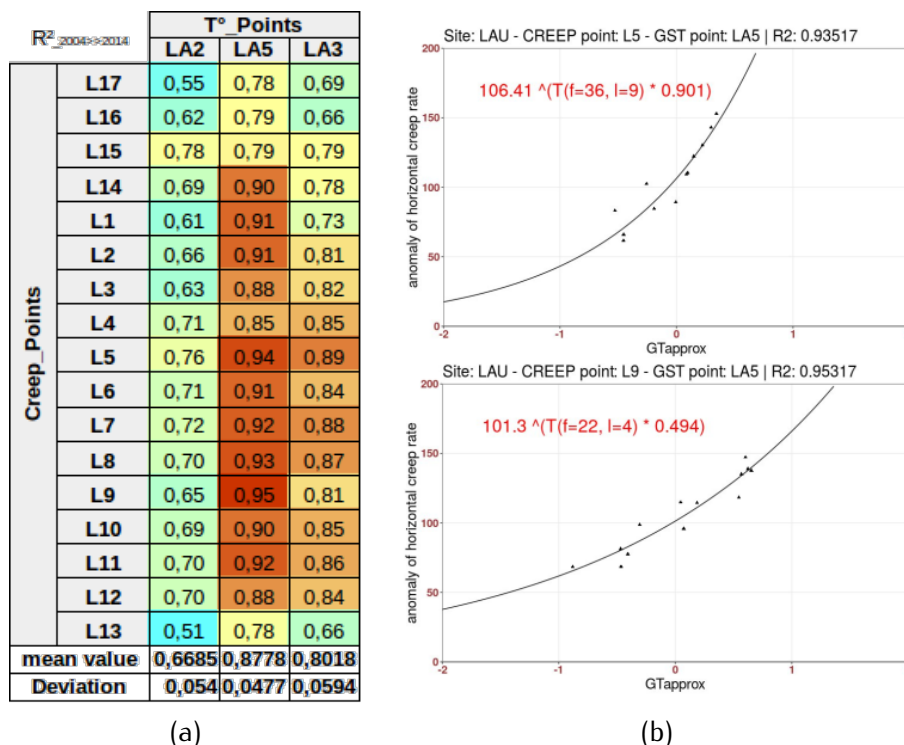


Figure 4: (a) Correlation between the kinetic data of the rock glacier and the temperature variation reconstructed with the surface temperature series. (b) exponential law obtained after computation the best correlation between velocities anomalies on central points and temperature anomalies on LA5.

For L5, the relation is $\Delta Vel = 106.41^{0.901\Delta Temp}$.

For L9, the relation is $\Delta Vel = 101.30^{0.494\Delta Temp}$.

The Laurichard rock glacier can be assumed to be a good marker of climatic changes in the French Alps as the correlation between its kinetic and surface temperature variations is quite good for a large part of its longitudinal profile.

3 Mechanical and Numerical modelling of rock glaciers: qualification of an effective viscosity on Laurichard rock glacier

Kinetics of surface rock glacier is measurable (either by topography, photometry or satellite images analysis), and quite interesting in order to have some predictions on the future evolution by varying scenarios at short or long terms and establishing a risk evaluation of collapse. It allows geomorphological projections like those made by [15] and also a better understanding of the influencing parameters by parametric studies after identification of local characteristics [7].

3.1 Theoretical mechanical relations

The mechanical behaviour is based on the Glen ice creep law, that represents the mechanical regime of the observed flow of glacier with a power law. It relates the stress in the flowing icy

material to his deformation flow using a non linear power law:

$$\dot{\epsilon} = A_G \sigma^n \quad (2)$$

where σ is the simple shear stress tensor, $\dot{\epsilon}$ is the deformation rate, and A_G is a creeping material parameter named fluidity (Glen 1955), n is a creep exponent (chosen equal to 3 for the usual bulk polycrystalline ice law but it may range between 1 to 4). Monnier and Kinnard (2016) preferred to calibrate a viscosity B_M on the Las Liebres rock glacier, related to the A_G fluidity by:

$$B_M = \sqrt[n]{1/A_G} = A_G^{-\frac{1}{n}} \quad (3)$$

Using the surface velocities of the glacier, geometrical characteristics at the measured surface points and simple shear stress in stationary flow regime under gravity they calculated B_M . The glacier geomorphological characteristics (slope inclination α , thickness and density of respectively the active layer (h_{al} , ρ_{al}) and of the rock glacier mass (h_{core} , h) including air and water fixed proportions, geometrical shape factor S_f – see [14] for more details). They assumed n equal to 3 (pure ice), and u_s versus B_M leads to the following equation, and considered a zero triggering minimum stress to initiate the flow:

$$u_s = \frac{2(h_{al}\rho_{al} + h\rho_{core})^{n+1}}{(n+1)\rho_{core}} \left(\frac{S_f g \sin \alpha}{B_M} \right)^n \quad (4)$$

Reversing the equation, B_M is calculated as function of u_s (measured surface velocity):

$$B_M = \sqrt[n]{\frac{2(h_{al}\rho_{al} + h\rho_{core})^{n+1}}{(n+1)u_s\rho_{core}}} S_f g \sin \alpha \quad (5)$$

In the year's 2000, Arenson & Springman worked on the parameters that may affect the Glen law applied to rock glacier. Conducting large experimental campaigns of triaxial mechanical tests in laboratory, varying temperature, and ice/particles proportions, they proposed a new viscosity power law taking into account those sensitive parameters. The Arenson power law [1], captures the influence of the ice/particle proportion and the temperature in a fluidity named here A_A . This laboratory study on sandy or glass particles incorporated in ice, has led to the following expressions of the relation:

$$\dot{\epsilon}(w_i, \sigma, T) = A_{Arenson} \sigma^{3w_i} \quad (6)$$

$$\text{with } \log(A_A) = \frac{2}{1+T} + \log(5 \times 10^{-11} e^{-10.2w_i}) \quad (7)$$

$$\text{so, } A_A = 10^{\frac{2}{1+T}} 5 \times 10^{-11} e^{-10.2w_i} \quad (8)$$

where T is the absolute value of the temperature in the rock glacier mass, w_i is the ice proportion, the simple shear stress tensor, the correspondent strain rate, and e the exponential function.

The relation is similar to the one used by Monnier [14] with a creep exponent corrected by the ice proportion factor and a fluidity depending on both ice proportion and temperature. Using the same methodology than Monnier, it is possible to identify a B_{MA} coefficient on the Laurichard glacier taking into account this ice proportion parameter.

$$B_{MA} = \sqrt[n]{\frac{2(h_{al} + \rho_{al}\rho_{core}h)^{n+1}}{(n+1)u_s\rho_{core}}} S_f g \sin \alpha \quad (9)$$

A pure ice approach may be obtain by considering

$$B_{PI} = \sqrt[3]{\frac{(H\rho_{ice})^4}{2u_s\rho_{ice}}} S_f g \sin \alpha \quad (10)$$

Then, by defining A_A as the product of a temperature dependent coefficient $C(T)$ and pure ice proportion coefficient leads to a B_{MA} viscosity coefficient taking into account the

$$A_A = C(T) 5 \times 10^{-11} e^{-10.2w_i} \quad (11)$$

$$\text{leading to } C(T) = \frac{B_M^{-3w_i}}{5 \times 10^{-11} e^{-10.2w_i}} \quad (12)$$

$$\text{and reversely } B_{MA} = (5 \times 10^{-11} C(T) e^{-10.2w_i})^{-\frac{1}{3w_i}} \quad (13)$$

3.2 Results on Laurichard data base

The analysis and calibration of mean value of B_M (from Eq. (5)) over the 30 years and 17 measurements points of the Laurichard glacier front of the mean velocities are condensed in Figure 5a and 5b. The chosen shape factor of the glacier, and other assumed parameters such as thickness, air and water proportions are summarized in Table 1. The glacier is assumed to have 3 zones distinguished by their mean altitude (head, central, tongue of the glacier).

Table 1: Glacier characteristics used for the viscosity identification.

	GPS surveyed points	Total thickness H (m)	Active layer h (m)	Section shape factor S_f	Ice/particle ratio w_i	Slope angle (°)
head	L15 to L17	~ 14	~ 2	0.799 to 0.849	~ 78%	~ 18
central zone	L1 to L9; L14	11 to 17	2.7 to 4.4	0.799 to 1.000	40-70%	~ 30
bottom	L10; L11; O2 to O5 L12	~ 16 14	~ 1 10	0.799 to 0.849 0.799	~ 31% 30%	~ 15 9.5

All other parameters are constant over the glacier and evaluated to be : ice density (0.916 g/cm³), air proportion (7,5%), water proportion (11%).

In Figure 5a, the velocities are represented for some years and for the oldest measured points. It clearly confirms a global acceleration has described in Figures 2 and 3a. More details show that two localisations (head and tongue of the glacier) have the slowest similar velocities. The central zone is delimited at its extremities by the highest velocities bounding a more homogeneous high velocity zone. it can be noticed that this correspond to the highest of active zone depth ie-“external” loading of the glacier mixture. In simple viscous analysis it may conduct higher viscosity values for slower velocity and lower viscosity for higher velocity (all other parameters are equal). Inverse identification analysis for viscosity applied on the glacier imposed to take into account realistic geometrical parameters (depth, shape, ice proportions... of the glacier see Table 1).

In Figure 5b, three approaches of the mechanical behavior are presented: the pure ice mechanical interpretation ($B_{GlacePUR-green}$, Eq. (10)), the Monnier one (with $n = 3$, Eq. (5)) and the Monnier-Arenson third one ($n = 3w_i$, Eq. (9)). As the bed rock slope angle is unknown, two approaches were proposed and compared: the first one uses the continuation manually of

the altitude level line below the glacier (*alphaDep-blues points*), and the second is defined by the slope angle of the velocity vector between tow years (*slopeBedrock-red points*).

The first option means that the surface of the glacier remains parallel to the bedrock. One can concluded that it gives different results for the viscosities but the shape of the curve are similar as it only generates a small shift in the range value of B . A way to avoid a choice may be to take a mean value of both curves. Points L14 to L17 are more recent measurements so the mean is calculated over a more warm period (2007 to 2019) and are not represented for better understanding as displacement are more important and special comparison over this reduced period is required.

The two options for the slope angle calculation show less influence than the mechanical behaviour law options: pure ice, Monnier with $n = 3$ and Monnier-Arenson with $n = 3w_i$ comparing both square and triangle options of same colour in Figure 5b. This means that particles in the ice are important factors even only included in the density of the material mixture for the gravity stresses calculations. Comparing the "Monnier-Arenson" approach it shows clearly a large variation of viscosity values in the bottom zone of the glacier, in comparison of the head and central one's that the both other approaches for which the values are really more homogeneous (L12 results have to be carefully appreciated due to its bottom position that may leads to fossil characteristics or prominent frictional behaviour instead of viscous one).

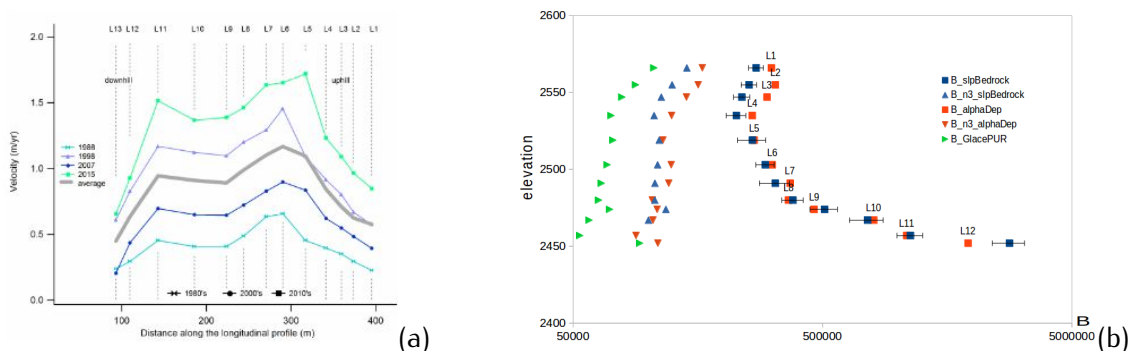


Figure 5: (a) Some velocity values on the periode over the glacier measured rock points. One can notice zones of higher variation and a certain homogeneity in the middle of the glacier. (b) mean B_{PI} , B_M and B_{MA} viscosity values (and standart deviation for B_{MA}) on the period for the 2 slope angle calculations. The green triangle represent the B values that may be obtained if the assumption is pure ice and in this case it does not take into account the rock particles even in the core density calculations.

Due to the positive results obtained with Monnier-Arenson approach the complete time period and measured point where treated and obtained curves are shown in Figure 6, two means curves are drawn to include the last experimental points followed since 2003.

Commenting the results of Figure 6, globally, B_{MA} values from dark curves show smaller range than blue and green one's showing the relation with the greater velocity observed over the recent decades. Regarding the Eq. (12) that demonstrates the ice proportion variation of B_{MA} : as the more de w_i the more the B_{MA} . Global thermal altitude variation should have seen that the higher the points, the colder the temperature, the higher the viscosity. Applied on the Laurichard rock glacier, an inverse variation is observed, probably due to the ice proportion variation as a more forcing parameters. This mean that the $C(T)$ function should balance the w_i evolution in an other way than the Arenson one, or that this influence is few regarding the lost of temperature of the assumed 0.6°C per hundred meters of elevation.

Extracting the $C(T)$ component of the behavior law has to be carefully studied and will not be developed in this report. Further detailed work has to be done before, such as evaluation

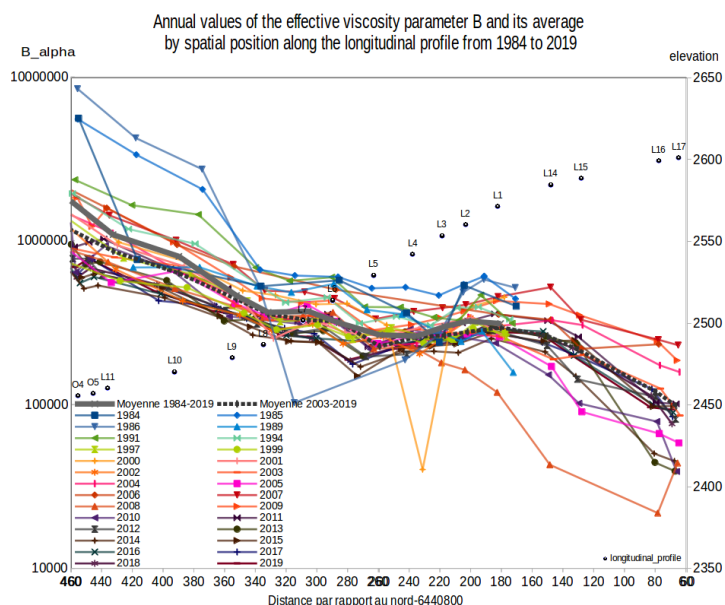


Figure 6: Evaluation of the effective viscosity B_{MA} over 30 years of measures each years at the 17 points (5 points at the top of the glacier were added in 2003). Decades are distinguished by colour, and measured points by symbols. Green large line is the mean value of B_{MA} over the 30 years for each point. Dashed line is the mean value for 2003–2019 period.

of the influence of the variability of assumed parameters (depth, slope angle...). The balance between this possible forcing have to be evaluated.

4 Conclusion

The Laurichard rock glacier data base has been studied in order to confirm the climatic forcing over temperature changes in the last 30 years. Using the Staub approaches it clearly shows that the central zone flow has the most correlation with the air temperature data at the corresponding altitude. As this central part remains to a zone that presents more slope angle, more active layer loading that leads to enhance mechanical forcing of the shear flow. it remains interesting then to focus on this zone to finely extract the internal temperature of the glacier mass as in contrary of the Swiss's rock glacier data sets used by Staub, boreholes data doesn't exist at Laurichard.

Calibrating creep factors over the 30 years data set has been done using the methodology of Monnier et Kinnard. It shows clearly again the relation between the kinematic behaviour and the mechanical one as a similar evolution between velocity and temperature, and viscosity is visible. Going furthermore, as Arenson develops an empirical mechanical behaviour law (based on the Glen's power law) that takes into account the internal temperature and the ice/particles proportions, remains possible to calibrate a pure temperature dependent factor directly from the surface velocity. This factor again shows more finely the forcing on the inter-annual variability of the velocity with temperature.

In summary, we have proposed a methodology in order to access to the temperature variation inside the glacier using a calibration from geomorphological parameters of the glacier, and measured surface velocities data over years.

Perspective of this work will be to studies the sensitivity to the arbitrary used factors that are not well known such as the bed rock slope angles, thickness, shape factors in order to estimate errors on the calibrated viscosity coefficient. Extracting temperature variation inside

the glacier mass thermal diffusivity and velocity evolution at short term may be estimated, in order to access to a susceptibility of collapse in the further decades.

References

- [1] L. U. Arenson, S.M. Springman (2005) *Mathematical descriptions for the behaviour of ice-rich frozen soils at temperatures close to 0°C*, Can. Geotech. J. **42**, pp. 431-442
- [2] X. Bodin, M. Fort, E. Thibert, D. Fabre, P. Schoeneich (2008) *Dynamics of Alpine permafrost as a possible response to global warming: results from a 1986-2006 survey and interpretation of recent field observations (French Alps)*.
- [3] X. Bodin, E. Thibert, O. Sanchez, A. Rabatel, S. Jaillet (2018) *Multi-Annual Kinematics of an Active Rock Glacier Quantified from Very High-Resolution DEMs: An Application-Case in the French Alps*, Remote Sens. **10**(4), p. 547
- [4] X. Bodin, E. Thibert, D. Fabre, A. Ribolini, P. Schoeneich, F. Francou, L. Reynaud, M. Fort (2009) *Two Decades of Responses (1986-2006) to Climate by the Laurichard Rock Glacier, French Alps*, 9th International Conference on Permafrost, Permafrost and Periglac. Process. **20**, pp. 331-344
- [5] X. Bodin, P. Schoeneich, S. Jaillet (2008) *High resolution DEM extraction from Terrestrial LIDAR topometry and surface kinematics of the Alpine permafrost: the Laurichard rock-glacier case study (French Southern Alps)*, Fairbanks, Kane DL, Hinkel KM (eds). Institute of Northern Engineering: University of Alaska, pp. 137-142
- [6] X. Bodin, J.M. Krysiecki, P. Schoeneich, O. Le Roux, L. Lorier, T. Echelard, M. Peyron, A. Walpersdorf (2017) *The 2006 Collapse of the Bérard Rock Glacier (Southern French Alps)*, Permafrost and Periglac. Process. **28**, pp. 209-223
- [7] A. Cicoira, J. Beutel, J. Faillettaz, I. Gärtner-Roer, A. Vieli (2019) *Resolving the influence of temperature forcing through heat conduction on rock glacier dynamics: a numerical modelling approach*, The Cryosphere **13**, pp. 927-942
- [8] B. Francou (1981) *Géodynamique des éboulis et formes associées de la Combe de Laurichard*, PhD thesis, Université Joseph Fourier, Grenoble
- [9] B. Francou (1988) *L'éboulisation en Haute Montagne*, Editec: Caen, p. 696
- [10] J.W. Glen (1955) *The creep of polycrystalline ice*, Proceedings of the Royal Society of London **228**(1175), pp. 519-538
- [11] P.-E. Jansson, L. Karlberg (2004) *COUP model – Coupled heat and mass transfer model for soil-plant-atmosphere system*, Dept. of Civil and Environmental Engineering, Royal Institute of Technology
- [12] P.-E. Jansson (2012) *CoupModel: model use, calibration and validation*, Transactions of the ASABE **55**(4), pp. 1335-1344.
- [13] M. Marcer, C. Serrano, A. Brenning, X. Bodin, J. Goetz, P. Schoeneich (2019) *Evaluating the destabilization susceptibility of active rock glaciers in the French Alps*, The Cryosphere **13**, pp. 141-155

- [14] S. Monnier, C. Kinnard C. (2016) *Interrogating the time and processes of development of the Las Liebres rock glacier, central Chilean Andes, using a numerical flow model*, Earth Surf. Process. Landforms **41**, pp. 1884-1893
- [15] J. Müller, A. Vieli, I. Gärtner-Roer (2016) *Rock glaciers on the run – understanding rock glacier landform evolution and recent changes from numerical flow modeling*, The Cryosphere **10**, pp. 2865-2886
- [16] B. Staub, A. Marmy, C. Hauck, C. Hilbich, R. Delaloye (2015) *Ground temperature variations in a talus slope influenced by perma-frost: a comparison of field observations and model simulations*, Geographica Helvetica **70**, pp. 45-62
- [17] E. Thibert, M. Bonnefoy-Demongeot, F. Finance, X. Bodin (2018) *Extracting the time signal in surface velocity changes along 3 decades at Laurichard rock glacier (French Alps)*

A simplified analytical method to estimate long term concrete lining stress in deep underground galleries

Valentin MARTYNIAK^{1,*}, Fabrice EMERIAULT^{1,†}, Roland PLASSART^{2,‡}, Francois LAIGLE^{2,§}

¹ Univ. Grenoble Alpes, CNRS, Grenoble INP, 3SR, 38000 Grenoble, France

² EDF-CIH, 73370 Le Bourget du Lac, France

Abstract: This paper proposes a simple analytical method to determine the stress in a concrete lining in deep underground structures that present long term deformation of the ground. This method is based on a Singh-Mitchell phenomenological model. It is validated through two cases of gallery and compared with FLAC simulation using a visco-plastic model.

1 Introduction

Traditionally, the convergence-confinement method is widely used to estimate the stress in concrete lining and design a tunnel. This simple analytical method developed by Panet-Sulem-Guenot [7] is used to model a complex 3D problem of a gallery excavation. The method initially only considered an elastic behavior for the ground but in the following decades, different authors have introduced in this method more complex phenomenon's such as plasticity in the ground, strain softening [1] or fictitious support pressure [3]. In order to estimate the stress in the lining in the case of deep underground structures presenting long term deformations, a new method has been developed and is detailed in this paper.

2 Problem statement

2.1 The Singh-Mitchel model

The stress-rate evolution with time measured in several deep galleries (St-Martin-de-la-Porte [2], Bure laboratory [9], Chamoise tunnel...) always seems to evolve with a t-n form. The original Singh-Mitchell model [8] proposes a phenomenological model following this function, which expresses the viscous strain rate $\dot{\epsilon}_v$ at time t with a normalized deviatoric stress level \bar{q}

$$\dot{\epsilon}_v(t, \bar{q}) = A e^{\bar{\alpha} \bar{q}} \left(\frac{1}{t} \right)^m \quad (1)$$

where A is a viscous parameter, $\bar{\alpha}$ is the dimensionless parameter that determines the slope of the logarithmic strain rate versus stress ratio.

In the Equation 1 the form of the viscous strain rate is not totally adapted for the analysis of deep underground structures in the sense that creep is observed in this type of material only if there is an existing deviatoric stress. In order to adapt it to the considered application, a new form of the strain rate is proposed:

$$\dot{\epsilon}_v(t, \bar{q}) = A (e^{\bar{\alpha} \bar{q}} - 1) \left(\frac{1}{t} \right)^m \quad (2)$$

*Email: valentin.martyniak@3sr-grenoble.fr

†Email: fabrice.emeriault@3sr-grenoble.fr

‡Email: roland.plassart@edf.fr

§Email: francois.laigle@edf.fr

This form enables the viscous strain rate to vanish if there is a pure compression load and no deviatoric stress. The Equation 2 shows that the viscous strain rate only depends on the normalized deviatoric stress. This is a strong hypothesis because, in reality, the viscous strain will depend on the confinement even for the same deviatoric stress ratio.

2.2 Basic assumptions

The opening is assumed to be circular and the initial stress field is isotropic. A plain stress condition is considered in the plan perpendicular to the axis of the gallery. The ground has an elastic behavior with a viscous strain based on the Singh-Mitchell model (Equation 2). The support pressure of the ground is determined by the longitudinal deformation profile during the excavation phase or with the pressure at the interface between the lining and the ground afterwards. The total strain is given by:

$$\varepsilon = \varepsilon_e + \varepsilon_v \quad (3)$$

where ε_e is the elastic strain and ε_v the viscous strain. The elastic strain has an analytical solution given by the expression of the ortho-radial strain depending on the radius:

$$\varepsilon_e = \varepsilon_{\theta\theta}(r, P_i) = \frac{1 + \nu_g}{E_g} (P_0 - P_i) \frac{r^2}{R^2} \quad (4)$$

P_i represents the pressure at the interface between the lining and the ground or the support pressure, P_0 is the initial isotropic stress. R is the radius of the excavation and r the radius in the polar coordinate system. ν_g and E_g are respectively the Poisson's ratio and the Young's modulus of the ground.

The viscous strain is found by integrating the viscous strain rate with time and assuming that the normalized deviatoric stress level is constant with time:

$$\varepsilon_v(t, \bar{q}) = A (e^{\bar{\alpha}\bar{q}} - 1) \left(\frac{t^{1-m}}{1-m} \right) \quad (5)$$

2.3 Failure criterion

The failure criterion used to determine the maximum deviatoric stress is the widely used Hoek-Brown criterion [5]. It is defined as follows:

$$f(\sigma_1, \sigma_3) = \sigma_1 - \sigma_3 - \sigma_c \left(m_{HB} \frac{\sigma_3}{\sigma_c} + s \right)^a \quad (6)$$

The solution of the stress field of a circular gallery in an elastic ground is given by:

$$\sigma_{rr}(r) = P_0 - (P_0 - P_i) \frac{r^2}{R^2} \quad (7)$$

$$\sigma_{\theta\theta}(r) = P_0 + (P_0 - P_i) \frac{r^2}{R^2} \quad (8)$$

where σ_{rr} and $\sigma_{\theta\theta}$ are respectively the radial and ortho-radial stress. The deviatoric stress can be calculated as the orthoradial stress minus the radial stress:

$$q(R) = 2(P_0 - P_i) \quad (9)$$

Considering the radial stress as the minor stress and the orthoradial stress as the major stress, the maximum deviatoric stress q_{\max} can be obtained as follows:

$$q_{\max}(P_i) = \sigma_c \left(m_{HB} \frac{P_i}{\sigma_c} + s \right)^a \quad (10)$$

In Equation 10, the maximum deviatoric stress is calculated near the wall of the tunnel, and is supposed constant in the ground even at large distance from the tunnel lining. The normalized stress \bar{q} is expressed as the ratio of the deviatoric stress q on the maximum deviatoric stress q_{\max} .

$$\bar{q}(P_i) = \frac{2(P_0 - P_i)}{q_{\max}(P_i)} \quad (11)$$

3 Determination of the Evolution of the stress in the lining

3.1 Methodology of resolution

In order to determine the evolution of the stress in the lining, the ground reaction curve (GRC) and the support pressure curve (SPC) are plotted at each time step and the pressure at the interface $P_i(t)$ is determined as the intersection of the two curves for a given time step t . The evolution of this pressure is plotted as the red curve in Figure 1. Once the evolution of the pressure is determined, the lining is supposed circular and the evolution of the stress is obtained as:

$$\sigma_l(t) = \frac{P_i(t)R}{e} \quad (12)$$

where R is the radius of the gallery and e the thickness of the lining

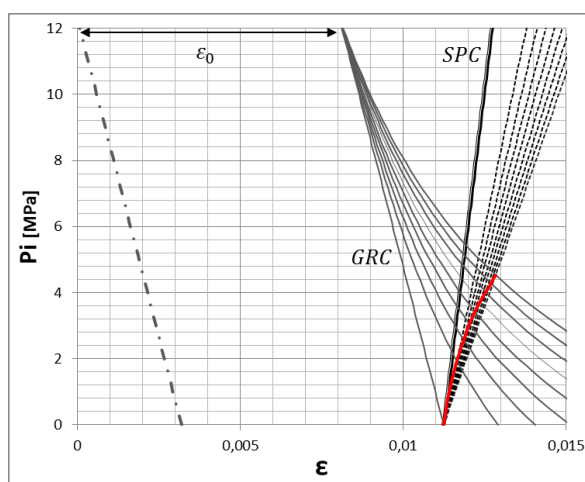


Figure 1: Example of ground reaction curve (GRC) and support pressure curve (SPC).

3.2 Support pressure curve

The support pressure curve represents the reaction of the concrete lining loaded by the ground. The concrete lining strain is the sum of elastic strain ε_{ce} and the creep strain ε_{cc} , the creep strain is proportional to the stress level and based on Eurocode creep strain [4]:

$$\varepsilon_{cc}(t, t_{0c}) = \varphi(t, t_{0c}) \frac{\sigma_c}{E_c} = \varphi_{RH} \beta(f_{cm}) \beta(t_{0c}) \left(\frac{t - t_{0c}}{\beta_H + t - t_{0c}} \right)^{0.3} \frac{\sigma_c}{E_c} \quad (13)$$

where φ_{RH} is a coefficient depending on the relative humidity, $\beta(f_{cm})$ a coefficient depending on the uniaxial stress resistance, $\beta(t_{0c})$ a coefficient depending on t_{0c} the age of the concrete when the loading phase starts. β_H is a coefficient depending on the relative humidity, and geometrical characteristics, σ_{comp} is the uniaxial compression stress and E_c the elastic modulus

of the concrete. As the creep strain of the concrete is proportional to the loading, a new elastic modulus can be defined depending on time as:

$$\varepsilon_c(t, t_{0c}) = \varepsilon_0 + \varepsilon_{ce} + \varepsilon_{cc}(t, t_{0c}) = \varepsilon_0 + \frac{\sigma_{comp}}{E_c} + \varphi(t, t_{0c}) \frac{\sigma_{comp}}{E_c} = \varepsilon_0 + \frac{\sigma_{comp}}{E_c(t, t_{0c})} \quad (14)$$

$$E_c(t, t_{0c}) = \frac{E_c}{1 + \varphi(t, t_{0c})} \quad (15)$$

with ε_0 the initial strain of the lining corresponding to the strain of the ground before the installation of the lining. The total strain of the lining is thus given by:

$$\varepsilon(t, t_{0c}) = \varepsilon_0 + P_i \left(\frac{R}{e E_c(t, t_{0c})} \right) \quad (16)$$

3.3 Determination of ε_0

As the support pressure is not constant with time during the excavation process and before the installation of the lining, the initial strain ε_0 is determined as the sum of the elastic strain and the viscous strain, integrated on each time step:

$$\varepsilon_0(P_{i0p}, t_{0p}) = \varepsilon_e(P_{i0p}) + \sum_{j=1}^n \dot{\varepsilon}_v \left(P_i \left(\frac{t_j + t_{j-1}}{2} \right), \frac{t_j + t_{j-1}}{2} \right) (t_j - t_{j-1}) \quad (17)$$

with P_{i0p} representing the support pressure P_i when the lining is put at $t = t_{0p}$ and n is the number of time steps used to calculate ε_0 . The sum of the n time steps is equal to t_{0p} .

3.4 Determination of the ground reaction curve

The ground reaction curve is obtained by varying the pressure at the interface P_i and plot the curve at different time step. The strain in the ground reaction curve is the sum of the elastic strain ε_{GRC}^{el} and the viscous strain ε_{GRC}^{visc} . These two strains write respectively:

$$\varepsilon_{GRC}^{el}(P_i) = \frac{1 + \nu_g}{E_g} (P_0 - P_i) \quad (18)$$

$$\varepsilon_{GRC}^{visc}(t, \bar{q}(P_i, P_{int}(t))) = A \left(e^{\alpha \bar{q} P_{int}(t)} - 1 \right) \frac{t^{1-m}}{1-m} \quad (19)$$

With $P_{int}(t)$ representing the pressure at the interface at the considered time step and $\bar{q}(P_i, P_{int}(t))$ as:

$$\bar{q}(P_i, P_{int}(t)) = \frac{2(P_0 - P_i)}{q_{max}(P_i(t))} \quad (20)$$

But as the ground already deformed before the installation of the lining, the total strain of the ground reaction curve needs to be corrected. So the total strain of the ground reaction curve is:

$$\varepsilon_{GRC}(t, P_i) = \varepsilon_0 + \varepsilon_{GRC}^{el}(P_i) - \varepsilon_{GRC}^{el}(P_{i0}) + \varepsilon_{GRC}^{visc}(t, \bar{q}(P_i, P_{int}(t))) - \varepsilon_{GRC}^{visc}(t_{0p}, \bar{q}(P_i, P_{int}(t))) \quad (21)$$

The problem is that this curves depends on q_{max} that depend on $P_{int}(t)$ the interface pressure at the considered time step that is the intersection between the GRC and the SPC at this time step. To solve this, an initial value of q_{max} is assumed as q_{max}^0 and a value of $P_{int}^1(t)$ is found. Then with this value of $P_{int}^1(t)$ a new value of $q_{max}(P_{int}^1(t)) = q_{max}^1$ is calculated and again until the error $\delta_n = |P_{int}^n(t) - P_{int}^{n-1}(t)|$ is lower than a minimum value of $\xi = 0.01$ MPa.

4 Verification

The Hoek–Brown parameters of the ground were found using triaxial tests on samples of Argillite (COx) at different confinement. The parameters of the Singh–Mitchell model were estimated using the same samples on laboratory creep test under 12 MPa of confinement and presented in Table 1 and Figure 2.

Table 1: Parameters of the Singh–Mitchell model and Hoek–Brown failure criterion estimated using laboratory test results.

σ_c MPa	m_{HB}	s	a	E_g GPa	ν_g	m	A	α
18	6	1	0.4	5.0	0.12	0.8	4.18	3.54

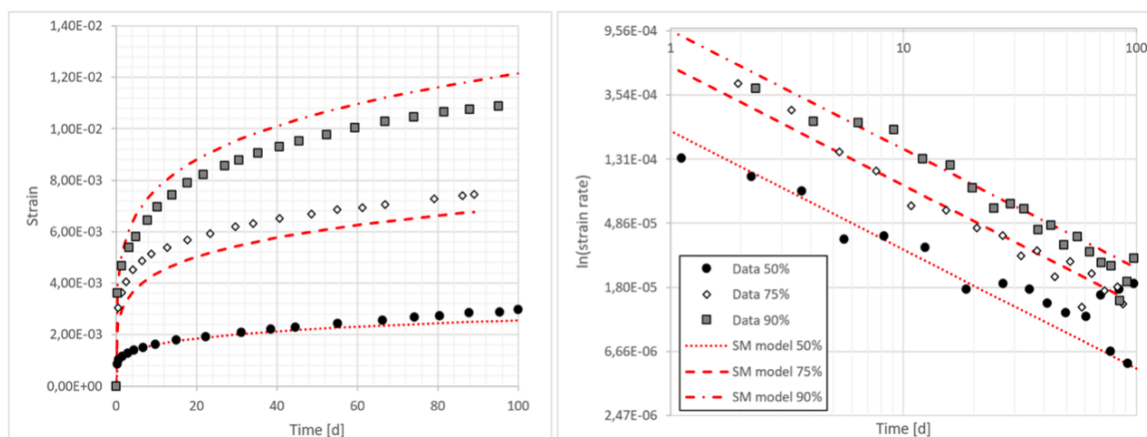


Figure 2: Creep laboratory test on Argillite (COx) at different values of \bar{q} compared to Singh–Mitchell model.

4.1 Definition of the two reference cases

In order to challenge the proposed method, two reference cases have been defined in order to compare the results of the analytical method with numerical modeling on FLAC 2D. The two cases are meant to represent the most common structures likely to be encountered in underground galleries. The first case is a circular gallery with a lining composed of segments. The excavation of the gallery is made by a TBM and the lining is put early after the excavation. The second case represents a classical gallery excavated sequentially with a roadheader with a horseshoe shape and a concrete lining installed six months after the excavation. Table 2 presents all the characteristics of the two galleries.

Table 2: Characteristics of the two reference galleries.

Case	E_c GPa	RH %	t_{0c} days	R_e m	R_i m	ν_a m/day	X_0 m	P_0 MPa
Circular gallery TBM	35	50	180	5	4.6	15	10	12.7
Horseshoe shape gallery	35	50	2	5	4.6	2	180	12.7

4.2 Assumptions for FLAC 2D modelling

The two numerical models have been developed in the finite difference software FLAC 2D using a visco-plastic model L&K implemented by Klein [6]. The parameters of the model have been calibrated on the same laboratory tests on the Argillite used to characterize the Singh-Mitchell/Hoek-Brown model. The conditions of the excavation are the same as in the analytical method (Table 2). Figure 3 presents the geometry of the two considered galleries.

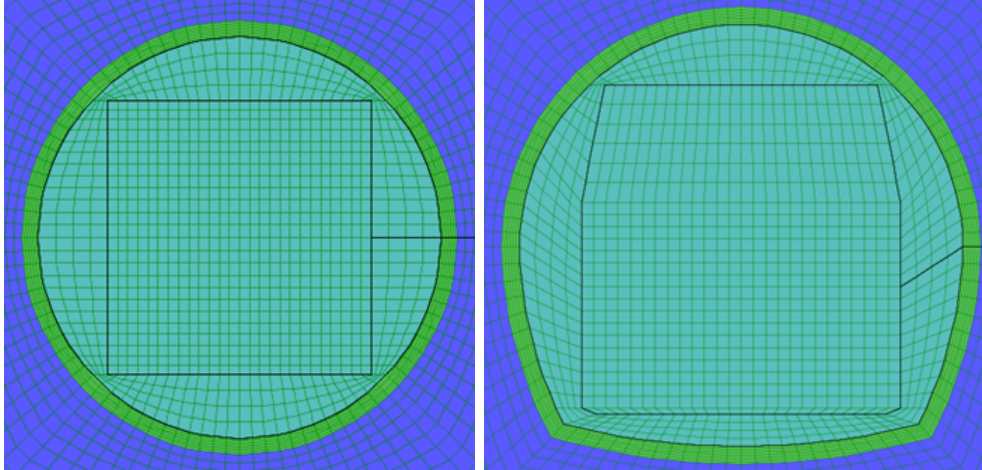


Figure 3: Geometry of the two reference cases used in FLAC 2D modeling.

4.3 Evolution of the orthoradial-stress in the lining

The evolution of the stress in the concrete lining is given in Figures 4a and 4b respectively for the circular gallery using a TBM and for the horseshoe shape gallery.

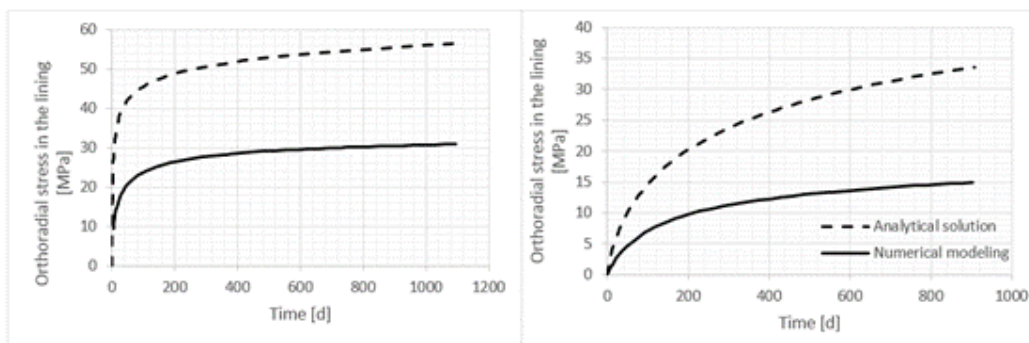


Figure 4: Evolution of the ortho-radial stress in the lining for TBM circular gallery (left) and horseshoe shape gallery (right).

In the case of the horseshoe shape gallery, the stress is compared on the top of the gallery that presents a circular shape in this area of the section.

The evolution of the stress seems higher in the analytical solution than in the numerical modeling. This difference might be due to the strong assumptions that have been made. First it assumed that the maximum deviatoric stress q_{max} is constant in the rock mass (it does not depend on the radius in a polar coordinate system), it only depends on the radial stress at the internal wall that is equal to P_i the pressure at the interface between the lining and the ground. Secondly the Singh Mitchell model does not take into account the confinement for a

same deviatoric stress ratio \bar{q} under different confinement, it predicts the same strain rate, and the parameters of the model used in the case study have been determined under a high value of confinement that leads to high values of viscous strain rate. The ratio between the two curves is constant and approximately equal to 2, being higher for the analytical solution than for the FLAC modeling, but their form are very similar.

By varying the isotropic stress P_0 , or the radius of the gallery, the ratio between the analytically predicted stress and the numerical modeling stress remains close to 2.

5 Conclusion

In this paper, an analytical method has been presented to evaluate, based on the convergence–confinement method, the stress in the lining for deep underground galleries that present long term stress evolution. It assumes that the ground follows a Singh–Mitchell model coupled with a Hoek–Brown criterion. This analytical method is compared to numerical modeling using a visco–plastic model. The results show that the stress is two times higher in the analytical method than in the numerical modeling, and this in both cases presented. Nevertheless, this method can be used to do a quick and conservative evaluation of the stress in the lining and perform a multi–parametric analysis to pre–design a gallery. It can be improved by developing a differential formulation, calculating the strain velocity depending on the time and the stress at the time step considered, and integrate it between two time step. It can also be improved by taking into account the confinement or the average stress, by varying the value of the pseudo viscosity A with the confinement for example.

References

- [1] Alejano, L. R., Alonso, E., Rodriguez-Dono, A., Fernandez-Manin, G. (2010) *Application of the convergence–confinement method to tunnels in rock masses exhibiting Hoek–Brown strain–softening behaviour*, International Journal of Rock Mechanics and Mining Sciences **47**(1), pp. 150–160
- [2] Bonini, M., Barla, G. (2012) *The Saint Martin La Porte access adit (Lyon–Turin Base Tunnel) revisited*, Tunnelling and Underground Space Technology **30**, pp. 38–54
- [3] Cui, L., Zheng, J. J., Zhang, R. J., Lai, H. J. (2015) *A numerical procedure for the fictitious support pressure in the application of the convergence–confinement method for circular tunnel design*, International Journal of Rock Mechanics and Mining Sciences **78**, pp. 336–349
- [4] NF EN 1992-1-1 2005, Eurocode 2: Design of concrete structures
- [5] Hoek, E., Carranza-Torres, C., Corkum, B. (2002) *Hoek–Brown failure criterion–2002 edition*. Proceedings of NARMS–Tac **1**(1), pp. 267–273
- [6] Kleine, A. (2007) *Modélisation numérique du comportement des ouvrages souterrains par une approche viscoplastique*, Doctoral dissertation, Institut National Polytechnique de Lorraine.
- [7] Sulem, J., Panet, M., Guenot, A. (1987) *An analytical solution for time-dependent displacements in a circular tunnel*. In International journal of rock mechanics and mining sciences geomechanics abstracts **24**(3), Pergamon, pp. 155–164
- [8] Singh, A., Mitchell, J. K. (1969) *Creep potential and creep rupture of soils*, In Soil Mech & Fdn Eng Conf Proc/Mexico/.

- [9] Zghondi, J., Carraretto, S., Noiret, A., Armand, G. (2015) *Monitoring and Behavior of an Instrumented Concrete Lining Segment of a TBM Excavation Experiment at the Meuse Haute-Marne Underground Research Laboratory (France)*, In CONCREEP 10, pp. 1430-1439

Discrete numerical modelling of a cohesive soil layer reinforced by geosynthetic sheet using an advanced constitutive law

Maria DELLI CARPINI^{1,}, Pascal VILLARD^{1,†}, Fabrice EMERIAULT^{1,‡}*

¹ Univ. Grenoble Alpes, CNRS, Grenoble INP, 3SR, 38000 Grenoble, France

Abstract: The occurrence of a sinkhole in an area may compromise the safety of the existing structures and infrastructures. Therefore preventive solutions are necessary. Recently, a coupled DEM-FEM numerical model has been developed to better account for the failure mode of reinforced soil layers during cavity openings and the interaction between the collapsed soil and the geosynthetic sheet. An experimental campaign on a small scale trapdoor model gave the possibility to validate the numerical model. In that case, a usual linear elasto - perfectly plastic Mohr Coulomb constitutive law and its failure criterion have been chosen to represent the cohesive soil. A good agreement with the experimental results has been observed. To be able to reproduce the behavior of various cohesive materials, an advanced constitutive law has been tested in place of the usual model based on the Mohr Coulomb criterion.

1 Introduction

The formation of a cavity under an embankment could occur for different reasons: carbonate dissolution in the limestone bedrock, digging of a mine, underground tunnels or chalk quarry. In any case, the collapse of the soil may compromise the structures (housing and general building) and infrastructures (road or railways) above. Trying to solve the problem when it has already happened, is technically generally difficult and expensive. Therefore a preventive solution as geosynthetic sheet is suitable both from an economic point of view and for its ability to provide enough time to react during a soil collapse. Its effectiveness has been proved for more than thirteen years [9]. A geosynthetic sheet is able to transfer a part of the load due to the collapsed soil to the stable areas outside the cavity. The main consequence is a significant reduction of the settlements recorded on the surface. Various load transfer mechanisms have been proposed in the literature in case of granular soils: british standard [2] and the works resulting from the French research program RAFAEL [4]. Recent improvements have been proposed to take into account the friction behavior of the sheet in the anchorage areas [1]. All procedures assume that the load transfer intensity can be estimated considering shear bands at the external face of the soil cylinder located above the cavity [11]. These researches have focused mostly on the granular soil behavior. More recently, new researches have been developed to account for the specificity of cohesive soil layers. An analytical formulation has been proposed [7] and validated on the base of a rich experimental campaign on a small scale trapdoor problem [6]. Recently an advanced numerical DEM-FEM code has been developed for this purpose [12]. The present paper describes the basic principles of the numerical model and its validity comparing its results with the experimental ones. First, a classical constitutive law using Mohr-Coulomb failure criterion has been chosen. Then, a new constitutive mechanism at micro scale has been

*Email: maria.dellicarpini@univ-grenoble-alpes.fr

†Email: pascal.villard@univ-grenoble-alpes.fr

‡Email: fabrice.emeriault@univ-grenoble-alpes.fr

adopted in order to better describe the mechanical behavior of various types of cohesive materials (brittle, soft, plastic).

2 Numerical simulation of the physical model

The 3D numerical model is implemented in SDEC (Spherical discrete element code) [3]. This coupled DEM-FEM code is able to represent both the discrete character of the granular soil and the fibrous nature of geosynthetic sheet. The microscopic contact law used between the spheres of the granular assembly follows the Mohr Coulomb criterion (cf. next section for the equations). The geosynthetic is modelled by triangular finite elements jointed together to create a plane structure. No bending or compression is accounted for. The macroscopic behavior of the interaction between the soil and the reinforcement is governed by tangential and normal forces to account for the friction behavior and to ensure small overlapping at the interface. The geometry and characteristics of the numerical model are similar to those of small scale trapdoor experiments carried out by [5].

In order to get the mechanical behavior of the membrane used in the experiments, eight different fiber directions are considered to reproduce the isotropy of the material. A specific tensile law is used to get the non-linearity of the material. The maximum tensile strength and deformation are respectively $T_{\max} = 1.2 \text{ KN/m}$ and $\varepsilon_{\max} = 20\%$. Generally, the initial idea was to reproduce the physical model used in the experimental campaign as accurately as possible [5]. The numerical physical model is composed by: a rigid support (10 956 discrete spheres, diameter of 6 mm), the elastic membrane (4141 finite elements), the cohesive soil mattress (40 000 spheres, diameters of 6-12 mm), the load plate centered on the soil (Fig. 1). Here, 40 000 spherical particles have been used to model the cohesive soil of the mattress under low confining pressure (natural sandy-clay soil). Due to the cohesion and low friction angle of the natural soil, it was not necessary to take account of complex particle shapes.

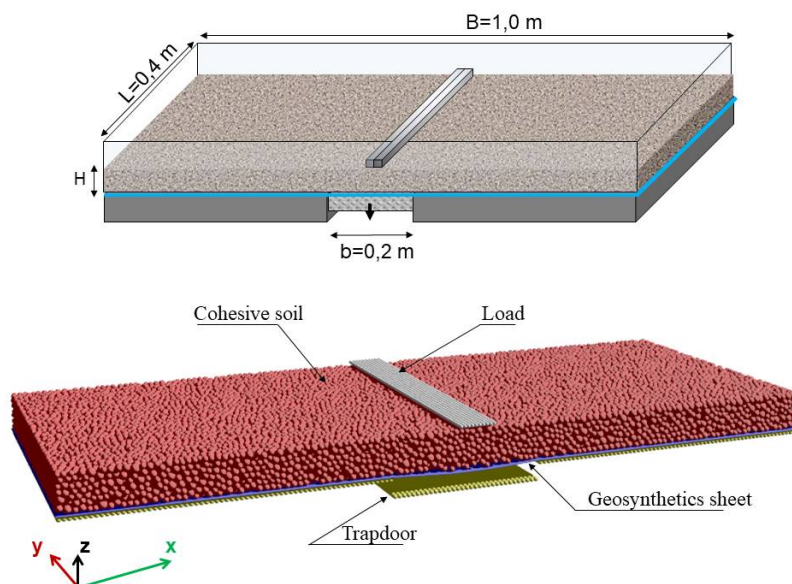


Figure 1: Trapdoor experiment geometry and the corresponding numerical model in SDEC.

The finite elements size of the membrane has to be of the same order of magnitude than the average diameter of the soil spheres to ensure a correct distribution of the soil's action on the geosynthetic sheet. At the beginning of the calculation, the spheres of the granular

Table 1: Geotechnical parameters of the cohesive soil (sandy-clay) used.

γ_d kN/m ³	w %	φ °	c kPa	σ kPa
13.8	15	35	5.5	8.04

layer are generated using the radius expansion method, at the same time as the friction angle is decreasing [10]. The gravity is first assigned to the granular soil and then one part of the spheres of the support move down to simulate the cavity opening. Afterwards, the model is loaded by a rigid slab until the collapse of the cohesive soil layer.

3 The constitutive model of Mohr Coulomb

The purpose of this article is to better understand the mechanical behavior of the cohesive soil layer during collapse and its interaction with the geosynthetic sheet after breakage. A material is defined as “cohesive” when some additional resisting forces are considered between the grains that stay all together without any confinement. The cohesion can be due to external factors (chemical links, capillary forces, electrostatic interaction, *etc.*) or just to the simple geometry of the grains [8]. According to the nature of this cohesion, the soil presents different mechanical behavior at the macroscale. Therefore, an adequate constitutive model at the micro scale has to be chosen. SDEC is able to use different constitutive models. First, a classical Mohr Coulomb law has been chosen for comparison between the numerical results and the experimental ones. An iterative process is implemented in the code according to the second law of Newton. The force is calculated at each contact point considering the relative positions between all elements (spheres and triangular finite element). To characterize the rupture of the contact, resulting in the failure of a block at the macroscale, Eqs. (1) and (2) are used.

$$|f_t| \leq c_t S_{co} + f_n \tan \phi_{co} \quad (1)$$

$$f_n \geq -c_n S_{co} \quad (2)$$

where f_t and f_n are the tangential and normal forces between two spheres. The parameters c_t and c_n are the tangential and normal cohesion parameters, expressed in kPa and assigned at the beginning of the calculation, and S_{co} is the equivalent section of the contact defined as a function of the square of the radii of the spheres in contact.

For the experimental campaign, a natural sandy-clay has been used. Table 1 shows the corresponding geotechnical parameters determined with several triaxial and flexions tests (respectively for c and φ and for σ the resistance in traction).

In order to get the same mechanical behavior numerically, several numerical triaxial and traction tests have been implemented in SDEC using various set of micro parameters (the constants c_t , c_n and ϕ_{co} in Eqs. (1) and (2)). The micro contact parameters that represent the mechanical behavior of cohesive soil under low confining pressure are: $c_t = 15$ kPa, $c_n = 15$ kPa and $\phi_{co} = 60^\circ$.

4 Investigation of a new constitutive model

In order to investigate different cohesive soil behaviors, it is proposed to implement in SDEC the microscale contact law formulated by Delenne [8] describes the relation used for that the

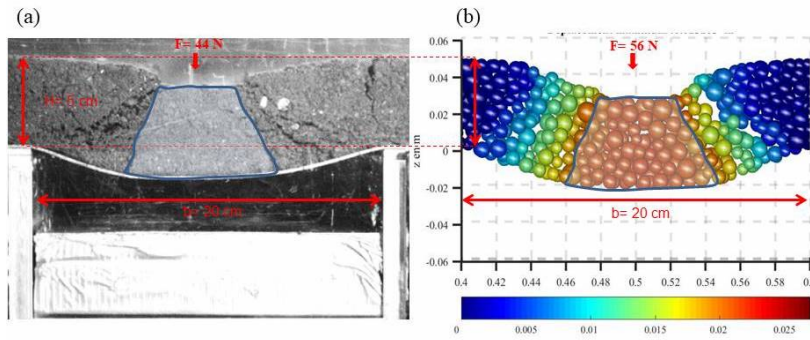


Figure 2: Geometries of the collapsed areas. Comparison between the experimental (a) and numerical (b) trapdoor tests.

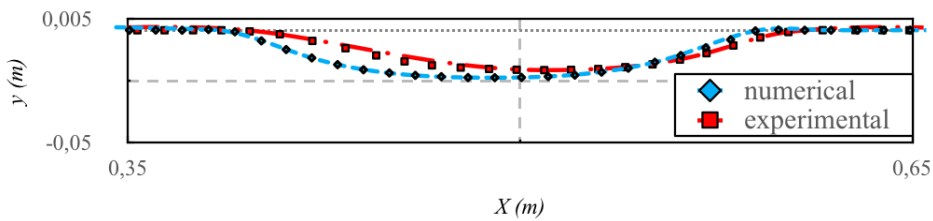


Figure 3: Geosynthetic deflection. Comparison between experimental and numerical trapdoor tests.

definition of the region in which the cohesion is active.

$$\zeta = \left(\frac{f_t}{f_t^{rupt}} \right)^n + \left(\frac{f_n}{f_n^{rupt}} \right) - 1 \quad (3)$$

The limit surface (Fig. 4) is plotted in the f_n - f_t axes (normal and tangential forces). The power n characterizes the shape that is given to the local cohesive material failure criterion. The constants f_t^{rupt} and f_n^{rupt} are the tangential and normal maximum forces defined in Fig. 4. respectively for pure traction and shear combined with a zero normal force.

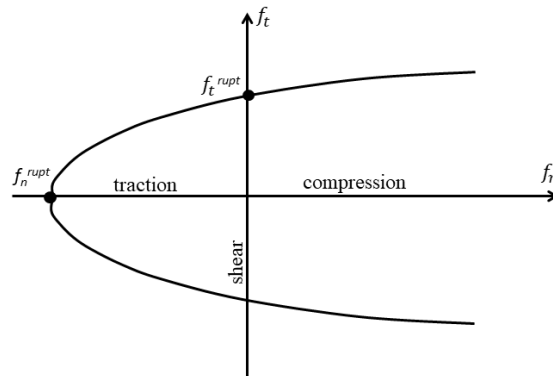


Figure 4: 2D failure surface.

Once the criterion defined by Eq(3) is reached, several strategies can be considered for the further behavior of the contact. In the present paper, it is assumed that the contact force stays on the criterion and the parameters f_t^{rupt} and f_n^{rupt} are not modified. In the case of Mohr Coulomb law (section 3), the same procedure has been considered.

The physical model has been simulated again considering now Delenne's microscale contact law. Several triaxial and traction tests have been necessary to calibrate the microscale parameters in order to reproduce the behavior of the real cohesive soil. The set of micro parameters required for Delenne model to approach the cohesive soil behavior is: $n = 2$, $f_n^{rupt}/S_{CO} = 15$ kPa and $f_t^{rupt}/S_{CO} = 50$ kPa. Its ability to maintain the cohesion at the contact level between grains after the failure is necessary to reproduce a real failure of a cohesive soil. Fig. 5 illustrates the differences between Delenne and Mohr Coulomb models in their respective ability to describe the failure process within the cohesive soil layer. The failure is reached with different load forces: a force approximately equal to 55-56 N is necessary to reach the collapse using the Mohr Coulomb contact law while a bigger force (approx. 67-68 N) is required to obtain the failure into the soil layer with Delenne model for the chosen set of parameters. In addition, the shape of the collapsing blocks is clearly different between the two models. In the small scale trapdoor experiments [5], a block of cohesive soil detaches from the entire layer. Therefore, it seems that Delenne law is more suitable than Mohr Coulomb to reproduce the real collapse situation.

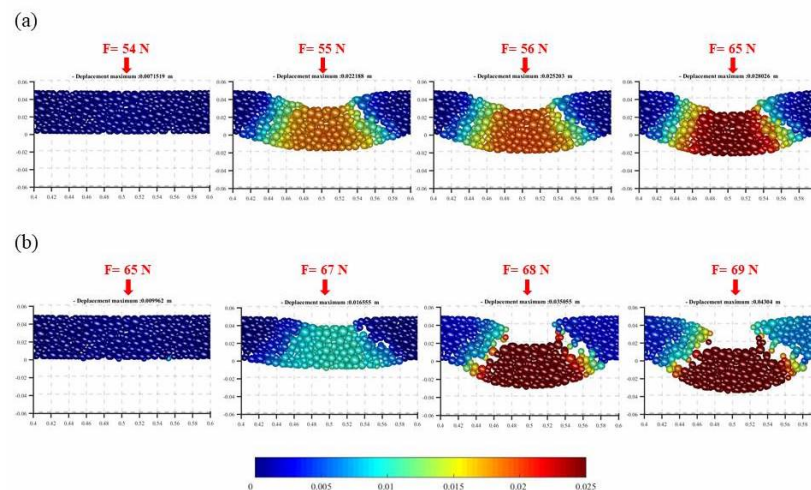


Figure 5: Field of displacements during the loading steps. Comparison between Mohr Coulomb (a) and Delenne (b) models.

The analysis of displacement fields proposed in Fig. 5 is confirmed by the stress analysis presented in Fig.6 in which the vertical stress applied by the cohesive soil onto the geosynthetic and transmitted below on the support soil is represented for four steps of the loading history: gravity application, cavity opening and loading applied before and after the collapse. A uniform stress corresponding to the self-weight of the soil is transmitted on the geosynthetic sheet during the first step (application of gravity). When the cavity is opened, the vertical stress distribution is modified with two large peaks at the vicinity of the edges of the trapdoor. In the meantime, the stress decreases down to zero above and below the reinforcement (no contact between the cohesive soil layer and the geosynthetic). After the collapse, the stress on the membrane clearly increases. Until the failure, no relevant differences can be observed between Mohr Coulomb and Delenne laws. Nevertheless, once the failure has occurred, bigger stresses are applied on the geosynthetic sheet for Delenne's law. The creation of a single block detached from the soil layer is really evident: two peaks are present at the center of the model about 2 kPa. On the opposite, at failure, Mohr Coulomb shows a more or less uniform stress of about 1.2 kPa.

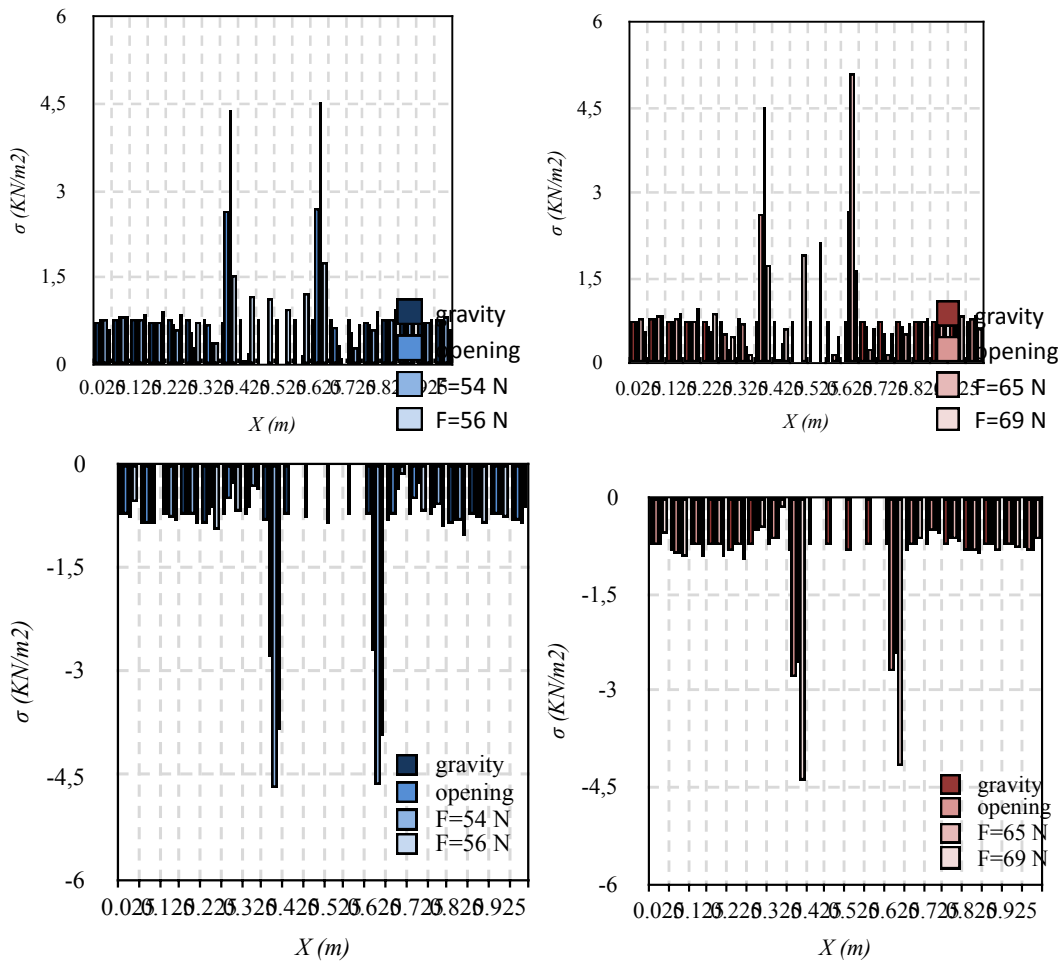


Figure 6: Stress transmitted over (a) and below (b) the membrane for Mohr Coulomb law; stress transmitted over (c) and below (d) for Delenne’s law.

5 Conclusions

In the present study, a numerical analysis has been carried out to evaluate the load transfer mechanisms when a cavity is forming under a cohesive soil layer. The comparison with experimental results has confirmed that the ability of the combined DEM-FEM numerical calculation to reproduced the observed phenomenon. Mohr Coulomb law is able to describe to a certain extent the observed shape of the collapsed block. Nevertheless, this collapsed block is not really detached from the rest of the soil as observed experimentally. The use of Delenne law provides a better description of the collapsed block and of the associated distribution of stress applied on the geosynthetic and therefore should be used for a more precise determination of the deformation of the geosynthetic layer.

Acknowledgements

The activity presented in this paper is part of the research project REGIC. The financial support of Ademe is acknowledged. The authors would like to thank all the partners of the project. This work was planned to be presented in Torino in July 2020 at the 16th International Conference of IACMAG (International Association for Computer Methods and Advances in Geomechanics) and will probably be presented to this conference in May 2021.

References

- [1] L. Briançon, P. Villard (2008) *Design of Geosynthetic-Reinforced Platforms Spanning Localized Sinkholes*, *Geotextiles and Geomembranes* **26**(5), pp. 416-28
- [2] BS 8006 (1995) *BSI Standards Publication Code of Practice for Strengthened / Reinforced Soils and Other Fills*, British Standards Institution
- [3] F. V. Donzé, S. A. Magnier (1997) *Spherical Discrete Element Code*. Discrete E. Université du Québec a Montreal.
- [4] H. Giraud (1997) *Renforcement Des Zones d'effondrement Localise - Modelisations Physique et Numerique*, PhD Thesis
- [5] M. Hassoun (2019) *Modélisation Physique Du Renforcement Par Géosynthétique Des Remblais Granulaires et Cohésifs Sur Cavités.*, PhD Thesis
- [6] M. Hassoun, P. Villard, M. Al Heib, F. Emeriault (2018) *Soil Reinforcement with Geosynthetic for Localized Subsidence Problems: Experimental Analysis and Analytical Developments*, *International Journal of Geomechanics* **18**(10), pp. 1-16
- [7] A. Huckert (2014) *Approches Expérimentale et Numérique Du Dimensionnement de Renforcements Géosynthétiques Sur Cavités et Inclusions Rigides*, PhD Thesis
- [8] J.-Y. Delenne. 2002. *Milieus Granulaires à Comportement Solide*, PhD Thesis
- [9] A. Nancey, P. Delmas (2019) *Basal reinforcement of embankment over soil subsidence area - New standard XP G38063-2*. pp. 233-40
- [10] C. Salot, P. Gotteland, P. Villard (2009) *Influence of Relative Density on Granular Materials Behavior: DEM Simulations of Triaxial Tests*, *Granular Matter* **11**(4), pp. 221-36.
- [11] K. Terzaghi (1943) *Theoretical Soil Mechanics*, Chapman And Hall Ltd., London.
- [12] P. Villard, B. Chevalier, B. Le Hello, G. Combe (2009) *Coupling between Finite and Discrete Element Methods for the Modelling of Earth Structures Reinforced by Geosynthetic*, *Computers and Geotechnics* **36**(5), pp. 709-17

Considerations for discrete modeling of geogrid-reinforced layers

Marcus GUARDAGNIN MORAVIA^{1,2,*}, Pascal VILLARD^{2,†}, Delma DE MATTOS VIDAL^{3,‡}

¹ Instituto Tecnológico de Aeronáutica, São José dos Campos, Brazil – Communauté
Université Grenoble Alpes, 3SR, Grenoble, France

² Univ. Grenoble Alpes, CNRS, Grenoble INP, 3SR, 38000 Grenoble, France

³ Divisão de Engenharia Civil, Instituto Tecnológico de Aeronáutica, São José dos
Campos, Brazil

Abstract: The topic is the modeling of geogrid-reinforced layers. The objective is to discuss possibilities that the numerical approach offers to study the problem, synthesizing the individual importance of some aspects related to the modeling by the Discrete Element Method (DEM). Soil-reinforcement interaction is still one of the geotechnical problems that require a better understanding. The three-dimensional configuration of geotextiles and geogrids shows complex behavior when granular media embedded these structures. Studying this behavior experimentally is often difficult since there are mechanisms of interaction between granular particles and geogrid members that are difficult to evaluate in a laboratory apparatus. In this case, the numerical approach represents a powerful alternative for the evaluation and development of this type of problem. DEM can handle the localized behaviors in the contacts as well as the nature of the granular material using a relatively small number of parameters. Thus, this work presents considerations for discrete modeling of geogrid-reinforced layers. An overview of three possible numerical approaches is presented, highlighting essential points for the problem. Given the potential for DEM modeling and the development of this approach recently, this paper emphasizes discrete modeling. Thus, it presents considerations on the modeling of granular and geogrid material, sample preparation, and types of simulation. The findings suggest great potential for geogrid modeling by deformable elements, which makes it possible to progress with purely discrete studies to understand the behavior of the interface between granular material and geogrid.

1 Introduction

1.1 Topic and background

Geosynthetic reinforcements are commonly used, for example, in embankment foundations to increase their strength and avoid ruptures due to excessive deformations or shear mechanisms. Geogrids have a history of successful applications and can compose both economically and environmentally interesting solutions. Its grid-like geometry creates mechanisms of interaction with the soil or other granular material that help in the mechanical improvement of the reinforced granular layer. Despite this, a better understanding of these mechanisms is necessary to improve solutions and optimize the design of layers reinforced with geogrid. The experimental study in this case is often difficult, which highlights the importance of the numerical approach for understanding the interaction between the reinforcement and granular materials. However, numerical models need to deal with the complexity of the problem, which requires specific

*Email: marcus.moravia@3sr-grenoble.fr

†Email: pascal.villard@univ-grenoble-alpes.fr

‡Email: delma@ita.br

formulations capable of simulating the nature of the granular material and the mechanical behavior of the geogrid.

This article comments on possible numerical approaches to the problem, with an emphasis on the Discrete Element Method (DEM). It also presents considerations on the modeling of granular material and geogrid, as well as aspects related to sample preparation. The objective is to discuss possibilities that the numerical approach offers to study the problem, synthesizing the individual importance of some aspects related to DEM modeling. The expectation is to contribute to future studies related to the interaction between granular material and geogrid, presenting considerations that can help new modeling proposals for the problem.

1.2 Possible numerical approaches

Although continuous numerical methods, for example, the Mohr-Coulomb linear elastic and perfectly plastic model of the classical soil mechanics, are widely used in engineering, there are problems where they are not suitable, such as those where discontinuities influence overall behavior. Discontinuous nature problems with significant levels of deformation require specific numerical models whose formulations admit localized behaviors in the contacts. Soil-reinforcement interaction has a complex behavior, especially under loading and unloading conditions, whose study requires the use of specific numerical models that can take into account the granular nature of the soil and its interaction with the reinforcement.

In reality, there is no numerical model capable of perfectly reproduce the behavior of soils with all its complex arrangements and heterogeneous compositions. However, the use of models that can take into account the main characteristics of soils or granular materials required by a given problem can lead to very realistic behaviors, providing proper results and assisting the development of geotechnical engineering.

The granular nature of the material and the mechanisms of interaction between the granular material and the reinforcement have a decisive impact on the mechanical behavior of the geogrid-reinforced layer. From this perspective, aiming at a numerical study that involves important aspects to reproduce a realistic behavior of the modeled structure, two classical approaches can be highlighted:

- Cosserat continuum mechanics;
- Discrete Element Method.

In the context of generalized continuous media, the Cosserat theory or micropolar elasticity is appropriate for modeling rupture mechanisms in materials with strong microstructure influence on their overall behavior. Cosserat continuum adds rotational degrees of freedom to the conventional continuum, which makes it possible to take into account moments at any point in a given material, in addition to the usual stress field [9]. Each particle is comparable to a small-size continuum around a point that characterizes it. Because of this, in the kinematics of the material point, additional rotational degrees of freedom occurs, and the gradient of these rotations is associated with a stress moment tensor by the principle of virtual works. Another aspect is the constitutive description of the material that considers intrinsic lengths. The introduction of these lengths in the constitutive relations allows indirect consideration of the particle size and geometry in the macroscopic behavior of the medium [21].

Ebrahimian et al. [12] simulated shearing at the interface between a layer of granular material and a rough structure using an improved model with Cosserat theory. Although the lack of both numerical and experimental studies that investigate deformations in the soil-structure interface regions makes it difficult to validate this model, the advances obtained by the author indicated the relevance of this approach. An interesting study was the comparison between parameters that control the thickness of the formed shear band. Between the initial void ratio,

average grain size, and vertical pressure, the first two indicated greater influence on the shear band. It is worth mentioning that the authors assumed simplifications that affect the model's behavior. For example, balancing factors, which reflect aspects of the microstructure in the constitutive model, such as slipping and shearing between particles, were defined as equal to one by simplification. The work also assumed full bonding in the interface region, so there are no relative horizontal displacements between the bottom surface of the granular layer and the rough surface. Regarding the kinematic boundary conditions in the interface, the study considered two antagonistic cases. The first one considers the model with zero couple stresses, that is, the free Cosserat rotation is assumed, which is a condition equivalent to that of classical continuum mechanics. The second case assumes fully constrained Cosserat rotation (*i.e.*, zero rotations). The two cases are antagonistic, so a study that includes an intermediate boundary condition to the described cases could represent a behavior closer to that expected in geotechnical soil-structure interaction problems. Simplifications are usually necessary to introduce very complex problems, and considering the lack of research on the subject, the authors' numerical results contribute to further advances in this topic.

The Discrete Element Method, also called the Distinct Element Method, models the material as constituent particles in which contacts can change during deformation. This method is essentially a set of numerical processes for calculating motion and its effect on a particular group of particles or elements whose behavior is governed by physical laws. Cundall [10], as cited in [11], originally proposed this method to study problems related to Rock Mechanics. However, its application has extended to the study of micromechanisms in granular media, as in [11, 16]. The simulation of a medium by a discrete body system (*i.e.*, elements) is a highly dynamic process with periodic changes of the forces acting on the contacts. Thus, the computational implementation of DEM is fundamental and allows the use of this numerical method in different types of problems. Consequently, the computational cost of a given problem becomes a crucial point for the discrete numerical approach.

A moderate increase in the number of elements for a more realistic numerical model can produce a significant increase in computational tasks. There is a high computational cost inserted in the task of updating the contact status between elements since the model performs this task whenever there are body displacements that, in turn, change the contact status. Many DEM codes take advantage of parallel processing capabilities (*i.e.*, a particular coupled form of distributed computing) to extend the number of elements in a simulation. With the enhancement of computer processing capabilities and the use of more agile numerical algorithms, the simulation of increasingly complex problems by DEM has become feasible and accessible.

Unlike critical state-based advanced models and Cosserat continuum mechanics approaches, DEM allows modeling the complex behavior of granular materials and their interaction with structural elements by using a relatively small number of parameters. For this reason and due to the discrete feature of the method, which provides effective modeling of the granular nature present in geogrid-reinforced layers and also the interaction mechanisms between material and reinforcement, this paper focuses on the use of DEM approach.

2 Discrete Element Method – DEM

2.1 Overview

A dry granular medium, for example, is composed of a large number of particles that can move separately and interact with each other at the contact points. This discrete aspect produces complex media behavior under loading and unloading conditions. Discrete modeling makes it feasible to study this behavior in an articulated manner. As mentioned in the previous section, the method is composed of numerical processes that calculate motion and its effect on a group

of particles or elements.

In a way, DEM can be considered similar to Molecular Dynamics, which studies the physical motion of atoms and molecules from the interaction potential between particles and the equations governing their movement [14], but including rotational degrees of freedom, contact state, and more complex geometries (*e.g.*, polyhedra). The first studies involved applying the method to the simulation of progressive movements in rock masses [10, 11]. Many studies today use DEM to model a wide variety of materials and applications have increasingly shown that the method is a helpful, powerful, and necessary tool for geotechnical problems involving discontinuous media.

According to [11], the basic principle for the formulation of the method is the idea of a dynamic process based on Newton's laws of motion, in which, from the propagation of perturbations applied to the limits or the elements themselves, individual movements in the particles are generated, which in turn result in contact forces and subsequent displacements until a equilibrium condition. In the numerical description of this dynamic process, accelerations and velocities are considered constant at the specified time intervals. The assumed time interval is so short that the above consideration is acceptable. The method also assumes that over a time interval, applied or generated perturbations can only propagate to immediate neighboring elements. Therefore, at each time step, the resultant force on any element are calculated exclusively by the sum of the contact forces and the field forces imposed on it, such as gravitational, magnetic, and electrostatic forces [1]. The flowchart of Figure 1 presents the basic scheme of a DEM simulation, which is characterized by the balance of forces on the elements at each time increment to reproduce the complex behavior of the material.

The DEM calculation steps alternate between applying a force-displacement law and Newton's second law of motion. The first law provides the contact forces resulting from displacements caused and the second law the movement of each element from the forces acting on it.

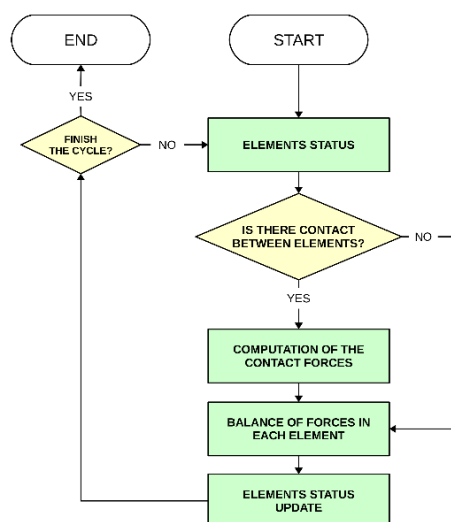


Figure 1: The sequence of a typical DEM modeling.

2.2 Granular material modeling

The arrangement and interlocking of the granular assembly can significantly influence its mechanical behavior. For example, [15] found greater shear strength in arrangements of elements that have more angular or non-convex shapes. The geometrical characteristics of the elements can develop particle roll constraints, which in turn makes the arrangement have greater shearing resistance. The bending moment generated in the interaction between non-convex elements also

contributes to increasing the overall strength of the granular assembly. Thus, classical discrete models based on independent spherical elements may not properly reproduce the shear strength of, for example, triaxial tests on granular soils.

There are numerical studies dedicated to more realistically mimicking grain rolling. They can involve two approaches. The first one comprises the definition of bodies with non-spherical geometries and the other one focuses on the integration of contact laws with rotation restrictions. Although the first approach requires a higher computational cost, especially for the contact detection task, it has the advantage of not artificially modifying contact laws.

Rigid aggregates of individual spheres can numerically recreate the non-convexity feature of granular materials. A non-convex volume occurs when a line segment formed by two internal points crosses the volume domain. Clumping spheres together, without relative displacement between these spheres during simulation, makes it possible to model different particle geometries.

2.3 Geogrid modeling

In cases involving geogrid-reinforced granular materials, the numerical study only by Finite Element Method (FEM) cannot adequately capture the interlocking of granular materials in the openings of the geosynthetic reinforcement and therefore does not consider proper interface features of such structures. In contrast, DEM has proven its efficiency in modeling micromechanical problems. In this context, some authors present alternatives involving discrete models for the study of this interaction of granular materials with the reinforcement layer.

One approach used is the FEM and DEM coupling [18] to take advantage of both methods, modeling in one single model the continuous behavior of structural elements by FEM and the discrete nature of granular materials by DEM. Although this multi-domain approach is already established, including open-source availability for it [19], there are still few studies focusing on modeling geosynthetic reinforcements (*e.g.*, geotextiles and geogrids). Works such as those presented by [22] and [20] still seek to improve understanding of interactions between granular materials and reinforcement elements.

Although multi-domain coupling is an interesting alternative to multi-scale problems, as presented by [7], in this approach, it is difficult to precisely define the contact behavior between discrete elements and finite elements, especially in cases involving complex three-dimensional geometries. It is necessary to use interface elements to make this contact between numerical methods, which in turn impose new parameters on the model. Moreover, when the FEM domain is composed of volumetric elements, the number of degrees of freedom of this domain may be very large, resulting in high computational cost simulations.

Another approach to the problem found in the literature is purely discrete models. Authors have modeled geogrids from rigid aggregates or agglomerates formed by less complex geometry elements linked together, such as spheres. The introduction of internal degrees of freedom in the rigid aggregate of spheres allows the modeled structures to be deformable. As an example of more recent studies, [6] presented two three-dimensional models of geogrids with square and triangular openings aiming at a realistic reinforcement shape. Another example is the work in which [6] performed two-dimensional numerical pullout tests with discretely modeled geogrids and evaluated the effect of geogrid tensile stiffness on the micro-mechanical behavior of the reinforced layer. Both cases model the geogrids connecting spherical elements. They use the parallel bond contact model to create different sphere arrangements. This contact model is like two parallel surfaces positioned in the contact plane that provides mechanical properties of an elastic bond between the two contacting spheres. Thus, it is possible to take into account the transmission of forces and moments between the particles that make up the geogrid.

This latter numerical approach has two downsides. The first is that modeling the geogrid or

geosynthetic reinforcement from sphere aggregates, for example, results in a significant increase in the total number of elements considered, which reduces the computational efficiency of the numerical model. The other one is an artificial numerical roughness on the reinforcement surface caused by the agglomerated elements, which may result in unrealistic behavior of the numerical model.

Contrary to the two approaches described, [17] modeled the geogrid three-dimensionally from deformable discrete elements [5, 2, 13]. The flattened shape of the geogrid members obtained in this work (*i.e.*, Figure 2) captures geometric attributes of real-generic geogrids that are important for the rolling mechanisms present in the reinforcement interaction with granular media. The use of this approach indicates a refined way of numerically simulating the geogrid, capturing the continuous nature of its members. Given its potential in modeling complex deformable structures interacting with other elements and its relevance to problems involving the behavior of geogrid-reinforced layers, further studies based on this technique are expected.

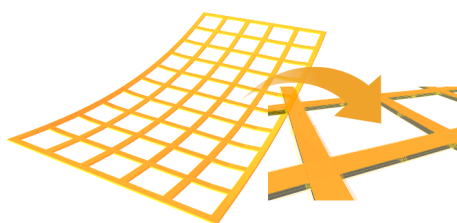


Figure 2: 3D modeling of a generic geogrid (Moravia et al., 2019).

3 Geogrid-reinforced layers

3.1 Aspects of sample preparation

The preparation of the numerical sample should focus on granular volumes reinforced with geogrid for given confinement. Obtaining a controlled compacted sample has a strong influence on the results of numerical analyses, which highlights the importance of this step in the model's response. There are numerical recipes for creating a well-controlled, homogeneous, and representative discrete sample. In this case, the sample preparation must comprise the evaluation of numerical and mechanical parameters, taking into account the sample's micro and macro domain, as well as boundary conditions.

Although the method of preparation depends on the type of numerical study, there are some aspects common to the cases. Normally, a geogrid-reinforced layer must be homogeneous and have an internal balance before simulations. Regarding homogeneity, it is possible to define algorithms for a random arrangement of particles, comprising an equal probability between different sizes and geometries, for example. For the internal balance of the sample, it is possible to take into account values of the ratio between the mean or maximum force acting on bodies (*i.e.*, particles) and the average force acting on interactions. The lower this ratio, the greater the system's static equilibrium condition.

Concerning the insertion of elements in the model to obtain controlled (*e.g.*, confinement and porosity) geogrid-reinforced layers, initially, it is possible to arrange the geogrid fully stretched between two random packages of loose granular material, as shown in Figure 3. After this step, it is possible to apply the Radius Expansion - Friction Decrease (REFD) method to obtain a dense-reinforced layer for a specific confinement and porosity condition. [4] describes the REFD procedure. Figure 4 shows a cross-section of a geogrid-reinforced layer prepared using the REFD method under a geogrid pullout test.

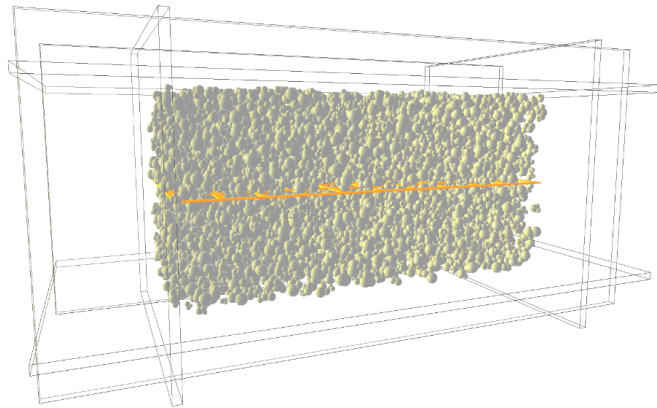


Figure 3: Geogrid arranged between two random packages of loose granular material.

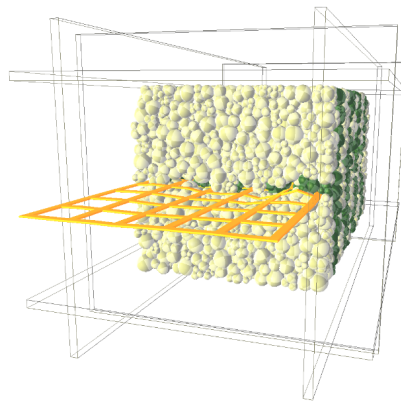


Figure 4: Dense-reinforced granular layer under a geogrid pullout test.

3.2 Considerations for numerical models

The great advantage of a numerical approach is the numerous work possibilities it provides. Further studies could address clumps of different geometry, but with the same angularity. A comparison between simulations involving the same amount of clumps may define the influence of the particle angularity on the shear strength at the interface between the granular material and geogrid.

Another possibility is to study the effect of geogrid multi-layers on the same sample. It would be very useful to understand the benefits of using multi-layers solutions compared to just one geogrid layer of higher strength and stiffness. BS 8006-1 (BSI, 2010) highlights that this topic is not yet fully understood.

The yarn crossovers modeling in the geogrid node region would be an addition or even an improvement to the numerical model of [17]. This modeling would allow representing more realistically two categories of geogrids that are the woven geogrids and bonded geogrids. Moreover, it would also make it possible to take into account node strength lower than that of yarns. Woven geogrids have the crossovers joined by knitting or intertwining and a coating that protects the entire unit (*e.g.*, bitumen, polyvinyl chloride, latex). Bonded geogrids comprise extruded strips of polyester or polypropylene welded together in a grid-like pattern.

4 Conclusion

Considerations for discrete modeling of geogrid-reinforced layers have been made to contribute to new studies related to the interaction between granular material and geogrid. The work pointed out three numerical approaches to the problem, highlighting the significant points of each one. Although there is no numerical model capable of perfectly reproducing the behavior of soils with all their complex arrangements and heterogeneous compositions, DEM models can take into account the main characteristics of granular materials and their interaction with geogrids, using a relatively small number of parameters. This paper also presented a DEM overview. The work emphasized this method and discussed the relevance of particle convexity for granular assembly. It also included considerations about the DEM modeling of the geogrid. In this case, the use of deformable elements to model complex structures, such as geogrids, is an approach that makes it possible to advance the understanding of the interaction between geosynthetic reinforcement and granular material. In the final part, considerations on numerical models dedicated to the study of geogrid-reinforced layers may help future work. To conclude, understanding the behavior at the soil-reinforcement interface is essential for an optimized design of reinforced structures. Therefore, the importance of developing numerical models that are increasingly capable of reproducing the attributes of real geogrids.

Acknowledgements

This study was financed in part by the Coordenação de Aperfeiçoamento de Pessoal de Nível Superior – Brasil (CAPES) – Finance Code 001. It was presented as part of the 4th Pan American Conference on Geosynthetics (GeoAmericas2020).

References

- [1] Bharadwaj, R. (2012). Using DEM to solve bulk material handling problems, *Chemical Engineering Progress*, 108, 9: 54-58.
- [2] Bourrier, F.; Kneib, F.; Chareyre, B.; Fourcaud, T. (2013). Discrete modeling of granular soils reinforcement by plant roots, *Ecological Engineering*, 61: 646-657.
- [3] BS 8006-1: Code of practise for strengthened/reinforced soils and other fills, British Standards Institution. London, England.
- [4] Chareyre, B.; Villard, P. (2002). Discrete element modeling of curved geosynthetic anchorages with known macro-properties, *International PFC Symposium – Numerical Modeling in Micromechanics via Particle Methods*, Swets & Zeitlinger, Gelsenkirchen, Germany, 1: 197-203.
- [5] Chareyre, B.; Villard, P. (2005). Dynamic spar elements and discrete element methods in two dimensions for the modeling of soil-inclusion problems, *Journal of Engineering Mechanics*, 131, 7: 689-698.
- [6] Chen, C.; McDowell, G.; Rui, R. (2018). Discrete element modelling of geogrids with square and triangular apertures, *Geomechanics and Geoengineering*, 16: 495-501.
- [7] Cheng, H.; Yamamoto, H.; Guo, N.; Huang, H. (2017). A simple multiscale model for granular soils with geosynthetic inclusion, *7th International Conference on Discrete Element Methods*, Springer, Singapore, 188: 445-453.

- [8] Chen, W.-B.; Zhou, W.-H.; Jing, X.-Y. (2019). Modeling geogrid pullout behavior in sand using discrete-element method and effect of tensile stiffness, *International Journal of Geomechanics*, 19, 5: 04019039–1-04019039–13.
- [9] Cosserat, E.; Cosserat, F. (1909). *Théorie des corps déformables*, Librairie Scientifique A. Hermann et Fils, Paris.
- [10] Cundall, P.A. (1971). A computer model for simulating progressive large scale movements in blocky rock systems, *Symposium of International Society of Rock Mechanics, ISRM, Nancy, France*, 1: 129–136.
- [11] Cundall, P.A.; Strack, O.D.L. (1979). A discrete numerical model for granular assemblies, *Géotechnique*, 29, 1: 47–65.
- [12] Ebrahimiyan, B.; Noorzad, A.; Alsaleh, M.I. (2012). Modeling shear localization along granular soil–structure interfaces using elasto-plastic Cosserat continuum, *International Journal of Solids and Structures*, 49, 2: 257–278.
- [13] Effeindzourou, A.; Chareyre, B.; Thoeni, K.; Giacomini, A.; Kneib, F. (2016). Modelling of deformable structures in the general framework of the discrete element method, *Geotextiles and Geomembranes*, 44, 2: 143–156.
- [14] Haile, J.M. (1992). *Molecular dynamics simulation: elementary methods*, John Wiley & Sons, New York, USA.
- [15] Matsushima, T.; Saomoto, H. (2002). Discrete element modeling for irregularly-shaped sand grains, *Numerical Methods in Geotechnical Engineering*, Presses de l'ENPC/LCPC, Paris, France, 1: 239–246.
- [16] Mirghasemi, A.A.; Rothenburg, L.; Matyas, E.L. (1997). Numerical simulation of assemblies of two-dimensional polygon-shaped particles and effects of confining pressure on shear strength, *Soils and Foundations*, 37, 3: 43–52.
- [17] Moravia, M.G.; Villard, P.; Vidal, D. de M. (2019). Geogrid pull-out modelling using DEM, *E3S Web Conf.*, 92: 13015–1– 13015–6.
- [18] Oñate, E.; Rojek, J. (2004). Combination of discrete element and finite element methods for dynamic analysis of geomechanics problems, *Computer Methods in Applied Mechanics and Engineering*, 193, 27: 3087–3128.
- [19] Stránský, J.; Jirásek, M. (2012). Open source FEM-DEM coupling, *Engineering Mechanics 2012: 18th International Conference – Svatka, Czech Republic*, Institute of Theoretical and Applied Mechanics, Academy of Sciences of the Czech Republic, v.v.i, Prague, Czech Republic, 1: 1237–1251.
- [20] Tran, V.D.H.; Meguid, M.A.; Chouinard, L.E. (2013). A finite-discrete element framework for the 3D modeling of geogrid-soil interaction under pullout loading conditions, *Geotextiles and Geomembranes*, 37: 1–9.
- [21] Vardoulakis, I. (2019). *Cosserat continuum mechanics with applications to granular media*, Springer International Publishing, Cham, Switzerland.
- [22] Villard, P.; Chevalier, B.; Hello, B.L.; Combe, G. (2009). Coupling between finite and discrete element methods for the modelling of earth structures reinforced by geosynthetic, *Geotextiles and Geomembranes*, 36, 5: 709–717.

Part III

Bio-chemo-mechanical interactions

Interaction between sand and a growing root studied by x-ray tomography

Floriana ANSELMUCCI^{1,}, Edward ANDÒ^{1,†}, Nicolas LENOIR^{1,‡}, Robert PEYROUX^{1,§},
Gioacchino VIGGIANI^{1,¶}, Glyn BENGOUGH², Chloé ARSON^{3,**}, Luc SIBILLE^{1,††}*

¹ Université Grenoble Alpes, CNRS, Grenoble INP, 3SR

² The James Hutton Institute, Invergowrie, School of Science and Engineering
University of Dundee

³ School of Civil and Environmental Engineering, Georgia Institute of Technology

Abstract: The influence of the soil on the growth of a root system has been largely investigated. By contrast, the aim of this work is to go deep into the details of how the soil may be influenced by the root system. In particular, the root growth process and its potential to improve soil strength is explored. Even though roots can be seen as fiber-like reinforcements, their growth changes the soil microstructure. Consequently, one of the objectives is to understand how the water content and the soil displacement fields evolve when an inclusion expands radially and axially. In particular, an investigation was carried on to characterise the deformation of the solid phase of the soil, due to the root growth. A series of in-vivo x-ray tomographies of Maize seeds roots have been acquired. The mentioned root system is grown into a coarse Hostun HN1.5-2 sand. Digital Image Correlation is used to measure the soil 3D displacement fields around the growing plant roots.

1 Introduction

Plants represent 99% of the Earth's biomass. Root-soil interactions greatly influence soil formation and erosion, together with soil mechanical and hydraulic properties. The effects of soil properties on root growth have been widely studied. A method for quantifying root-macropore associations from horizontal soil sections are illustrated in [2], where it was shown that root growth in arable soils is often limited by soil strength [3, 4], or by the availability of macropores that provide low-resistance pathways for root growth in very strong soils [5]. More recently, the effect of root hairs has been studied. They have a key role in anchoring the root tip during soil penetration [6]. The aim of this work is to investigate which soil properties are altered when a root element grows, i.e., looking at the same process from the point of view of the soil. X-ray tomography is a promising non-destructive method, allowing a time-series of 3D volumes to be acquired. This technique has been extensively used in soil science, to understand the response of the Root System Architecture (RSA) to the soil texture [7] and to visualize the root system itself [8]. This paper ([1]) presents the methodology used to create samples composed of granular soil and plant roots. Through this specific protocol, reproducible samples are analysed through x-ray tomography. Detailed identification of each phase in the sample is performed, leading to

*Email: floriana.anselmucci@3sr-grenoble.fr

†Email: edward.ando@3sr-grenoble.fr

‡Email: nicolas.lenoir@3sr-grenoble.fr

§Email: robert.peyroux@3sr-grenoble.fr

¶Email: cino.viggiani@3sr-grenoble.fr

Email: a.bengough@dundee.ac.uk

**Email: chloe.arson@ce.gatech.edu

††Email: luc.sibille@3sr-grenoble.fr

the qualitative description of the evolution of the structure, and the quantitative study of the kinematics of the system.

2 Materials and methods

2.1 Sample preparation

A specific protocol was followed to prepare the specimens used for the experiment, in order to obtain reproducible cylindrical samples. In this study, coarse Hostun sand (namely HN1.5-2) [9] with $D_{50} = 1.5\text{mm}$ [Fig. 1] was pluviated into cylindrical transparent PMMA pipes (5 cm in diameter and 10 cm in height). The pluviating was done with a controlled drop height, with the objective to obtain a reproducible dry bulk density (1.69 g/cm^3). A germinated maize seed was placed in the upper part of the sample, during sand pluviating. The water content of the sample (0.1 g/g), was chosen to optimise seedling growth [10]. Nutrients were added as required to sustain good growth.

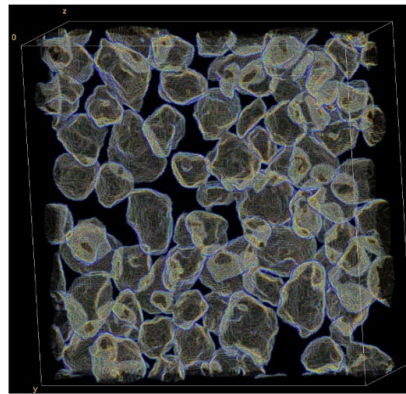


Figure 1: 3D representation of a sub-volume ($250 \times 250 \times 50$ pixels) extracted from the whole sample, showing the morphology of the Hostun sand grains. The pixel size of the image is $40\text{ }\mu\text{m/px}$.

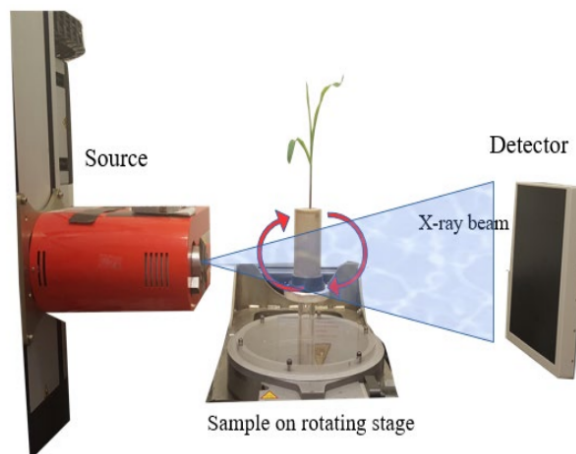


Figure 2: X-ray microtomography set-up used to image the root-soil systems in a cylindrical specimen. The sample is placed on a rotation table and the distance between the x-ray source, the sample, and the detector was fixed throughout the whole observation.

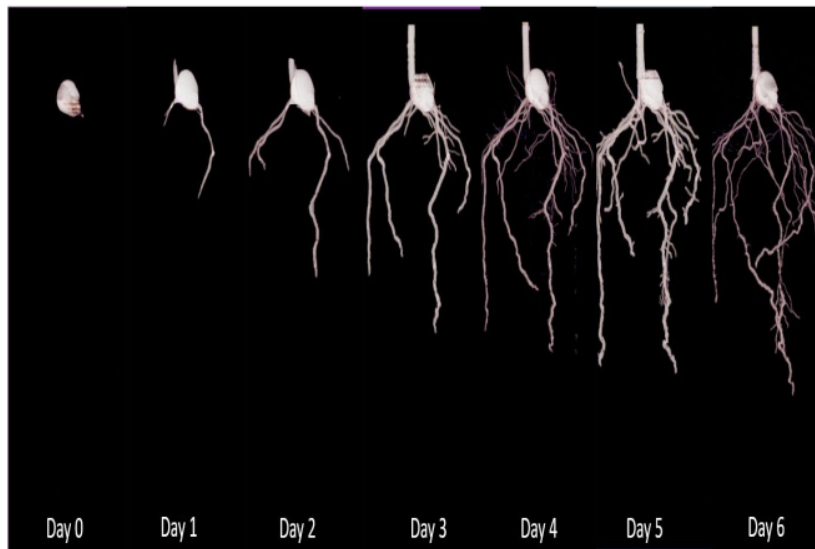


Figure 3: 3D rendering of the daily root development.

2.2 Image acquisition

X-ray tomographies allow a detailed image to be acquired of both the root system and the sand particles. The tomographies are taken with a time-lapse of 24 hours throughout 7 days. Each scan lasts less than 2 hours, with a pixel size of $40\ \mu\text{m}/\text{px}$. Given the dimensions of the sample and the setup of the machine [Fig. 2], this was the highest reachable pixel size.

The main components of the maize root system [11] develop over a week, hence the sample is scanned for 7 days. The one week old root system is composed both of embryonic primary and seminal roots, and of post embryonically formed crown roots and lateral roots. Fig. 3 shows the daily progress of the root system inside the sand specimen.

3 Analysis

3.1 Phase identification

A new image processing technique was developed to identify each phase of the specimen, *i.e.*, sand grains, plant roots, pore water, and pore air. We started by excluding the outside of the sample from the analysis. With a combination of thresholding and denoising filters, to smooth images while preserving edges, sand grains were identified. Root voxels are separated from the rest of the matrix, according to their grey values. That way, the seed time evolution could be established. Note that root and water grey values are very close, so the small volumes of pore water are recognized as root phase, in a volume where the root selection is removed. Once the grains and root have been determined, the identification of the air is easy, since it has a grey values range that does not belong to the other elements in the system. Accuracy of the phase volumes obtained by image analysis at day 0 are compared against the volume fractions of water and sand introduced in the medium. After day 0, segmentation parameters were kept identical for further image analysis (corresponding to the following days). A typical result of the phase segmentation is shown in Fig. 4. Each phase is defined with a different colour detailed in the legend.

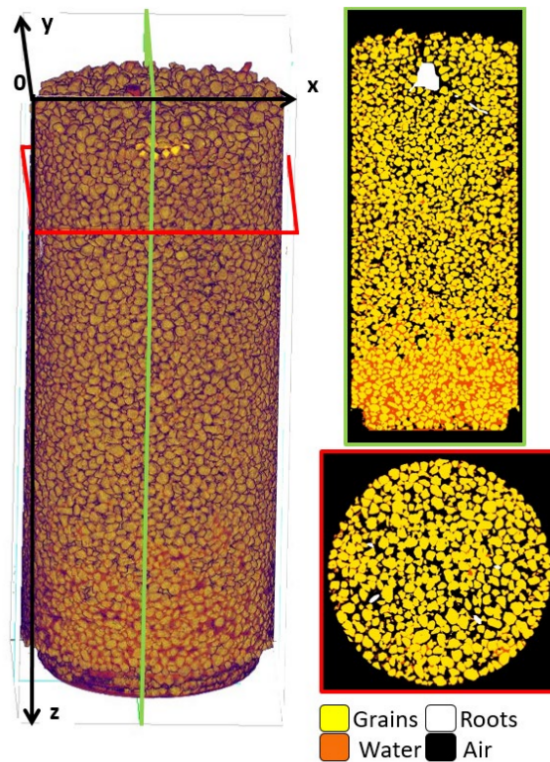


Figure 4: 3D sample volume and identification of the phases in vertical and horizontal slices.

3.2 Displacements field

Both continuous and discrete (*i.e.*, grain-based) displacement fields of the sand solid phase are measured with image correlation. We focus here on the discrete displacement fields representing the translation and the rotation of the center of mass of each sand grain. The discrete displacement fields are computed from the labelled image of the sand matrix by applying discrete digital image correlation (discrete DIC). Labelled images, to identify each grain of the sand sample, are obtained by using a 3D watershed algorithm applied on the segmented grain phase to separate touching grains.

The discrete DIC is performed with an image processing code dedicated to granular materials [12]. The configuration of the root-soil system at day 0 (*i.e.*, the day when the germinated seed was placed in the specimen) is used as the reference configuration, for the reason that the root was not able to cross the soil yet. Hence, total discrete displacement fields are computed between different time configurations (day 0 and day 2, day 0 and day 3, up to day 0 and day 6).

The maps showing the vertical (Z axis) and horizontal (Y axis) displacements of the sand particles at different times are shown in Fig. 5 in horizontal and vertical slices, respectively. The parts of the roots included in those sections are displayed in green.

4 Results

As a first step, the investigation focuses on the sand grains in direct contact with the roots which are the most prone, *a priori*, to move during root growth. First, the root structure at the last day of observation (day 6) is characterised, then, the sand particles at the surface of the final root system are selected, as shown in Fig. 6. In total, we analyse 1004 out of 32000 particles

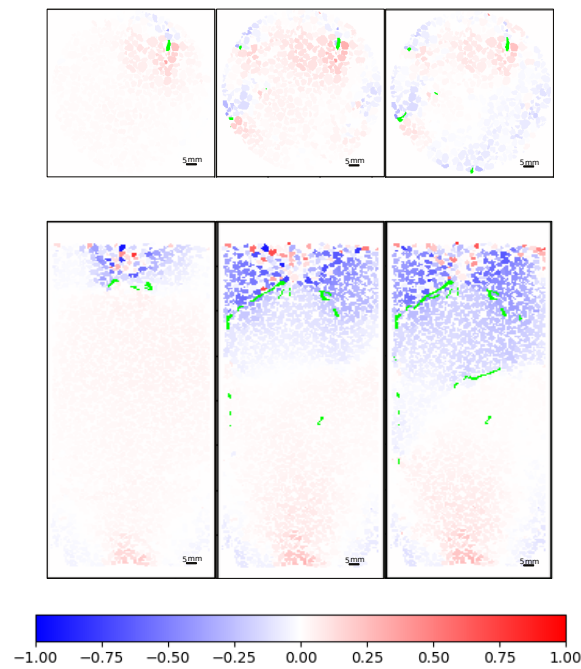


Figure 5: Discrete displacement field with root shown in green color. First row: Horizontal slices regarding the displacements along Y. Second row: Vertical slices regarding the displacements along Z. Negative values indicate that root is pushing the grains upwards (for vertical 'z' displacements) and to the left (for horizontal 'y' displacements). Displacement maps are shown between days 0 and 2 (left), days 0 and 4 (middle), and between days 0 and 6 (right). Day 0 corresponds to the day when the germinated seed was inserted. The colour bar unit mm.

present in the specimen. The origin of the axes is placed at the top of the sample (Fig. 4).

Fig. 7 shows the evolution of the displacement fields. Such displacements are calculated with reference to the position of the sand grains at day 0. Note that the values shown are in mm. In line with the resolution of the scans after $2 \times 2 \times 2$ downscaling, here 1 pixel corresponds to 80 microns. The highest vertical displacement detected in the vicinity of the root is 1.44 mm—almost one grain size of displacement. The largest horizontal displacement, reached on the last day of observation, amounts to 2.39 mm. This last displacement value is about 1.5 the mean grain size D_{50} . According to the orientation of the axes, when a displacement value is negative, it means that the particle is pushed upward and vice versa. Note that even if the root is initially present in the top part of the sample, grains located at the bottom of the sample are impacted by the root growth. In addition, when the root is pushing down, and absorbing the water, that it is at the base of the pipe, the grains are pulled up in some cases.

5 Conclusions

In this paper we analysed x-ray tomography scanned images of a specimen made of Hostun sand HN1.5-2 with a $D_{50} = 1.5$ mm and a maize root system.

The plant is growing healthily, following the typical scheme of the maize complex architecture reported in the literature, in the correct time frame. During the experiment, it was decided not to introduce additional water in the specimen, to preserve the sand grains structure.

Using segmentation techniques grains, roots, water, and air voxels can be classified. Individual grains are numbered and those in contact with the root can be enumerated with ease. Sand grain displacements are observed since the very beginning. These displacements may be

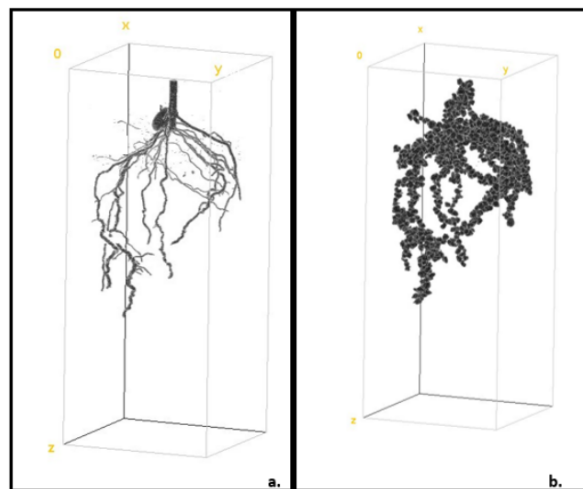


Figure 6: Identification of the grains surrounding the root system. **a.** Root system architecture of the maize on the last day of observation; **b.** Grains surrounding that root system.

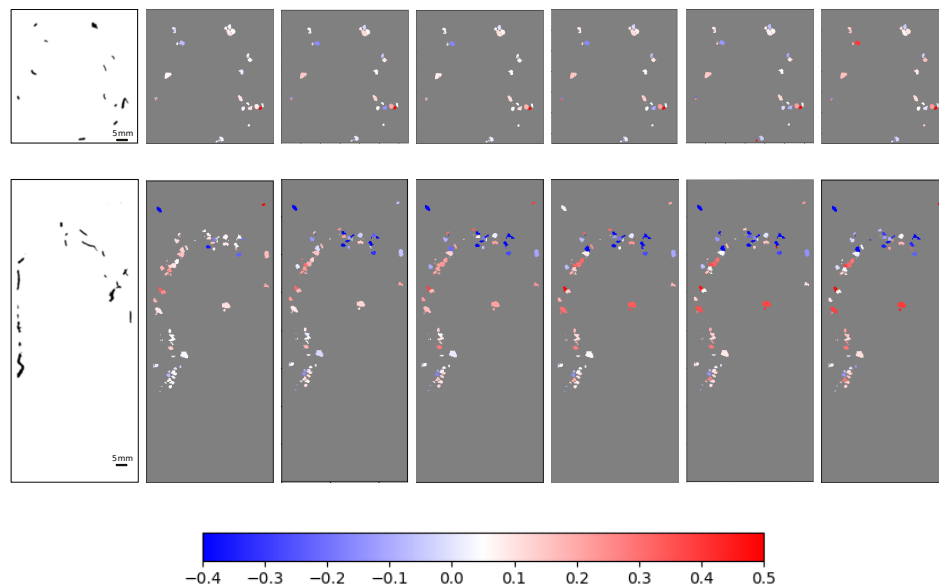


Figure 7: Identification of the root and displacement of the grains surrounding the roots. The first row represents the horizontal displacement along Y, the second row, instead, the vertical displacement along Z. Negative values indicate that root is pushing the grains upwards (for vertical 'z' displacements) and to the left (for horizontal 'y' displacements). The first images on the left in the first and second rows represent the amount of root present in these specific vertical and horizontal sections at day 6. The displacements are expressed in mm.

correlated both to the evolution of the seedling and the water uptake, resulting in a change of the distribution of the pore water in the sand sample.

Further investigations are needed to distinguish, in detail, the influence of each phenomenon (root development and change in local water content). According to the displacement maps obtained, the grains are mainly moving downward, thus in the same main direction as the elongation of the root. In particular, the roots are able to displace the grains over a length of about 2.4 mm, which is almost the size of two sand particles. Once the root tip is passed, the grains do not experience apparently any further significant displacement. Further kinematic

measurements will be performed to understand the length of the root tip that it is actually influencing the soil, and to understand the type of strain field produced in the soil for predicting any failure mechanisms upon root growth. The same analysis is ongoing with finer sand. Indeed, one of the perspectives of this work is to investigate the influence of the grain distribution on the way the root growth influences sand microstructure, among others the local porosity [13].

Acknowledgments

This work is supported by the French National Research Agency in the framework of the "Investissements d'avenir" programs referenced ANR-15-IDEX-02 (IDEX Université Grenoble Alpes) and ANR-11-LABX-0030 (LABEX Tec 21). This contribution is published in the proceeding of the 7th International Symposium on Deformation Characteristics of Geomaterials (IS-Glasgow 2019). Issue: E3S Web Conf. Volume 92, 2019; Article Number: 12011.

References

- [1] Anselmucci, F., Andó, E., Sibille, L., Lenoir, N., Peyroux, R., Arson, C., Viggiani, G. & Bengough, A. G. (2019, June). Root-reinforced sand: kinematic response of the soil. In 7th International Symposium on Deformation Characteristics of Geomaterials, IS-Glasgow 2019 (p. 12011). EDP Sciences.
- [2] Stewart, J. B., Moran, C. J., & Wood, J. T. (1999). Macropore sheath: quantification of plant root and soil macropore association. *Plant and Soil*, 211(1), 59-67.
- [3] Bengough, A. G., McKenzie, B. M., Hallett, P. D., & Valentine, T. A. (2011). Root elongation, water stress, and mechanical impedance: a review of limiting stresses and beneficial root tip traits. *Journal of experimental botany*, 62(1), 59-68.
- [4] Valentine, T. A., Hallett, P. D., Binnie, K., Young, M. W., Squire, G. R., Hawes, C., & Bengough, A. G. (2012). Soil strength and macropore volume limit root elongation rates in many UK agricultural soils. *Annals of botany*, 110(2), 259-270.
- [5] White, R. G., & Kirkegaard, J. A. (2010). The distribution and abundance of wheat roots in a dense, structured subsoil—implications for water uptake. *Plant, cell & environment*, 33(2), 133-148.
- [6] Bengough, A. G., Loades, K., & McKenzie, B. M. (2016). Root hairs aid soil penetration by anchoring the root surface to pore walls. *Journal of Experimental Botany*, 67(4), 1071-1078.
- [7] Rogers, E. D., & Benfey, P. N. (2015). Regulation of plant root system architecture: implications for crop advancement. *Current Opinion in Biotechnology*, 32, 93-98.
- [8] Perret, J. S., Al-Belushi, M. E., & Deadman, M. (2007). Non-destructive visualization and quantification of roots using computed tomography. *Soil Biology and Biochemistry*, 39(2), 391-399.
- [9] Flavigny, E., Desrues, J., & Palayer, B. (1990). Note technique: le sable d'Hostun «RF». *Revue française de géotechnique*, (53), 67-70.
- [10] Croser, C., Bengough, A. G., & Pritchard, J. (1999). The effect of mechanical impedance on root growth in pea (*Pisum sativum*). I. Rates of cell flux, mitosis, and strain during recovery. *Physiologia Plantarum*, 107(3), 277-286.

- [11] Hochholdinger, F., & Tuberosa, R. (2009). Genetic and genomic dissection of maize root development and architecture. *Current opinion in plant biology*, 12(2), 172-177.
- [12] Andò E. , Cailletaud R., Roubin E. , Stamati O. and the spam contributors, spam : The Software for the Practical Analysis of Materials - [https://ttk.gricad-pages.univ-grenoble-alpes.fr/spam/\(2017\)](https://ttk.gricad-pages.univ-grenoble-alpes.fr/spam/(2017)).
- [13] Anselmucci F., Andò E. , Sibille L. , Lenoir N. , Viggiani G., Peyroux R. , Arson C., Bengough A.G., Quantifying micro-structural changes in soils due to plant root growth, IS-B2G Symposium on symposium is multi- scale bio-mediated and bio-inspired geotechnics, Atlanta, Georgia, USA, 10-13 september 2018, (2018).

Part IV

Thermo-hydro-mechanical coupling

Micromechanical interpretation of thermo-plastic behaviour of clays

Angela CASARELLA^{1,*}, Alessandro TARANTINO^{1,†} Alice DI DONNA^{1,‡}

¹ Univ. Grenoble Alpes, CNRS, Grenoble INP, 3SR, 38000 Grenoble, France

Abstract: The effect of temperature on mechanical behaviour of clay-based geomaterials is relevant in a number of geotechnical applications (e.g. low enthalpy geothermal systems and energy geostructures, nuclear waste disposal, and heating in rapid shear deformation). Mechanical response of (saturated) clays upon heating is not always intuitive as volume changes may occur due to both thermal expansion of clay constituents and temperature-induced changes of clay microstructure. This paper first revisits the macroscopic thermally-induced mechanical behaviour of saturated clays available in the literature via an advanced thermo-elastoplastic constitutive model and then elucidates the dependence on clay mineralogy of the two key parameters of the model (mechanical hardening and thermal softening respectively) by inspecting differences in clay inter-particle electro-chemical forces occurring in kaolinitic, illitic, and smectitic clays. The micromechanically-based interpretation of constitutive parameters can serve as a guidance for soil parameter selection in the design of energy geostructures.

1 Introduction

The effect of temperature on mechanical behaviour of geomaterials is a relevant problem of growing concern in geoenvironmental engineering.

During the last decades, the response of soils to the combined effects of stress and temperature has been studied in depth. Nonetheless, most investigations have been carried out within the context of nuclear waste geological disposal [24, 2] focusing on the study of high-swelling clays subjected to high stress and temperature. The effect of temperature changes has not been extensively investigated in non-swelling or moderately active clays, which are of interest in a number of applications including shallow geothermal plants [21], energy geostructures [17], and shear heating in rapid shear movements [27].

The thermal behaviour of granular materials is governed by the thermal expansion of the grains. When a sandy soil is heated under drained conditions, its volume increases as both grains and water dilate thermo-elastically (proportionally to their thermal expansion coefficients). Due to drained conditions that establish coarse-grained materials, soil water thermal expansion does not contribute to the volume variation of the material itself [17].

Volume changes in (saturated) clays occur due to both thermal expansion of clay mineral and soil water and temperature-induced changes of clay microstructure. The interaction between these two mechanisms is complex and, as a result, mechanical response of clays upon heating is not always intuitive. This includes the volumetric ‘collapse’ observed in normally consolidated clays upon heating.

As a result, a detailed characterisation of the coupled thermo-mechanical behaviour of clays subjected to varying temperature turns out to be fundamental at the design stage.

*Email: angela.casarella@3sr-grenoble.fr

†Email: alessandro.tarantino@strath.ac.uk

‡Email: alice.didonna@3sr-grenoble.fr

This paper presents an insight into the experimental evidence available in the literature concerning the macroscopic thermomechanical behaviour of clays. The Advanced Constitutive Model for Environmental Geomechanics with Temperature effect, ACMEG-T [12], developed at EPFL (Switzerland), is deployed to interpret these macroscopic observations. The two key parameters of the constitutive model (mechanical hardening and thermal softening respectively) are interpreted in the light of the different electro-chemical forces assumed to control clay particle interactions in clays of different mineralogy (kaolinite, illite, and smectite).

2 Thermomechanical response of saturated clays

For the case of (saturated) clays, the mechanical response to thermal loading depends on loading history, being thermo-elasto-plastic for Normally Consolidated (NC) clays and thermo-elastic for highly Over-Consolidated (OC) clays (Figure 1) [6, 3, 14, 1, 9]. The material irreversibly and non-linearly undergoes contraction upon heating in NC conditions, while OC materials experience a reversible volume expansion during heating. An intermediate case is represented by slightly OC clays: the material shows initial dilation and subsequent contraction upon heating, followed by contraction during cooling.

This macroscopic response of clayey soils to temperature cannot be explained solely in terms of thermal expansion of the solid and pore fluid phases, as is the case of granular materials. Thermal dilations of water and clay minerals are positive (Table 1, [10]) and volumetric response upon heating should be characterised by a volumetric (elastic) expansion if controlled only by thermal dilations of individual phases. However, NC clays undergo volumetric contraction when subjected to an increase in temperature and this volume change is not recovered during subsequent cooling.

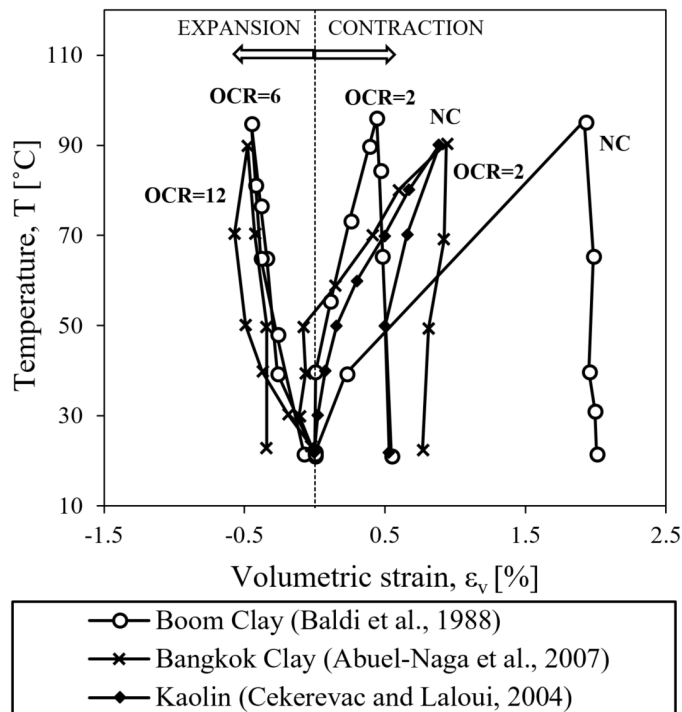


Figure 1: Thermal volumetric behaviour of saturated clays.

Temperature therefore appears to affect the electro-chemical interactions between clay particles giving rise to a more complex response of the clay-water-electrolyte system. According to

Material	Volumetric thermal expansion coefficient $\beta_s [10^{-5} \text{ }^\circ\text{C}^{-1}]$
Kaolinite	2.90
Smectite	3.90
Illite	2.50
Chlorite	3.12
Water* (β_w)	$13.9 + 0.61T$

* T is the temperature in $^\circ\text{C}$, considering constant pressure

Table 1: Volumetric thermal expansion coefficients of minerals and water [10].

[22], the clay particle surface is negatively charged and the particle edge is positively charged when the clay is mixed with 'ordinary' acidic water. Under these conditions, clay microstructure occurs as a house of cards where particles arrange themselves in face-to-face (non-contact) or edge-to-face (contact) configurations (Figure 2). Plastic volumetric deformation occurring upon mechanical loading has been associated with disengagement of edge-to-face contact with particles moving from edge-to-face to face-to-face [22]. For the case of thermally-induced plastic volumetric collapse observed in NC clays, it can therefore be tentatively assumed that an increase in temperature encourages the weakening of the net attractive force at the edge-to-face contact promoting disengagement with consequent plastic deformation [4]. Accordingly, thermally-induced plastic deformation should depend on electro-chemical forces generated between clay-particles, which depend in turn on clay mineralogy. This micro-macro interaction is further explored in the next sections.

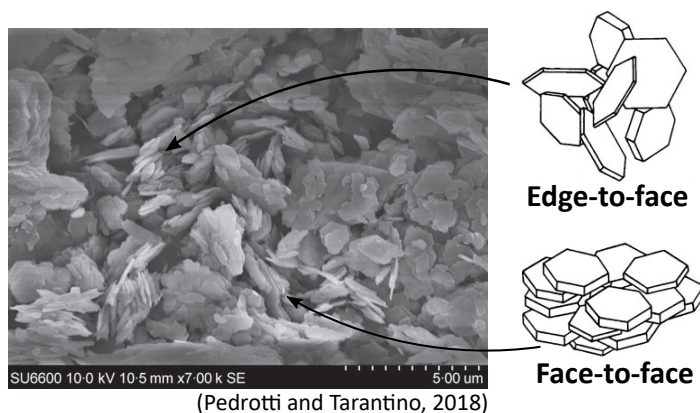


Figure 2: consolidated at 70 kPa [22] from which kaolin clay particles can be identified.

3 Constitutive model

Modelling the complex non-linear and irreversible behaviour of clay, when subjected to combined thermal and mechanical loading, requires advanced constitutive models. During the last thirty years, several elastoplastic models have been developed to take into account the effects of temperature variations on the behaviour of clayey soils [20, 8, 13, 15]. A Cam-Clay-based constitutive model was formulated at EPFL in Lausanne to unify the different peculiar aspects characterising the thermo-mechanical response of fine-grained soils: the Advanced Constitutive Model for Environmental Geomechanics, with Temperature effects (ACMEG-T) [12].

The model is based on the thermo-elastoplasticity theory and the critical state theory [25]. As the Original Cam-Clay model suffers from some inconsistencies in the prediction of the

behaviour of normally consolidated soils, an isotropic yielding mechanism was added to the Original Cam-Clay deviatoric yielding mechanism. According to the theory of multi-mechanism plasticity [18], two thermo-plastic mechanisms are considered: the isotropic mechanism, f_{iso} , and the deviatoric mechanism f_{dev} . This means that there are two different dissipative processes described through two evolution laws, activated by two yield functions, through two dissipative potentials and through two plastic multipliers [16]. The two yield functions define a closed domain in the isotropic effective stress - deviatoric stress - temperature space inside which the behaviour of the material is reversible (Figure 3).

As our purpose is to calibrate temperature-dependent constitutive parameters driving the volumetric thermal response, we will focus on the isotropic yield function with respect to temperature (horizontal plane in Figure 3).

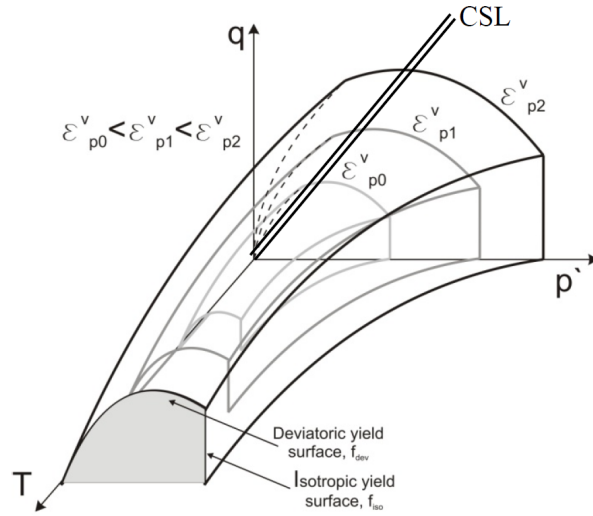


Figure 3: Yield locus of the ACMEG-T model [17].

3.1 Thermo-elastic strain

According to [12], the total deformation is composed of volumetric and deviatoric parts. In the elastic non-isothermal domain, the volumetric deformation is represented by the superposition of a reversible thermal induced strain and a mechanical elastic strain (under isothermal conditions):

$$\epsilon_v^{Te} = \beta_s(T - T_0) + (p' - p'_0)/K \quad (1)$$

where ϵ_v^{Te} [-] is the volumetric thermo-elastic strain, β_s [$^{\circ}C^{-1}$] is the volumetric thermal dilation coefficient, $(T - T_0)$ [$^{\circ}C$] is the temperature variation, $(p' - p'_0)$ [kPa] is the mean effective stress variation (assuming negative stresses when a compression occurs) and K [kPa] the bulk elastic modulus.

3.2 Isotropic Thermoplastic Mechanism

The development of thermo-plastic strain starts when the stress point reaches the yield limit. The yield limit of the isotropic thermoplastic mechanism is expressed by:

$$f_{iso} = p' - p'_c = 0 \quad (2)$$

where p'_c is the preconsolidation pressure which evolves with the generated volumetric plastic strain ϵ_v^p :

$$p'_c = p'_{c0} e^{\beta \epsilon_v^p} \quad (3)$$

with p'_{c0} being the initial preconsolidation pressure at temperature T and β the plastic rigidity index, i.e. the reciprocal of the slope of the linear function ($\epsilon_v^p - \log p'$).

Several results from the literature show a decrease in the preconsolidation pressure with increasing temperature. Therefore, the elastic domain under isotropic loading is reduced as temperature increases, which is representative of thermal-softening. The thermal effect on the yield limit is taken into account by considering [11]:

$$p'_{c0} = p'_{c0,T_0} [1 - \gamma_T \log(T/T_0)] \quad (4)$$

where p'_{c0,T_0} [kPa] is the initial preconsolidation pressure at temperature T_0 and γ_T [-] is a model parameter.

Finally, the expression of the isotropic thermoplastic yield limit in (2) can be re-written as follows:

$$f_{iso} = p' - p'_{c0,T_0} e^{\beta \epsilon_v^p} [1 - \gamma_T \log(T/T_0)] = 0 \quad (5)$$

(5) depends on two material parameters: β , expression the evolution of mechanical hardening and γ_T controlling the evolution of thermal softening. The thermal response is actually a combination of these two mechanisms: mechanical hardening and thermal softening [19].

This model has been validated on several THM paths but its formulation depends on a number of parameters, which are not easy to identify other than by curve fitting. The challenge addressed in this paper is to provide a micromechanical interpretation to the temperature-related constitutive parameter γ_T and β .

In the mean effective stress-temperature plane shown in Figure 4 the initial isotropic yield function defines an elastic domain (grey space). The value p'_{c0} represents the isotropic preconsolidation pressure at the initial stage. Points A, B and C exemplify three different initial states of the material before applying a drained thermal load at constant mean effective stress. Both points A and C have a current mechanical stress lower than p'_{c0} , thus they are overconsolidated (OC) and their thermal stress path starts in the elastic domain. Point B lies on the yielding locus and represents a normally consolidated material.

Point A represents a highly overconsolidated stress state. This means that when drained heating occurs, the stress state moves from A to A' within the elastic domain without crossing the yield surface. As shown on the (T, ϵ_v) plane in Figure 4, the material elastically dilates upon heating.

Starting from point B, a positive temperature changes induce thermoplastic strain from B to B', which results in the contraction of the material.

The temperature-stress path of point C starts in the elastic domain but encounters in C'' the isotropic yield surface. The material therefore responds elasto-plastically, dilating elastically until it reaches C'' and then starting contracting when the yield surface is dragged from C'' to C'. Mechanical loading from B to B'' at constant temperature induces plastic deformation (mechanical strain hardening).

3.3 Calibration of parameters β and γ_T on experimental results

The ACMEG-T model was used to simulate experimental results on five different types of normally consolidated (NC) clays ([6, 3, 14, 1, 9]). According to (5) and (1), the key model parameters to be determined to characterise the thermo-plastic response are γ_T , β and β_s . All the considered tests are done under NC conditions, thus by definition at initial state $p' = p'_{c0}$.

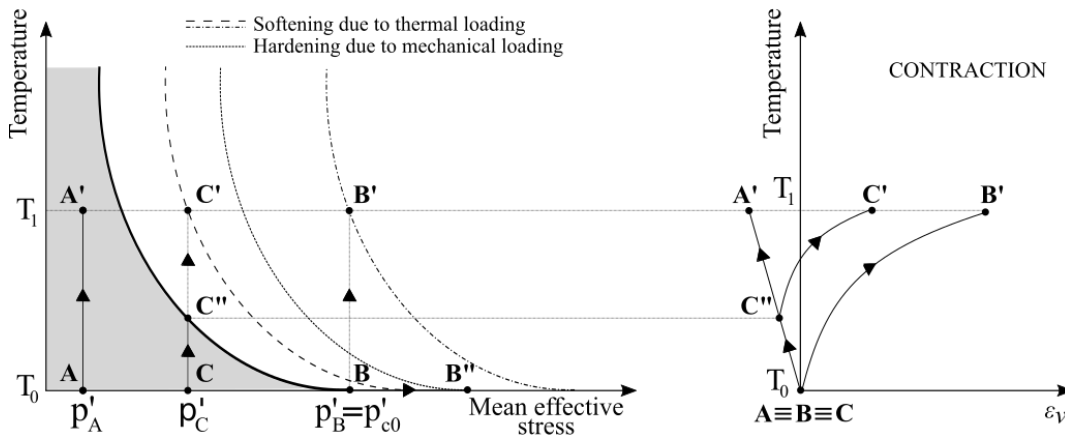


Figure 4: Yield locus of the ACMEG-T model on (T, p') plane and effects recorded on (T, ϵ_v) .

For each experimental dataset, the parameter γ_T in the ACMEG-T model was calibrated by fitting the volumetric strain accumulated during thermal loading at constant isotropic effective stress. The parameter β , corresponding to the plastic rigidity index at constant temperature, was calibrated on isothermal standard mechanical tests provided by the same authors, as proposed by [12]. The volumetric thermal dilation coefficients were chosen according to characteristic values available in the literature [10].

The first example [6] consists of an isotropic drained non-isothermal test on NC remoulded Kaolin clay. The mineralogical content of the tested material was analysed by mean of X-ray diffraction [6]. It revealed the presence of kaolinite ($\sim 65\%$) and quartz ($\sim 35\%$). The heating-cooling cycle ($22^\circ C \rightarrow 90^\circ C \rightarrow 22^\circ C$) was performed at a confining pressure of $600 kPa$. The NC sample contracted during heating with a non-linear volume variation, which was irreversible upon cooling.

The same calibration was performed on a remoulded NC Illite specimen tested in [3] under isotropic condition. After applying an isotropic effective stress equal to $200 kPa$, the sample was subjected to a low rate temperature increase until reaching $60^\circ C$ and subsequently to a controlled cooling down to $5^\circ C$.

The model parameter γ_T of the Boom clay was calibrated against an isotropic consolidation test at constant effective stress ($p'_c = 6 MPa$) performed by [14] on natural Belgian Boom Clay. The tested material was a relatively soft, highly plastic, smectitic clay composed by 20% smectite, 20% kaolinite and 20% illite. Even in this case the thermal loading was applied at a very low heating rate under computer controlled zero pore pressure condition, from $20^\circ C$ to $95^\circ C$ and then back to $20^\circ C$.

Natural soft Bangkok clay, obtained from 3.0 to 4.0 m depth, was used in the isotropic and non-isotropic experimental campaign conducted by [1]. The mineralogical composition of the material was analyzed by X-ray diffraction, revealing that this soft Bangkok clay consisted of smectite and illite, ranging from 54 to 71% with kaolinite 28-36% and mica [1]. After imposing an isotropic effective stress of $300 kPa$, the specimen was subjected to drained heating and subsequent cooling ($22^\circ C \rightarrow 90^\circ C \rightarrow 22^\circ C$), showing a marked irreversible volumetric strain.

Finally, a natural Clay collected in situ near Geneva, in Switzerland was analysed by [9]. According to the material characterisation performed by [9], the tested clay is poorly plastic ($PI < 20\%$) but there is no specific record of the mineralogical content. In this case, the NC specimen underwent a thermal cyclic loading ($20^\circ C \rightarrow 60^\circ C \rightarrow 5^\circ C$) under oedometer condition ($\sigma'_v = 200 kPa$).

The calibrated values of β and γ_T are given in Table 2 while the comparison between experimentally observed and predicted volumetric strains for the three aforementioned clays is

presented in Figure 5 and Figure 6.

Clay type	Mineralogical composition				Test	β [-]	β_s [$10^{-5} \circ C$]	γ_T [-]
	Kaolinite [%]	Illite [%]	Smectite [%]	Others [%]				
Kaolin [5]	65	~ 0%	~ 0%	35 (quartz)	ISO	21.0	2.9	0.14
Illite [3]	~ 0%	~ 96%	~ 0%	~ 4%	ISO	22.2	2.5	0.17
Boom Clay [14]	29	19	22	30 (quartz)	ISO	18.0	1.8	0.21
Bangkok Clay [1]	28-36		54-71	1-18 (mica)	ISO	5.5	3.5	0.21
Natural Clay [9]	unknown mineralogical composition				OED	67.0	1.8	0.25

Table 2: Constitutive parameters β , β_s and γ_T evaluated for five different types of clay.

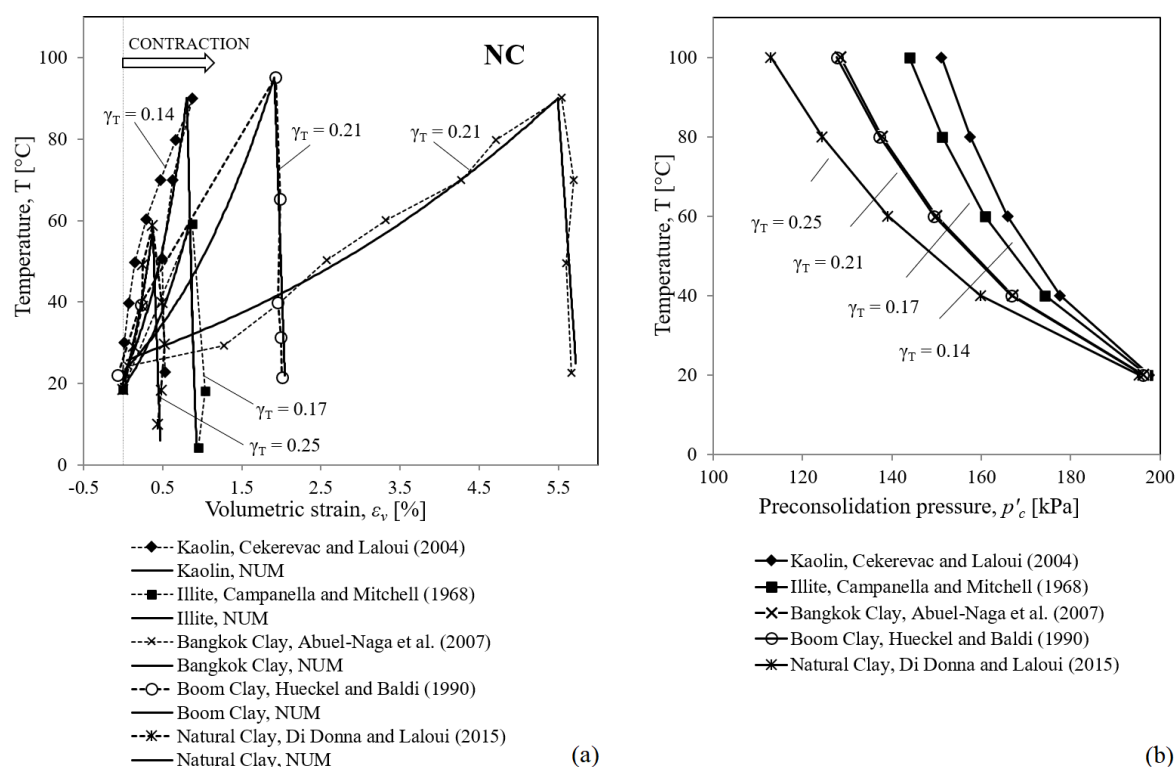


Figure 5: Calibration of the ACMEG-T parameter γ_T for five different type of clay.

Figure 6: Shape of the isotropic thermomechanical yield limit for different values of the parameter γ_T .

The dependency of the shape of the yield locus on the parameter γ_T is shown in Figure 6. It appears that γ_T increases as the fraction of active minerals (e.g. smectite). Similarly, the plastic rigidity index β seems to decrease with the fraction of active minerals (compressibility increases).

4 Discussion

The effect of active clay fraction on the parameters β and γ_T is consistent with the micromechanical model discussed in Section 2. Plastic compression at constant temperature is associated with the disengagement of edge-to-face contacts. The weaker is the edge-to-face net attractive force, the higher is the rate of loss of edge-to-face contacts and, hence, the compressibility.

According to [19], alumina, which is exposed at the edges of clay particles, is amphoteric, and it ionizes positively at low pH and negatively at high pH. As a result, positive diffuse layers

can develop at the edges of some clay particles in an acid environment.

The force developing at the edge to face-to-face contact is the sum of two opposite forces, the van der Waals attraction (activated between the positively charged edge and the negatively charged surface)) and the Coulombian repulsion between the adjacent negatively charged surfaces as shown in Figure 7. Since van der Waals forces prevail, the resulting force is attractive. Nonetheless, the intensity of the edge-to-face ‘net’ attractive force is influenced by the Coulombian (double-layer) repulsion between the negatively charged faces.

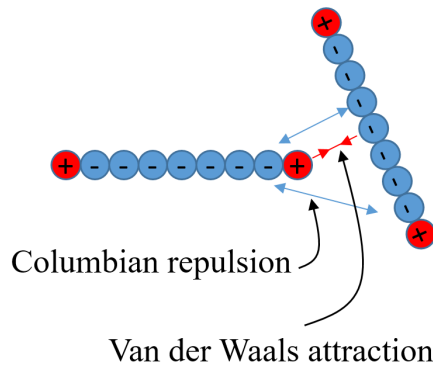


Figure 7: Sketch of the electrochemical interaction at the edge-to-face contact [4].

The existence of positive edge charges in low pH environment is of greatest importance in kaolinite, lesser importance in illite, and relatively unimportant in smectite [19]. This can be due to the smaller thickness-to-length ratio of the particle of active clay minerals.

Individual particles of non-swelling clay minerals (such as kaolinite and illite) are much thicker than smectite unit layer platelets and may consist of up to several hundred unit cell layers (see thickness t and diameter a in Table 3).

Natural clay	$a[\mu m]$	$t[\mu m]$
Kaolinite	0.5 - 4	0.5 - 2
Illite	0.5 - 10	0.003 - 0.1
Smectite (single platelet)	0.05 - 10	0.00095

Table 3: Particle thickness and particle diameter of some clay minerales [7]

Smectite clay particles are usually assumed to be a single unit layer platelets in the double layer theory. In reality, this is usually not the case, and the platelets stack into quasi-crystals [23]. For instance, when the adsorbed cation is a divalent cation, a typical quasi-crystal consists of four to seven smectite platelets interspersed by two or three molecular layers of water [26].

For clay minerals with a small thickness-to-diameter ratio such as smectite, the contribution of the termination sites at the edges is small relative to the total charge of the particles. In low pH environment, the positively charged surface-to-total surface area ratio is significantly lower than in illite and kaolinite. The effect of the double layer repulsion between negatively charged faces is predominant in active clay minerals and it influences the intensity of the edge-to-face ‘net’ attractive force. Therefore, the edge-to-face disengagement turns out to be slightly easier for active minerals thus explaining the decreasing value of β with increasing active clay fraction.

In addition, the derivative of the repulsion force F_δ [N] with respect to temperature T [°C] according to [4] can be written as:

$$\frac{dF_\delta}{dT} = -\frac{\pi a^2}{8\epsilon} \rho^2 \left(\frac{z}{\sqrt{a^2 + \delta^2} - 1} \right) \frac{1}{\epsilon 2} \frac{d\epsilon}{dT} \quad (6)$$

where a [m] is the clay particle diameter, ρ [$C \cdot m^{-2}$] is the uniform surface charge distribution, δ [m] is the mid-distance between particle, and ϵ [$C^2 \cdot N^{-1} \cdot m^{-2}$] is the static dielectric permittivity of the pore fluid. Since $d\epsilon/dT$ is negative, the derivative dF_δ/dT is positive, i.e. the repulsive force increases with temperature and, hence the net edge-to-face attraction decreases with temperature. This would explain the shape of the yield locus in the plane (p' , T) in Figure 3, i.e. the thermal softening. At the same time, the derivative dF_δ/dT is proportional to the clay particle diameter a , i.e. the thermal softening increases with the fraction of larger particles. This would partially explain the values of γ_T found for kaolin are slightly lower than those for illite, which are slightly lower than those for smectite.

5 Conclusions

Mechanical response of (saturated) clays upon heating is not intuitive and includes the volumetric "collapse" observed in normally consolidated clays. Numerical modelling of thermal effects in clays is relevant in many specific applications. In this paper, an advanced thermo-plastic constitutive model was employed to interpret the macroscopic behaviour of saturated clays.

Some of the thermoelastic-thermoplastic evidences available in literature were reproduced with the aforementioned model. The effect of mineralogy on two key parameters of the model, namely the plastic rigidity index and the thermal softening, was explained in the light of temperature effects affecting electrochemical interactions between clay particles.

Acknowledgements

This work was funded by the ANR project GEO2 (ANR-19-CE05-0003-01). The laboratory 3SR is part of the LabEx Tec 21 (Investissement d'avenir – grant agreement n. ANR-11-LABX-0030).

References

- [1] H. Abuel-Naga, D.T. Bergado, and A. Bouazza. Thermally induced volume change and excess pore water pressure of soft Bangkok clay. *Engineering Geology*, 89:144–154, 2007.
- [2] P. Braun, P. and Delage, J. Sulem, and N. Conil. Determination of multiple thermo-hydro-mechanical rock properties in a single transient experiment: Application to shales. *Rock Mechanics and Rock Engineering*, 2019.
- [3] R.G. Campanella and J. K. Mitchell. Influence of temperature variations on soil behavior. *ASCE*, 94(3), 1968.
- [4] A. Casarella, M. Pedrotti, A. Tarantino, and A. Di Donna. A critical review of the effect of temperature on clay inter-particle forces and its effect on macroscopic thermal behaviour of clay. In *16th IACMAG, Torino (2021)*, 2021.
- [5] C. Cekerevac. *Thermal effects on the mechanical behaviour of saturated clays: an experimental and constitutive study*. PhD dissertation, École polytechnique fédérale de Lausanne, 2003.
- [6] C. Cekerevac and L. Laloui. Experimental study of thermal effects on the mechanical behaviour of a clay. *International Journal for Numerical and Analytical Methods in Geomechanics*, 28:209–228, 03 2004.
- [7] F.H. Chen. *Foundations on expansive soils*. Elsevier Scientific Pub. Co., 1975.

- [8] Yu Cui, Nabil Sultan, and Pierre Delage. A thermomechanical model for saturated clays. *Canadian Geotechnical Journal*, 37:607–620, 2000.
- [9] A. Di Donna, A. F. Rotta Loria, and L. Laloui. Numerical study of the response of a group of energy piles under different combinations of thermo-mechanical loads. *Computers and Geotechnics*, 72:126–142, 2015.
- [10] D. A. Dixon, M. N. Gray, B. Lingnau, J. Graham, and S. L. Campbell. Thermal expansion testing to determine the influence of pore water structure on the water flow through dense clays. In *46th Canadian Geotechnical Conference, Saskatoon 177-183*, 1993.
- [11] B. François. *Thermo-plasticity of fine-grained soils at various saturation states: application to nuclear waste disposal*. PhD dissertation, Ecole Polytechnique Fédéral de Lausanne, EPFL, 2008.
- [12] B. François and L. Laloui. ACMEG-TS: A constitutive model for unsaturated soils under non-isothermal conditions. *International Journal for Numerical and Analytical Methods in Geomechanics*, 32, 2008.
- [13] J. Graham, N. Tanaka, T. Crilly, and M. Alfaro. Modified cam-clay modelling of temperature effects in clays. *Canadian Geotechnical Journal*, 38(3):608–621, 2001.
- [14] T. Hueckel and G. Baldi. Thermoplasticity of saturated clays: Experimental constitutive study. *Journal of Geotechnical Engineering*, 116:1778–1796, 1990.
- [15] T. Hueckel and R. Pellegrini. Thermoplastic modeling of undrained failure of saturated clay during heating-cooling cycles. *Soil Foundations*, 31:1–16, 1991.
- [16] L. Laloui and C. Cekerevac. Numerical simulation of the non-isothermal mechanical behaviour of soils. *Computers and Geotechnics*, 35:729–745, 2008.
- [17] L. Laloui and A. Di Donna. *Energy geostructures: innovation in underground engineering*. ISTE Ltd and John Wiley & sons Inc., 1 edition, 2013.
- [18] J. Mandel. Une généralisation de le théorie de la plasticité de w.t. koiter. *International journal of solid strucutres*, 1:273–295, 1965.
- [19] J. K. Mitchell and K. Soga. *Fundamentals of Soil Behavior, 3rd Edition*. John Wiley & Sons, 2005.
- [20] H. Modaressi and L. Laloui. A thermo-viscoplastic constitutive model for clays, 1997.
- [21] K. D. Murphy and J. S. McCartney. Seasonal response of energy foundations during building operation. *Geotechnical and Geological Engineering*, 33:343–356, 2015.
- [22] M. Pedrotti and A. Tarantino. An experimental investigation into the micromechanics of non-active clays. *Géotechnique*, 68:1–18, 11 2018.
- [23] J. P. Quirk and L. A. G. Aylmore. Domains and quasi-crystalline regions in clay systems, 1971.
- [24] E. Romero, M. Villar, and A. Lloret. Thermo-hydro-mechanical behaviour of two heavily overconsolidated clays. *Engineering Geology*, 81:255–268, 11 2005.
- [25] A. N. Schofield and C. P. Wroth. *Critical state soil mechanics*. McGraw-Hill, 1968.
- [26] G. Sposito. *The Chemistry of Soils*. Oxford University Press, 2008.

- [27] J. Sulem, P. Lazar, and I. Vardoulakis. Thermo-poro-mechanical properties of clayey gouge and application to rapid fault shearing. *International Journal for Numerical and Analytical Methods in Geomechanics*, 31:523–554, 2007.

Imaging hydromechanics of water-sensitive granular media

Ilija VEGO^{1,*}, Alessandro TENGATTINI^{1,†}, Edward ANDÒ^{1,‡},
Giacchino VIGGIANI^{1,§}, Nicolas LENOIR^{1,¶}

¹ Univ. Grenoble Alpes, CNRS, Grenoble INP, 3SR, 38000 Grenoble, France

Abstract: The interaction of some granular materials with water affects their morphology and mechanical behaviour, making the wetting and drying process of high relevance and interest for pharmaceutical and food industry. Former studies were conducted on their flowability or on the individual grain mechanical response, but what happens at the micro-level and how this affects the overall behaviour is yet to be fully understood. Goal of this research is to use the complementarity of x-ray and neutron tomography to explore this dark area and study the interaction between water and these water-sensitive granular media and hopefully help calibrating and improving DEM (Discrete Element Method) numerical models.

1 Introduction

Several engineering problems originate from the complex chemo-hydro-mechanical interactions of granular media. In food or pharmaceutical industry, most materials (*e.g.*, rice, pasta, sugar, seeds...) are highly affected by the presence of humidity and/or moisture. The phenomena that occur when these granular media interact with water have direct consequences on industrial processes. The product loses its quality and might be wasted, presenting economical and most importantly ethical issues.

While the role of moisture on the mechanical response of impermeable granular media is relatively well understood, or at least thoroughly studied (*e.g.*, the so-called apparent cohesion in sand [1]), organic materials have the additional complexity of the chemical interaction with water, and they are thus referred as *water-sensitive*, enclosing the subset of effects that has to do with water influencing the mechanics of the individual grains in terms of chemistry and swelling as opposed to the capillarity effect on the granular skeleton induced by partial saturation.

Some effects of grain(s)-water interaction on mechanical properties or on flowability have been already investigated, highlighting numerous problems, such as agglomeration (bridging and caking) [2] [3], swelling [4] [5], mucilage or starch release [6] [7], loss of resistance [8] [9], creation of fissures [10], etc. The existing literature tends to concentrate on the behaviour of the individual grains or on the flow behaviour, leaving a dark area around what happens at the micro level or at macro-response in quasi-static conditions, which are the ones at which the product is stored (for instance silos).

The aim of this research is to obtain, by means of neutron and x-ray tomography, images of the wetting and drying process of water-sensitive granular materials. The interaction of x-rays and neutrons with matter is quite different. In particular, a light atom like the hydrogen is "invisible" to x-rays, while for neutrons is quite visible. On the other hand, some other elements, such as metals, which have a high atomic weight, are detectable with x-rays, but not neutrons.

*Email: ilija.vego@3sr-grenoble.fr

†Email: alessandro.tengattini@3sr-grenoble.fr

‡Email: edward.ando@3sr-grenoble.fr

§Email: cino.viggiani@3sr-grenoble.fr

¶Email: nicolas.lenoir@3sr-grenoble.fr

Consequently, using simultaneously these two different types of tomography, it is possible to distinguish the three phases (solid, water and air) of a partially saturated sample.

Once data are obtained with tomography, the images will be analysed, measuring different properties (total or single grains volume, particle radius, area and number of contact between particles...).

The ultimate aim, once image processing have provided a *quantitative* description of the processes, is to take advantage of the wealth of information to implement a numerical model, using DEM (Discrete Element Method), together with other members of Caliper ITN (Horizon 2020 funded Initial Training Network), a project of which this research is part of (www.caliper-itn.org).

2 Experimental work

2.1 Preliminary experimental campaign

A preliminary experimental campaign has been conducted on mustard seeds and pasta 'pearls' (see Figure 1). The aim was to have a qualitative overview of how water-sensitive materials behave and to observe which issues could occur while wetting them.

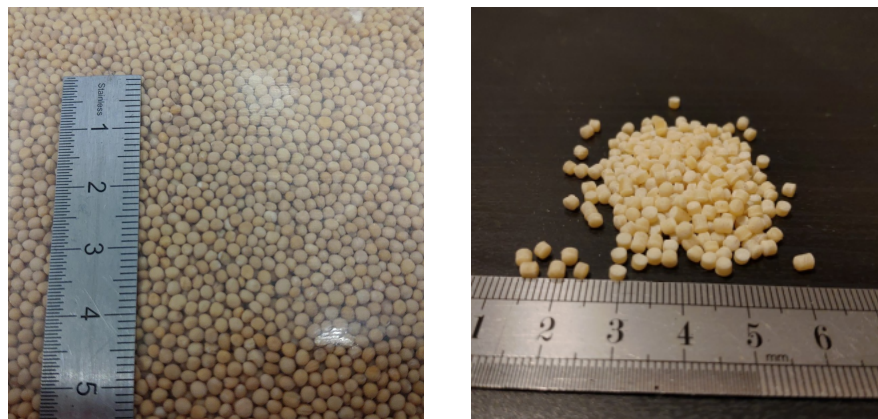


Figure 1: Water-sensitive granular materials used for the preliminary experimental campaign. *Left*: yellow mustard seeds. *Right*: pasta 'pearls' grains.

Three different tests were performed while acquiring x-ray tomographies: a soaking test on mustard seeds and a wetting test for both mustard and pasta. For all the experiments, in order to detect the fast rate of the processes occurring inside the sample, a scanning time of 4 min for each step was chosen. This fast scanning rate returned images with a $30 \mu\text{m}$ pixelsize.

In the first test, two single seeds were submerged in water to detect volume increase. It is possible to see in Figure 2 how swelling was not the only phenomena occurring. In fact, cracks open inside the seeds and they also start peeling away. At the end of the wetting process cracks are no longer visible at the scan resolution.

Wetting tests, for both mustard and pasta, were performed in the same way. The grains were placed in a impermeable cylinder of 15 mm diameter. At the bottom it was placed a layer of sponge, allowing the water to enter the sample, while radial strain was prevented. The first scan was taken at dry conditions, before allowing the water to enter the cylinder (water was poured outside the cylinder, and a thin layer of cotton allowed the water to enter).

In Figure 3 is presented a detail of images collected from mustard seeds, illustrating all phenomena that occurred in the soaking process, plus mucilage release (as expected from [6]).

The pasta 'pearls' showed more drastic and quicker response to the presence of water (see Figure 4). Grains swelled, cracked and released starch, creating mucilage that has a similar attenuation coefficient of the particles, so that it is difficult to make a distinction between solid and liquid phase.

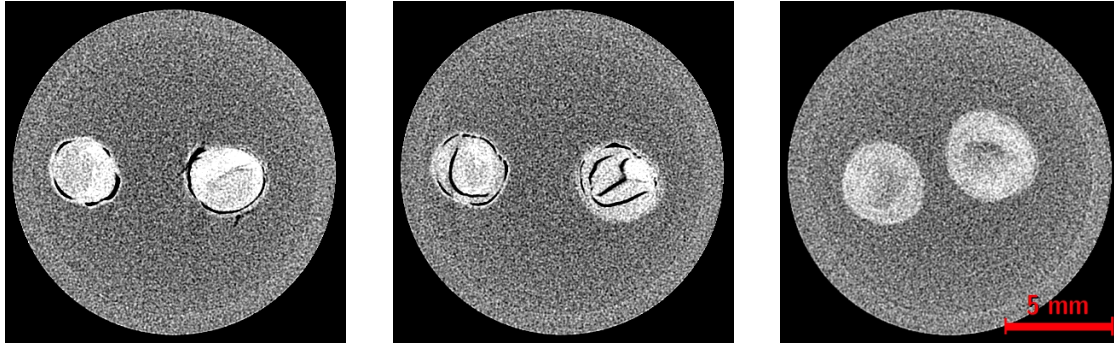


Figure 2: Submerged test on mustard seeds: horizontal slices of at $t=0$ h (right after submerging the seeds), $t=0.5$ h and $t=19$ h.

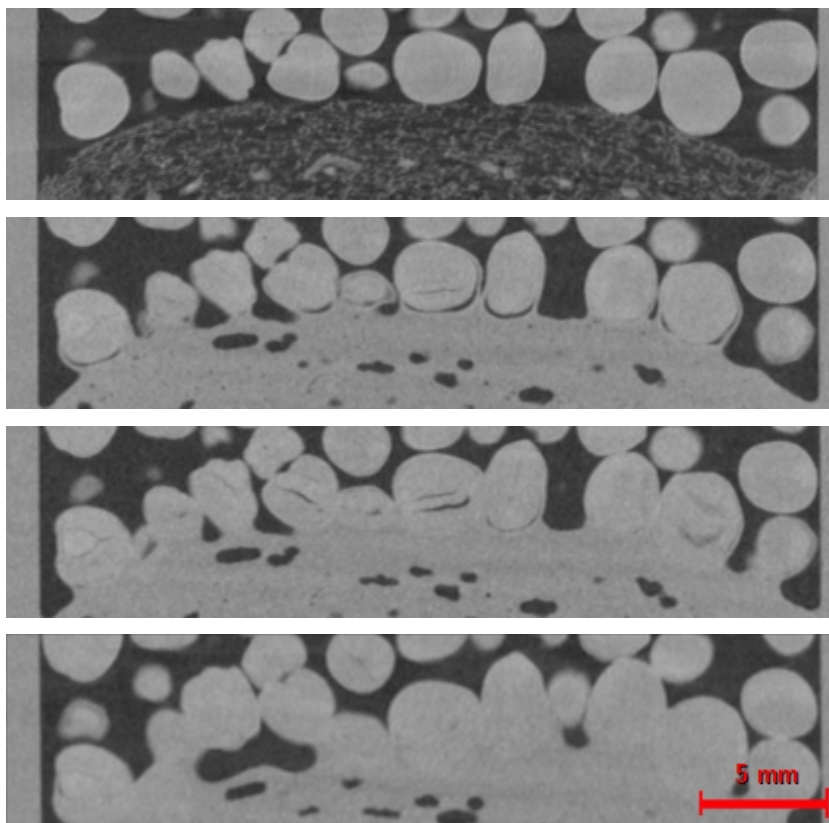


Figure 3: Wetting test on mustard seeds. Detail of vertical slices at $t=0$ h (dry), $t=0.5$ h and $t=3.5$ h.

2.2 Image analysis

spam (the Software for the Practical Analysis of Materials) has been used to analyse data collected from x-ray tomography [11]. Despite its numerous functions implemented, there are several new challenges to be faced related to water-sensitive grains. In fact, the grains change

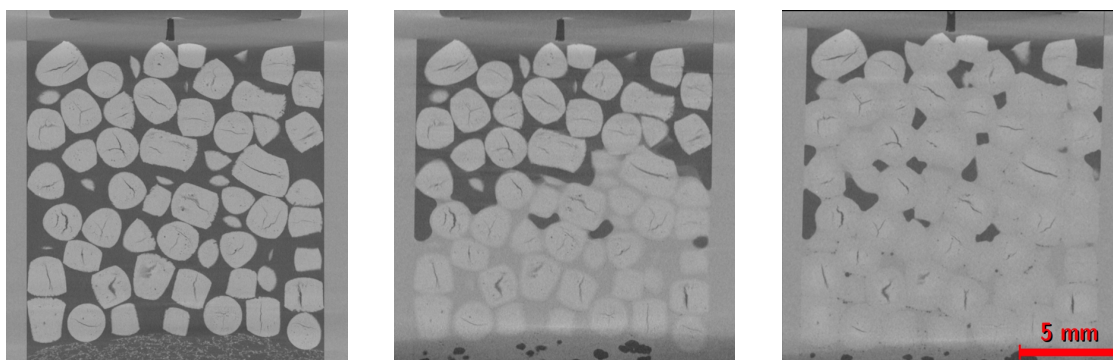


Figure 4: Wetting test on pasta 'pearls': vertical slices at t=0 min, t=4 min and t=31 min.

shape, the contact area between particles becomes bigger, the number of contact might increase too (see Figure 5), and in the sample 4 phases would be identified (solid, mucilage, liquid and air).

Consequently, analysis issues appear from the first steps, such as the threshold greyvalue to be chosen to binarise images. For example, mucilage has a x-ray "high" attenuation coefficient, so it is difficult to separate it from the solid phase, considering also that the greyvalue of the grain itself is decreasing due to swelling process.

Another issue is the correct separation of individual grains (known as segmentation). The area of contact between them increases, so the *watershed* algorithm used to label particles is visibly not capable anymore to segment them properly (Figure 5).



Figure 5: Labelled grains of pasta during wetting test, detail.

To fix this problem, a statistical approach is being implemented. Starting from a labelled image of the sample under dry conditions, the idea is to assign a belonging probability value to voxels that are close to a labelled grain g_i . The further a voxel is from the grain, the lower is its probability of being part of g_i in the future, while swelling is happening. The process is repeated for all grains, and then the results are compared, so to decide to which grain that voxel belongs and also define the contact surface. The concept is summarized in the following equation:

$$\begin{aligned} \forall v \in D_i, \quad i = 1, \dots, n \text{ and } j \in N_i \\ \text{where } p(v \in g_i) \sim p(v \in g_j) \\ \Rightarrow v \in C \end{aligned} \quad (1)$$

where v is voxel, n is the number of grains, N_i is the list of neighbours of the analysed grain, D_i the domain of voxels r around g_i and C is the contact domain between g_i and g_j .

3 Conclusion

These preliminary results on the wetting process of water-sensitive granular media confirmed how the interaction of some granular materials with water is a relevant aspect that must be considered while studying their behaviour. X-ray tomography showed how the hydro-mechanics behind this process are more complex than expected. The phenomena occurring at the macro and micro-level are numerous and not easily interpretable or predictable (for instance peeling, cracking, contact areas increase, ...).

The analysis of the images is also directly affected. Mucilage release and its high x-ray attenuation does not allow proper detection of the grains, affecting the grains segmentation and therefore all the consequent measurements (volume, contacts, ...).

The results obtained until now still have to be fully analysed, but they are a starting point for future and upcoming studies. New experimental setups have been designed and new tools are being implemented for image analysis, so that it will be possible to obtain consistent and reliable measurements of what is really happening at the micro-scale.

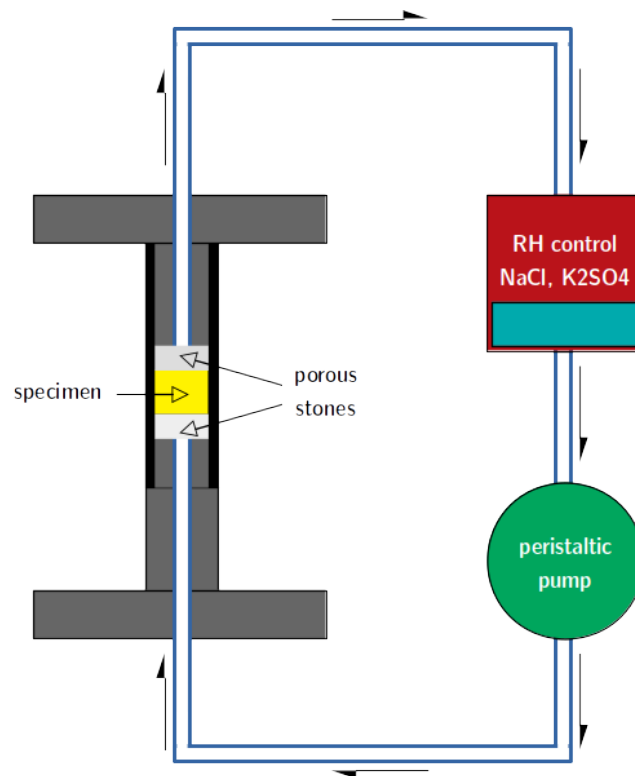


Figure 6: New setup.

3.1 Upcoming experiments

A new experimental campaign will be conducted to have more information on the wetting and drying processes. Specimens of water-sensitive granular media will be exposed to high relative humidity (RH) air (which means no liquid water, only vapour) and scanned with x-ray tomography (and in the future also neutrons), to observe what happens at the micro-scale. To do so, the specimen is placed in an oedometer and high RH air is slowly injected (≈ 15 mL/h) from the bottom with a peristaltic pump from a humidity control chamber. The air can flow outside the sample through a tube placed on the top, which is again connected to the chamber (see Figure 6). The humidity inside the chamber is kept constant by means of binary saturated aqueous

solutions, which are known to give constant RH environments [12] (for instance, sodium chloride (NaCl) → 75% RH or potassium sulphate (K₂SO₄) → 95% RH).

References

- [1] D. G. Fredlund and H. Rahardjo, *Soil mechanics for unsaturated soils*. John Wiley & Sons, 1993.
- [2] J. Aguilera, J. del Valle, and M. Karel, "Caking phenomena in amorphous food powders," *Trends in Food Science & Technology*, vol. 6, no. 5, pp. 149–155, 1995.
- [3] G. Lumay, K. Traina, F. Boschini, V. Delaval, A. Rescaglio, R. Cloots, and N. Vandewalle, "Effect of relative air humidity on the flowability of lactose powders," *Journal of Drug Delivery Science and Technology*, vol. 35, pp. 207–212, 2016.
- [4] M. Amin, M. Hossain, and K. Roy, "Effects of moisture content on some physical properties of lentil seeds," *Journal of Food Engineering*, vol. 65, no. 1, pp. 83–87, 2004.
- [5] T. Morita and R. P. Singh, "Physical and thermal properties of short-grain rough rice," *Transactions of the ASAE*, vol. 22, no. 3, pp. 630–636, 1979.
- [6] I. Siddiqui, S. Yiu, J. Jones, and M. Kalab, "Mucilage in yellow mustard (brassica hirta) seeds," *Food Structure*, vol. 5, no. 1, p. 17, 1986.
- [7] T. Sasaki and J. Matsuki, "Effect of wheat starch structure on swelling power," *Cereal chemistry*, vol. 75, no. 4, pp. 525–529, 1998.
- [8] G. Kamst, C. Bonazzi, J. Vasseur, and J. Bimbenet, "Effect of deformation rate and moisture content on the mechanical properties of rice grains," *Transactions of the ASAE*, vol. 45, no. 1, p. 145, 2002.
- [9] W. Cao, Y. Nishiyama, and S. Koide, "Physicochemical, mechanical and thermal properties of brown rice grain with various moisture contents," *International journal of food science & technology*, vol. 39, no. 9, pp. 899–906, 2004.
- [10] A. D. Sharma and O. R. Kunze, "Post-drying fissure developments in rough rice," *Transactions of the ASAE*, vol. 25, no. 2, pp. 465–468, 1982.
- [11] E. Andò, R. Cailletaud, E. Roubin, and O. Stamati, "the spam contributors, spam: The software for the practical analysis of materials," 2017.
- [12] L. Greenspan *et al.*, "Humidity fixed points of binary saturated aqueous solutions," *Journal of research of the national bureau of standards*, vol. 81, no. 1, pp. 89–96, 1977.

Modelling the evolution of porosity distributions in compacted clay pellets during imbibition

Robert CAULK^{1,*}, Nadia MOKNI^{1,†}, Bruno CHAREYRE^{1,‡}

¹ Univ. Grenoble Alpes, CNRS, Grenoble INP, 3SR, 38000 Grenoble, France

Vertical sealing systems for deep geological disposals are one of the key elements for long term containment, since they constitute the main potential pathway between nuclear wastes and the biosphere. One of the candidate materials for these vertical seals consists of a mixture of swelling clays (Na-montmorillonite) in the form of a polydisperse assembly of highly compacted pellets and crushed pellets in a strongly desaturated initial state (> 100 MPa). Since the behaviour of these highly compacted pellets during anisotropic imbibition contributes significantly to gas migration processes, the Institute of Radiation Protection and Nuclear Safety (IRSN) initiated in-situ and laboratory experiments aimed at understanding the evolution of MX80 clay pellet structure during combined hydraulic-gas loading. X-ray microtomography and CT observations reveal the development of intricate crack patterns due to vapour transport and free swelling [1].

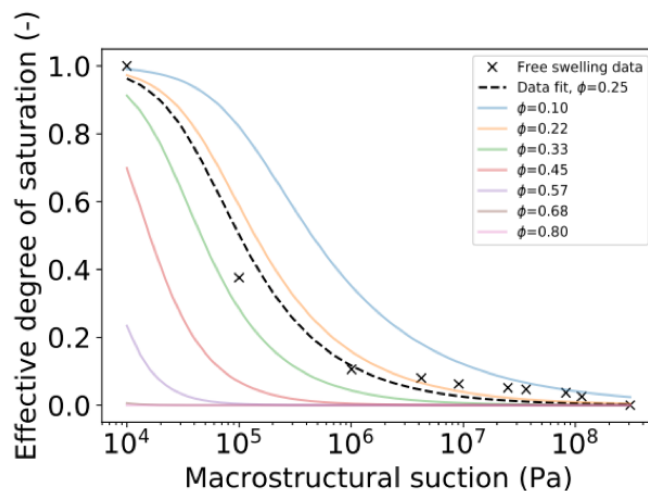


Figure 1: Heterogeneous distribution of porosity dependent water retention curves applied to the spatial discretization of the DEM+FVM model. Lower porosity regions saturate more quickly than high porosity regions.

The present work approaches the problem numerically in an effort to further elucidate the complex behaviour of the multi-scale clay pellet material during asymmetric hydraulic and gas loadings. The study starts with an introduction to the numerical framework which is based on the Discrete Element Method (DEM) coupled with the Finite Volume Method (FVM). Two key components of the novel framework include the hertzian contact law-based DEM structural

*Email: robert.caulk@3sr-grenoble.fr

†Email: nadia.mokni@irsn.fr

‡Email: bruno.chareyre@3sr-grenoble.fr

mechanics and the dependence of the partially saturated flow field on local porosity/water retention curves (Figure 1). Additionally, the methodology includes an entry–pressure based crack model (Figure 2, right), a suction based swelling model, and a porosity/saturation dependent permeability model.

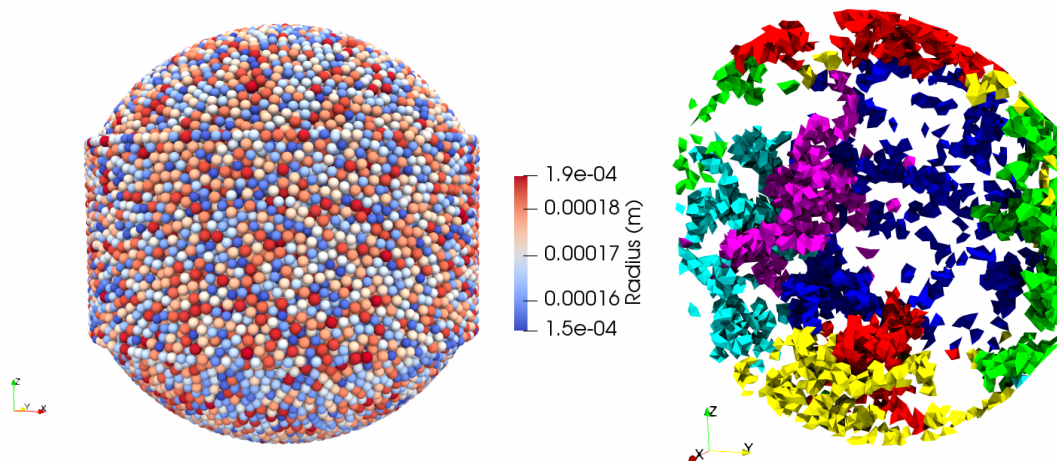


Figure 2: (left) DEM clay pellet discretization; (right) Crack network developed during saturation (colors define disconnected fractures).

The complex interaction of crack network developments is explored by simulating the genesis and imbibition of an MX80 clay pellet (Figure 2, left) which has a heterogeneous initial porosity distribution based on x-Ray CT scan imagery. Hydration of the pellet starts at 130 MPa suction and continues to 0 MPa, during which the volumetric swelling results in heterogeneous porosity field development and the development of crack networks (Figure 2, right). The evolution of the porosity is shown in Figure 3, where the mean and standard deviation both increase with hydration. These porosity evolution results follow MIP results; low porosity regions contract and saturate more quickly than large porosity regions. At the same time, high porosity regions swell and desaturate leading to the development of cracks.

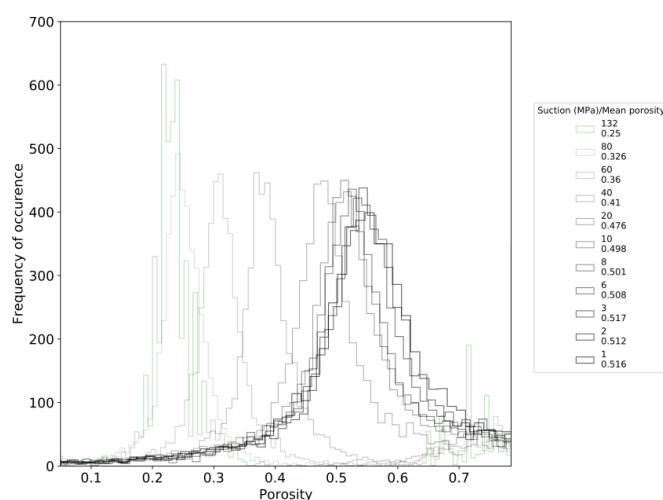


Figure 3: Evolution of porosity distribution, green line showing initial state at 132MPa. Mean and standard deviation of porosity distribution both increase during imbibition.

As shown in Figure 4, permeability evolution of the heterogenous pellet is marked by 3

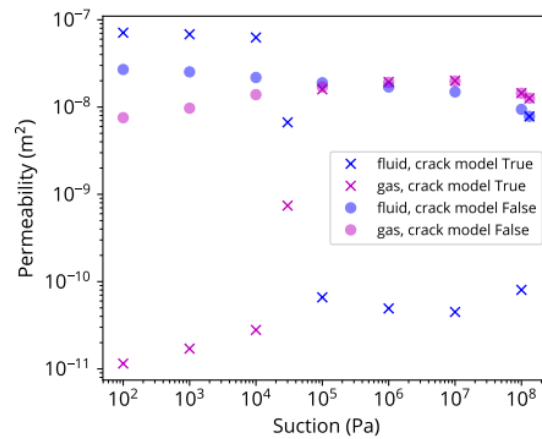


Figure 4: Evolution of macroscopic permeability during imbibition. Onset of reduced permeability due to crack network shown at 10 MPa suction followed by onset of saturated cracks contributing to permeability at 2 MPa suction.

stages: 1) increase of permeability by 1 order of magnitude (10^{-11} to 10^{-10} m²) between 100-10 MPa due to increased saturation/porosity 2) decreasing permeability by 0.5 orders of magnitude (3×10^{-10} to 9×10^{-11} m²) between 10-2 MPa due to the development of a crack network blocking pathways in the partially saturated flow field 3) increase of permeability by 3 orders of magnitude (9×10^{-11} to 10^{-7} m²) due to full saturation and the water pressure exceeding the crack entry pressure (saturated crack ratio, Figure 4).

References

- [1] Molinero, A. G. (2018). Experimental and numerical characterizations of the hydro-mechanical behavior of a heterogeneous material: pellet / powder bentonite mixture. Université Paris-Est.